UNIVERSITY OF CALIFORNIA,
IRVINE

Transient Supramolecular Interactions for Templating Peptide Folding and Designing New Self-Healing Polymers

DISSERTATION

submitted in partial satisfaction of the requirements
for the degree of

DOCTOR OF PHILOSOPHY

in Chemistry

by

Davoud Mozhdehi

Dissertation Committee:
Professor Zhibin Guan, Chair
Professor Kenneth J. Shea
Assistant Professor Aaron P. Esser-Kahn

2015

DEDICATION

To

My family

Mahboubeh, Behrooz, and Dariush

For their unconditional support of my journey

even when it separated us for six years

TABLE OF CONTENTS

LIST OF FIGURES

LIST OF TABLES

LIST OF SCHEMES

ACKNOWLEDGMENTS

I owe the completion of this dissertation to many people who have supported me throughout the past six years. This is an acknowledgment to those who believed in me, celebrated my success, comforted me in times of failure, and inspired me to finish this difficult journey.

I would like to first thank my family for their unconditional support. The photo, capturing the moment that we spent together during the last week before my departure, was always on my desk and buoyed my hopes during my darkest days. I felt your love and care, even when an ocean and two continents separated us. In addition, I am grateful for the support of my extended families, aunts, uncle and cousins in the United States. Your calls, visits and support warmed my heart and helped reassure me.

In addition, I would like to thank my advisor, Professor Zhibin Guan, who provided me with the freedom to pursue my interests in organic chemistry and polymer sciences. I am grateful for this opportunity, which has helped transformed me from a science enthusiast into a researcher with a broad skillset. His encouraging remarks motivated me even while I faced the challenges of research. I am also thankful for my thesis defense committee members, Professors Kenneth Shea and Aaron Esser-Kahn. I always enjoyed discussing my progress (and at times, the lack thereof) with them and, ultimately, benefited from their perspective and advice. I would like to thank all three for helping me to take my career to the next level by helping me in my quest for a postdoctoral position.

Furthermore, I was very fortunate to work with a great group of people in the Guan lab, who not only supported me as colleagues in the lab, but also as friends. I cherish your friendship and wish you the very best in your future endeavors. Jae Chung, Olivia Cromwell, and James

Neal (from the biomimetic subgroup) provided significant help with the projects discussed in the last two chapters of this dissertation. I learned much from your critical analysis of my work and enjoyed discussing science with you. I am grateful for your willingness to proofreading this dissertation despite your hectic schedules. You have been great friends and colleagues, and I will always appreciate it. I only wished that we could have spent more time together had I started the self-healing projects earlier.

Even though I did not get the chance to work on a project with the catalysis subgroup, Tobias Friedberger, Justin Crumrine, Dr. Miguel Camacho Fernandez were always willing to help and support me, and for that, I am grateful. They brought a unique inorganic perspective to our scientific discussions, and each one of them (through their unique personalities) helped me face the challenges of graduate school in different ways. I can only hope to integrate Tobias's rationality and calm manner, Justin's easygoing personality, and Miguel's cynicism throughout the rest of my life. I will miss our discussions, coffee breaks, lunches, and laughs. Finally, I would like to thank the other lab members, including Mark Johnson, Dr. Aaron Kushner, Nathan Oldenhuis, and Jonathan Ruiz.

In addition to the graduate students in the Guan lab, I am also grateful for the input and influence of a number of the undergraduate students I work alongside with. I would also like to thank Sergio, my undergraduate assistant, who spent about two years working with me. His hard work and great personality significantly changed the trajectory of my research projects. I wish him the very best now as he started his own graduate career at UCSD. It was also a pleasure to work with Yves Cordeau on the incorporation of different metals during his SURF rotation. I enjoyed our time together and appreciated his work on expanding our work to other transition

metals. Finally, although we never worked on a project together, I appreciated LeeAnne Wang's unique perspective on many subjects and enjoyed our discussions.

When I joined the Guan lab, I greatly benefited from the support and guidance of many of the senior members of the Guan group. In particular, I would like to thank Dr. Ting-Bin Yu for his patience and support. He thought me everything that I know about peptide synthesis and characterization. Jason Lusk was another great colleague and friend who brighten up my experience in the lab. I would like to thank Dr. Sophia Liao for the islet encapsulation collaboration and Dr. Kanika Chawla for her educational lecture series. I am also thankful to Kevin Chen, Dr. Jens Hentschel, Hannah Little Dr. Yi-Xuan Lu, Tim Tiambeng, Dr. Gregory A. Williams, Max Yen, and Dr. Hanxiang Zeng.

Special thanks is also given to Prof. Ali Mohraz, Jessica Witt, and Max Kaganyuk for their help in conducting rheological experiments and interpreting the data. Additionally, I am grateful for the UCI chemistry staff and facility directors for their help in using the instruments and providing support troubleshooting any issues during the experiments, specifically Ahmad Alshawa, Beniam Berhane, Philip Dennison, Dmitry Fishman, John Greaves, and Shirin Sorooshian.

To the many current and former graduate students and postdocs in the Department of Chemistry who assisted with different aspects of my research or proofread my manuscripts, grant proposals and advancement papers, my heartfelt thanks goes out to you. I am grateful for all the time and support you provided: Dr. Jessica Arter, Dr. Jack M. Beierle, Dr. Pin-Nan Cheng, Dr. Joshua Dibble, Dr. Glenn Eldridge, Dr. Melody Esfandiari, Dr. Agi Hajduczki, Stan Hiew, Richard Hill, Dr. Joshua J. Hirner, Dr. Dave Jackson, Evelyn Khamou, Dr. Avinash Khanna, Juliet Khosrowabadi, Dr. Maya Kleiman, Chris Kotyk, Jonathan Lam, Kim Le, Dr. Sudipta

Majumdar, Dr. Rock Mancini, Amir Mazaheripour, Dr. Shawn Miller, Kritika Mohan, Dr. Issa Moody, Du Nguyen, Dr. Cathie Overstreet, Jonathan Paretsky, Dr. Mike Shaghafi, Janine Tom, Samuel Tartakoff, Alexander Wagner, Adam Weisman, and Dr. Keiichi Yoshimatsu.

Last, I would like to thank all my friends in Irvine, Mehrdad, Saedeh, Cyrus, Makan, Ali Ahmad, Omid, Anastasia, and Shannon. I enjoyed your companionship and had so much fun being around you.

Finally, I would like to thank the National Science Foundation (NSF) and the Department of Energy (DOE) for their support of my research and the UCI Department of Chemistry and the UCI Pedagogical Fellowship for the opportunity to advance my teaching skills. I would also like to acknowledge the Royal Society of Chemistry and the American Chemical Society for permission to use some of my published works in this dissertation.

DAVOUD MOZHDEHI

UNIVERSITY OF CALIFORNIA, IRVINE
DEPARTMENT OF CHEMISTRY
1123 FREDRICK REINES HALL
IRVINE, CA. 92697-2025

DMOZHDEH@UCI.EDU
WORK: (949) 824-9172

EDUCATION

Ph.D., Organic Chemistry, **University of California, Irvine** 2009–2015
Advisor: Professor Zhibin Guan
Dissertation**:** Self-healing Elastomeric Metallopolymers Utilizing Labile Metal-Ligand Interactions

Advanced Pedagogy and Academic Job Preparation, **University of California, Irvine** 2013-2014
Teaching, Learning, & Technology Center (TLTC)

B.S., Chemistry, **Sharif University of Technology**, **Tehran, Iran** 2008
Valedictorian

RESEARCH EXPERIENCE

Graduate Student Researcher, University of California, Irvine 2009-2015

- **Templating Peptide Folding Using Supramolecular Amino Acids**
  Designed and synthesized two unnatural supramolecular amino acids (SAA). Incorporated SAAs into various peptide sequences and studied the folding using NMR spectroscopy.
- **Synthesis of Saccharide-Peptide Hydrogels For Islet Encapsulation**
  Synthesized and characterized various saccharide-peptide copolymers for islet encapsulation.
- **Self-Healing Metallopolymers Using Dynamic Metal-Ligand Interactions**
  Designed and synthesized monomer with an imidazole moiety. Incorporated this monomer into brush copolymers and studied mechanical and self-healing properties after cross-linking with various transition metals.
- **Self-Healing Polymers From Inexpensive And Commercially Available Building Blocks**
  Developed protocols for rapid and large-scale synthesis of self-healing polymers from commercially available building blocks.

Undergraduate student researcher, Sharif University of Technology 2007-2008

- **Production of Alkaline Proteases from Microbial Sources for Laundry Detergents**

Worked on optimizing the production of proteases from *Bacillus licheniformis*.

AWARDS AND HONORS

People's choice award, Association of Graduate Students symposium, UC Irvine	2014
Teaching Excellence & Service to Academic Community	2014
UCI Pedagogical Fellowship	2013
UCI Department of Chemistry Teaching Award	2012
Top Student Award, Sharif University of Technology	2009
Silver Medalist, Iran National Chemistry Olympiad	2003

PUBLICATIONS

1. **Mozhdehi, D.**; Guan Z. Design of Supramolecular Amino Acids to Template Peptide Folding. *Chem. Commun.* **2013,** *49,* 9950.
2. Liao, S. W.; Rawson, J.; Omori, K.; Ishiyama, K.; **Mozhdehi, D.**; Oancea, A. R.; Ito, T.; Guan, Z.; Mullen, Y. Maintaining Functional Islets Through Encapsulation in an Injectable Saccharide-Peptide Hydrogel. *Biomaterials* **2013,** *34,* 3984.
3. **Mozhdehi, D.**; Ayala S.; Cromwell O. R.; Guan Z. Self-Healing Polymers Using Dynamic Metal-Ligand Interactions.

J. Am. Chem. Soc. **2014,** *136*, 16128.

6. Neal, J.; **Mozhdehi, D.**; Guan, Z. Enhancing Mechanical Performance of a Covalent Self-Healing Material by Sacrificial Non-Covalent Bonds. *Submitted*
5. **Mozhdehi, D.**; Kushner, A. M.; Ayala S.; Cromwell, O. R.; Guan, Z. Multiphasic Self-Healing Polymers From Inexpensive Building Blocks. *Manuscript in preparation.*
6. **Mozhdehi, D.**; Neal, J.; Cordeau, Y. J.; Ayala, S.; Guan, Z. Role of Metal−ligand Bond Strength and Exchange Dynamics on the Mechanical Properties of Self-Healing Metallopolymer. *Manuscript in preparation.*

POSTERS AND PRESENTATIONS

248th ACS National Meeting Fall 2014
Mozhdehi, D.; Ayala, S.; Guan Z. San Francisco, CA
Poster: Multiphasic Self-Healing Materials from Simple Building Blocks.

UCI AGS symposium Spring 2014
Mozhdehi, D.; Ayala, S.; Guan Z. Irvine, CA
Talk: Lessons From Wolverine: Advanced Self-Healing Materials.
This 10-minute TED-style talk was aimed at general public. http://vimeo.com/102998893.

247th ACS National Meeting Spring 2014
Mozhdehi, D.; Guan Z. Dallas, TX
Talk: Supramolecular Amino Acids Assisted Peptide Folding.

247th ACS National Meeting Spring 2014
Mozhdehi, D.; Ayala, S.; Guan Z. Dallas, Tx
Poster (Sci-Mix): Application of Metal-Ligand Interactions to a Multiphasic Self-Healing Metallopolymer.

247th ACS National Meeting Spring 2014
Mozhdehi, D.; Ayala, S.; Guan Z. Dallas, Tx
Poster: Enhanced Proteolytic Resistant Saccharide-Peptide Hydrogels.

International Pancreas & Islet Transplant Association Spring 2013
Liao, S.; Omori K.; Rawson J.; **Mozhdehi, D.**; Nair I.; Ayala S.; Todorov I.; Guan Z.; Mullen Y. Monterey, CA
Talk: The Effect of Cell-Matrix Interaction on Encapsulated Human Islets.

243th ACS National Meeting Spring 2013
Mozhdehi, D.; Guan Z. San Diego, CA
Poster: Design and Application of Unnatural Supramolecular Amino Acids As Templates For Peptide Folding.

TEACHING EXPERIENCE

Teaching Assistant, UC Irvine 2009-2014
15+ quarters of teaching experience: general chemistry series, organic chemistry series, honors organic chemistry, advanced lab in the chemistry and synthesis of materials.
A sample of evaluation and my teaching philosophy can be found at: http://goo.gl/V1M0DH

Mentor for the UC Irvine's Summer Undergraduate Research Fellowship (SURF) 2013-2014
Mentored two undergraduate students (Sergio Ayala and Yves Cordeau) in development and implementation of their summer research projects. The results of these projects are presented in national meetings or incorporated in future manuscripts.

TA Professional Development Program (TAPDP) 2013
Organized and conducted a series of workshops to prepare first year chemistry graduate students for their TA assignments. TAPDP is a day and half series of discipline specific workshops that are designed by pedagogical fellows with the assistance of the Teaching, Learning and Technology Center. These interactive workshops cover a broad range of topics such as UCI student demographics, TA roles and responsibilities, diversity in classroom,

learning styles, etc.

SERVICE

Volunteer judge for Intel International Science and Engineering Fair (Intel ISEF) regional competition	2014
TA professional development program for chemistry department	2013
Coordinator and organizer of a monthly symposium for graduate students and postdocs	2012

SKILLS

Laboratory:

Synthesis

Organic synthesis, Schlenk techniques, polymer synthesis techniques such as interfacial polymerization, atom transfer radical polymerization (ATRP) , reversible addition fragmentation chain transfer polymerization (RAFT), solid-phase synthesis of peptides, peptoids, and peptide nucleic acids, molecular cloning, bacterial over-expression of recombinant proteins, protein purification.

Characterization

1D and 2D nuclear magnetic resonance (NMR), infrared spectroscopy (IR), UV/Vis spectroscopy, Raman spectroscopy, circular dichromism spectroscopy (CD), polarimetry, mass spectrometry (ESI-MS, GC-MS,LC-MS, and MALDI), high-pressure liquid chromatography (HPLC), size exclusion chromatography (SEC), dynamic light scattering (DLS), differential scanning calorimetry (DSC), thermal gravimetric analysis (TGA), dynamic mechanic analysis (DMA), rheology.

Computer:

OS: Windows, Linux, familiarity with Macintosh. *Software:* ChemDraw, Chem3D, E-Notebook, Maestro, PyMol, MacroModel, MS Word, MS excel, MS PowerPoint, MS Publisher, Igor Pro, Origin, Adobe Photoshop, ImageJ.

REFERENCES

Available Upon Request.

ABSTRACT OF THE DISSERTATION

Molecular Engineering of Transient Interactions to Template Peptide Folding and Synthesis of New Self-Healing Polymers

By

Davoud Mozhdehi

Doctor of Philosophy in Chemistry

University of California, Irvine, 2015

Professor Zhibin Guan, Chair

Engineering transient interactions is a powerful method that can be used to encode structure and function in chemical systems. This is the common theme in all three chapters of this dissertation, despite the slight differences in initial motivations. I begin my dissertation by describing my efforts to direct peptide folding in organic environments using supramolecular amino acids (SAAs). The incorporated supramolecular motif has a strong driving force to dimerize in a sequence- and orientation-specific manner. By introducing SAAs into the primary sequence of peptides, we envisioned to perturb the native hydrogen bond patterns and facilitate the folding of the peptides through specific and directional dimerization of the supramolecular units.

In Chapter 2, I describe the synthesis and characterization of a new self-healing multiphase polymer, in which, a pervasive network of dynamic metal–ligand (zinc–imidazole) interactions are programmed in the soft matrix of a hard/soft two-phase brush copolymer system. Following mechanical damage, these thermoplastic elastomers show excellent self-healing

ability under ambient conditions without any intervention. The mechanical and dynamic properties of the materials can be tuned by varying a number of molecular parameters (e.g., backbone/brush degree of polymerization and brush density) as well as the ligand/metal ratio. This chapter concludes by noting an attempt to correlate the observed mechanical properties to the small molecule parameters of metal-ligand complexes.

Synthesis of multiphasic self-healing polymers prepared from simple commercially-available monomers in a facile and scalable manner was the motivation behind the work described in the Chapter 3. The mechanical properties of these new polymers are easily tunable across a broad range (from soft rubber to hard plastic) by changing several molecular parameters. Self-healing ability was investigated at mild conditions, and most notably, most samples demonstrate excellent self-healing abilities with minimal intervention.

CHAPTER 1 Supramolecular Amino Acids to Template Peptide Folding

1.1 Introduction

Proteins are the machinery of life as we know it, performing a broad range of structural, and functional roles in living cells. It is fascinating that this magnificent array of roles are conducted by linear copolymers of 20 amino acids that fold into a compact information rich nanomachinery. I have remained envious of the dazzling collection of function and structures that is encoded by these relatively simple building blocks. Through groundbreaking work of Anfinsen[1,2] and others,[3] it is now well-established that the structure and function of proteins are encoded at the level of primary structure through linear arrangement of amino acids (or protein sequence). Still, my scientific curiosity is stimulated by many unanswered questions. What is special about these 20 building blocks? Is it possible to find another sets of monomers to display similarly complex folding and function? What if the evolution of life was occurring in a non-water based environment? Even more straightforward questions about the protein folding and prediction of higher order structures from the linear sequence are still unanswered or remain challenging to answer.

While there is no shortage of creative examples of utilizing naturally evolved protein to design structural material and functional molecules,[4] further understanding of protein folding unleashes tremendous potentials to design functional peptides or peptidomimetics. Despite major progress made in the last several decades, the *de novo* design of a peptide that can fold into a predicted 3-dimensional structure remains a grand challenge.[5,6] With the aim to control the spatial arrangement of sequences that are rich in information and function and to design new functional peptide-based materials for biomedical purposes, a tremendous amount of effort has been devoted

to the design of synthetic mimics of protein secondary structural elements including α-helices[7,8], β-sheets[9], β-turns, and loops.[10,11]

Before reviewing some of these approaches, it is useful to consider the folding process from purely thermodynamic perspective using a simple model reaction. This simple Tetramer Toy Model (TTM) still captures many of the critical aspects of protein and peptide folding. It also provides a thermodynamic rationale for the designs that will be discussed later on.

1.2 Folding reaction: a thermodynamic perspective

To better understand the forces that govern and steer the folding process from a thermodynamic point of view, let us consider a chain made out of four building blocks with confined degrees of freedom on a 2D lattice. In the absence of any favorable or pre-programmed interactions between the building blocks, the chain will adopt one of the four possible conformations, after the exclusion of conformers that occupy restricted space (i.e. having more than one building block in a cell). As shown in the Figure 1.1, the structure will not fold and merely exist as an ensemble of four possible configurations, maximizing the entropy of the system.

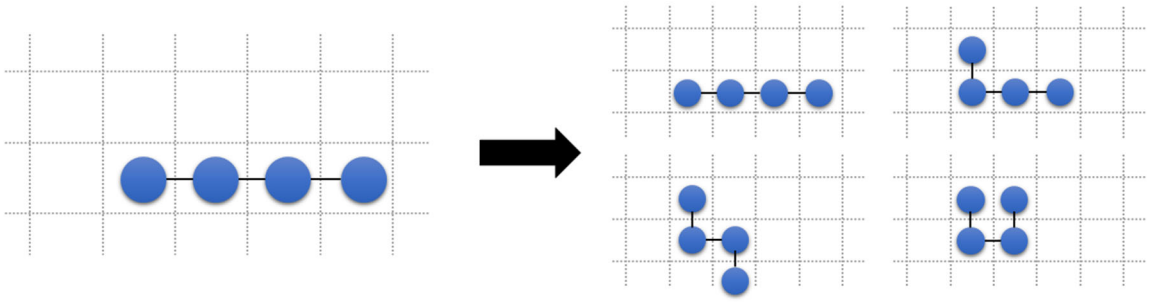

Figure 1.1 Tetramer Toy Model representation of the folding process. In the absence of favorable interactions, folding cannot occur and an ensemble of four structures are obtained.

On the other hand, if a favorable interaction (defined by an energetic reward upon satisfaction of spatial arrangement) is programmed by introducing two self-associating units at the end of the chain, an interesting situation can arise. Only one of the four possible configurations places the associating units (green monomers in Figure 1.2) in the adjacent cells allowing them to form the energetically favorable bond. This association breaks the energetic degeneracy between the equivalent structures and separates their energy level by a gap with the magnitude of the favorable interaction.

The unfolded chain can populate any of the three configurations, S= k ln(3), while there is only one folded structure, S=k ln(1). On the other hand, the folded structure is stabilized by the favorable interaction. From this simple picture, it is clear that the folding reaction is the trade of the system entropy to form energetically favorable interactions and the change in the free energy of the system during the folding process can be written as $\Delta G = \Delta H - T\Delta S = \varepsilon + kT \ln \omega$. The first term in this equation is the sum of enthalpic contributions and the second term represents the loss of degrees of freedom upon folding.

This simple calculation suggests that an energetically favorable process is necessary for proper folding since the folding process is always accompanied by the loss of entropy through reduction of degrees of freedom of the chain. This reduction in energy of the system can either be a result of the formation of new bonds across building blocks (i.e. hydrogen bond, disulfide bridge, and etc.) or by minimizing the unfavorable interactions (such as violation of Van der Waals radii or reduction of solvophobic interactions).

Despite the insight that is provided by TTM model, this simple thermodynamic consideration fails to justify the surprisingly fast kinetics of folding. It appears that a (peptide)

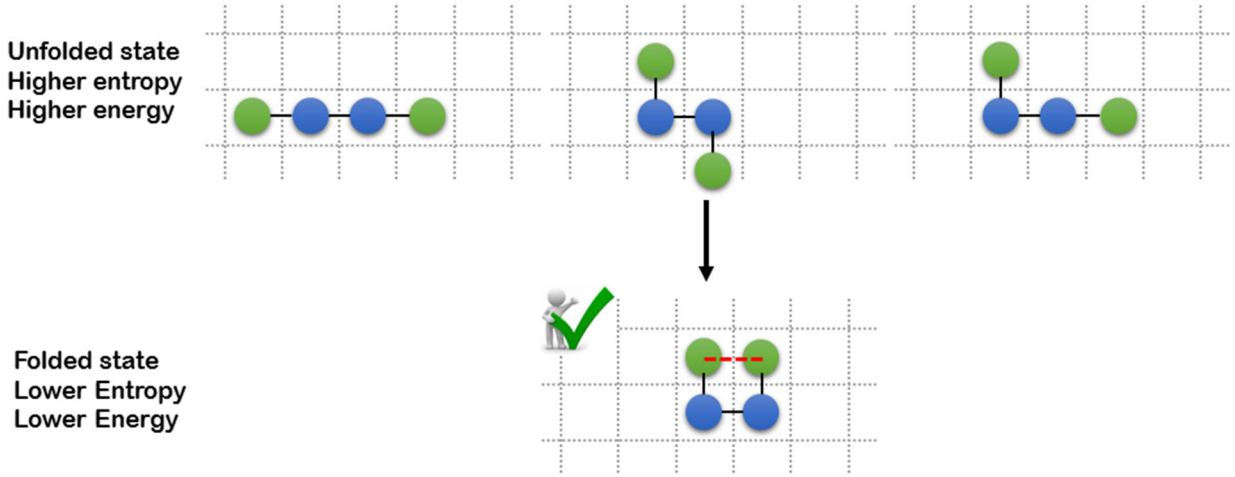

$$\Delta G = \Delta H - T\Delta S = \epsilon + kT \ln \omega$$

Figure 1.2 TTM folding upon the introduction of non-adjacent energetically favorable interactions. Folding requires the trade of enthalpic stabilization to compensate for the loss of degrees of freedom (adapted from reference 13).

chain cannot simply sample all of the available conformational space before reaching the folded state in a reasonable time. For chains with even a small number of building blocks, ~100, and very fast sampling time, ~picoseconds, a complete sampling of the conformational space will take longer than the age of the universe. This is in contrast with our experimental observations that most proteins fold in the time scales of minutes (also known as Levinthal's paradox[12]).

Visualization of the free energy potential of system (constructed by contributions from the change in the free energy of the chain and solvent molecules) can provide an answer to this paradox while setting the scene to discuss the important role of solvent molecules in the folding process. Figure 1.3a is a visualization of the free energy surface of our simple model which is described as the "golf course energy surface". In the absence of any driving force, peptide chain will have a low chance of finding the minimum energy state in a reasonable time. As it is described before, it is unlikely that protein or any higher order foldamer (molecule that can adopt a well-defined

structure in solution)[13] exhibit such energy profiles given the inconsistencies between the experimentally observed time of folding and the time required to fully explore this conformational space toward the global minimum. Instead, it is more likely that the shape of the energy surface for these macromolecules are similar to a funnel (Figure 1.3b), in which there is a driving force for a molecule to navigate toward the minima of this graph from any part of the energy landscape.[14]

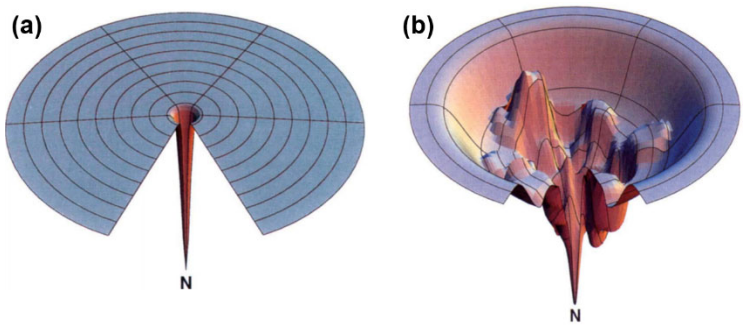

Figure 1.3 Two possible energy landscape for foldamers. (a) Golf-course energy landscape (b) A rugged folding funnel consistent with the fast kinetic of folding from (adapted and reprinted from reference 14).

As we will see in the next section, in aqueous environment, the overall shape of this funnel is significantly influenced by the hydrophobic interaction. The driving force in this case, is the reduction of solvent accessible surface area of hydrophobic amino acids and concurrent release of the immobile solvent layer around the side chains, thus increasing the overall entropy of the system. Solvent also plays a critical role in the folding process since it can also modulate the strength of other favorable interactions (such as H-bond) through its shielding effect. It is therefore necessary to consider the changes in the enthalpy and entropy of the system in the presence of solvent when building energy profiles such as Figure 1.3b.

To summarize our discussion, it is necessary to consider three factors while designing foldamers:

1) Maximize the energy gap between the folded and the unfolded states

2) Reduce the entropy of unfolded state

3) Allow interconversion of conformers toward folded state

Increasing the energy gap between the folded and unfolded states can increase the chance for the proper folding. One way to achieve this goal is to program stronger interactions, but theoretical and experimental work have revealed an interesting mechanism to increase the gap through the introduction of heterogeneity, i.e. having more than one building block with different self-association interaction parameters.[15,16]

Reducing the total number of conformational spaces available to the system through the design of building blocks with higher rigidity can enhance the chances of proper folding. Finally, it is also necessary that the energy landscape is relatively smooth all the way to the proximity of the global minima to avoid the kinetic entrapment of the folding intermediates along the folding pathway. In the next section, I briefly review the implementation of these strategies in the context of controlling peptide folding.

1.3 Strategies to control peptide folding

For small peptides, <30 amino acids, the balance between entropic and enthalpic factors are delicately dictated by a combination of forces between polypeptide chain and solvent. A simple chemical strategy to tip the balance in favor of the desired folding conformation is to apply conformational constraints into the peptide or peptidomimetic systems. By reducing the entropy of the unfolded state, one can reduce the negative entropic contributions from loss of polypeptide degrees of freedom and increase the free energy gap between the folded and unfolded states.

One method is to introduce a cyclic molecular topology to reduce conformational flexibility.[17] Alternatively, conformational constraints can be introduced into peptide sequences through incorporation of rigid organic templates[18,19] or various reinforcing molecular forces including both covalent (e.g., double bonds[20], disulfides[21] and side chain cross-linking[22-24]) and non-covalent (e.g., metal-ligand binding[25-28], hydrogen-bonding[29-32], and etc.) interactions (Figure 1.4).

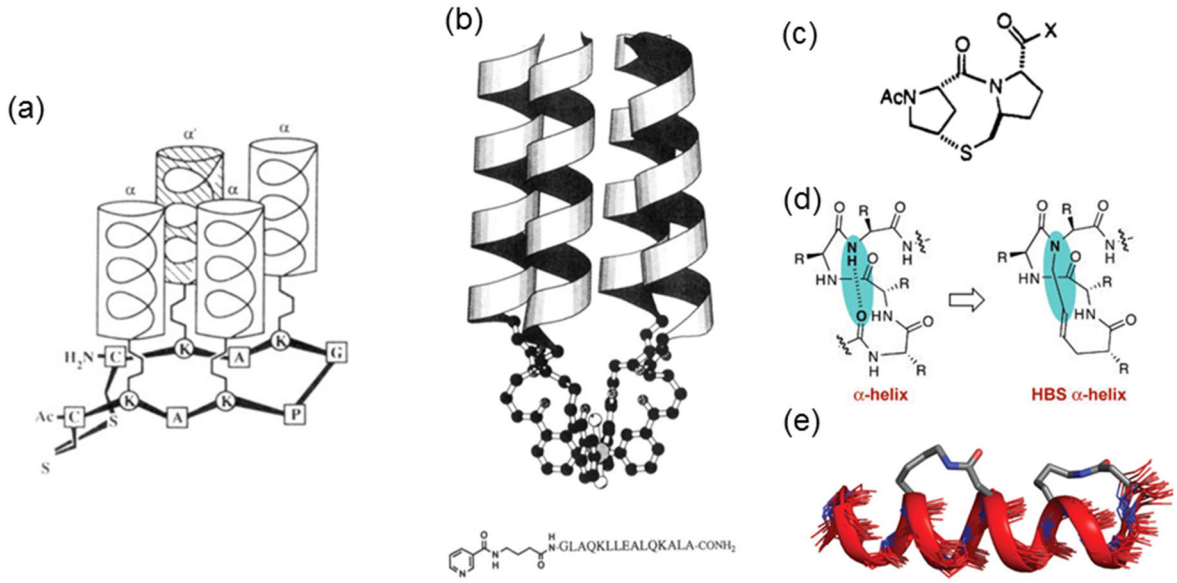

Figure 1.4 Examples of templates utilized to promote peptide folding. Commonly, these templates reduce the entropic cost of folding process. (a) Rigid organic templates (b) Metal-ligand interarctions (c) hydrogen bond/rigid template (d) and (e) covalent reinforcers (reprinted from refrences 18, 25, 29, 20, and 24).

Our simple thermodynamic model also predicts that increasing the energy gaps between the folded and unfolded state can increase the reliability of the folding process. While it is true that protein structures are stabilized by a variety of interactions such as H-bond, ion pairs, and disulfide bonds, the early stages of protein folding is driven by the collapse of hydrophobic residues to form a semi compact structure which shields their sidechains from the bulk solvent molecules.

Indeed, this aggregation event also reduces the number of conformational spaces available for proteins during their folding event. Many of *de novo* designed proteins and small peptides are stabilized by strategically incorporating hydrophobic amino acids in their primary sequence.[33]

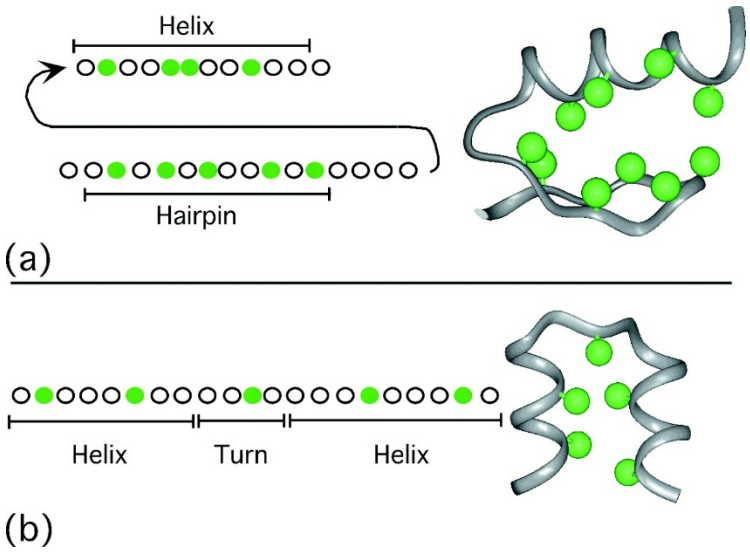

Figure 1.5 Strategic incoropration of hydrophobic amino acids to control the peptide folding in aqueous environment. The binary code of hydrophobic/hydrophilic paptterns dictate the final folding (a) helix-hair pin and (b) helix-turn-helix (reprinted from reference 33).

Our understanding of the critical role of the hydrophobic residues in peptide and protein folding is shaped by the pioneering work of Kauzmann.[34] A seminal work by Hecht and coworkers also elucidated that the peptide folding is controlled by a binary code of hydrophobic and hydrophilic amino acids (without explicitly assigning their identities).[35] Important contributions by Degrado[7,36,37], Imperiali[38], and others[39] have successfully demonstrated the possibility of controlling peptide structure and oligomerization through strategic incorporation of hydrophobic amino acids (Figure 1.6).

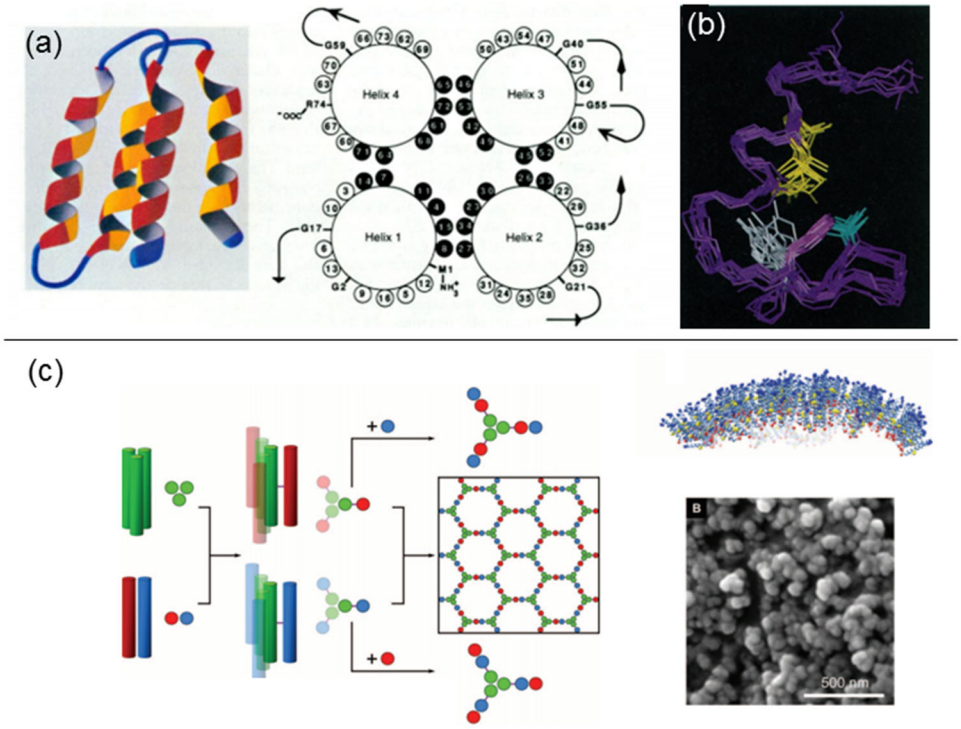

Figure 1.6 Some examples of *de novo* designed structures through incorporation of hydrophobic amino acids. (a) Helix bundle is one of the most studied example. (b) ββα motif where the amino acids forming the hydrophobic core are colored. (c) Rationally designed peptide spheres using higher order assembly of coiled-coiled motif (reprinted from references 35, 38, and 39).

1.4 Motivation for templating peptide folding in an organic environment

Given the importance of hydrophobic interaction in the peptide folding process, it is not surprising that many folded peptides and proteins are denatured in an organic solvent. The remainder of this chapter is dedicated to explaining our approach to develop a general strategy to program secondary structure in organic media.

To a skeptical reader, it may seem that the field has grown from organosoluble foldamers, and that such molecules will have no biological significance given that the protein folding and

function occurs predominately in aqueous environment. Before delving further into the details of my design, I would like to state the motivation for our efforts to template peptide folding in a nonnative environment such as organic solvents.

The first part of my argument originates from my background as an organic chemist. There is no doubt that very significant progress is being made toward design of enzymes with improved or novel catalytic properties. However, water is not the best reaction media for many organic reactions. As mentioned previously, many of the *de novo* designed peptides or peptidomimetics will not function in organic solvents as the structure denatures in the absence of main driving forces for their self-assembly, hydrophobic collapse.

The power of organocatalysts in stereoselective catalysis or enantioseparation is well-established.[40,41] As such, though an organic chemist who might be interested in trying an organic catalyst for a reaction cannot basically even attempt to use or screen any of these novel enzymes. Our approach may provide a general strategy to template complex structures in an organic media as the first step toward obtaining functional peptidomimetics that are catalytically active for organic reaction.

Secondly, studies on peptide folding in organic environment can advance our understanding of the interaction of proteins and cell membrane lipids.[42] Examples of membrane penetrating peptides and natural poisons capable of piercing through the lipid bilayer are wide-spread. Rational design and incorporation of orthogonal folding elements that are activated in non-aqueous environment can have potential impacts on the design and synthesis of macromolecules for drug delivery.[43] The rules for programming peptide folding during the transmembrane dislocation could be similar to templating peptide folding in organic medium.

1.5 Challenges of peptide folding in organic media

Motivated by the goals mentioned in the previous section, I looked at this problem of templating peptide folding in an organic medium. From previous arguments, it is clear that in such media, one cannot effectively use the hydrophobic collapse as the driving force for the peptide folding. Nonetheless, the reduction of dielectric constant increases the magnitudes of the polar interactions such as H-bond and ion-pairs in organic medium. Thus, one might first wonder if the collective combination of these strengthened polar interactions can provide sufficient energetic driving force for reliable folding? And if so, why do small peptides not automatically fold in the organic medium?

From an energetic point of view, it is plausible to replace the hydrophobic collapse with strong attractive forces such as hydrogen bonds if the entropic penalty is managed (through incorporation of strong hydrogen bonds in a rigid template).[44]

1.6 Rewriting the hydrogen bonding pattern

The main problem, in my opinion, is the simple pattern of hydrogen bonds along the peptide backbone as it is shown in the Figure 1.7. Hydrogen bond donors (D) and acceptors (A) are regularly presented on the peptide backbone, as a monotonous $(DA)_n$ script. It is clear that many possible combination for the associations of these hydrogen bonds donor/acceptor units are available and their stability are predominantly function of thermodynamic rules such as the ring size.

I looked at this problem and pondered about the possibility of rewriting this script (H-bond patterns) by simple perturbation in the patterns of H-bond acceptor and donor. For example, switching the location of one of the donor and acceptor sites in a trimeric repeat of DA significantly alters the energetic outcome and readout for the self-association of these units (DADADA→DAADDA). As shown in the Figure 1.7, now a specific hydrogen bond (shown with green arrow) is stabilized through secondary interactions of proximal donor/acceptor sites.

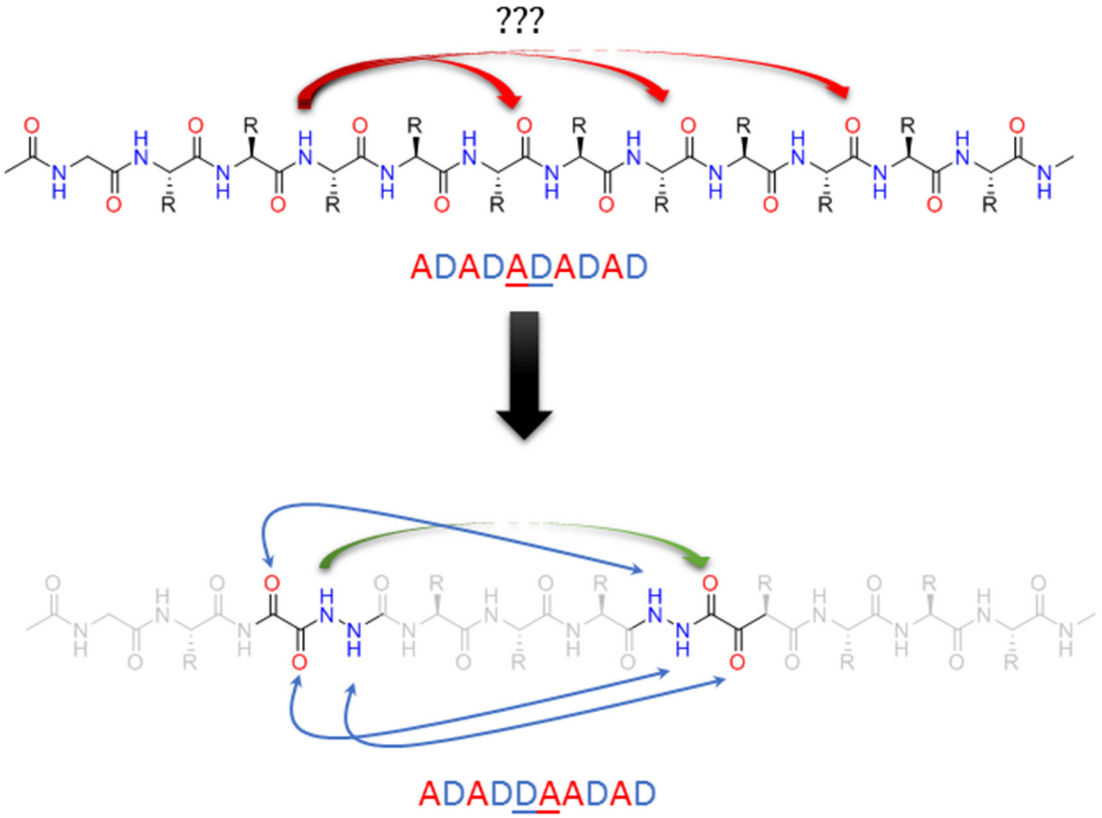

Figure 1.7 Conceptual rewriting of the H-bond pattern in the peptide backbone. Simple perturbation can be used to introduce specific recognition motifs into the peptide backbone.

This general strategy, rewriting of hydrogen bonding patterns, can be applied to incorporate sequence- and direction- specific codes to control and program peptide folding in organic media where the H-bonds are strengthened. Our goal was to introduce these specific patterns in a modular

fashion and in a manner that is compatible with current peptide synthesis technologies, e.g. solid phase peptide synthesis (SPPS).

1.7 Design of Supramolecular Amino Acids (SAA)

To this end, we designed two supramolecular amino acids (SAAs) to template peptide folding (Figure 1.8a). The designed SAAs can be viewed as analogues of regular amino acids by inserting a well-defined strong hydrogen-bonding supramolecular motif into the main-chain hydrogen bond pattern. The incorporated supramolecular motif has a strong driving force to dimerize in sequence- and orientation-specific manner. By introducing such SAAs into the primary sequence of peptides, the specific and directional dimerization of the supramolecular units should facilitate the folding of the peptides. For initial concept demonstration, we chose to incorporate our SAAs into a short peptide chain to induce the formation of a hairpin (Figure 8b). We envision that this strategy can be applied to longer peptides to induce the folding into other secondary and more complex structures.

Specifically, in this study we chose 2-ureido-4-pyrimidinone (UPy) as the strong and specific hydrogen-bonding supramolecular motif to direct peptide folding.[45,46] The DDAA hydrogen-bonding pattern (D = H-bonding donor, A = H-bonding acceptor) in UPy ensures strong and complementary dimerization in a specific orientation. To make it amenable for normal peptide synthesis, we devised two SAAs based on the UPy scaffold, CUPy and NUPy (Figure 1.8a). The two SAAs differ in the directionality of H-bonding pattern. Going from N to C terminus, the H-bonding pattern in CUPy is DDAA while in NUPy is AADD. The opposite H-bonding pattern in CUPy and NUPy would allow for templating peptide folding by strategic incorporation of these SAAs.

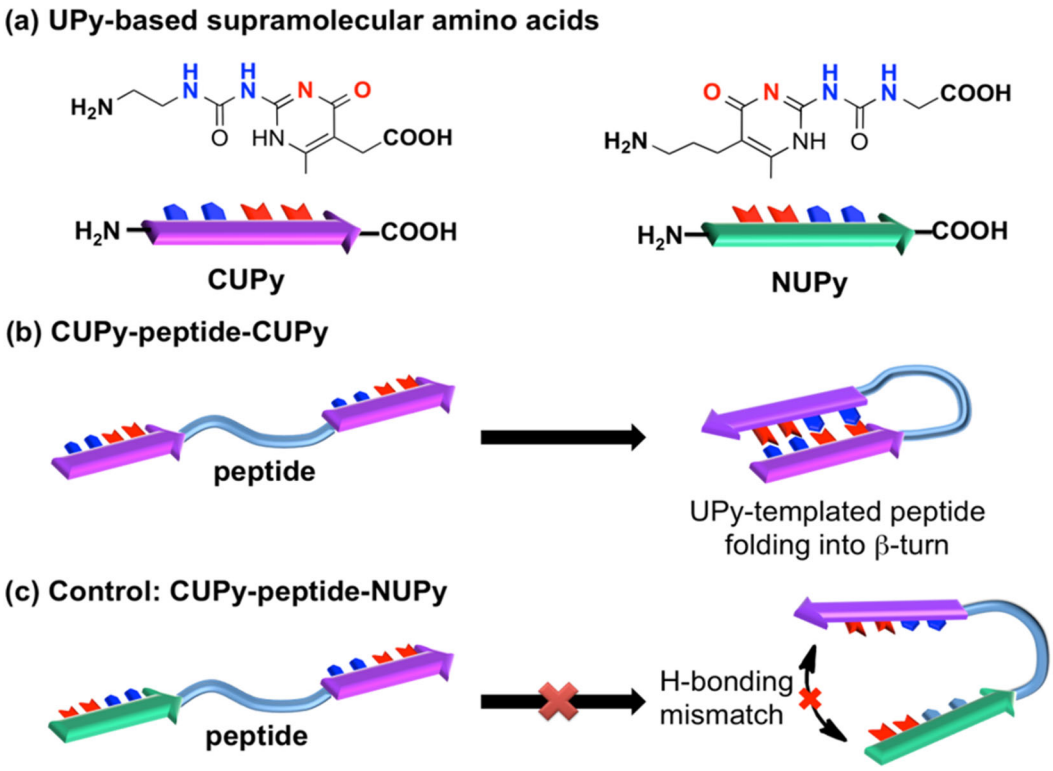

Figure 1.8 The design of supramolecular amino acids (SAAs) to template peptide folding. (a) Two UPy-derived amino acids, CUPy and NUPy, with the H-bonding donor (blue) and acceptor (red) positioned in opposite orientations. The arrows are drawn from N to C terminus. (b) Homo CUPy-CUPy dimerization directs the folding of the peptide into a β-hairpin. (c) As a control, the hetero CUPy-NUPy pair cannot dimerize in similar geometry due to the mismatch of H-bonding donor and acceptor pairs. In addition, the short peptide sequence precludes CUPy-NUPy intramolecular dimerization in an alternative orientation.

1.8 Synthesis of CUPy and NUPy

To facilitate peptide synthesis and prevent premature dimerization of UPy units, the two SAAs were prepared with their amino groups protected with Fmoc and UPy moieties protected with benzyl (Bn) group. Synthesis of CUPy, as shown in Scheme 1.1, began with functionalization of ethyl acetoacetate with *tert*-butyl bromoacetate followed by condensation with guanidine

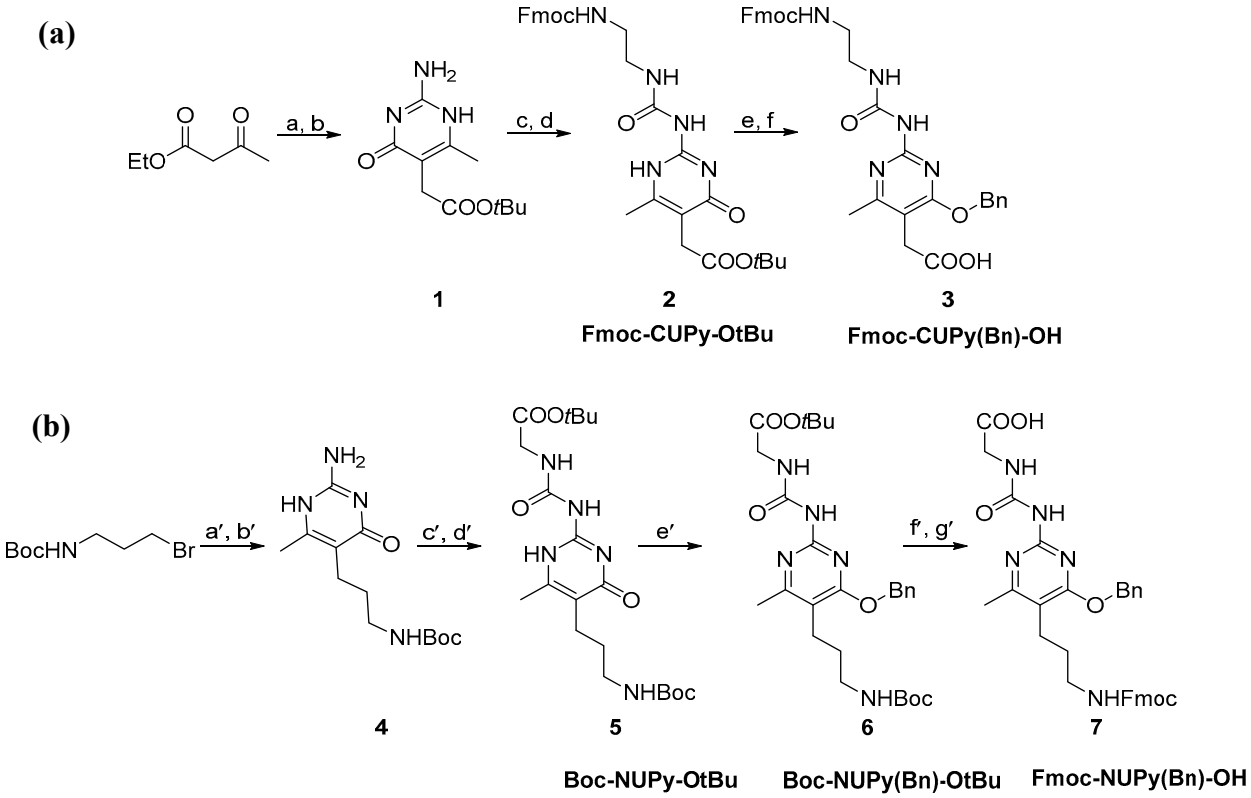

Scheme 1.1 Syntheses of Fmoc-CUPy(Bn)-OH (a) and Fmoc-NUPy(Bn)-OH (b). **(a)** Reagents and conditions for synthesis of Fmoc-CUPy(Bn)-OH (**3**): (a) *tert*-butyl bromoacetate, potassium carbonate, DMF; (b) guanidine hydrocarbonate, ethanol, reflux, 6 h (c) CDI, $CHCl_3$, 3 h; (d) mono-Fmoc ethylenediamine hydrochloride, N,N-diisopropylethylamine, $CHCl_3$, 6 h; (e) benzyl bromide, potassium carbonate, DMF; (f) TFA:DCM (30:70), 3 h, 90%. **(b)** Reagents and conditions for synthesis of Fmoc-NUPy(Bn)-OH (**7**): (a') ethyl acetoacetate, potassium carbonate, DMF; (b') guanidine hydrocarbonate, ethanol, reflux, 6h; (c') CDI,$CHCl_3$, 3 h (d') tert-butyl glycine ester, DIPEA, $CHCl_3$, 8 h; (e') benzyl bromide, potassium carbonate, DMF; (f') TFA:DCM (30:70), 3 h; (g') Fmoc-OSU, water:acetonitrile (1:1), potassium carbonate.

hydrocarbonate to form an isocytosine derivative, **1**.[47] The isocytosine **1** was further activated with 1,1'-carbonyldiimidazole followed by urea formation through reaction with mono-Fmoc ethylene diamine to yield Fmoc-CUPy-OtBu, **2**. To avoid premature hydrogen bonding or aggregation of the nascent sequence during the peptide synthesis, it was necessary to block the hydrogen bonding

capabilities of the UPy motif. We chose the benzyl protecting group for its resistance to acid cleavage, as typical peptide cleavage conditions require trifluoroacetic acid. This method allows the cleavage of peptide and removal of typical amino acids protecting groups while preserving the UPy hydrogen bond blocking protecting groups. Finally, the *tert*-butyl protecting group was removed by acid hydrolysis to yield Fmoc-CUPy(Bn)-OH, **3**.

Fmoc-NUPy(Bn)-OH, **7**, was prepared by following a similar route developed for CUPy synthesis (Scheme 1.1). Due to the sensitivity of the Fmoc protecting group to the guanidine condensation conditions, it was necessary to initially protect **4** with Boc group and eventually replace it with Fmoc group in the end. The products have been characterized using ^{1}H NMR, ^{13}C NMR, HRMS and analytical HPLC (details of synthesis and characterization can be found in the experimental section).

1.9 Peptide sequence design, synthesis and purification

Following our design concept (Figure 1.8), we further incorporated the synthesized SAAs into peptides to template and control the folding. For our initial study, we chose a short tetrapeptide, Phe-Ala-Gly-Leu (FAGL), to demonstrate the effects of the orientation for UPy derived amino acids on the folding. Our choice of peptide sequence was based on the following criteria:

i) hydrophobic for good solubility in organic media

ii) minimal side chain interactions between residues

iii) non-overlapping ^{1}H NMR chemical shift values of all residues to facilitate NMR structural analysis

The homo CUPy-CUPy dimer should encourage the folding of the connecting peptide into a β-hairpin mimic (Figure 1.8b). On the other hand, the CUPy-NUPy peptide does not allow folding in this geometry due to the mismatch of hydrogen bonding donor and acceptor sites (Figure 1.8c). Computer modeling also confirms that a short tetrapeptide sequence precludes CUPy-NUPy intramolecular dimerization in an alternative orientation. A series of SAA-containing peptides were synthesized by following standard SPPS Fmoc protocol using the Wang resin (Table 1.1). For enhanced solubility, the N-termini of all peptides were converted to pivaloyl amides after deprotection of the final Fmoc group. The peptides were then cleaved from the resin and the C-terminus was esterified using methoanolic HCl.[48] The crude product was then purified by reverse phase HPLC using a water/acetonitrile gradient as the mobile phase. After purification, the benzyl protecting group on UPy units was removed by hydrogenolysis to reveal the active UPy motifs. The deprotected peptides were again purified by reverse phase HPLC using a water/acetonitrile gradient and then lyophilized from the water/acetonitrile mixture to obtain a fluffy, white powder. The purity of all the peptides was analyzed by analytical HPLC, and their structures were established by 1D and 2D NMR as well as mass spectrometry (see detailed characterization in experimental section, Figure. 1.22 – 1.44.

Table 1.1 List of peptide sequences studied for β-turn mimic and their molecular weights.

	Peptide Sequence [a]	Calc'd MW	Obs MW [b]
I	Piv-CUPy(Bn)-FAGL-CUPy(Bn)-OMe	1186.59	1187.52
II	Piv-CUPy-FAGL-CUPy-OMe	1006.50	1007.45
III	Piv-NUPy(Bn)-FAGL-CUPy(Bn)-OMe	1200.61	1201.61
IV	Piv-NUPy-FAGL-CUPy-OMe	1020.51	1021.43
V	Piv-CUPy(Bn)-LGVA-CUPy(Bn)-OMe[c]	1138.59	1139.57
VI	Piv-CUPy-LGVA-CUPy-OMe[c]	958.50	959.80

[a] Piv stands for pivaloyl group. [b] ESI/MS $[M+H]^+$.[c] discussed in section 1-11.

1.10 Solution ^{1}H NMR studies of peptide I-IV

1.10.1 1D NMR studies

Both the protected and deprotected peptides were then subjected to solution ^{1}H NMR investigation. UPy dimerization can be identified by the onset of downfield shifts corresponding to hydrogen- bonded protons. The peptide **II** (CUPy-CUPy) NMR spectrum revealed two sets of well-defined three H-bonded signals between 9.5 and 12.9 ppm corresponding to the hydrogen-bonded protons on CUPy-CUPy pair (Figure 1.9b). The two sets of peaks arise from the non-equivalence of the two CUPy units in the peptide. According to a previous study by Meijer and coworkers,[45] intermolecular dimerization of UPy at our experimental condition (4 mM peptide in 20% DMSO in CD_2Cl_2) should be relatively weak and dynamic. Therefore, the observed well-defined hydrogen bonding is most likely due to intramolecular dimerization between CUPy-CUPy pair. In contrast, the spectrum of peptide **IV** does not exhibit these characteristic signals, indicating the inability of CUPy-NUPy pair to form an intramolecular dimer due to directionality of UPy dimerization and topological constraints by the short peptide linker.

The broad peaks between 9.6 to 11.6 ppm on peptide **IV** spectrum are presumably due to weak and dynamic intermolecular interactions (Figure 9d). Similar intermolecular assemblies have been reported in cases of symmetrical bis-UPy compounds connected by alkyl chain.[49,50] For comparison, the benzyl protected peptides **I** and **III** were unable to form hydrogen bond mediated dimers (Figure 1.9a and 1.9c).

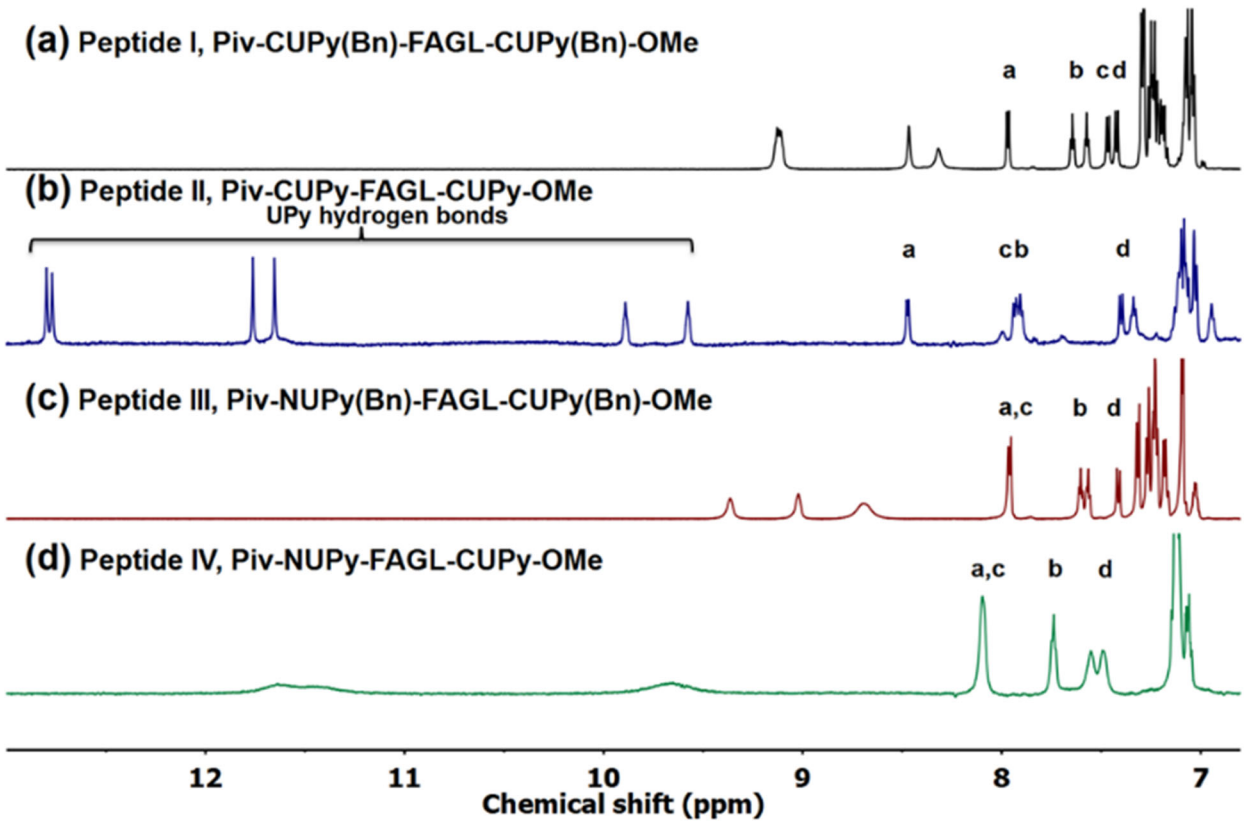

Figure 1.9 ^{1}H NMR spectra of peptide **I-IV** (4 mM in 20/80 DMSO-d_6 /CD_2Cl_2, 24 °C)**.** The amide protons of peptide segment are labelled with a-d on the spectra: a = NH_{Ala} , b = NH_{Gly}, c = NH_{Phe}, d = NH_{Leu}. All peaks are assigned using COSY and TOCSY techniques (see SI for details of each peptide and Figure S21 for complete assignments).

The amide and α–protons of the four peptides were further analyzed to reveal more information about the conformation of the peptides (detailed residue specific assignments were made by COSY and TOCSY techniques, Figure 1.40).[51] According to computer modeling, peptide **II** containing a CUPy-CUPy pair should be able to dimerize intramolecularly and template the folding of the tetrapeptide into a β-turn mimic. Peptide **IV** (NUPy-CUPy), on the other hand, would not be able to form such intramolecular dimer due to the topological constrains exerted by the SAA orientation. Comparison of the spectra of peptides **I** and **II** clearly shows the effect of intramolecular UPy dimerization on the conformation of peptide (Figure 1.9a&b, Figure 1.38 and

1.39). Firstly, it is apparent that the amide protons for NH_{Ala} (a), NH_{Gly} (b) and NH_{Phe} (c) were shifted significantly downfield.

1.10.2 Analysis of changes in α-protons chemical shift

Many differences in the α-proton region are also notable. It is well-established that α-proton chemical shift is sensitive to the secondary structure and the environment of the peptide backbone.[51] Therefore, $\Delta\delta H^{\alpha}$ (the difference in chemical shift for an α-proton between folded and unfolded conformations) has been routinely utilized to evaluate the change in peptide folding. We have measured the chemical shifts for all α-protons in peptides **II** and **IV** and compared to their protected analogues **I** and **III** to reveal the effect of UPy dimerization on the peptide conformation. The $\Delta\delta H^{\alpha}$ values for peptide **II/I** and peptide **IV/III** are plotted in Figure 1.10. For peptide **II/I**, the Ala, Phe, and Gly α-protons all show relatively large upfield shift upon deprotection of UPy benzyl group, suggesting intramolecular folding induced by UPy dimerization. The negative values for $\Delta\delta H^{\alpha}$ are consistent with other experimental and theoretical reported values for residues in units.[52]

In contrast, the $\Delta\delta H^{\alpha}$ values for peptide **IV/III** are very small (< 0.05 ppm), consistent with a random conformation. Additionally, the magnetic anisotropy experienced by the two Gly methylene α–protons was significantly higher in peptide **II/I** as compared to peptide **IV/III**, (0.37 ppm versus 0.0 ppm). This data provides additional evidence to support that dimerization of CUPy-CUPy in peptide **II** templates the formation of β-turn mimic.

For comparison, we synthesized and characterized two other model peptides, Ac-FAGL-OH and a cyclic pentapeptide, c-(KFAGL) (Figure 1.46). The cyclic peptide exhibited a similar pattern for α-protons chemical shift changes compared to peptide **II**, agreeing with the proposed b-turn structure for peptide **II** (Figure 1.47).

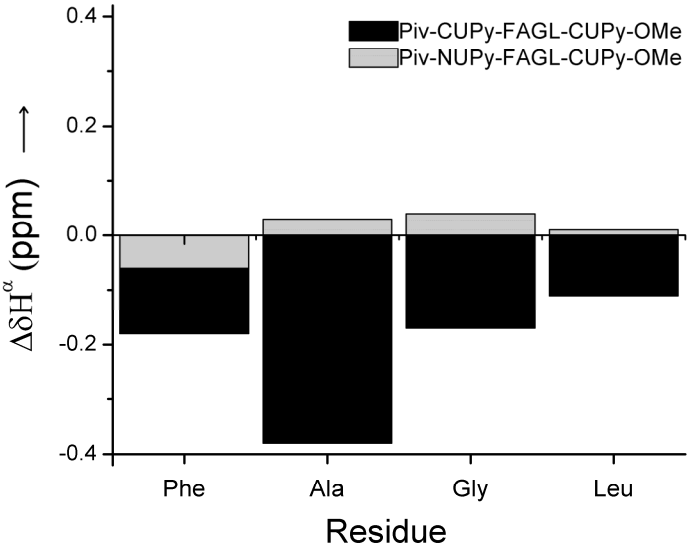

Figure 1.10 $\Delta\delta H^{\alpha}$ [δH^{α} (UPy-deprotected) - δH^{α} (UPy-protected)]. Values for each residue is plotted for Peptides **II/I**, black column bar, and **IV/III**, grey column bar. In case of glycine, chemical shift for low field methylene proton has been plotted in each case. Peptide **II** shows negative $\Delta\delta H^{\alpha}$ values consistent with a β-turn structure, whereas peptide **IV** has very small $\Delta\delta H^{\alpha}$ values, suggesting a random conformation.

1.10.3 2D ROESY experiments

Furthermore, the detection of nuclear Overhauser effects (NOEs) should provide important insight into the three-dimensional structure of these peptides. Due to their intermediate sizes, ROESY was used to obtain additional information about the folding and structure of peptides **II** and **IV**. As shown in Figure 1.11, peptide **II** displayed a number of key NOE cross-peaks,

consistent with the proposed β-turn mimic structure induced by UPy dimerization. In particular we have observed cross-peaks between methylene protons of N-terminal CUPy and amide protons of C-terminal CUPy. Another important NOE was observed between N**H**$_{Ala}$ and Leu α-proton. Peptide **IV**, on the other hand, did not show any of these cross peaks and only intra-residual and sequential NOEs were observed (Figure 1.55). Notably, we also observed chemical exchange cross-peaks (EXSY) in ROESY spectra for peptide **II** (Figure 1.54), suggesting that the minor peaks observed in the ^{1}H NMR spectrum (Figure 1.11) originate from an alternative conformation, possibly an unfolded minor conformer. Previous studies have shown that polar solvents such as DMSO can compete for UPy hydrogen bonding and break up the resulting dimer. It is therefore possible that this secondary conformer is the result of disruption of UPy dimerization by DMSO in the solution.

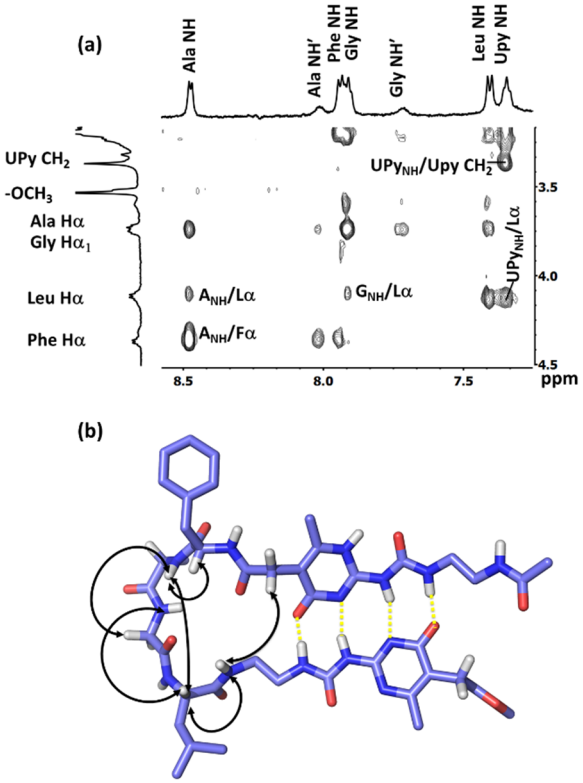

Figure 1.11 (a) Cross-section of ROESY spectrum of peptide **II** in 20/80 DMSO-d_6/CD_2Cl_2. The small peaks marked with prime correspond to alternative minor conformation as proven by EXSY cross-peaks. Single letter amino acid codes are used to label NOE cross-peaks: A=Ala, G=Gly, F=Phe, L=Leu, (b) A computer model of peptide **II** with important observed NOEs marked with curved arrows.

1.10.4 Concentration dependence of SAA association

Intermolecular and intramolecular hydrogen bonds can usually be distinguished by examining their concentration dependence, as the former is more sensitive to the concentration of the sample. Therefore, to further verify that UPy dimerization of peptide **II** was intramolecular, we collected NMR spectra for peptide **II** by varying concentration from 4 mM to 0.1 mM (in 20/80 DMSO-d_6/CD_2Cl_2). For the entire concentration range, we did not observe any significant change for the UPy hydrogen bonded protons in the range from 9.2 to 12 ppm (Figure 1.45), strongly supporting the proposed intramolecular dimerization between two CUPy units in peptide **II**. Upon further addition of more DMSO-d_6 (50 vol%) to the NMR sample, these UPy peaks were shifted upfield and both the peptide amide and α-proton regions became very similar to those of peptide **I** (Figure 1.45). At such a high concentration of DMSO-d_6, it is understandable that UPy dimerization is disrupted so that peptide **II** adopts a random conformation.

1.10.5 Temperature dependence of amide chemical shifts

The temperature dependence of amide ^{1}H NMR chemical shifts should also provide information on the state of hydrogen bonding for amide NH protons. In competitive solvents, the solvent-exposed amide protons exhibit large temperature dependences, while solvent-shielded protons display small temperature dependences.[53]

Nonetheless, this simple analysis does not apply in the case of non-competitive solvents. Previous studies have established that in non-polar solvents, peptide amide protons that are locked in a hydrogen-bonded conformation have low temperature dependences while protons that participate in intramolecular hydrogen bonding can show large temperature dependences only if increasing temperature can result in unfolding of the hydrogen bonds.[54]

We investigated the temperature dependence of amide ^{1}H NMR chemical shifts of peptide **I-IV** to obtain additional insight into the effect of SAA association on the amide NH protons (Table 1.2). The changes in temperature dependence of chemical shift between **I** and **II** is consistent with an intramolecularly folded conformation for peptide **II**. No significant difference between **III** and **IV** were observed, agreeing with a random conformation for peptide **IV.**

1.10.6 Diffusion-ordered NMR experiments

Translational self-diffusion measurements using pulsed-field gradient spin echo (PFG) NMR methods are commonly used to study the oligomerization of the peptides and proteins as translational diffusion coefficient (D) is related to the mass of a compound through its hydrodynamic radius.[55] In principle, it is possible to use this technique to monitor the change in the peptide conformation as the approximate solvodynamic radius of the peptide depends on its conformation.[56] Investigation of these subtle changes can provide additional information about the

Table 1.2 Temperature Dependence of the ^{1}H NMR Chemical Shifts (ppb/K) of the NH Protons of peptides **I-IV** (20% DMSO-d_6 and 80% CD_2Cl_2)[a]

	NH(Phe)	NH(Ala)	NH(Gly)	NH(leu)	UPy(NH amide)		UPy(Urea)		UPy(Urea)		UPy(internal)	
I	9.5	8.5	6.0	6.5	n.d.[b]	6	14.5	14.5	2.5	2.5	n.a[c]	n.a[c]
II	6.5	7.0	3.5	3.0	6	3.5	1	1	1.0	1.5	1.0	0.5
III	6.0	6.0	3.7	4.7	7.0	n.d.[b]	12.9	12.9	1.2	1.5	n.a.[c]	n.a.[c]
IV	5.6	5.6	3.5	3.1	3.0	n.d.[b]	-7.0		1.0	1.0	-7.0	

[a] spectra recorded at 5 °C intervals from -5 °C to 35 °C. [b] The value was not calculated due to the signal overlap. [c] The protected Upy does not contain internal hydrogen bonding.

conformational changes in the peptide structure. We used pulse field gradient diffusion NMR to obtain more information about the change in the structure and oligomerization of peptides **I-IV**. The diffusion coefficient of each peptide was measured in 20/80 DMSO-d_6/CD_2Cl_2 by and are reported in Table 1.3.

As expected, the protected peptides, **I** and **III**, had similar diffusion coefficients. Diffusion coefficients for peptides **II** and **IV** were noticeably smaller than the protected peptides and slightly different from each other. It is challenging to extract more detailed information about the peptide folding state from the diffusion coefficient data. One possible explanation is that the conformational differences in peptide **II** and **IV** and differences in the intermolecular association is responsible for this additional change in diffusion coefficients.[57]

Table 1.3 The calculated diffusion coefficients for peptides **I-IV** from PFG DOSY studies.

Peptide	Calculated Diffusion Coefficient ($\times 10^{-6}$cm^2/s)
I	9.66 ± 0.70
II	6.67 ± 0.84
III	9.54 ± 0.19
IV	7.70 ± 0.10

1.10.7 Hydrogen-deuterium exchange experiments

Hydrogen-deuterium exchange experiments are usually used to provide insights into the hydrogen bond network in foldamer with exchangeable protons.[58] In this case, peptides can be exposed to the excess amount of protic deuterated solvents and the decay of ^{1}H NMR signals corresponding to amides can be observed at known intervals. Protons that are exposed to solvents will undergo deuterium exchange at higher rates than shielded protons or hydrogens that are participating in strong hydrogen bonding. We decided to elucidate the state of hydrogen bonds in different peptides using H–D exchange.

We have attempted to calculate the H–D exchange rate constants (min^{-1}) by fitting a single exponential decay function on the intensity of proton signals. Exchange is initiated after the addition of CD_3OD to the peptide mixture in 20/80 DMSO-d_6/CD_2Cl_2. Unfortunately, the rapid exchange reaction for all peptides **I-IV** hampered our effort to obtain reliable exchange rates. In all cases, the equilibrium was reached in the time between the addition of deuterated methanol and the first NMR scan (< 30s). Further analysis of signal intensities over defined intervals using a least square fit of a single exponential decay did not demonstrate any decay above the background noise. As an example, ^{1}H NMR spectrum of peptide **II** is shown after addition of CD_3OD in Figure 12. The black line represent the spectrum before the addition of CD_3OD. After the addition of 20 μL of CD_3OD, another spectrum was immediately recorded and the peak intensity was monitored for 20 min. It is clear from Figure 1.12 that the decay is within background noise. After 20 minutes, another 15 μl of CD_3OD was added and exchange was monitored again. The discontinuity in the peak decay is apparent and is marked by two arrows in Figure 1.12.

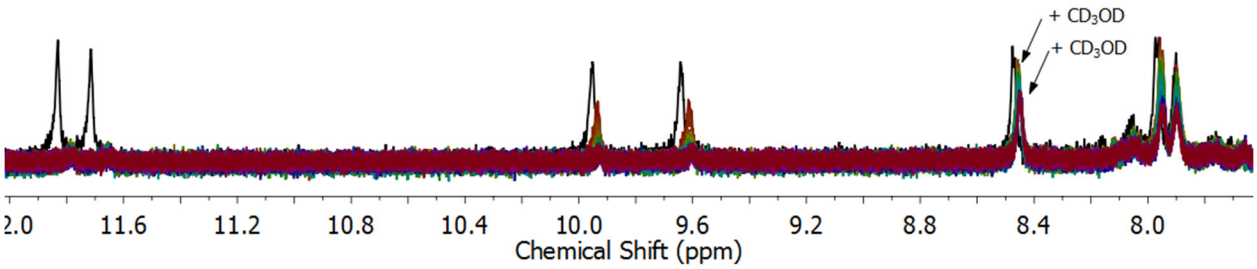

Figure 1.12 H–D exchange experiment for peptide **II**. The rapid H–D exchange rate can be correlated to dynamic of SAA association and the lack of compact sturcutre in the loop conformation. The two arrows represents the rapid decay of signal after the additions of CD_3OD.

Similar results were obtained when the c-(KFAGL) peptide was analyzed by this method. In this case, it was possible to measure H–D exchange rates for some of the amide bonds even though the exchange rate was still very rapid ($t_{1/2}$ = ~1.7 min).

Comparison of these results demonstrate that the exchange in our system, which is held together by supramolecular interactions, is faster than the covalently stapled peptide. An explanation can be sought in the dynamic nature of UPy association. The k_{off} of UPy motif has been determined experimentally in previous studies and is known be in order of seconds (0.6 s^{-1}).[59] Concomitantly, the dynamic nature of SAA association can expose the amide protons to the solvent in the open state. In Figure 1.12, signals corresponding to the UPy dimer disappear first (11.6-12 ppm). It is also possible that our structure even in the absence of dynamic UPy interaction is not compact and protons are presumably exposed to solvent in this environment. This notion is supported by the rapid rate of H/D exchange in the covalently cyclized peptide, c-(KFAGL).

1.11 Conclusion and notes on the generality of our method

In conclusion, we have described here a novel concept of using supramolecular amino acids (SAA) for directing peptide folding in organic environments. Specifically, we have designed and

synthesized two UPy-derived SAAs, CUPy and NUPy presenting opposite hydrogen bonding patterns on the backbone. For initial concept demonstration, we have incorporated the two SAAs into a short tetrapeptide for templating peptide folding into β-turn mimic. For CUPy-CUPy peptide (**II**), our extensive NMR studies have confirmed that it adopts a folded β-turn structure in 20/80 DMSO-d_6/CD_2Cl_2 solution. This proves our hypothesis that energetic gain from intramolecular dimerization of the incorporated SAAs can provide the driving force for templating peptide folding into secondary structure.

Before discussing my efforts toward stabilizing a more complex structures using SAAs, it is necessary to discuss the generality of this method. As it is mentioned before, our choice of peptide sequence was driven by the consideration of solubility and ease of analysis in the first study. To provide additional evidence for the generality of our strategy, we randomly selected another tetra residue peptide sequence, LGVA, and studied the protected and deprotected peptides **(V/VI)** using a similar protocol (by monitoring changes in the location of α-proton signals). In this case, the peptide sequence was chosen from hydrophobic non-aromatic residues which slightly complicated the ^{1}H NMR analysis. Nonetheless, comparison of chemical shifts of various protons before and after deprotection of UPy followed a trend similar to peptide **II/I**. α-protons of valine and glycine, two residues most likely to occupy the turn position, exhibited a comparable shift in the case of peptide **VI/V (**-0.4 for valine and -0.3 glycine). Leucine and alanine α-protons did not shift significantly but the magnetic anisotropy between two glycine methylene protons also increases significantly after deprotection of UPy (from 0.3ppm in peptide **V** to 0.7 ppm in peptide **VI**).

It appears that in the absence of competing interactions between the side chains of amino acids in a hydrophobic environment, the UPy dimerization still provide the driving force for intramolecular folding of this tetra residue peptide chain, validating the generality of our method.

In further search to demonstrate the generality of our approach, we found that computer modelling demonstrated the feasibility of our SAAs templating the folding of a three residue peptide sequence. Therefore, a three residue peptide sequence (FGL) was also briefly investigated for its folding propensity. Consistent with our hypothesis, NMR experiments demonstrated the formation of discrete UPy dimers similar to peptide **II** in a mixture of polar and non-polar solvents ($CDCl_3$/DMSO). Although, turns with more than four residues were not investigated, it is expected that beyond a certain length, the entropic cost of folding will surpass the enthalpic gain of two SAA dimerization. In such cases, serial incorporation of more than one pair of SAAs in a longer peptide chain may provide enough driving force to template the peptide folding. Additionally, due to the larger size of these two amino acids, their serial incorporation can generate hybrid building blocks within the length scale of larger secondary structures such as alpha helices.

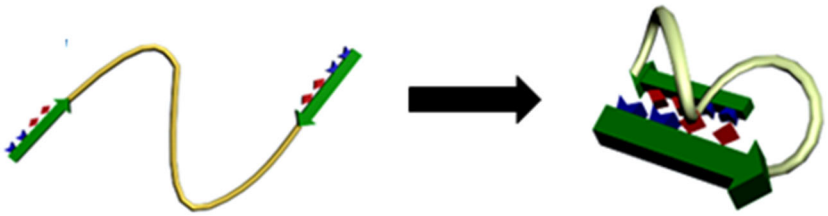

Figure 1.13 Conceptual design of SAA stabilized βαβ mimic if UPy derived amino acids are placed in strategic orientations.

1.12 Toward the stabilization of more complex structure

We envisioned that this strategy can be general and we thus set to investigate the incorporation of these SAAs into longer peptides to stabilize and obtain additional secondary structures as well as novel peptide architectures. In the second step of our study, we chose to mimic a βαβ motif in organic solvents (Figure 1.13). In our first demonstration, the short length of the connecting peptide sequence precluded the CUPy/NUPy dimerization (**III/IV**) due to the topological constrains. We envisioned that a longer peptide chain can be used between CUPy/NUPy pair to allow for pairing of H-bond donor and acceptor sites. Based on modelling, we postulated that it might be possible to incorporate a compact α-helix in the space above the SAA heterodimer. Since a minimum number of hydrogen bonds are necessary to stabilize an α-helix, most short helices are not stable on their own.[24,60] We proposed that it is possible to find an optimum length for the peptide segment that can fold into an α-helix only if it is stabilized by formation of SAA heterodimer.

1.13 βαβ mimic design

Similar to the design of the β-turn, a peptidic segment was flanked by two SAAs. In this case, the peptide sequence was adapted from natural helical segments in transmembrane proteins. We hypothesized that such sequence inherently possess a tendency to fold into an α-helix in a hydrophobic medium. The SAAs were chosen as a mimic of the β section so the energetic gain from their dimerization is utilized to provide additional stability for a short helical peptide thus mimicking a βαβ structure as shown in the Figure 1.14.

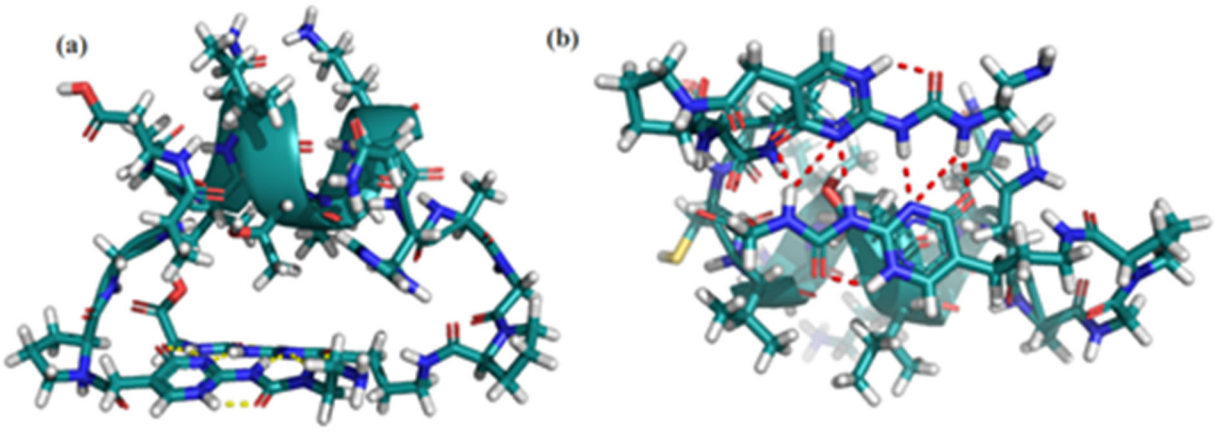

Figure 1.14 The model of βαβ mimic designed for this study (a) side view (b) bottom view. Modeling procedure and models of other structures can be found in supporting information section.

The sequence of peptide segment was adapted from a membrane bound segment of a prion protein (PrP).[61] Molecular modelling through MacroModel was used to determine the optimum linker size to connect the helix forming sequence to SAAs. Proline residues were selected to provide a change of direction through a kink in the backbone so that the helical segment could occupy the space above the SAAs. Glycine was chosen due to its flexibility to form the loop region, while for the third position, alanine was preferred over glycine to avoid excessive flexibility in the loop region. The primary sequences of these peptides are reported in Table 1.4. We decided to use circular dichromism (CD) to guide our design due to the difficulties in unambiguous structural assignments using ^{1}H NMR arising from the added structural complexity of peptides **VII-XI**. We expected that in a successfully designed peptide, CD signature of an alpha helix should appear after the deprotection of UPy groups.[62]

Table 1.4 The sequence of different peptides synthesized for mimicking the βαβ motif. The linker region is colored in blue and the helical section is in green color.

	Peptide	Sequence
First generation	**VII**	NUPY(Bn)PGADCVNITIKQHAGPCUPy(Bn)G
Second generation	**VIII**	NUPy(Bn)PAQLIAKGPCUPy(Bn)G
	IX	NUPyPAQLIAKGPCUPyG
Third generation	**X**	NUPy(Bn)PAILIAFAGPCUPy(Bn)G
	XI	NUPyPAILIAFAGPCUPyG

1.13.1 First generation design

Peptide **VII** had limited solubility in (mixture of) nonpolar solvents required for preserving UPy association. During the course of this study, we found that the deprotected peptides are even less soluble than their protected analogues. Despite the lack of solubility of peptide **VII** in suitable solvents, we decided to probe the structure of these peptides using CD in 3% TFA in acetonitrile. As demonstrated in the Figure 1.15, CD spectroscopy demonstrated that the peptide adopted a considerable helical conformation, even before the deprotection of UPy(Bn) groups. Despite the initial setback, we found it promising that our first sequence formed an alpha helix in a non-aqueous environment which corroborated our reasoning for choosing the peptide sequence from a transmembrane α-helix.

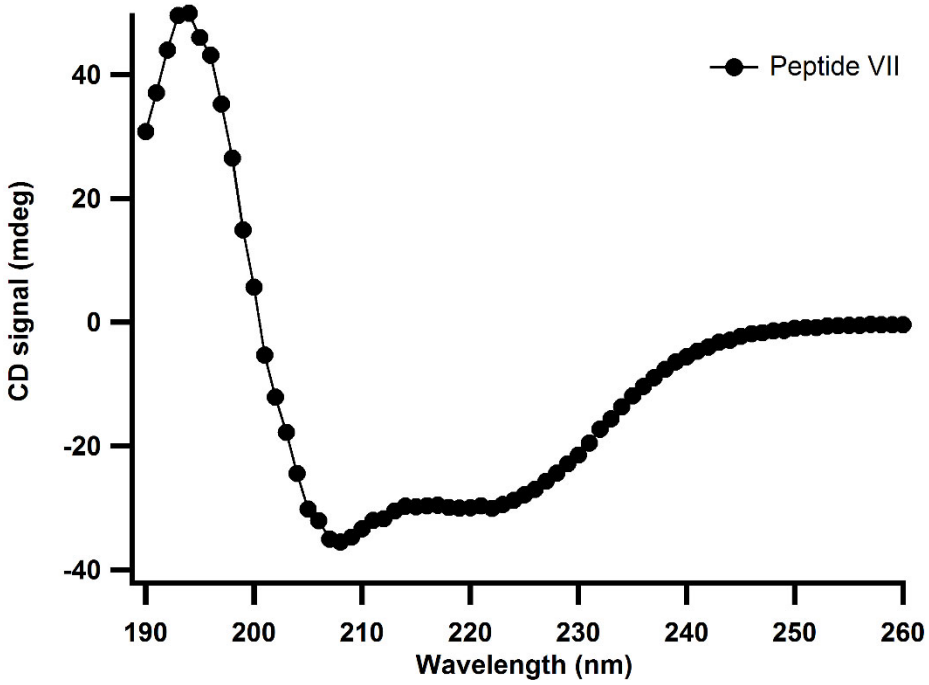

Figure 1.15 CD signal of peptide **VII** measured in 3% TFA in CH_3CN. Peptide adopted a helical structure even before deprotection of UPy groups.

1.13.2 Second generation design

Due to the low solubility of these peptides in organic solvents, we decided to mutate the helical sequence to increase the hydrophobic content by incorporating more nonpolar amino acids in our second generation system and also to truncate the peptide sequence to destabilize the alpha helix before formation of the SAA dimer.[63] To balance the effect of truncation, mutations were chosen to increase the helical propensity.

Peptide **VIII** was also not soluble in organic solvents such as $CHCl_3$ or mixtures of 0.1%-0.7% of TFA in $CHCl_3$. Even when the solution turned clear at 0.7% TFA in $CHCl_3$, the NMR spectrum showed significant aggregation of the peptide evident by broad peaks and low signal intensity. Attempts to dissolve **VIII** or **IX** in neat organic solvents such as THF, acetonitrile and acetone were also not successful. Deprotected peptide **IX** was only soluble in more polar mixtures

such as 10% water in acetonitrile. Unfortunately, in all these cases, solvents that dissolved the peptides also disrupted the association of SAAs and no change in the peptide ^{1}H NMR and CD spectra was observed.

As the last resort, we also studied the structure of these peptides in water hoping that due to the hydrophobicity of the peptide sequence and SAAs, an intermolecular association between peptide chains results in the stacking of UPy dimers in water.

Despite some changes in the C_{α} region between peptide **VIII/IX**, CD spectrum demonstrated that both peptides primarily adopted a random coil conformation (Figure 1.16).

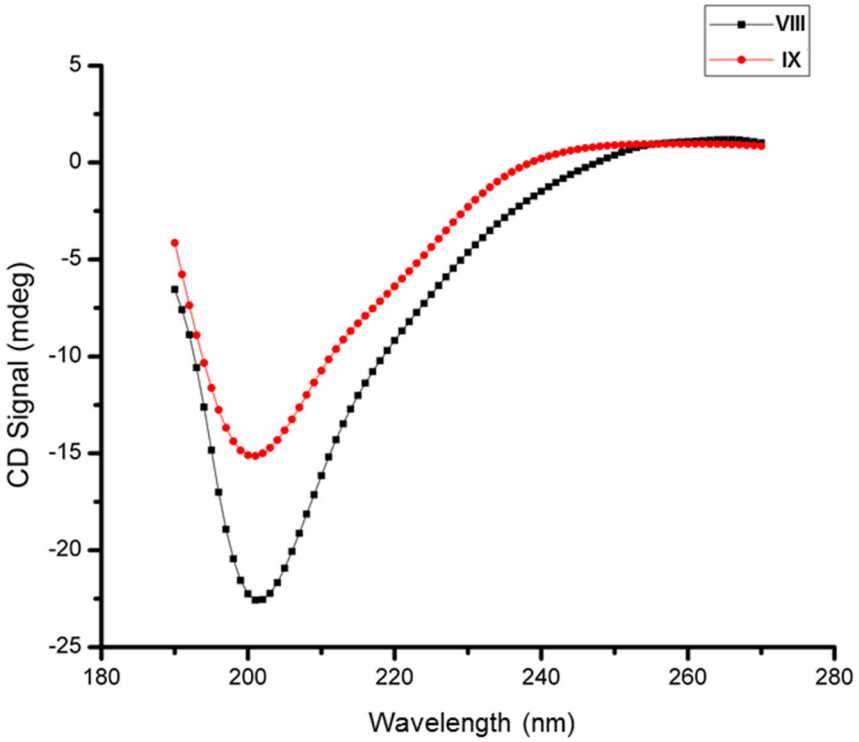

Figure 1.16 CD signal of peptide **VIII and IX** measured in water. Both peptides primarily adopted a random coil structure.

1.13.3 Third generation design

To overcome the solubility issue and preserve UPy hydrogen bonding in nonpolar solvents such as $CHCl_3$, we decided to choose a more hydrophobic peptide fragment. Our third design was selected from a membrane spanning helix from bacteriorhodopsin, (pdb code: 1AIJ).[64] We faced a similar setback again where neither the peptide **X** nor the deprotected version of it, **XI**, were soluble in organic solvents that preserved UPy dimerization.

1.13.4 Exploring peptoids as the helical segment

Initially, we attributed this solubility problem to the presence of numerous hydrogen bonding acceptor and donor sites in the peptide backbone. Our hypothesis was that the nonspecific aggregation of these unsatisfied hydrogen bonds in hydrophobic solvents was the global minimum in the energy landscape and trapped the intermediates toward the folded structure. To alleviate this problem, we decided to remove the H-bond donor sites from the backbone to enhance the solubility of our peptides.[65] N-substituted glycines, or peptoids, are non-natural analogue of peptides, in which the substituents are attached to the amide nitrogen atoms instead of the alpha carbons.[66] As shown in Scheme 1.2, this modification renders the backbone achiral and also transforms secondary amides to their tertiary analog, hence perturbing the H-bond patterns of the backbone. Peptoids are generally more soluble in the organic solvents and can be synthesized through a modified procedure on solid phase; both of these criteria were compatible with our original design.

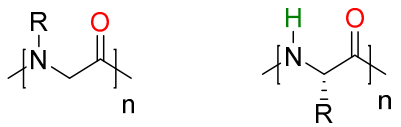

Peptoids *Peptides*

Scheme 1.2 The structure of peptoids and α-peptides.

Peptoids have also been shown to adopt certain secondary structures such as helix and beta loops in hydrophobic solvents, despite their achiral backbone and the absence of long range interactions.[66-68] These findings encouraged us to incorporate our SAA in a model peptoid chain. Scheme 1.3 depicts two reported strategies to synthesize peptoids. Sub monomer synthesis method developed by Zuckerman and further optimized by Blackwell was chosen due to its success in the synthesis of longer peptoids.[69,70]

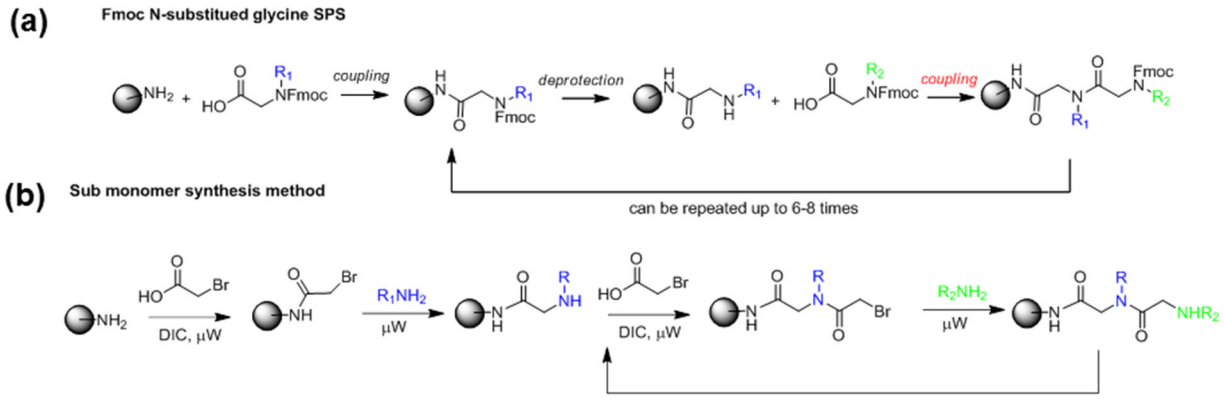

Scheme 1.3 Two synthetic pathway to obtain peptoids using solid phase methodology.

We first synthesized a model peptoid an using (S)-1-phenylethan-1-amine, (*N*spe)$_8$, and investigated its folding in acetonitrile by CD spectroscopy, Figure 1.17. The spectra confirmed that the model peptoid adopted a polyproline type I helix evident by the negative peaks at 220 and 200 and a positive peak at 190.[68,71] The next step was to incorporate UPy derived amino acids in this sequence. After modification of the synthetic protocol, we synthesized CUPy(Bn)-(*N*spe)$_8$-NUPy(Bn). Despite removal of all H-bond donor sites from the backbone, the synthesized peptoid was again insoluble in solvents that were conducive to UPy dimerization.

After observing this lack of solubility even in the presence of longer hydrophobic backbones such as peptoids, we hypothesized that nonspecific hydrogen bonding and stacking of

urea motifs in the SAA may the culprit, dominant contributing factor to the peptide's insolubility.[65] Regardless of the exact cause, this nonspecific aggregation unfortunately hampered the progress toward synthesizing larger cyclic peptides with incorporated SAAs. These efforts are not discussed in the interest of brevity but they delineate the limitation of using UPy motifs in templating the peptide folding in the organic solvents.

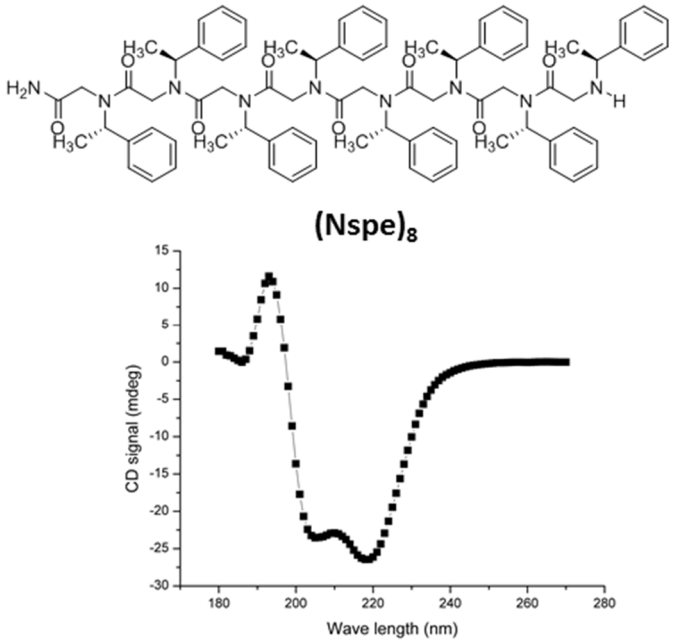

Figure 1.17 Structure and CD spectrum of model peptoid, (*N*spe)$_8$

1.14 Peptide Nucleic Acids (PNAs) as folding scaffold

In the previous sections, I outlined my journey to control peptide folding through introduction of specific array of hydrogen bonds in the peptide backbone. To further extend this idea, I envisioned replacing the SAAs with other supramolecular motif to introduce strong and specific interactions along the peptide backbone to control the peptide folding. This search was also motivated to find an alternative supramolecular motif, to overcome the aforementioned

problem of UPy aggregation and even possibly finding system compatible with both organic and aqueous environment.

This search eventually led me to consider other natural biopolymers, specifically nucleic acids. Hydrophobic interactions, manifested in base stacking, and hydrogen bonding mediated molecular recognition base pairing are the main driving forces for the folding of nucleic acids.[72] In particular, RNA folding into complex secondary and tertiary structures is well-established. RNA based catalysts (Ribozymes) are even more astonishing given the lack of diverse functional groups in nucleic acids unlike proteins.[73] I envisioned to combine the unique base pairing and complementarity of nucleic acids recognition motifs with diverse functional groups in amino acids to generate functional foldamers.

The charged phosphodiester backbone of DNA and RNA limits their solubility in organic solvents and renders their synthesis incompatible with solid phase peptide synthesis protocols. These two limitations encouraged us to use peptide nucleic acids[74] (Scheme 1.4) as a platform for the presentation of nucleobases as the supramolecular motif and synthesize a hybrid PNA-peptide.

PNA was first invented by Nielsen and coworkers as a ligand for recognition of DNA major groove.[74] Interest in PNAs has grown since the discovery of their strong association with DNA or RNA and their resistance to ribonucleases activity.[75] The building blocks are commercially available, albeit more expensive than their peptide counterparts, and the synthesis is compatible with regular SPPS of peptides.

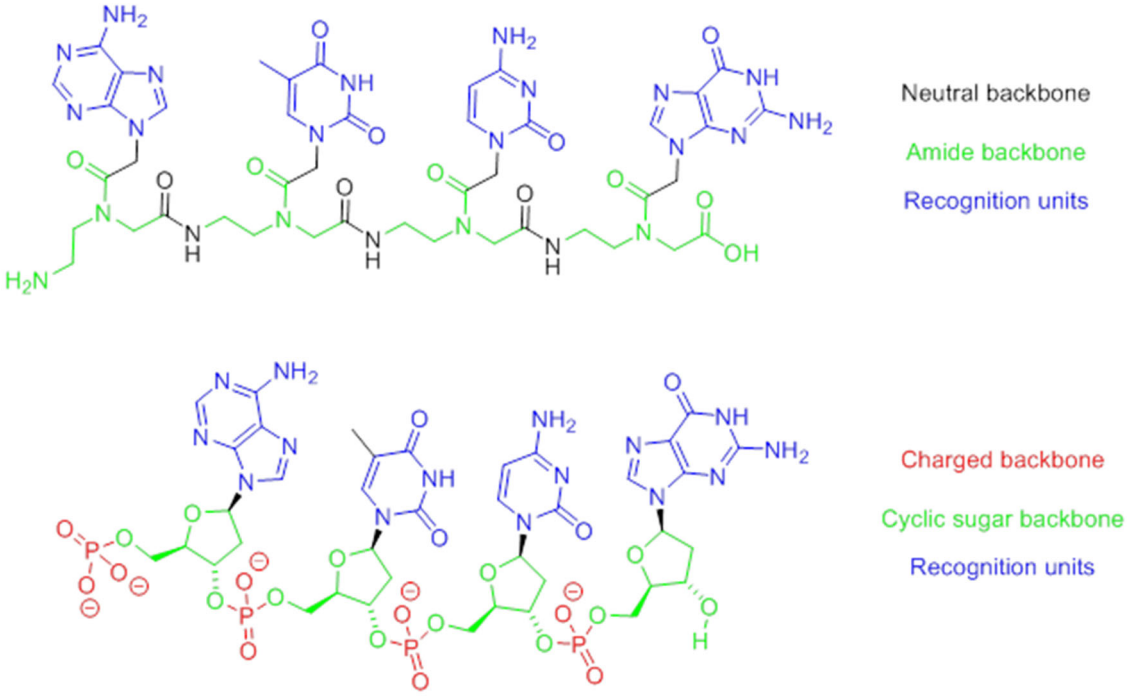

Scheme 1.4 Structural comparison of PNA and DNA.

I was particularly intrigued by G-quadruplex (GQ) motif [76,77] given the simplicity of the sequence and the level of control that can be achieved by varying the cation stabilized structure.[78] The general idea here was to flank a sequence of peptide by tandem repeats of guanine and then use the cation mediated self-assembly to form GQ to template peptide folding into a specific secondary structure, such as β-turn, β-sheet, and peptide loops decorated with functional groups (Figure 1.18a).

The following PNA-peptide hybrid (**PNA-1**), Figure 1-18b, was synthesized using Fmoc solid phase protocols as the first example in this study. Since the PNA backbone lacks chirality, a chiral amino acid, L-valine, was attached to the C-terminus of the sequence to induce chirality in the quadruplex structure.[79] The four amino acids were chosen based on their propensity to form type II β-turn and were flanked by two sets of tandem repeats of four PNA guanine residues.

We hypothesized that this sequence can form higher order structure though the formation of GQ and subsequent formation of a β-turn in peptide segment, as schematically depicted in Figure 1.18. Preliminarily, the **PNA-1** structure was probed using CD spectroscopy in the presence of 0.1 mM potassium chloride after thermal annealing (heated to 90 °C for 10 min, then cooled to 5 °C at the rate of 1 °C/min and incubated at this temperature for 12 h). The CD spectrum of the **PNA-1** after the annealing was subtracted from the spectrum taken before this treatment and is shown on Figure 1.18c. Unfortunately, extensive data are not available for the CD signature of PNA-peptide hybrids in the literature. However, we were encouraged by the observation of a negative peak at 220 nm (which could correspond to β-sheet formation) and 295 nm (reported in

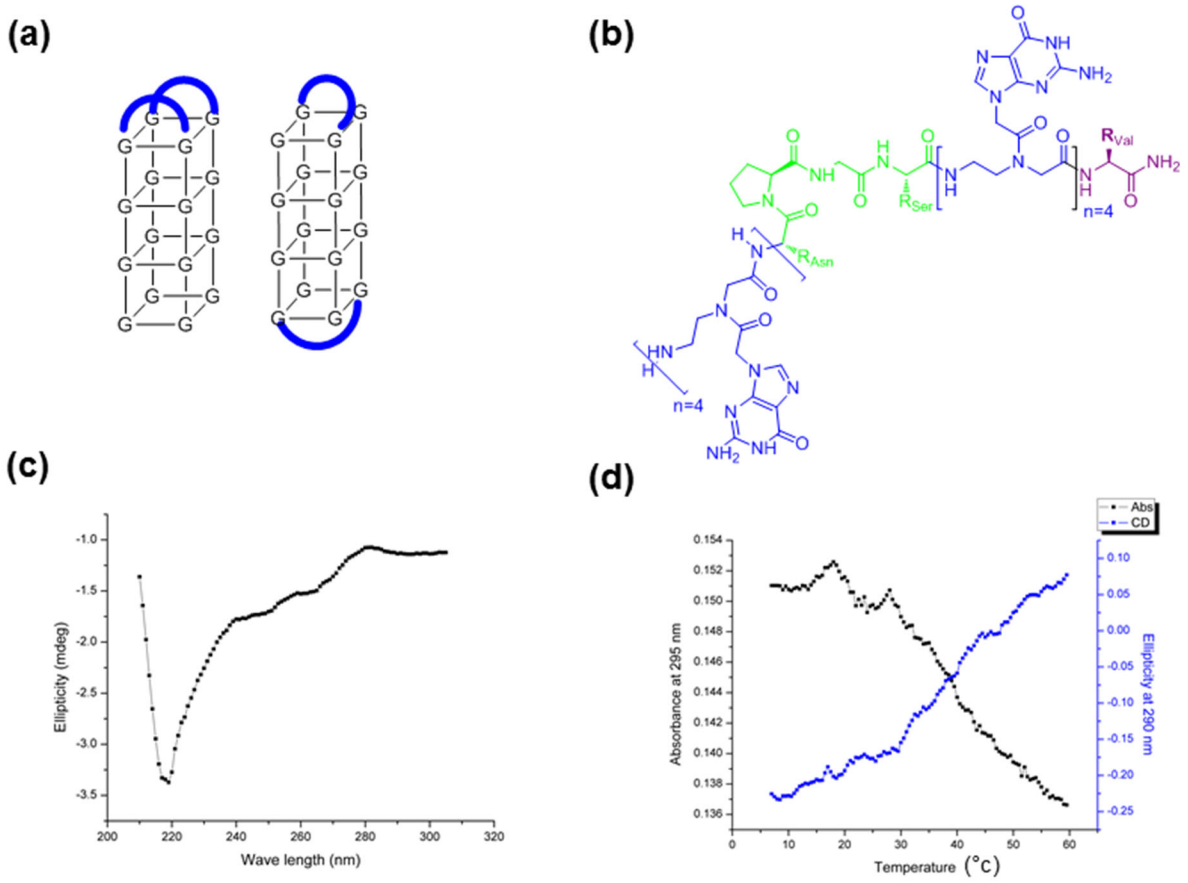

Figure 1.18 GQ as a template for peptide folding. (a) Concept of coupling the GQ assembly to peptide folding and (b) the structure of PNA-peptide hybrid, **PNA-1**. c) The CD signal of **PNA-1** in the presence of 0.1 M potassium d) UV and CD melting curves at 295 nm.

previous PNA based GQ systems).[80] Upon increasing the temperature, the CD signal at 295nm slowly disappeared and an inverse sigmoidal UV melting curve was observed as shown in Figure 1.18d. An inverse sigmoidal melting curve at this wavelength has been described as characteristic of quadruplex formation.[81]

The lack of chirality in the PNA backbone complicated the analysis of the structure using CD spectroscopy. Additionally, more detailed molecular modelling suggested that a longer peptide sequence is necessary to accommodate the loop topology connecting the GQ stems. I then set to synthesize another peptide-PNA hybrid (**PNA-2**, Ac-(pG)4KVKPGEAD(pG)$_4$V where pG is the guanine PNA) at larger scale and study the GQ formation by ^{1}H NMR spectroscopy instead of CD. **PNA-2** was synthesized using SPPS and studied using ^{1}H NMR in the presence of potassium ions. Alas, no difference in the NMR of **PNA-2** was observed before and after the addition of potassium salt. It is likely that the CD signal of **PNA-1** was the result of the inherent properties of the peptide sequence to adopt a turn geometry.

The combination of high cost of PNA synthesis, low scale, and low yield of resulting peptide conjugates motivated to look for an alternative backbone, to further pursue this idea toward first demonstration. I will not get into the details of these efforts for the sake of brevity but a publication from Ghosh and Hamilton in 2012 brilliantly demonstrated the validity of the original idea in a synthetically simpler system (Figure 1-19).[82] In this work, they used click chemistry to conjugate the peptide sequence to two single strand of DNA containing four guanine bases and used GQ assembly to template the peptide sequence to adopt a loop structure. There is a practical lesson in this unsuccessful endeavor: there is a steep price for losing the big picture, while trying to overcome the synthetic hurdle for initial demonstration.

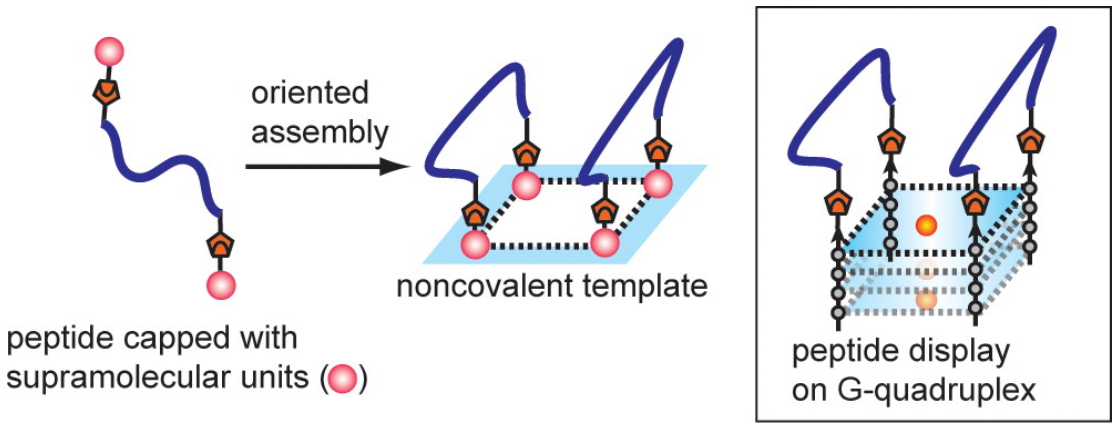

Figure 1.19 Schematic of GQ mediated mimicry of a multi-loop protein (reprinted from reference 82).

1.15 Summary

In conclusion, I discussed my approach to template peptide folding in organic media. We started by looking at simple loop/turn structure stabilized by assembly of two designed SAAs and then briefly covered additional efforts to expand this idea into more complex structure and additional supramolecular motif. I hope that the present chapter makes case for validity of templating peptide folding using supramolecular interactions.

1.16 References

(1) Anfinsen, C. B. *Science* **1973**, *181*, 223.
(2) Anfinsen, C. *Biochem. J.* **1972**, *128*, 737.
(3) Dill, K. A. *Biochemistry* **1990**, *29*, 7133.
(4) Apostolovic, B.; Danial, M.; Klok, H.-A. *Chem. Soc. Rev.* **2010**, *39*, 3541.
(5) Suárez, M.; Jaramillo, A. *J. R. Soc. Interface* **2009**, *6*, S477.
(6) Dill, K. A.; Ozkan, S. B.; Weikl, T. R.; Chodera, J. D.; Voelz, V. A. *Curr. Opin. Struct. Biol.* **2007**, *17*, 342.
(7) Eisenberg, D.; Wilcox, W.; Eshita, S. M.; Pryciak, P. M.; Ho, S. P.; Degrado, W. F. *Proteins: Structure, Function, and Bioinformatics* **1986**, *1*, 16.
(8) Henchey, L. K.; Jochim, A. L.; Arora, P. S. *Curr. Opin. Chem. Biol.* **2008**, *12*, 692.
(9) Searle, M. S. *J. Chem. Soc., Perkin Trans. 2* **2001**, *0*, 1011.
(10) Schneider, J. P.; Kelly, J. W. *Chem. Rev.* **1995**, *95*, 2169.

(11) Venkatraman, J.; Shankaramma, S. C.; Balaram, P. *Chem. Rev.* **2001**, *101*, 3131.
(12) Levinthal, C. *J. Chim. Phys.* **1968**, *65*, 44.
(13) Hill, D. J.; Mio, M. J.; Prince, R. B.; Hughes, T. S.; Moore, J. S. *Chem. Rev.* **2001**, *101*, 3893.
(14) Dill, K. A.; Chan, H. S. *Nat. Struct. Mol. Biol.* **1997**, *4*, 10.
(15) Riddle, D. S.; Santiago, J. V.; Bray-Hall, S. T.; Doshi, N.; Grantcharova, V. P.; Yi, Q.; Baker, D. *Nat. Struct. Mol. Biol.* **1997**, *4*, 805.
(16) Wolynes, P. G. *Nat. Struct. Mol. Biol.* **1997**, *4*, 871.
(17) Kessler, H. *Angew. Chem. Int. Ed. Engl.* **1982**, *21*, 512.
(18) Mutter, M.; Dumy, P.; Garrouste, P.; Lehmann, C.; Mathieu, M.; Peggion, C.; Peluso, S.; Razaname, A.; Tuchscherer, G. *Angew. Chem. Int. Ed. Engl.* **1996**, *35*, 1482.
(19) Tuchscherer, G.; Grell, D.; Mathieu, M.; Mutter, M. *J. Pept. Res.* **1999**, *54*, 185.
(20) Liu, J.; Wang, D.; Zheng, Q.; Lu, M.; Arora, P. S. *J. Am. Chem. Soc.* **2008**, *130*, 4334.
(21) Leduc, A.-M.; Trent, J. O.; Wittliff, J. L.; Bramlett, K. S.; Briggs, S. L.; Chirgadze, N. Y.; Wang, Y.; Burris, T. P.; Spatola, A. F. *Proc. Natl. Acad. Sci. U. S. A.* **2003**, *100*, 11273.
(22) Zhang, F.; Sadovski, O.; Xin, S. J.; Woolley, G. A. *J. Am. Chem. Soc.* **2007**, *129*, 14154.
(23) Osapay, G.; Taylor, J. W. *J. Am. Chem. Soc.* **1992**, *114*, 6966.
(24) Harrison, R. S.; Shepherd, N. E.; Hoang, H. N.; Ruiz-Gómez, G.; Hill, T. A.; Driver, R. W.; Desai, V. S.; Young, P. R.; Abbenante, G.; Fairlie, D. P. *Proc. Natl. Acad. Sci. U. S. A.* **2010**, *107*, 11686.
(25) Ghadiri, M. R.; Choi, C. *J. Am. Chem. Soc.* **1990**, *112*, 1630.
(26) Kelso, M. J.; Beyer, R. L.; Hoang, H. N.; Lakdawala, A. S.; Snyder, J. P.; Oliver, W. V.; Robertson, T. A.; Appleton, T. G.; Fairlie, D. P. *J. Am. Chem. Soc.* **2004**, *126*, 4828.
(27) Ihara, T.; Takeda, Y.; Jyo, A. *J. Am. Chem. Soc.* **2001**, *123*, 1772.
(28) Tashiro, S.; Matsuoka, K.; Minoda, A.; Shionoya, M. *Angew. Chem. Int. Ed. Engl.* **2012**, *51*, 13123.
(29) Kemp, D. S.; Allen, T. J.; Oslick, S. L. *J. Am. Chem. Soc.* **1995**, *117*, 6641.
(30) Zeng, H. Q.; Yang, X. W.; Flowers, R. A.; Gong, B. *J. Am. Chem. Soc.* **2002**, *124*, 2903.
(31) Khakshoor, O.; Nowick, J. S. *Curr. Opin. Chem. Biol.* **2008**, *12*, 722.
(32) Woods, R. J.; Brower, J. O.; Castellanos, E.; Hashemzadeh, M.; Khakshoor, O.; Russu, W. A.; Nowick, J. S. *J. Am. Chem. Soc.* **2007**, *129*, 2548.
(33) DeGrado, W. F.; Summa, C. M.; Pavone, V.; Nastri, F.; Lombardi, A. *Annu. Rev. Biochem.* **1999**, *68*, 779.
(34) Kauzmann, W. *Adv.Protein Chem.* **1959**, *14*, 1.
(35) Kamtekar, S.; Schiffer, J. M.; Xiong, H. Y.; Babik, J. M.; Hecht, M. H. *Science* **1993**, *262*, 1680.
(36) Hill, R. B.; DeGrado, W. F. *J. Am. Chem. Soc.* **1998**, *120*, 1138.
(37) Lombardi, A.; Summa, C. M.; Geremia, S.; Randaccio, L.; Pavone, V.; DeGrado, W. F. *Proc. Natl. Acad. Sci. U. S. A.* **2000**, *97*, 6298.
(38) Struthers, M. D.; Cheng, R. P.; Imperiali, B. *Science* **1996**, *271*, 342.
(39) Fletcher, J. M.; Harniman, R. L.; Barnes, F. R. H.; Boyle, A. L.; Collins, A.; Mantell, J.; Sharp, T. H.; Antognozzi, M.; Booth, P. J.; Linden, N.; Miles, M. J.; Sessions, R. B.; Verkade, P.; Woolfson, D. N. *Science* **2013**, *340*, 595.
(40) Jarvo, E. R.; Copeland, G. T.; Papaioannou, N.; Bonitatebus, P. J.; Miller, S. J. *J. Am. Chem. Soc.* **1999**, *121*, 11638.
(41) Miller, S. J. *Acc. Chem. Res.* **2004**, *37*, 601.

(42) Lee, A. G. *Biochim. Biophys. Acta* **2003**, *1612*, 1.
(43) Fonseca, S. B.; Pereira, M. P.; Kelley, S. O. *Adv. Drug Deliv. Rev.* **2009**, *61*, 953.
(44) Doig, A. J.; Williams, D. H. *J. Am. Chem. Soc.* **1992**, *114*, 338.
(45) Beijer, F. H.; Sijbesma, R. P.; Kooijman, H.; Spek, A. L.; Meijer, E. W. *J. Am. Chem. Soc.* **1998**, *120*, 6761.
(46) Sijbesma, R. P.; Beijer, F. H.; Brunsveld, L.; Folmer, B. J. B.; Hirschberg, J. H. K. K.; Lange, R. F. M.; Lowe, J. K. L.; Meijer, E. W. *Science* **1997**, *278*, 1601.
(47) Keizer, H. M.; Sijbesma, R. P.; Meijer, E. M. *Eur J Org Chem* **2004**, 2553.
(48) Turner, R. A.; Weber, R. J.; Lokey, R. S. *Org. Lett.* **2010**, *12*, 1852.
(49) ten Cate, A. T.; Dankers, P. Y. W.; Kooijman, H.; Spek, A. L.; Sijbesma, R. P.; Meijer, E. W. *J. Am. Chem. Soc.* **2003**, *125*, 6860.
(50) Lafitte, V. G. H.; Aliev, A. E.; Horton, P. N.; Hursthouse, M. B.; Hailes, H. C. *Chem. Commun.* **2006**, 2173.
(51) Fesinmeyer, R. M.; Hudson, F. M.; Olsen, K. A.; White, G. W. N.; Euser, A.; Andersen, N. H. *J. Biomol. NMR* **2005**, *33*, 213.
(52) Ösapay, K.; Case, D. *J. Biomol. NMR* **1994**, *4*, 215.
(53) Ribero, A.; Goodman, M. *Int. J. Pept. Protein Res.* **1979**, 414.
(54) Gellman, S. H.; Adams, B. R. *Tetrahedron Lett.* **1989**, *30*, 3381.
(55) Khakshoor, O.; Demeler, B.; Nowick, J. S. *J. Am. Chem. Soc.* **2007**, *129*, 5558.
(56) Pei, H.; Germann, M. W.; Allison, S. a. *J. Phys. Chem. B* **2009**, *113*, 9326.
(57) Erdélyi, M.; Karlén, A.; Gogoll, A. *Chemistry* **2005**, *12*, 403.
(58) Bai, Y.; Milne, J. S.; Mayne, L.; Englander, S. W. *Proteins: Structure, Function, and Bioinformatics* **1993**, *17*, 75.
(59) Söntjens, S. H. M.; Sijbesma, R. P.; van Genderen, M. H. P.; Meijer, E. W. *J. Am. Chem. Soc.* **2000**, *122*, 7487.
(60) Scholtz, J. M.; Baldwin, R. L. *Annu. Rev. Biophys. Biomol. Struct.* **1992**, *21*, 95.
(61) Gasset, M.; Baldwin, M. A.; Lloyd, D. H.; Gabriel, J. M.; Holtzman, D. M.; Cohen, F.; Fletterick, R.; Prusiner, S. B. *Proc. Natl. Acad. Sci. U. S. A.* **1992**, *89*, 10940.
(62) Kelly, S. M.; Price, N. C. *Curr. Protein Pept. Sci.* **2000**, *1*, 349.
(63) Nick Pace, C.; Martin Scholtz, J. *Biophys. J.* **1998**, *75*, 422.
(64) Stowell, M. H. B.; McPhillips, T. M.; Rees, D. C.; Soltis, S. M.; Abresch, E.; Feher, G. *Science* **1997**, *276*, 812.
(65) Nowick, J. S. *Org. Biomol. Chem.* **2006**, *4*, 3869.
(66) Kirshenbaum, K.; Barron, A. E.; Goldsmith, R. A.; Armand, P.; Bradley, E. K.; Truong, K. T. V.; Dill, K. A.; Cohen, F. E.; Zuckermann, R. N. *Proc. Natl. Acad. Sci. U. S. A.* **1998**, *95*, 4303.
(67) Huang, K.; Wu, C. W.; Sanborn, T. J.; Patch, J. A.; Kirshenbaum, K.; Zuckermann, R. N.; Barron, A. E.; Radhakrishnan, I. *J. Am. Chem. Soc.* **2006**, *128*, 1733.
(68) Wu, C. W.; Sanborn, T. J.; Huang, K.; Zuckermann, R. N.; Barron, A. E. *J. Am. Chem. Soc.* **2001**, *123*, 6778.
(69) Figliozzi, G. M.; Goldsmith, R.; Ng, S. C.; Banville, S. C.; Zuckermann, R. N. In *Methods in Enzymology*; John, N. A., Ed.; Academic Press: 1996; Vol. Volume 267, p 437.
(70) Gorske, B. C.; Jewell, S. A.; Guerard, E. J.; Blackwell, H. E. *Org. Lett.* **2005**, *7*, 1521.
(71) Armand, P.; Kirshenbaum, K.; Falicov, A.; Dunbrack Jr, R. L.; Dill, K. A.; Zuckermann, R. N.; Cohen, F. E. *Fold Des.* **1997**, *2*, 369.
(72) Andersen, E. S. *N. Biotechnol.* **2010**, *27*, 184.

(73) Wochner, A.; Attwater, J.; Coulson, A.; Holliger, P. *Science* **2011**, *332*, 209.
(74) Nielsen, P.; Egholm, M.; Berg, R.; Buchardt, O. *Science* **1991**, *254*, 1497.
(75) Nielsen, P. E.; Haaima, G. *Chem. Soc. Rev.* **1997**, *26*, 73.
(76) Doluca, O.; Withers, J. M.; Filichev, V. V. *Chem. Rev.* **2013**, *113*, 3044.
(77) Davis, J. T. *Angew. Chem. Int. Ed. Engl.* **2004**, *43*, 668.
(78) González-Rodríguez, D.; van Dongen, J. L. J.; Lutz, M.; Spek, A. L.; Schenning, A. P. H. J.; Meijer, E. W. *Nat. Chem.* **2009**, *1*, 151.
(79) Wittung, P.; Eriksson, M.; Lyng, R.; Nielsen, P. E.; Norden, B. *J. Am. Chem. Soc.* **1995**, *117*, 10167.
(80) Sharma, N. K.; Ganesh, K. N. *Org. Biomol. Chem.* **2011**, *9*, 725.
(81) Krishnan-Ghosh, Y.; Stephens, E.; Balasubramanian, S. *J. Am. Chem. Soc.* **2004**, *126*, 5944.
(82) Ghosh, P. S.; Hamilton, A. D. *J. Am. Chem. Soc.* **2012**, *134*, 13208.

1.17 Experimental details and supporting information

General information

Wang resin was purchased from Aapptec and mono-Fmoc ethylene diamine hydrochloride was purchased from Novabiochem. Commercial solvents and reagents were used without further purification, unless otherwise stated. Reactions were carried out under an atmosphere of nitrogen. Column chromatography was performed on 40–63 μm silica gel (EMD Science) using flash chromatography. Solvents were removed by rotary evaporation. Residual solvents were removed under vacuum (< 0.01 mmsHg). Precipitated products were dried under vacuum (< 0.01 mmHg) or by air suction through a filter funnel. High resolution mass spectra were obtained by electrospray ionization (ESI) on a Waters Micromass LCT Premier (instrument variation σ < 5 ppm). NMR spectra were recorded using 500 MHz Bruker AVANCETM, 600 MHz Bruker AVANCETM spectrometers. 125 MHz ^{13}C NMR spectra were obtained using a cryoprobe. ^{1}H spectra NMR were referenced with TMS (δ = 0.00 ppm), $CDCl_3$ (δ = 7.26 ppm), CD_2Cl_2 (δ = 5.32 ppm) and DMSO-d_6 (δ = 2.50 ppm). ^{13}C NMR spectra were referenced either with TMS (δ = 0.00 ppm), $CDCl_3$ (δ = 7.26 ppm) and DMSO-d_6 (δ = 77.2 ppm). Chemical shifts are reported in parts per million (ppm) on the δ scale. Analytical reverse phase HPLC (RP-HPLC) was performed on a Beckman gold system (Agilent Zorbax® Eclipse-XDB-C18 80 Å; 150 x 4.6 mm; particle size 5 μm; solvent A: H_2O/0.1% TFA, solvent B: CH_3CN/0.1% TFA), and preparative RP-HPLC was carried out on a Waters 600 HPLC machine (Agilent prep-C18 column, 250 x 21.2 mm; particle size 10 μm; solvent A: H_2O/0.1% TFA, solvent B= CH_3CN/0.1% TFA).

Synthesis of supramolecular amino acids

Synthesis of Fmoc-CUPy(Bn)-OH

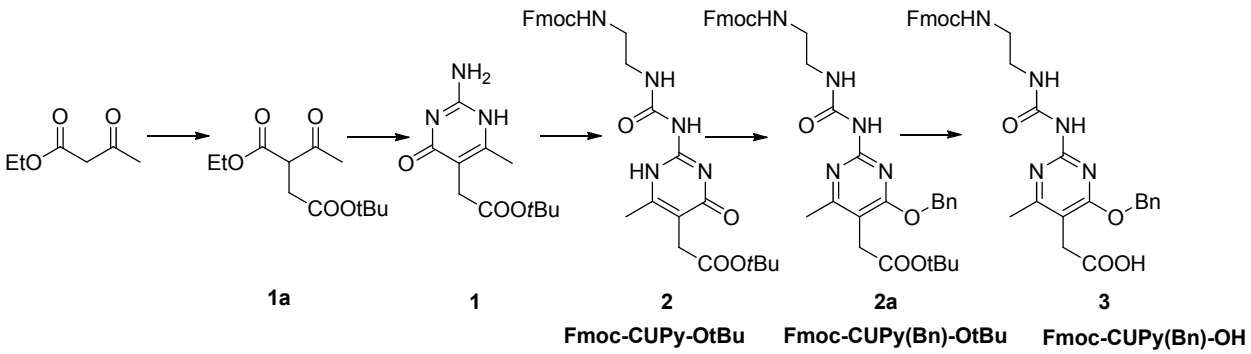

Scheme 1.5 The synthetic scheme for Fmoc-CUPy(Bn)-OH (**3**).

Synthesis of 1a

To a round bottom flask containing ethyl acetoacetate (10 g, 76 mmol) and *tert*-butyl bromoacetate (12.6 g, 63.4 mmol) in 210 mL of DMF, was added potassium carbonate (11.39 g, 82 mmol). The reaction mixture was stirred at room temperature overnight. The mixture was then partitioned between 250 mL of EtOAc and 250 mL of water. The layers were then separated, and the aqueous layer was extracted with 2 × 200 mL of EtOAc. The combined organic layers were then dried ($MgSO_4$), filtered and concentrated *in vacuo* to afford a yellow oil. The crude oil was dissolved in chloroform and purified by flash chromatography (10:90 EtOAc:hexane). The fractions containing pure product were combined and evaporated to afford compound **1a** as yellow oil (11.1g, 72%). ^{1}H NMR (500 MHz, $CDCl_3$, 298 K) δ 1.2 1.3(m, 3H), δ 1.4 (s, 9H), δ 2.3 (d, 3H,), δ 2.8 (dd, 2H), δ 3.0 (dd, 2H), δ 4.2 (m, 2H). MS(ESI) *m*/*z* calcd for $C_{12}H_{20}O_5$ $(M + Na)^+$ 267.13, found 267.1.

Synthesis of 1

To the solution of **1a** (10 g, 41 mmol) in 100 mL of ethanol was added guanidine hydrocarbonate (5.9 g, 33 mmol). The mixture was heated to reflux for 12 hours, cooled to the room temperature. The solvent was evaporated *in vacuo* to afford orange crude oil. The residue was diluted with chloroform and purified by flash chromatography (12:88 MeOH:$CHCl_3$). The fractions containing pure product were combined and concentrated to afford compound **1** as yellow solid (4.8 g, 49%). ^{1}H NMR (500 MHz, DMSO-d_6, 298 K) δ 1.4 (s, 9H), δ 2.0 (s, 3H), δ 3.2 (s, 2H), δ 6.3 (s, 2H). MS(ESI) *m*/*z* calcd for $C_{11}H_{17}N_3O_3$ $(M + H)^+$ 240.13, found 240.1.

Synthesis of 2 (Fmoc-CUPy-O^{t}Bu)

To a suspension of **1** (2.98 g, 12.4 mmol) in 60 mL of chloroform was added 1,1'-carbonyldiimidazole (4.44 g, 27.4 mmol). The reaction mixture was heated at reflux for 2 h under nitrogen gas flow until clear solution was obtained. To the reaction mixture was added 100 mL of chloroform, and the organic layer was extracted with 3 × 50 mL of brine. The aqueous layers were then combined and extracted with 2 × 50 mL of chloroform. The combined chloroform layers were dried (Na_2SO_4) and filtered. Solvent was then evaporated *in vacuo* which resulted in a light yellow powder and was used without further purification. To the CDI activated imidazolide (3.7 g, 11 mmol) and mono-Fmoc ethylenediamine hydrochloride, NovaBiochem, (4.60 g, 14.4 mmol) in 40 mL of chloroform was added 4.83 mL, (27.7 mmol), of N,N-diisopropylethylamine ,DIPEA. The reaction mixture was stirred for 6 hours under the flow of nitrogen gas. The solvent was then evaporated under reduced pressure. The residue was diluted with chloroform and purified by flash chromatography (6:94 MeOH:$CHCl_3$) to afford compound **2** as off white solid (5.39 g, 89%). ^{1}H NMR (500 MHz, $CDCl_3$, 298 K) δ 1.4 (s, 9H), δ 2.2 (s, 3H), δ 3.33 (m, 2H), δ 3.4 (m, 2H and m, 2H), δ 4.21 (t, H, *J* = 8), δ 4.35 (d, 2H, *J* = 7), δ 6.5 (s, 2H) , δ 7.25 7.45 (m, 5H), δ = 7.6 (d, 2H,

J = 7.5), δ 7.75 (d, 2H, *J* = 7.5), δ 10.2 (s, H), δ 11.8 (s, H), δ 12.9 (s, H). ^{13}C NMR (125 MHz, $CDCl_3$, 298 K) δ 17, 28, 30, 32, 40.3, 40.5, 47, 66, 81, 112, 119, 125, 127, 127.6, 141.3, 144, 146, 156.5, 157, 170. HRMS (ESI) *m/z* calcd for $C_{29}H_{33}N_5O_6$ $(M + Na)^+$ 570.2328, found 570.2314.

Synthesis of 2a Fmoc-CUPy(Bn)-O^{t}Bu

To a round bottom flask containing **2** (5.4 g, 9.9 mmol) and benzyl bromide (2.58 g, 14.8 mmol) in 100 mL of DMF wad added potassium carbonate (2.04 g, 14.8 mmol). The reaction was then stirred at room temperature overnight. 110 mL of water was added to the reaction mixture and the aqueous layer was extracted with 2 × 100 mL chloroform. The organic layer was then washed with 100 mL of brine, dried ($MgSO_4$) and filtered. Finally the solvent was evaporated to afford a yellow solid. The crude solid was dissolved in chloroform and purified by flash column chromatography (50:50 EtOAc:hexane). The fractions containing pure product were combined and evaporated to afford **2a** as off-white solid (4.2 g, 67%). ^{1}H NMR (500 MHz, $CDCl_3$, 298 K) δ 1.4 (s, 9H), δ 2.32 (s, 3H), δ 3.32 (m, 2H), δ 3.46 (s, 2H), δ 3.50 (m, 2H), δ 4.21 (t, H, *J* = 8), δ 4.35 (d, 2H, *J* = 7), δ 5.32 (s, 2H) , δ 7.04 (s, 1H), δ 7.25 7.45 (m, 10H), δ = 7.6 (d, 2H, *J* = 7.5), δ 7.75 (d, 2H, *J* = 7.5), δ 9.4 (s, H). ^{13}C NMR (125 MHz, $CDCl_3$, 298 K) δ 22, 28, 32, 39.5, 42, 47, 67, 68, 81,107, 119, 125, 127.1, 127.7,128.1,128.5, 136,141.3, 144, 146, 155.5,156, 157, 168, 169, 170. HRMS (ESI) *m/z* calcd for $C_{36}H_{39}N_5O_6$ $(M + Na)^+$ 660.2798, found 660.2791.

Synthesis of 3 (Fmoc-CUPy(Bn)-OH)

2a, (3.5 g, 5.5 mmol) was dissolved in 6 mL of 30% Trifluoroacetic acid, TFA, in DCM (% v/v). The clear solution was stirred until the deprotection was complete, judged by TLC or mass spectroscopy. The reaction mixture was then concentrated *in vacuo* and the product was precipitated by slow addition of reaction mixture to the 25 mL of cold Et_2O. The product was collected by centrifugation at 3000 rpm for 10 min and decantation of organic layer. The solid was dispersed in 20 mL of Et_2O and centrifuged at 3000 rpm for 10 min. After decantation of organic

layer, **3** was obtained as off-white solid (2.9 g, 90%). ^{1}H NMR (500 MHz, DMSO-d_6, 298 K) δ 2.29 (s, 3H), δ 3.16 (m, 2H), δ 3.31 (m, 2H), δ 3.50 (s, 2H), δ 4.21 (t, H, J = 7), δ 4.4 (d, 2H, J = 7), δ 5.38 (s, 2H) , δ 7.25 7.45 (m, 10H), δ = 7.6 (d, 2H, J = 7.5), δ 7.8 (d, 2H, J = 7.5), δ 9.15 (s, H), δ 9.5 (s, H), δ 13.2 (s, H). ^{13}C NMR (125 MHz, DMSO-d_6, 298 K) δ 22, 31, 41, 47, 66, 68, 107, 120, 125, 127.5, 128.1, 128.2, 128.5, 128.8, 137, 141, 144, 155, 156, 157, 168, 172. HRMS (ESI) m/z calcd for $C_{32}H_{31}N_5O_6$ $(M + H)^+$ 582.2352 , found 582.2341.

Fmoc-CUPy(Bn)-OH HPLC trace

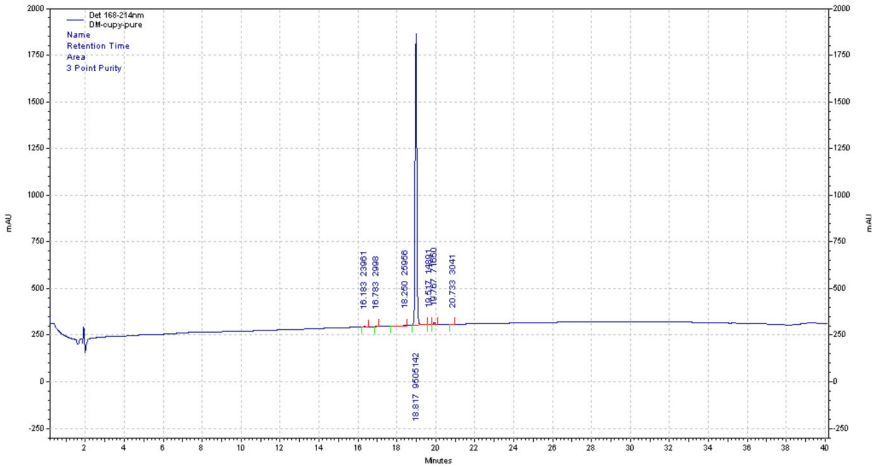

Figure 1.20 The HPLC trace of purified Fmoc-CUPy(Bn)-OH (**3**).

Synthesis of Fmoc-NUPy(Bn)-OH

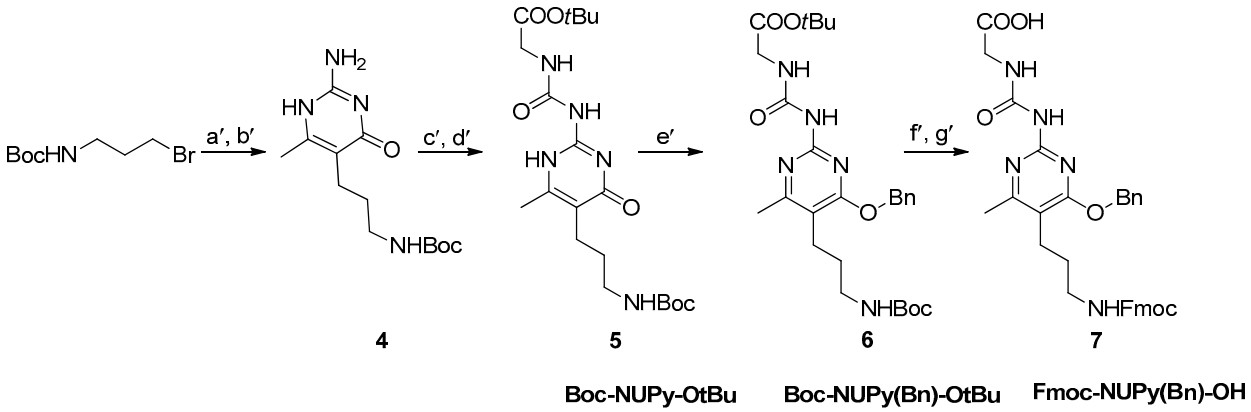

Scheme 1.6 The synthetic scheme for Fmoc-NUPy(Bn)-OH (**7**).

Synthesis of 4

To a round bottom flask containing ethyl acetoacetate (4.89 g, 37.6 mmol) and tert-butyl (3-bromopropyl)carbamate (8.14 g, 34.2 mmol) in 115 mL of DMF, was added potassium carbonate (8.03 g, 58.1 mmol). The reaction mixture was stirred at room temperature overnight. The mixture was then partitioned between 150 mL of EtOAc and 250 mL of water. The layers were then separated, and the aqueous layer was extracted with 2 × 100 mL of EtOAc. The combined organic layers were then dried ($MgSO_4$), filtered and concentrated *in vacuo* to afford a yellow oil. The crude oil was then dissolved in 170 mL of ethanol and guanidine hydrocarbonate (6.99 g, 37.6 mmol) was added to this mixture. The mixture was heated to reflux for 12 hours and subsequently cooled to room temperature. The solvent was evaporated *in vacuo* to afford orange crude oil. The residue was diluted with chloroform and purified by flash chromatography (12:88 MeOH:$CHCl_3$). The fractions containing pure product were combined and concentrated to afford compound **4** as a yellow solid (5.79 g, 60%). ^{1}H NMR (500 MHz, DMSO-d_6, 298 K) δ 1.36 (s, 9H), δ 1.43 (m, 2H), δ 2.92 (s, 3H), δ 2.23 (m, 2H), δ 2.86 (m, 2H), δ 6.24 (s, 2H), δ 6.74 (s,1H). MS (ESI) *m*/*z* calcd for $C_{13}H_{22}N_4O_3$ $(M+H)^+$: 283.34,found 283.1.

Synthesis of 5 (Boc-NUPy-O^{t}Bu)

To a suspension of **4** (5.70 g, 20.19 mmol) in 100 mL of chloroform was added 1,1'-carbonyldiimidazole (8.33 g, 50.5 mmol). The reaction mixture was heated at reflux for 2 h under nitrogen gas flow until clear solution was obtained. To the reaction mixture was added 200 mL of chloroform, and the organic layer was extracted with 2 × 200 mL of brine. The aqueous layers were then combined and extracted with 200 mL of chloroform. The combined chloroform layers were dried (Na_2SO_4) and filtered. Solvent was then evaporated *in vacuo* which resulted in a light yellow powder that was used without further purification. To the CDI activated imidazolide solution (6.00 g, 15.94 mmol) and glycine *tert*-butyl ester hydrochloride (4.01 g, 23.91 mmol) was added 8.33 mL of DIPEA (47.8 mmol). The reaction mixture was stirred for six hours under the flow of nitrogen gas. The solvent was then evaporated under reduced pressure. The residue was diluted with chloroform and purified by flash chromatography (8:92 MeOH:$CHCl_3$) to afford compound **5** as an off white solid (4.97 g, 71%). ^{1}H NMR (500 MHz, $CDCl_3$, 298 K) δ 1.4 (s, 9H and s, 9H), δ 1.65 (m, 2H), δ 2.26 (s, 3H), δ 2.50 (t, 2H, J = 7), δ 3.06 (m, 2H), δ 3.89 (d, 2H, J = 5), δ 5.5 (s, H), δ 10.64 (s, H), δ 12.04 (s, H), δ = 12.75 (s, H). MS (ESI) m/z calcd $C_{20}H_{33}N_5O_6$ $(M+H)^+$: 440.51, found 440.1.

Synthesis of 6 (Boc-NUPy(Bn)-O^{t}Bu)

To a round bottom flask containing **5** (3.5 g, 7.96 mmol) and benzyl bromide (2.04 g, 11.9 mmol) in 80 mL of DMF wad added potassium carbonate (1.65 g, 11.95 mmol). The reaction was then stirred at room temperature overnight. 200 mL of water was added to the reaction mixture and the aqueous layer was extracted with 2 × 150 mL chloroform. The organic layer was then washed with 100 mL of brine, dried ($MgSO_4$) and filtered. Finally the solvent was evaporated to afford a yellow solid. The crude solid was dissolved in chloroform and purified by flash column chromatography (50:50 EtOAc: hexane). The fractions containing pure product were combined and evaporated to afford compound **6** as off-white solid (2.18 g, 52%). ^{1}H NMR (500 MHz, $CDCl_3$,

298 K) δ 1.4 (s, 9H), δ 1.5 (s, 9H), δ 1.5 (m, 2H), δ 2.4 (s, 3H), δ 2.57 (t, 2H, *J* = 8), δ 3.11 (m, 2H), δ 4.05 (d, 2H, *J* = 5), δ 5.4 (s, 2H), δ 7.08 (s, H), δ 7.32 7.41 (m, 5H), δ = 9.7 (s, H).^{13}C NMR (125 MHz, $CDCl_3$, 298 K) δ 22, 28, 32, 39.5, 42, 47, 67, 68, 81,107, 119, 125, 127.1, 127.7,128.1,128.5, 136,141.3, 144, 146, 155.5,156, 157, 168, 169, 170. HRMS (ESI) *m*/*z* calcd for $C_{27}H_{39}N_5O_6$ $(M + Na)^+$ 552.2798, found 552.2803.

Synthesis of 7 (Fmoc-NUPy(Bn)-OH)

Compound **6** (2.0 g, 3.78 mmol) was dissolved in 5 mL of 30% TFA in DCM (% v/v). The clear solution was stirred until the deprotection was complete, judged by TLC or mass spectroscopy. The reaction mixture was then concentrated *in vacuo* and the product was precipitated by slow addition of reaction mixture to the 25 mL of cold Et_2O. The product was collected by centrifugation at 3000 rpm for 10 min. The organic layer was decanted, and the solid was dispersed in 80 mL of 1:1 mixture of acetonitrile and water. To the resulting suspension was added K_2CO_3 (0.8 g, 5.79 mmol). Fmoc-OSu (1.3 g, 3.85 mmol) was then slowly added to the mixture under vigorous stirring, after that the reaction mixture was stirred for 12 hours. pH of the solution was adjusted to 1 by slow addition of concentrated HCl. The precipitate was then extracted from aqueous layer by 3 × 100mL of EtOAc. The organic layer was then washed with 2 × 100 mL of cold water and 100 mL of brine. The solvent was evaporated and the purity of product was analyzed using NMR. Further purification was accomplished using preparative HPLC where needed to afford compound **7** as white solid (1.35 g, 60%). ^{1}H NMR (500 MHz, DMSO-d_6, 298 K) δ 1.6 (m, 2H), δ 2.36 (s, 3H), δ 2.52 (solvent peak and m, 2H), δ 3.0 (m, 2H), δ 3.9 (d, 2H, *J* = 4.5), δ 4.1 (t, 2H, *J* = 4.5), δ 4.3 (d, 2H, *J* = 6.5), δ 5.3 (s, 2H), δ 7.25 7.45 (m, 10H), δ = 7.7 (d, 2H, *J* = 7.5), δ 7.9 (d, 2H, *J* = 7.5), δ 9.4 (s, H), δ 9.6 (s, H), δ 12.8 (s, H). ^{13}C NMR (125 MHz, DMSO-d_6, 298 K) δ 21, 22, 29, 43, 47, 65, 68, 112, 121, 126, 127, 128, 128.3, 128.4, 128.8, 136,

141, 144, 154, 155, 156, 165, 167, 172. HRMS (ESI) *m/z* calcd for $C_{33}H_{33}N_5O_6$ $(M + H)^+$ 596.2509, found 596.2513.

Fmoc-NUPy(Bn)-OH HPLC trace

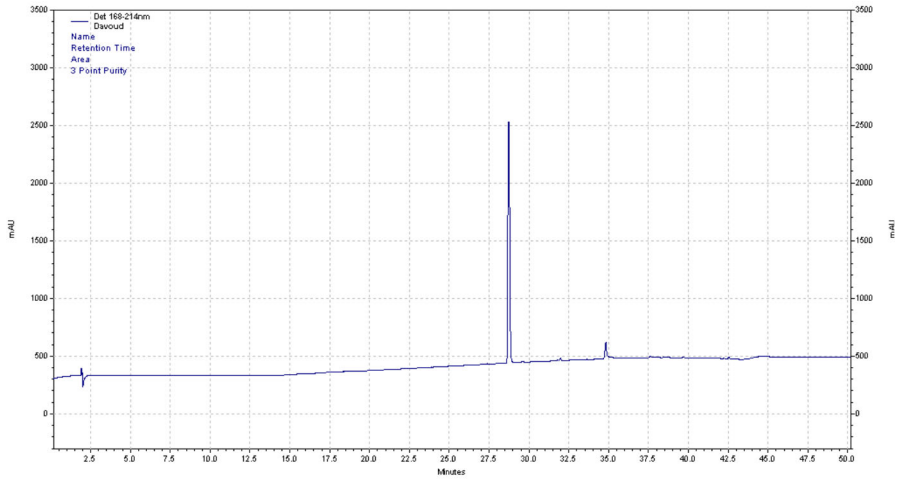

Figure 1.21 The HPLC trace of the purified Fmoc-NUPy(Bn)-OH (**7**).

Molecular modeling procedure

Maestro Molecular modeling package with MacroModel engine was utilized to aid the design process. A model of each peptide was created and subjected to energy minimization using AMBER* forcefield with $CHCl_3$, GB/SA implied solvent parameter after constraining the distance between hydrogen bonding edge of UPy amino acids to 2±0.1 Å. Minimized structures were then visually inspected for the orientation of UPy supramolecular amino acids.

The models that passed previous test, were further optimized by 5000 steps Monte Carlo conformational search and minimized using AMBER* force field and $CHCl_3$ implied solvent parameter. Constrained parameters were chosen similar to energy minimization calculations. The 30 lowest energy structures were then visually inspected for unwanted torsions or strains.

Peptide synthesis

Typical peptide synthesis procedure

Weighted solid support resin, 90 mg Wang resin 0.58mmol/g, was added to a Bio-Rad Poly-Prep chromatography column and was soaked with DMF (2 × ca. 5 mL, 10 min each) and drained under nitrogen pressure. Standard amino acids (3 equiv) were activated with HCTU (3 equiv) and DIPEA (6 equiv) in ca. 1 mL solution of DMF and after 30 s were added to the resin. The resin was gently agitated for 20 min and was subjected to second coupling. Fmoc-CUPy(Bn)-OH or Fmoc-NUPy(Bn)-OH was coupled to the resin using 2 equiv with HCTU (2 equiv) and DIPEA (4 equiv) in a ca. 1-mL DMF. The solution was added to the resin and the resin was gently agitated for 4–12 h. Fmoc deprotection was carried out by soaking the resin with a solution of 20% piperidine–DMF (2 × ca. 5 mL for 10 min) and gently agitating the resin. After deprotection of the Fmoc group, the resin was soaked with DMF (5 × ca. 3 mL for 1 min) and CH_2Cl_2 (5 × ca. 3 mL for 1 min). Couplings to the amino groups were monitored by the 2,4,6-trinitrobenzene sulphonic acid to determine coupling completeness. The peptide was cleaved from resin using 5 mL of TFA/water/triisopropylsilane (9/0.5/0.5, v/v/v) and mixed for ca. 3 h. The cleavage mixture was then concentrated *in vacuo* and precipitated by addition to cold ether followed by centrifugation and decantation of ether layer. Purification was accomplished using preparative RP-HPLC (water–CH_3CN buffers with 0.1 % TFA) after esterification.

Typical Esterification Procedure

The crude white precipitate from the peptide synthesis was then dissolved in small amount of DCM and was slowly added to cooled solution of 1M acetyl chloride in anhydrous methanol and was stirred overnight. The solution was then concentrated *in vacuo* and the residues was dissolved in water and acetonitrile and purified by RP-HPLC. Typical peptide yields were between 16-20%.

Typical Hydrogenolysis Procedure

A 17x60 mm scintillation vial, with plastic septum, a gas inlet adapter fitted with a hydrogen balloon, and a magnetic stirring bar was charged with 0.6-1 mL of methanol, and protected peptide (5.0 mg in 250 μL DCM). 5% $Pd/CaCO_3$ (2 mg) was added to the reaction mixture under a nitrogen flow. The vial filled with hydrogen and then maintained under the hydrogen atmosphere for 6 h. The reaction mixture was then diluted by addition of 4 mL of acetonitrile and 1 mL of water. The Pd catalyst was removed by centrifugation and the reaction mixture was purified using RP-HPLC.

Synthesis of Peptide I

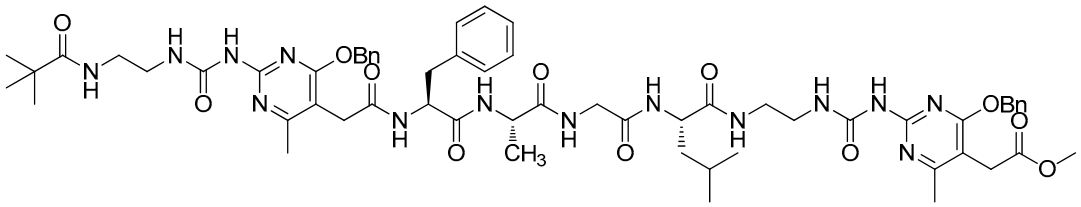

Chemical Formula: $C_{60}H_{78}N_{14}O_{12}$
Exact Mass: 1186.59

Peptide	Sequence
I	Piv-CUPy(Bn)-FAGL-CUPy(Bn)-OMe

MS (ESI), m/z calcd for $[(C_{60}H_{78}N_{14}O_{12} + H)/ 1]^+$ = 1187.59; found 1187.52; MS (ESI), m/z calcd for $[(C_{60}H_{78}N_{14}O_{12} + 2H)/ 2]^+$ = 594.29; found 594.23.

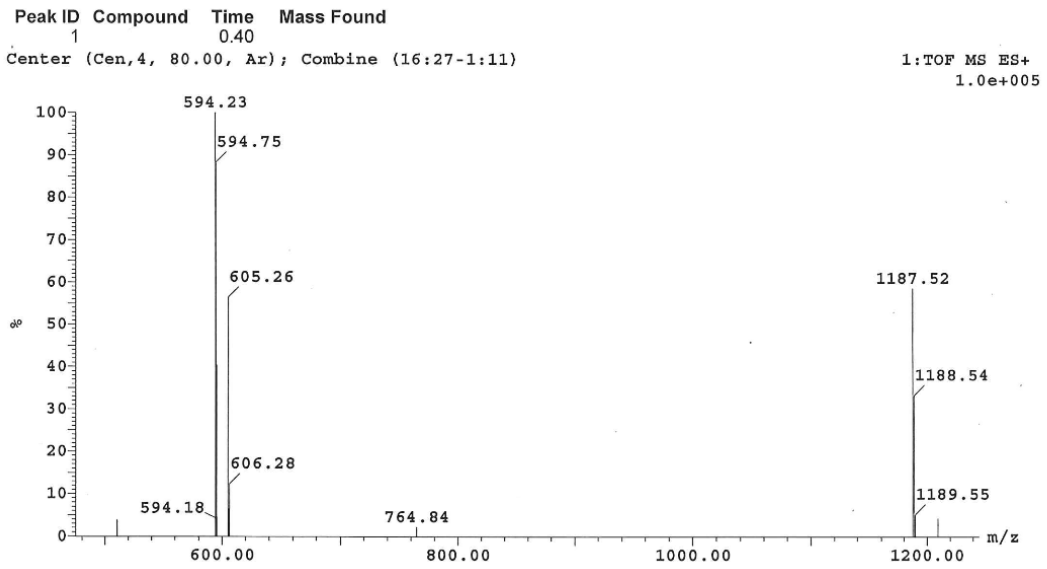

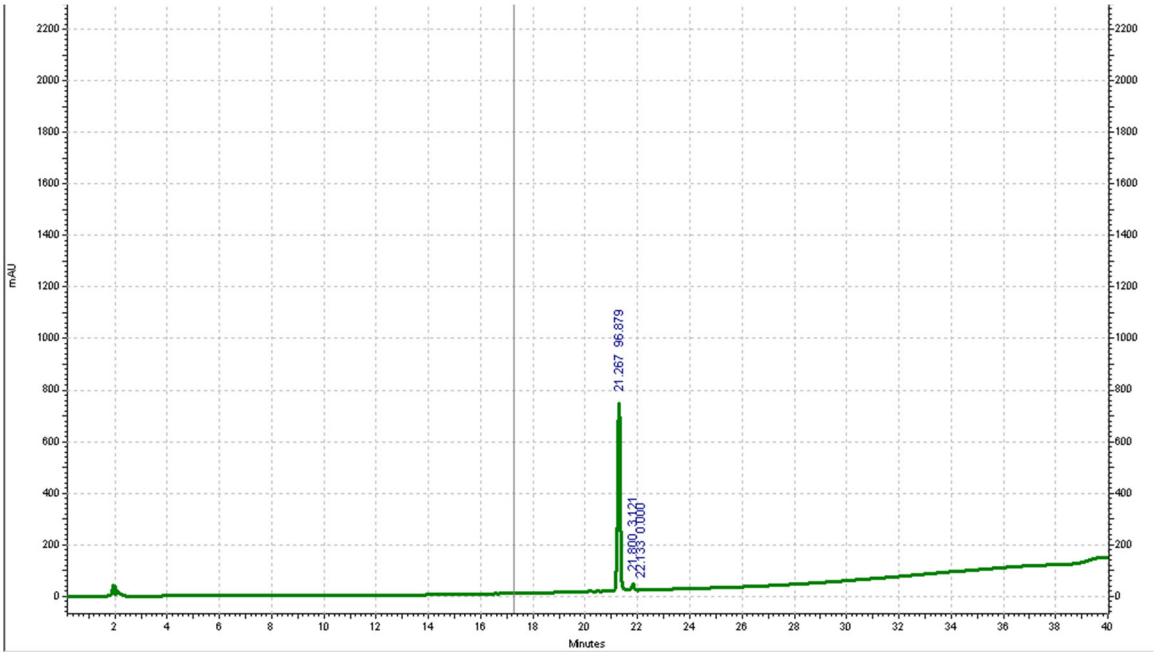

Figure 1.22 ESI-MS and analytical HPLC trace for Peptide **I**. (Agilent Zorbax® Eclipse-XDB-C18 80 Å; 150 x 4.6 mm; particle size 5 µm; solvent A: H_2O/0.1% TFA, solvent B: CH_3CN/0.1% TFA, 0-100% CH3CN over 35 minutes)

Synthesis of Peptide II

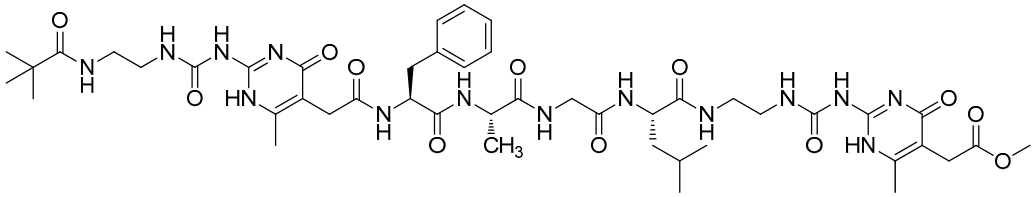

Chemical Formula: $C_{46}H_{66}N_{14}O_{12}$
Exact Mass: 1006.50

Peptide	Sequence
II	Piv-CUPy(Bn)-FAGL-CUPy(Bn)-OMe

MS (ESI), m/z calcd for $[(C_{46}H_{66}N_{14}O_{12} + H)/ 1]^+ = 1007.50$; found 1007.45; MS (ESI), m/z calcd for $[(C_{46}H_{66}N_{14}O_{12} + 2H)/ 2]^+ = 504.25$; found 504.23.

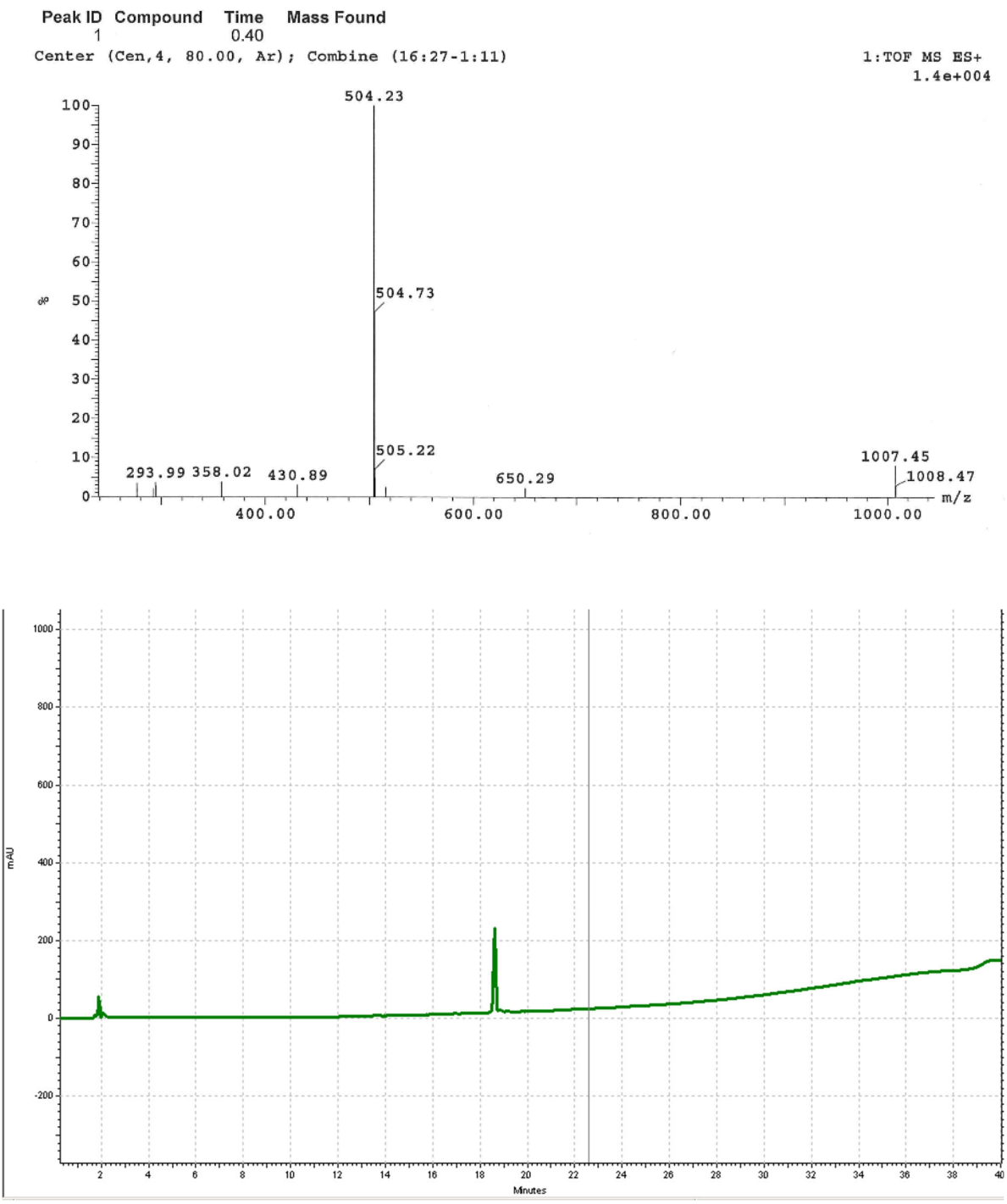

Figure 1.23 ESI-MS and analytical HPLC trace for Peptide II. (Agilent Zorbax® Eclipse-XDB-C18 80 Å; 150 x 4.6 mm; particle size 5 µm; solvent A: H_2O/0.1% TFA, solvent B: CH_3CN/0.1% TFA, 0-100% CH3CN over 35 minutes)

Synthesis of Peptide III

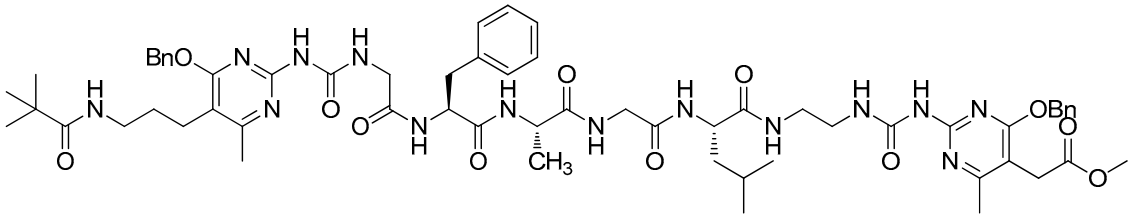

Chemical Formula: $C_{61}H_{80}N_{14}O_{12}$
Exact Mass: 1200.61

Peptide	Sequence
III	Piv-NUPy(Bn)-FAGL-CUPy(Bn)-OMe

MS (ESI), m/z calcd for $[(C_{61}H_{80}N_{14}O_{12} + H)/ 1]^+$ = 1201.61; found 1201.45; MS (ESI), m/z calcd for $[(C_{61}H_{80}N_{14}O_{12} + 2H)/ 2]^+$ = 601.30; found 601.24.

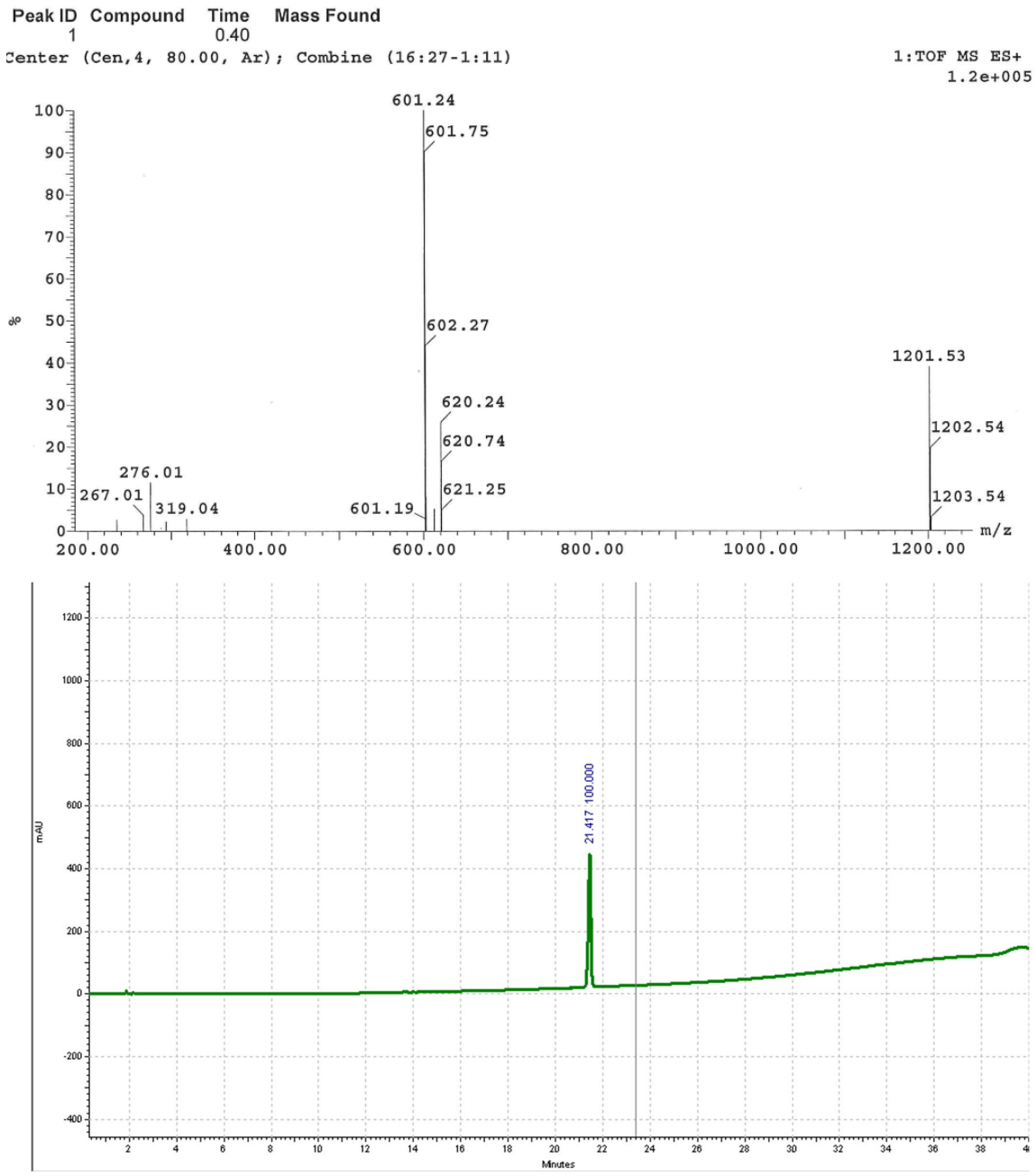

Figure 1.24 ESI-MS and analytical HPLC trace for Peptide **III**. (Agilent Zorbax® Eclipse-XDB-C18 80 Å; 150 x 4.6 mm; particle size 5 µm; solvent A: H_2O/0.1% TFA, solvent B: CH_3CN/0.1% TFA, 0-100% CH3CN over 35 minutes)

Synthesis of Peptide IV

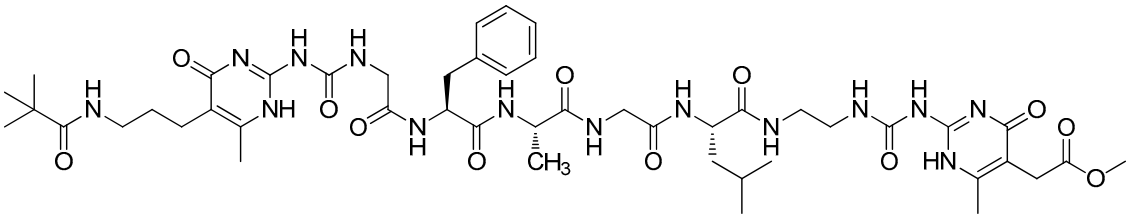

Chemical Formula: $C_{47}H_{68}N_{14}O_{12}$
Exact Mass: 1020.51

Peptide	Sequence
IV	Piv-NUPy-FAGL-CUPy-OMe

MS (ESI), m/z calcd for $[(C_{61}H_{80}N_{14}O_{12} + 2H)/ 2]^+ = 511.25$; found 511.22.

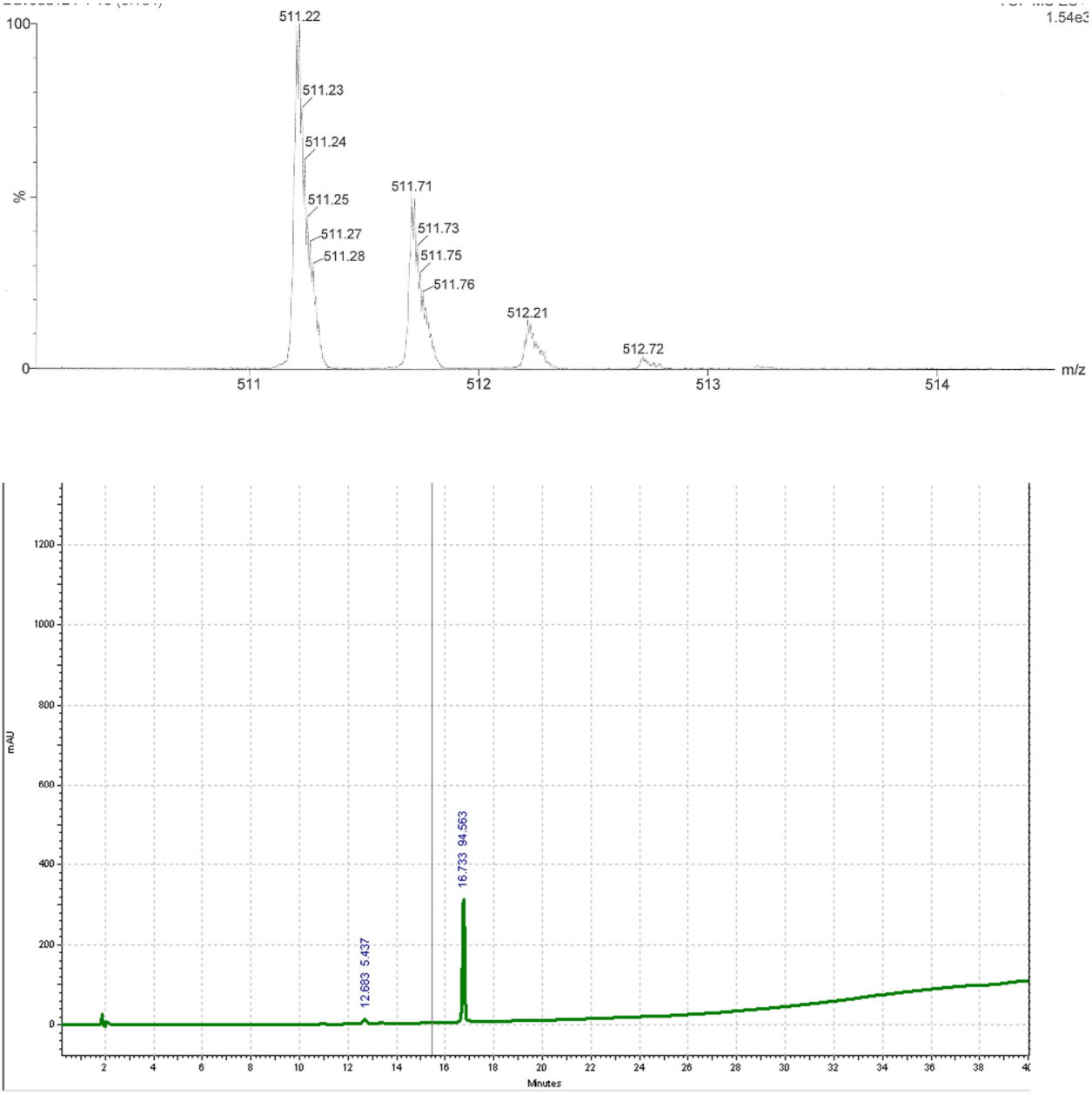

Figure 1.25 ESI-MS and analytical HPLC trace for Peptide **IV**. (Agilent Zorbax® Eclipse-XDB-C18 80 Å; 150 x 4.6 mm; particle size 5 µm; solvent A: H_2O/0.1% TFA, solvent B: CH_3CN/0.1% TFA, 0-100% CH3CN over 35 minutes)

Synthesis of Ac-FAGL-OH

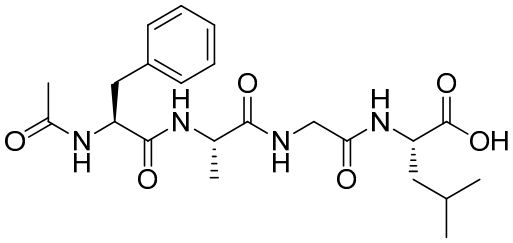

Chemical Formula: $C_{22}H_{32}N_4O_6$
Exact Mass: 448.23

MS (ESI), m/z calcd for $[(C_{22}H_{32}N_4O_6 + H)]^+$ = 449.23; found 449.33.

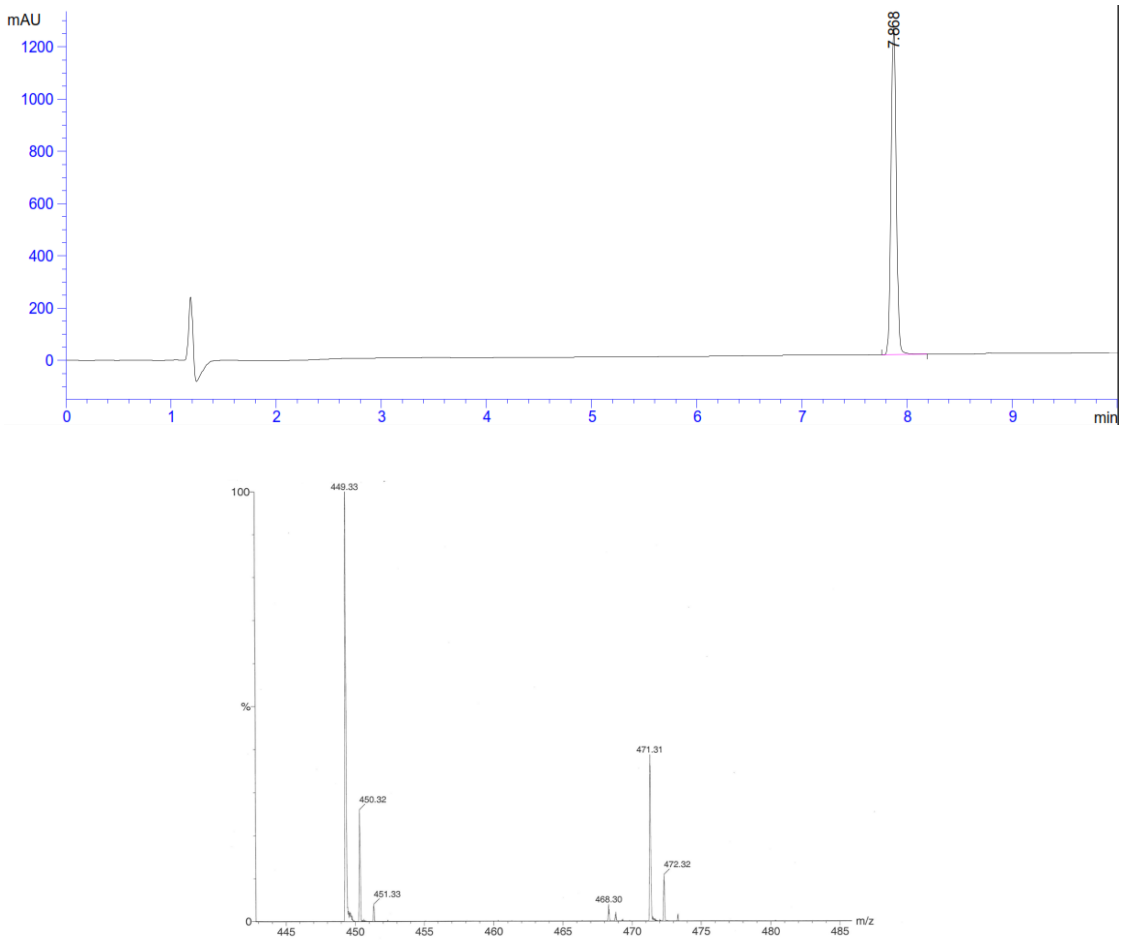

Figure 1.26 ESI-MS and analytical HPLC trace for Ac-FAGL-OH. (Kinetex™ LC Column 80 Å; 100 x 4.6 mm; particle size 2.6 µm; solvent A: H_2O/0.1% TFA, solvent B: CH_3CN/0.1% TFA**,** 0-100% CH_3CN over 20 minutes)

Synthesis of c-(KFAGL)

Crude Ac-LysFAGL-OH was synthesized according to the general peptide synthesis procedure on the wang resin. The crude peptide mixture was dissolved in 200mL DMF (1mM) and 5eq of HCTU and DIPEA was added to the mixture. The reaction was stirred for 24 hours after which the DMF was completely removed. The residue was dissolved in CH_3CN/water (1:1) and purified by HPLC.

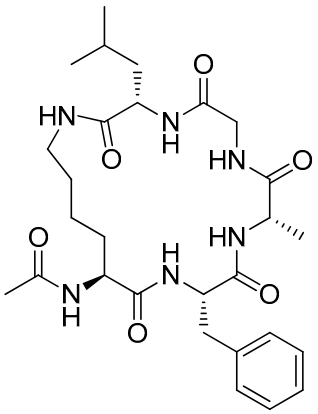

Chemical Formula: $C_{28}H_{42}N_6O_6$
Exact Mass: 558.32

MS (ESI), m/z calcd for $[(C_{28}H_{42}N_6O_6 + H]^+$ = 559.32; found 559.40.

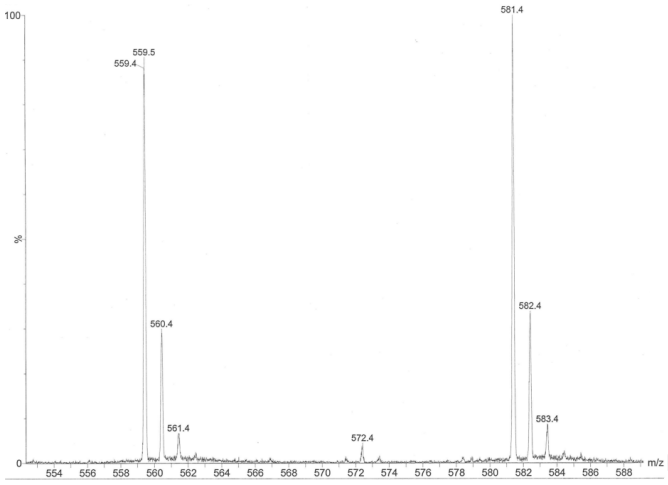

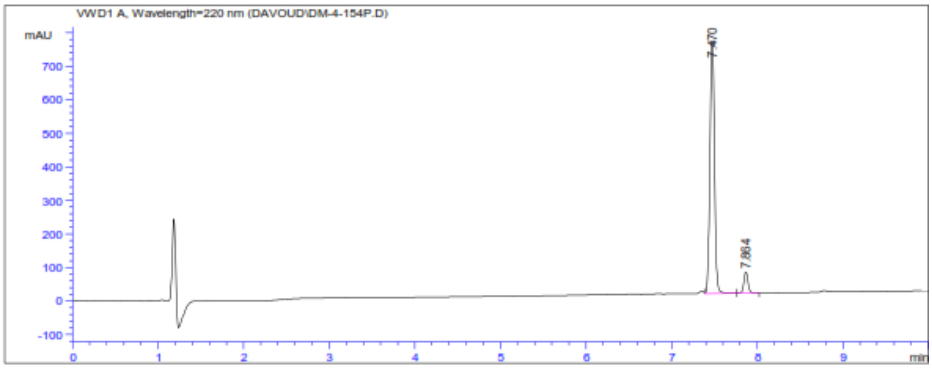


```
=====================================================================
                      Area Percent Report
=====================================================================

Sorted By             :      Signal
Multiplier:                   :      1.0000
Dilution:                     :      1.0000
Sample Amount:                :     20.00000  [ng/ul]   (not used in calc.)
Use Multiplier & Dilution Factor with ISTDs


Signal 1: VWD1 A, Wavelength=220 nm

Peak RetTime Type  Width     Area      Height     Area
  #   [min]        [min]  mAU   *s    [mAU   ]      %
----|-------|----|-------|----------|----------|--------|
   1   7.470 VV    0.0580 2781.83252  747.85638  93.0145
   2   7.864 VB    0.0541  208.91887   61.61217   6.9855
```

Figure 1.27 ESI-MS and analytical HPLC trace for c-(KFAGL). (Kinetex™ LC Column 80 Å; 100 x 4.6 mm; particle size 2.6 µm; solvent A: H_2O/0.1% TFA, solvent B: CH_3CN/0.1% TFA**,** 0-100% CH_3CN over 20 minutes)

600 MHz ^{1}H NMR spectrum of peptide I in 20% DMSO-d_6 in CD_2Cl_2

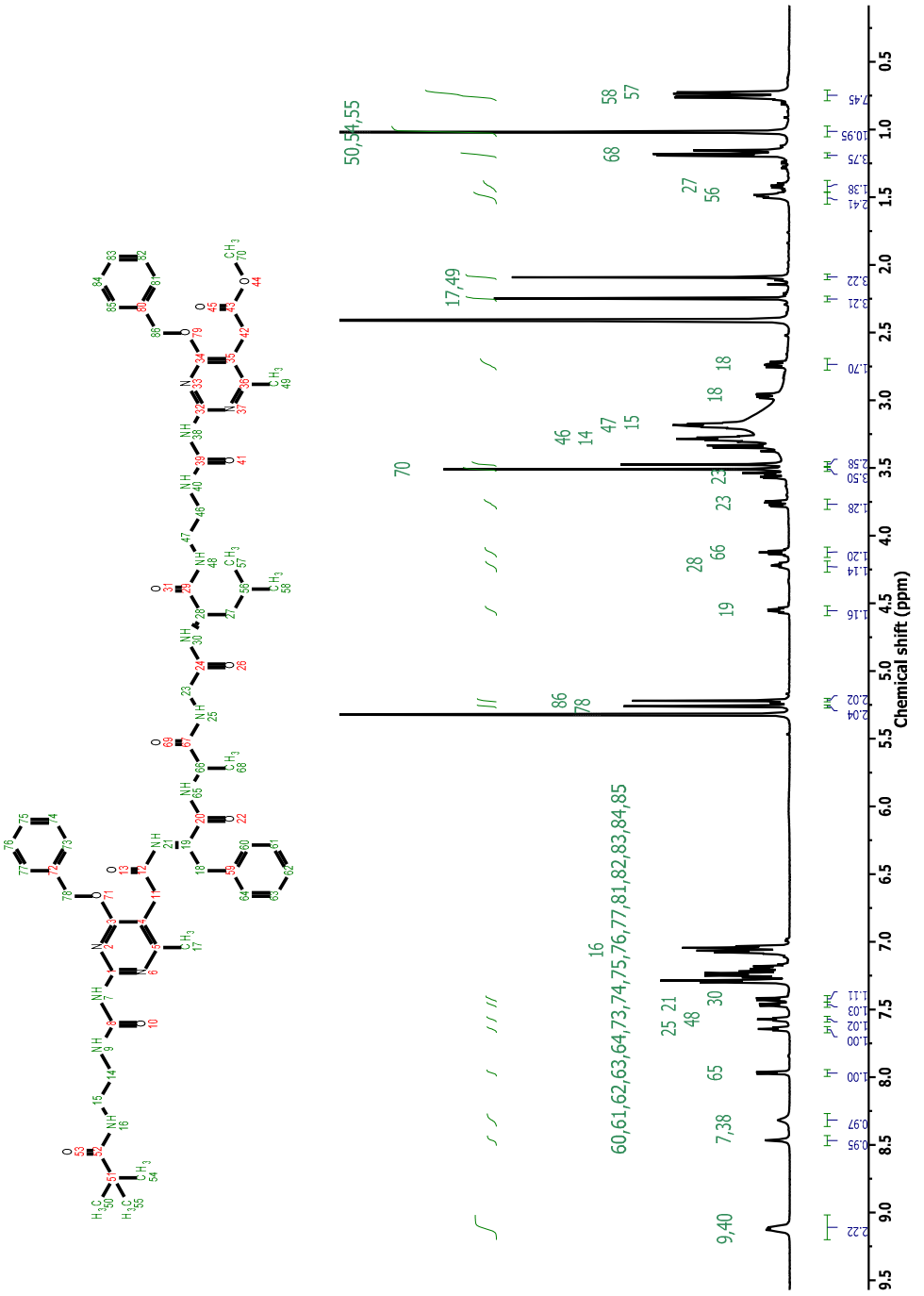

Figure 1.28 600 MHz ^{1}H NMR spectrum of peptide **I** in 20% DMSO-d_6 in CD_2Cl_2.

600 MHz COSY spectrum of peptide I in 20% DMSO-d_6 in CD_2Cl_2

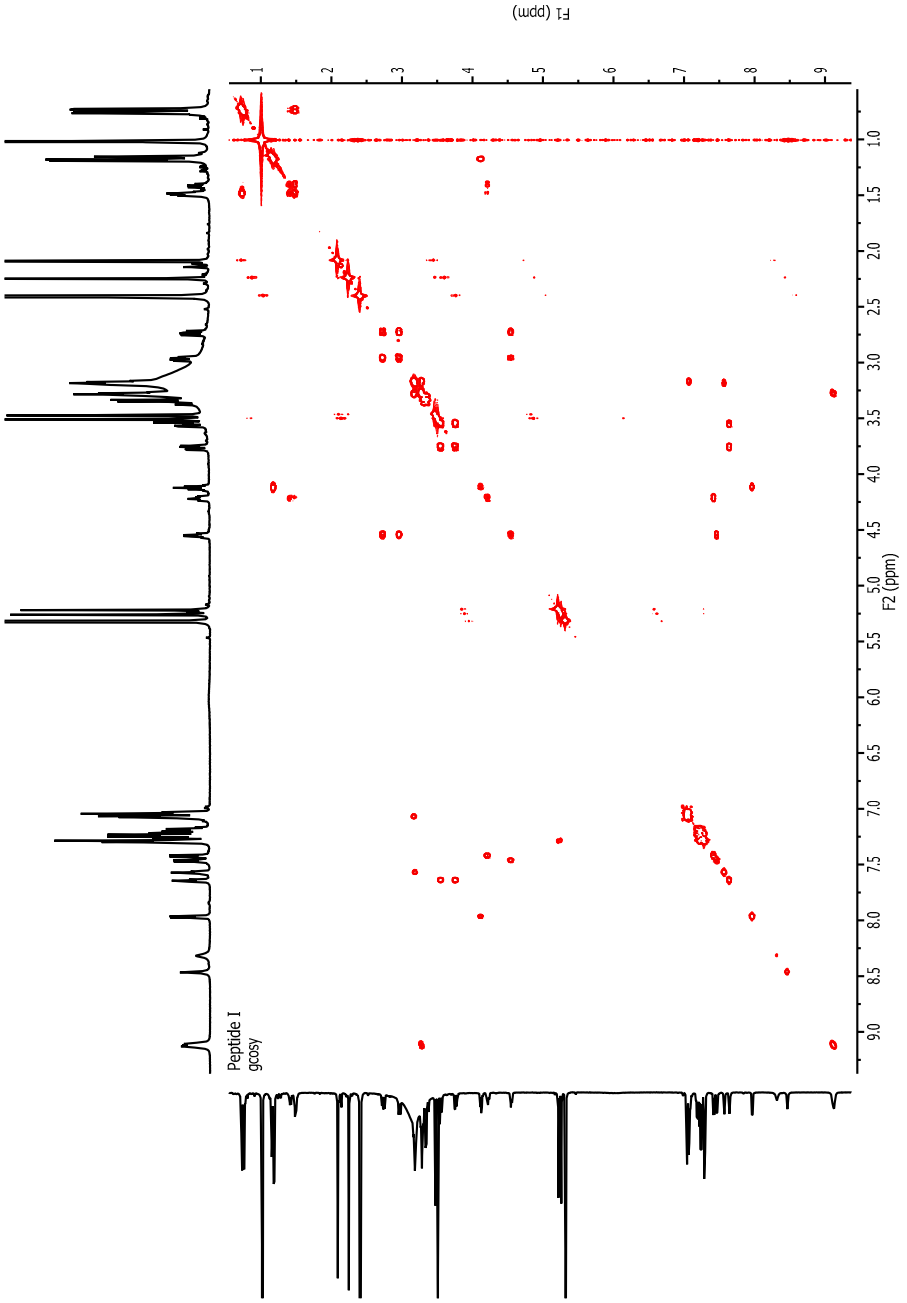

Figure 1.29 600 MHz COSY spectrum of peptide **I** in 20% DMSO-d_6 in CD_2Cl_2.

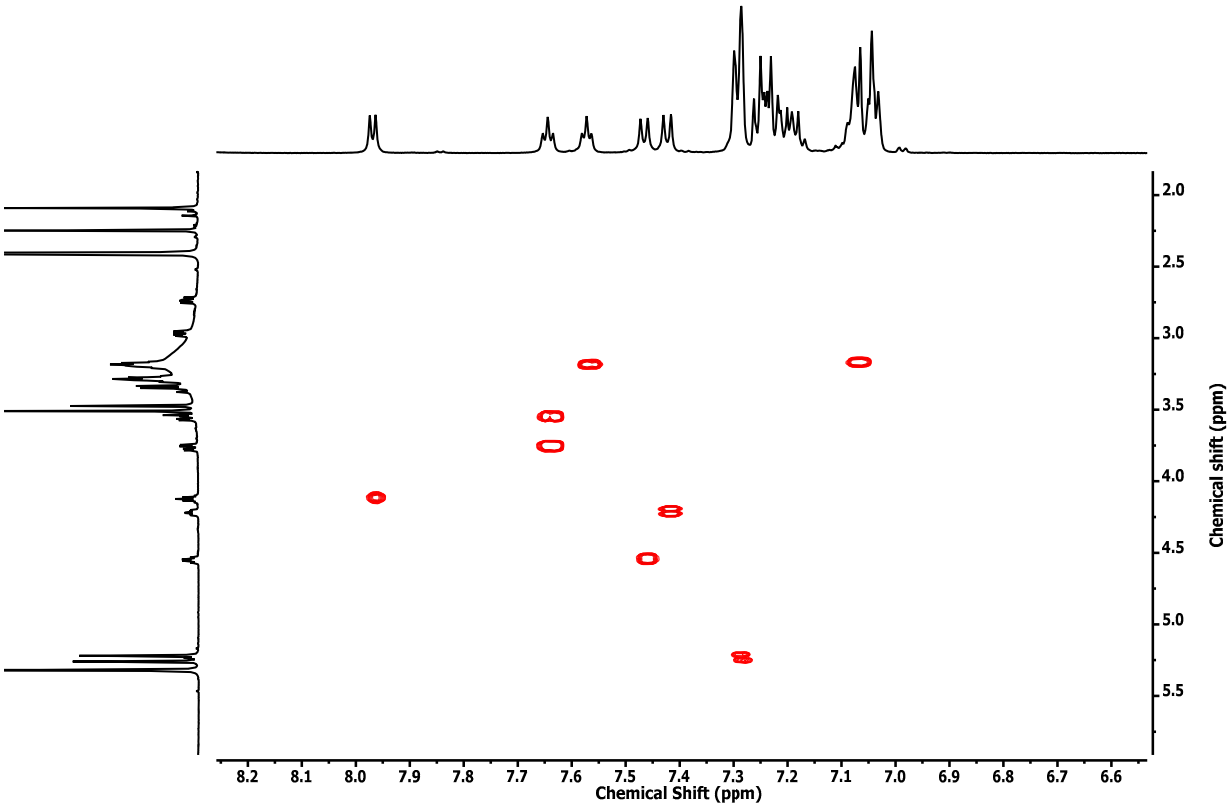

Figure 1.30 Cross-section of 600 MHz COSY spectrum of peptide **I** in 20% DMSO-d_6 in CD_2Cl_2 that is used to assign amide peaks.

500 MHz ^{1}H NMR spectrum of peptide II in 20% DMSO-d_6 in CD_2Cl_2

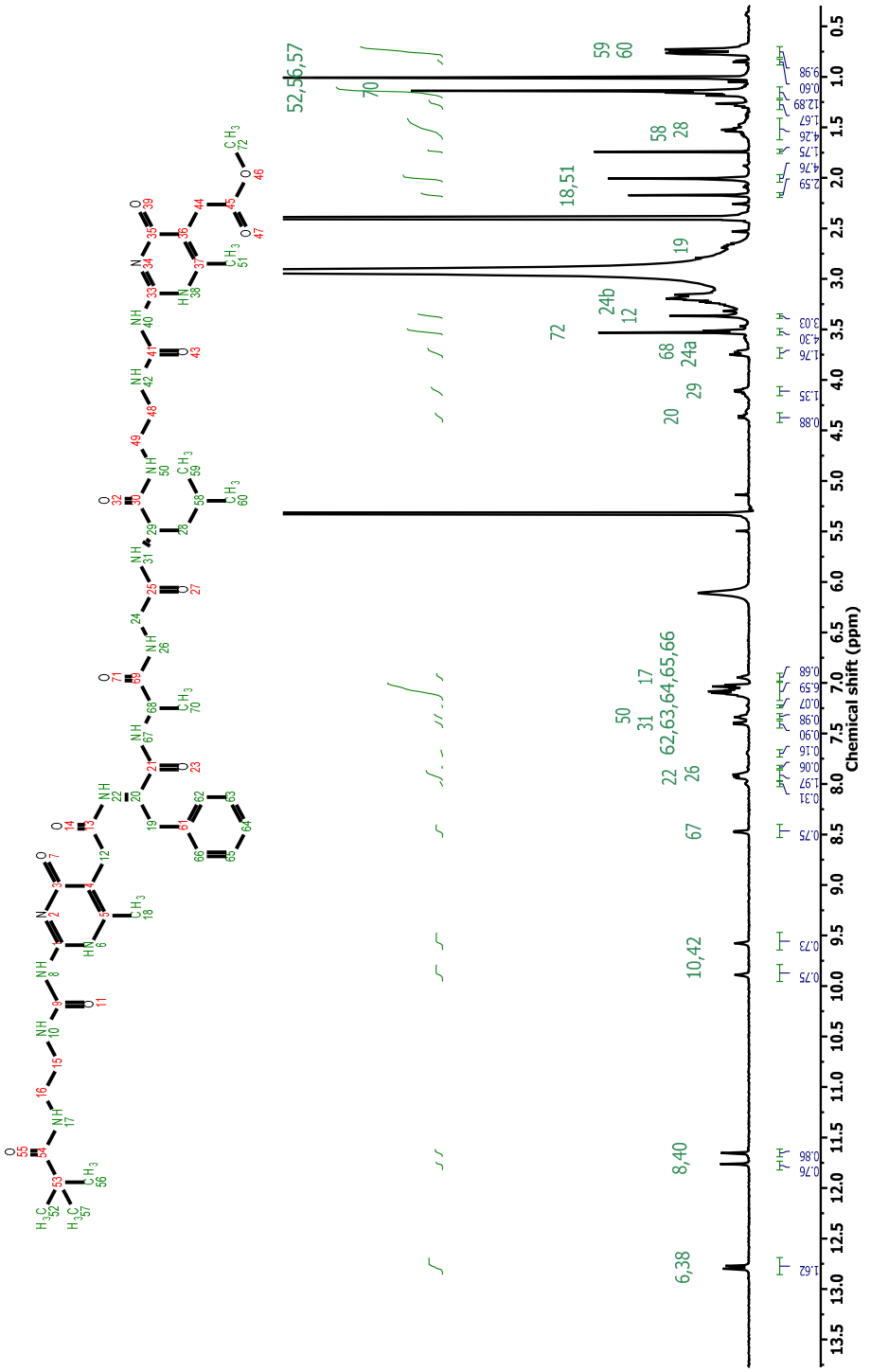

Figure 1.31 500 MHz ^{1}H NMR spectrum of peptide **II** in 20% DMSO-d_6 in CD_2Cl_2.

500 MHz COSY spectrum of peptide II in 20% DMSO-d_6 in CD_2Cl_2

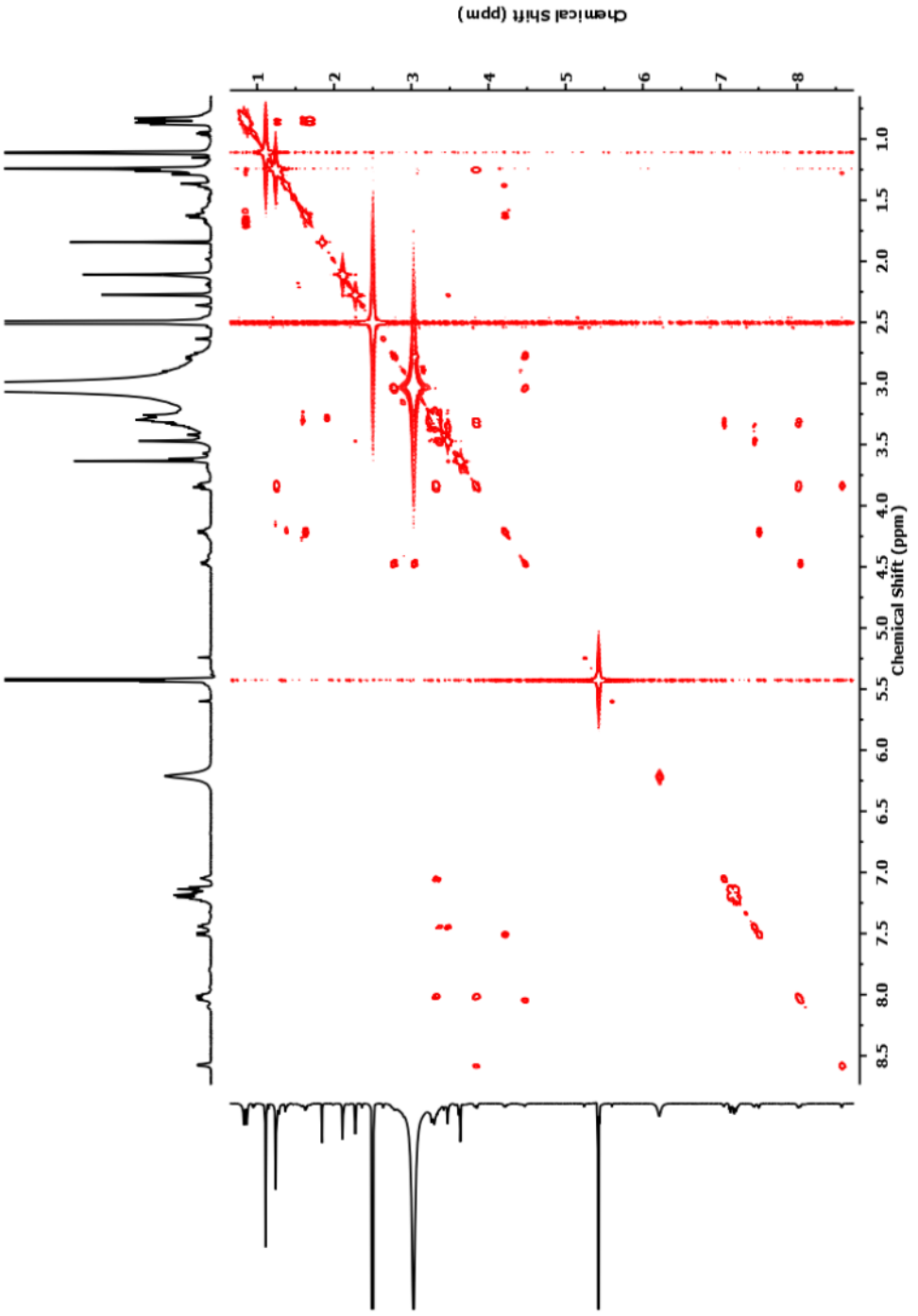

Figure 1.32 500 MHz COSY spectrum of peptide **II** in 20% DMSO-d_6 in CD_2Cl_2.

500 MHz TOCSY spectrum of peptide II in 20% DMSO-d_6 in CD_2Cl_2

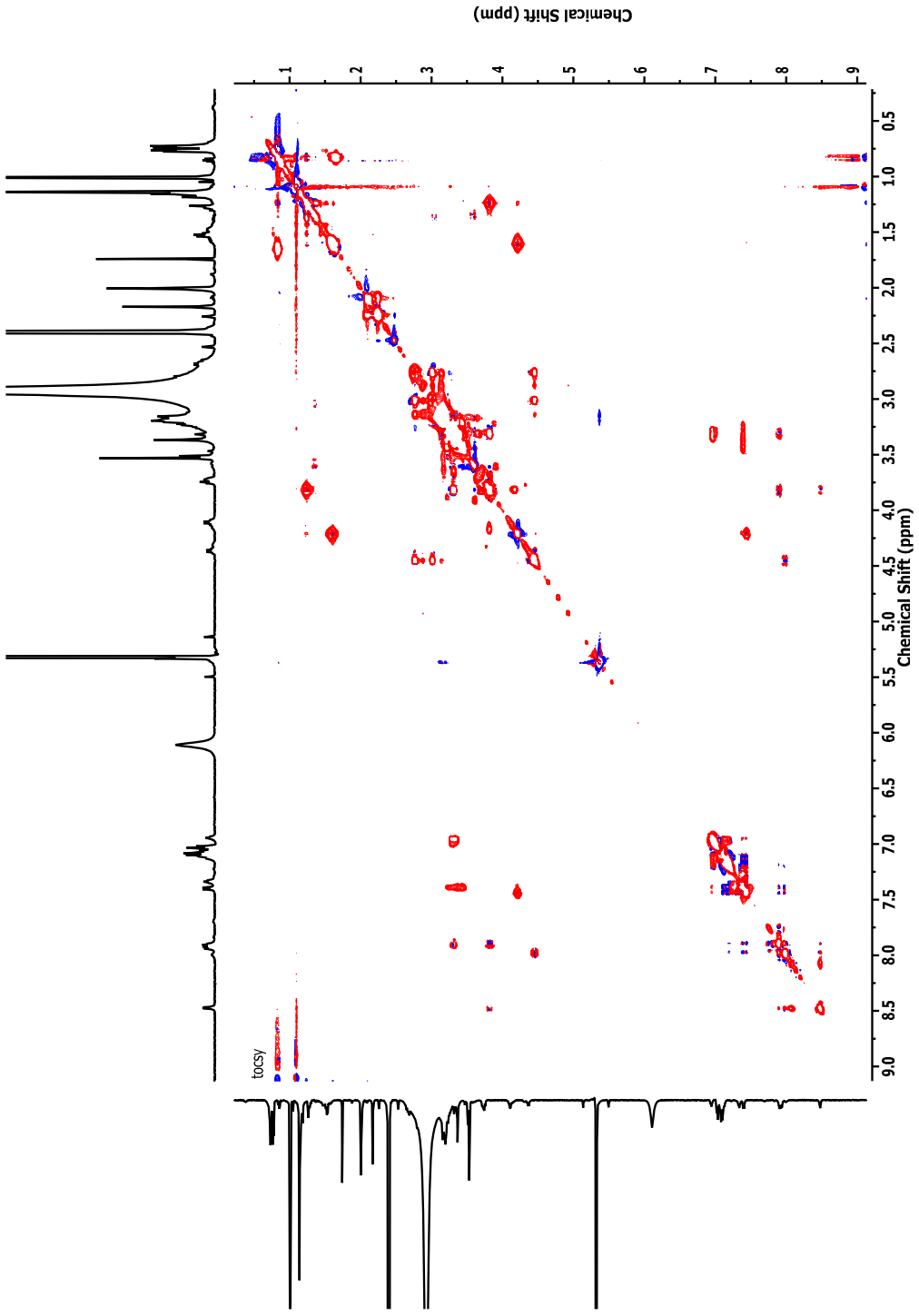

Figure 1.33 600 MHz TOCSY spectrum of peptide **II** in 20% DMSO-d_6 in CD_2Cl_2.

600 MHz ^{1}H NMR spectrum of peptide III in 20% DMSO-d_6 in CD_2Cl_2

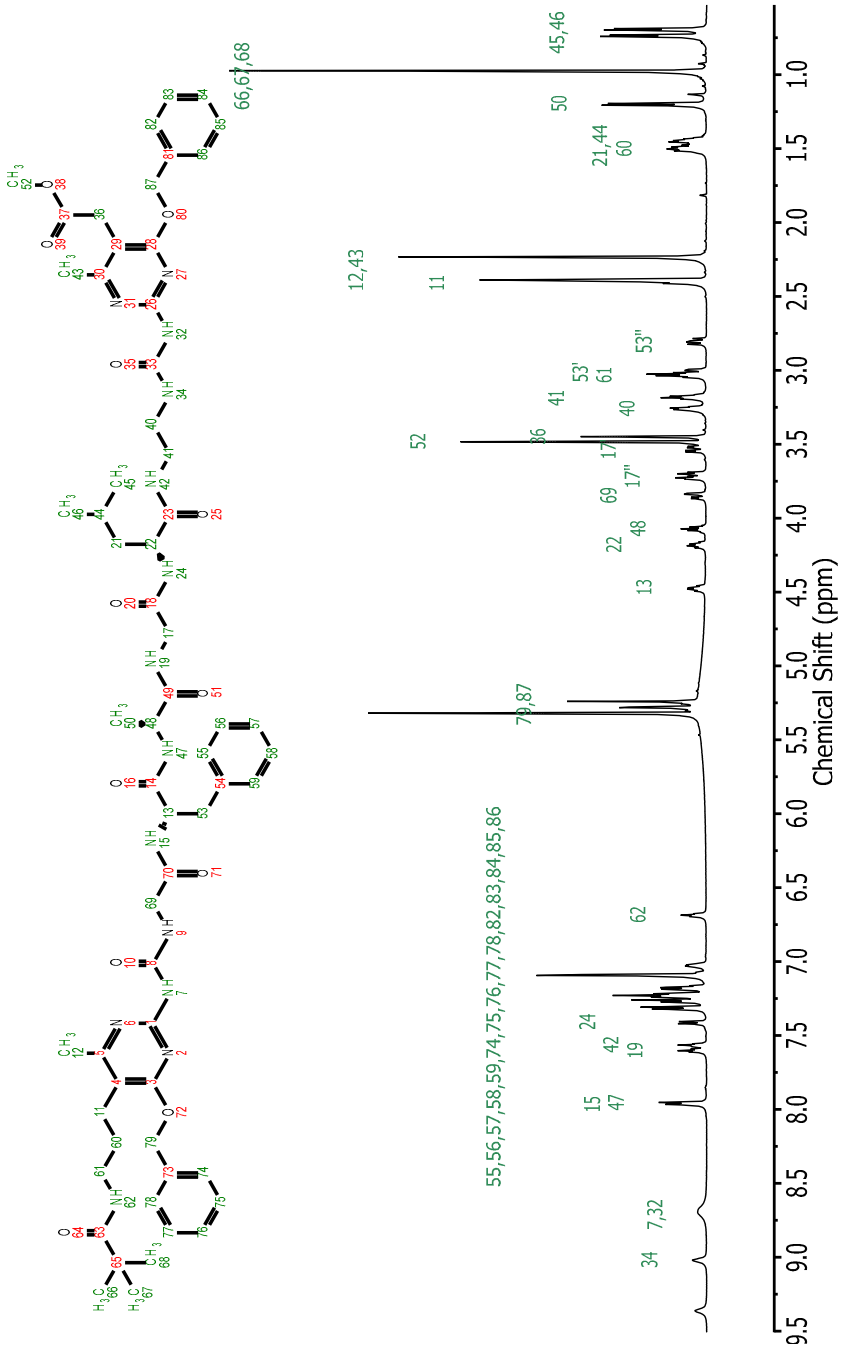

Figure 1.34 600 MHz ^{1}H NMR spectrum of peptide III in 20% DMSO-d_6 in CD_2Cl_2.

600 MHz COSY spectrum of peptide III in 20% DMSO-d_6 in CD_2Cl_2

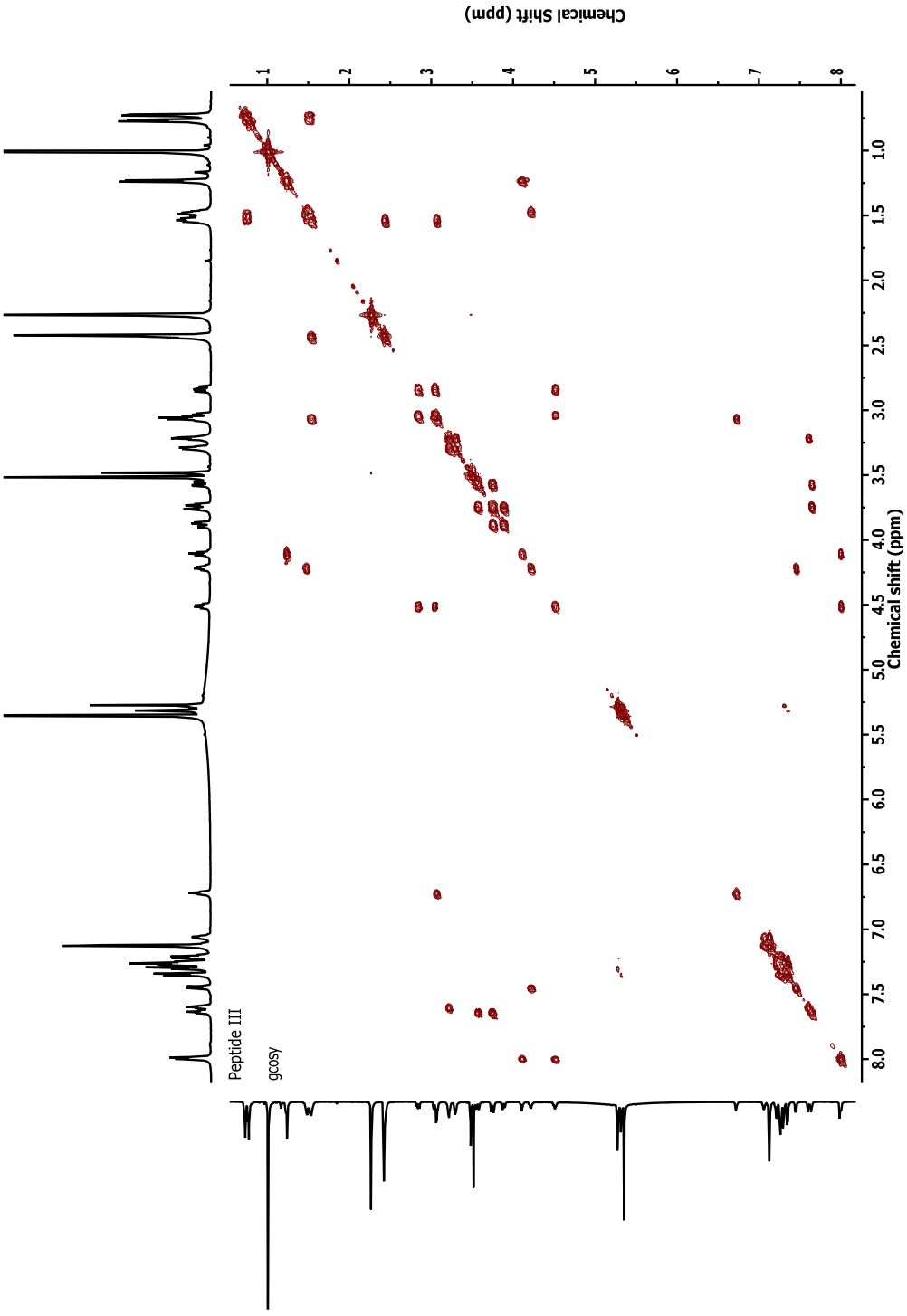

Figure 1.35 600 MHz COSY spectrum of peptide **III** in 20% DMSO-d_6 in CD_2Cl_2.

500 MHz ^{1}H NMR spectrum of peptide IV in 20% DMSO-d_6 in CD_2Cl_2

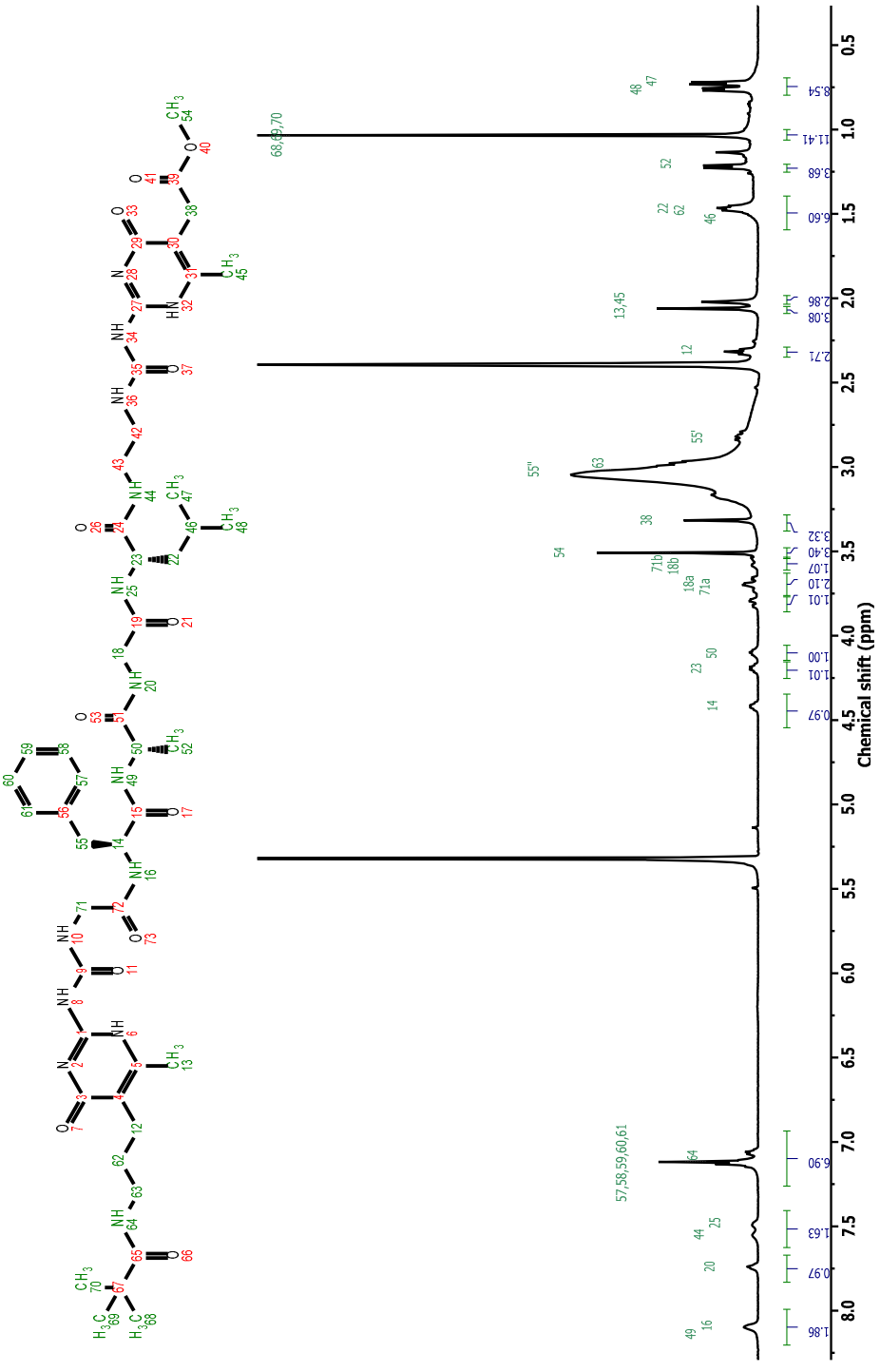

Figure 1.36 500 MHz ^{1}H NMR spectrum of peptide **IV** in 20% DMSO-d_6 in CD_2Cl_2.

500 MHz COSY spectrum of peptide IV in 20% DMSO-d_6 in CD_2Cl_2

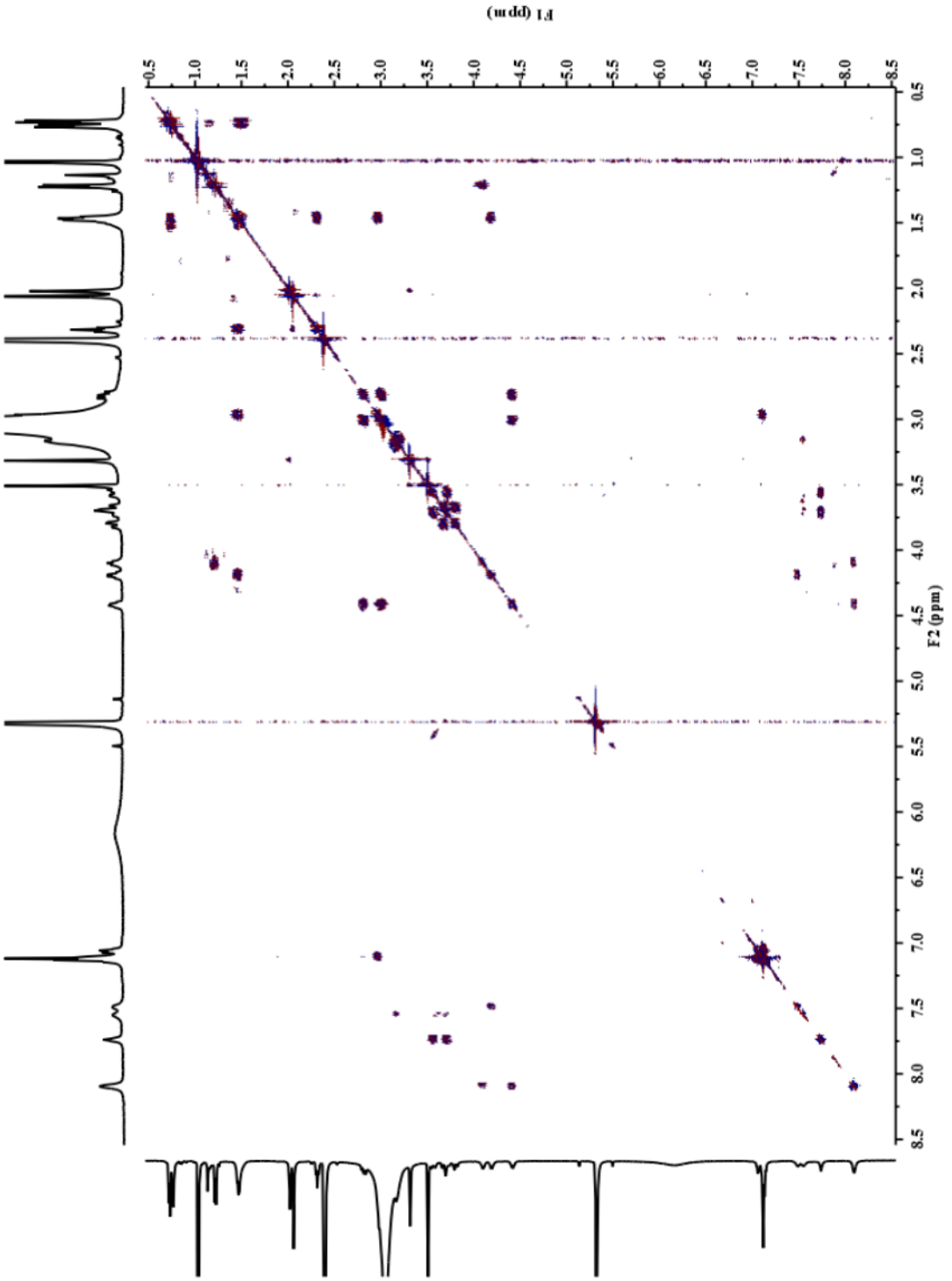

Figure 1.37 500 MHz COSY spectrum of peptide **IV** in 20% DMSO-d_6 in CD_2Cl_2.

Comparison of peptide I and II ^{1}H NMR spectra in 20% DMSO-d_6 in CD_2Cl_2 (folding conformer)

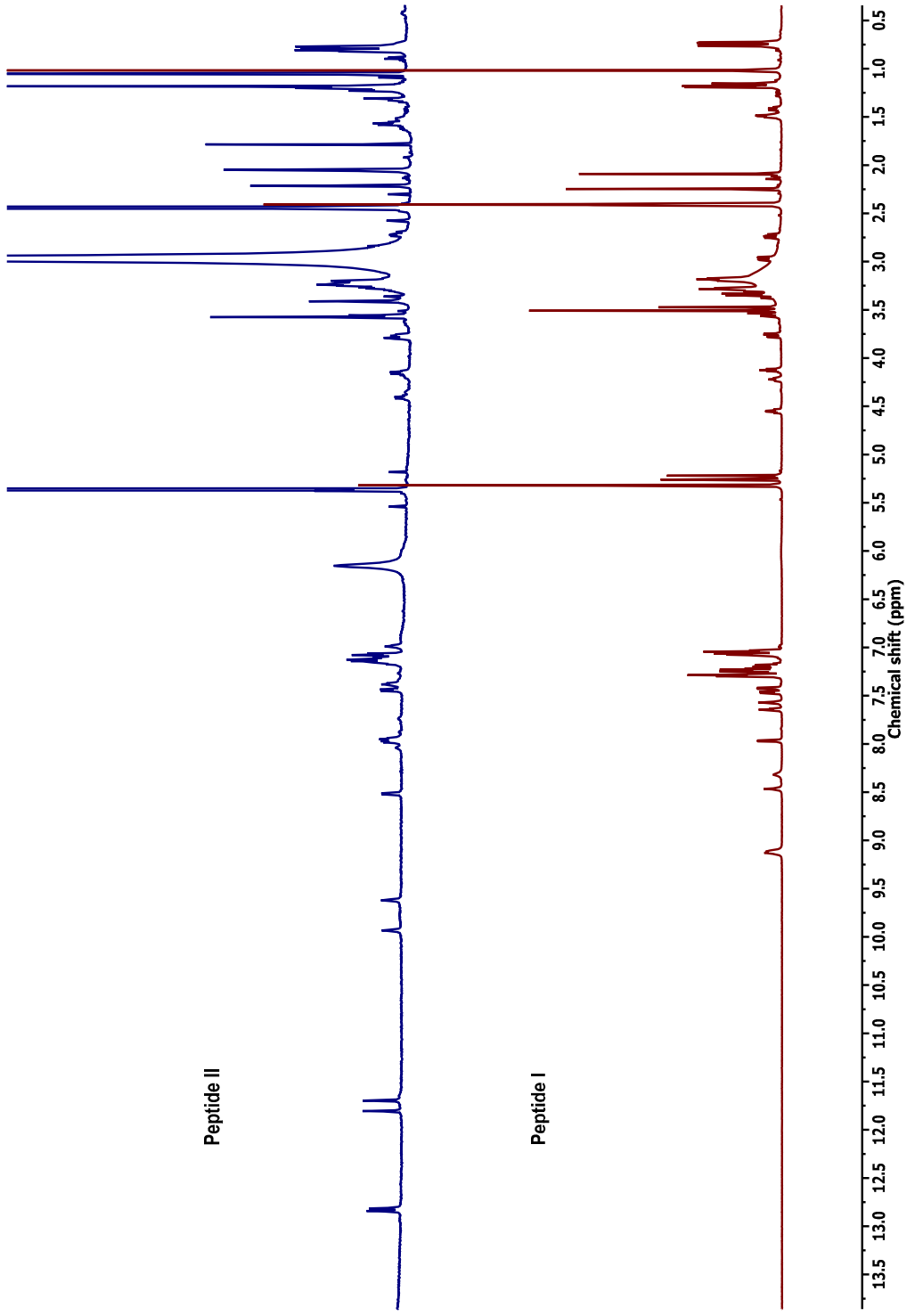

Figure 1.38 Comparison of ^{1}H NMR spectrum of peptide **I** and **II** in 20% DMSO-d_6 in CD_2Cl_2 (folding conformer).

Comparison of peptide III and IV ^{1}H NMR spectra in 20% DMSO-d_6 in CD_2Cl_2 (nonfolding conformer)

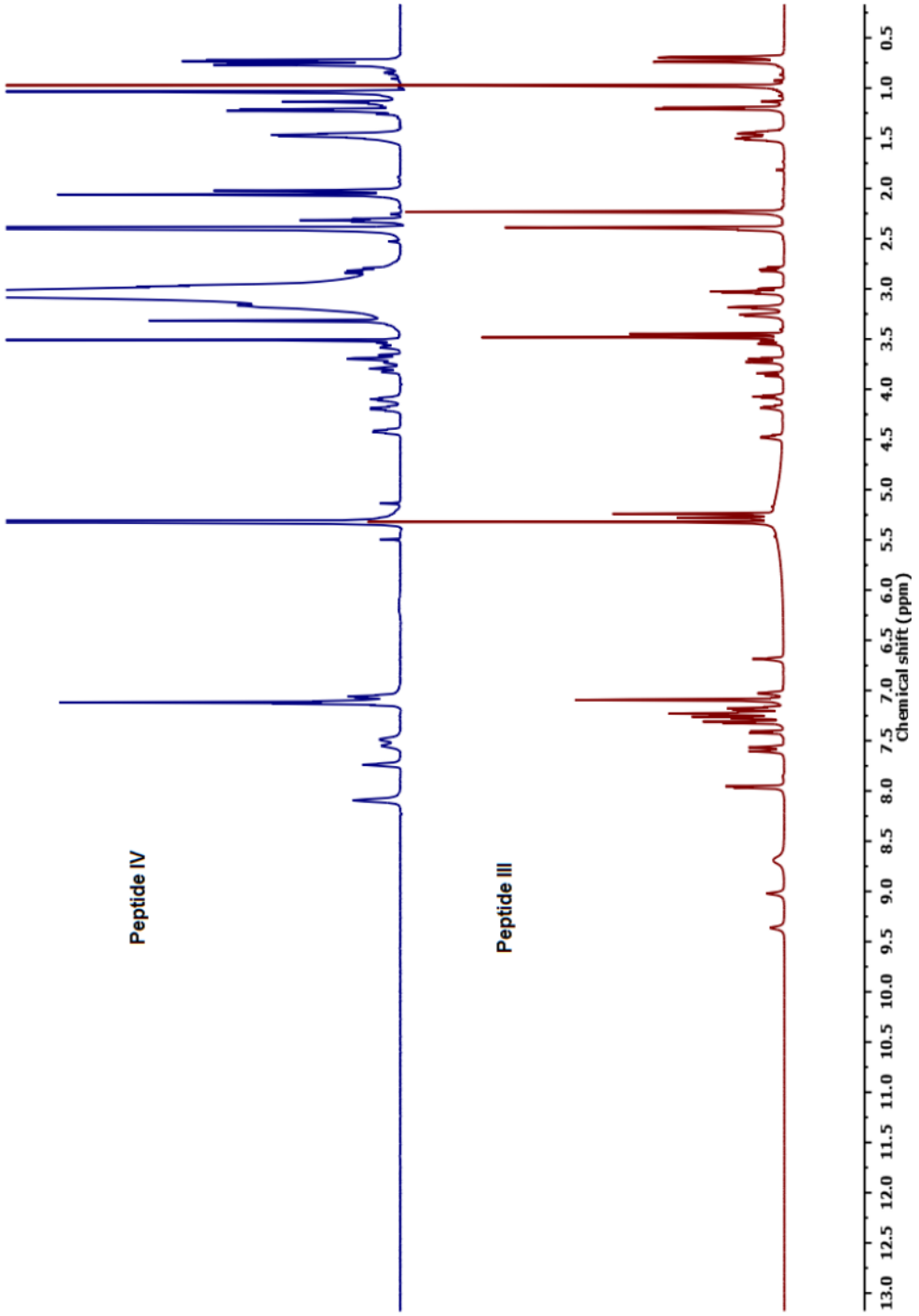

Figure 1.39 Comparison of ^{1}H NMR spectrum of peptide **III** and **IV** in 20% DMSO-d_6 in CD_2Cl_2 (nonfolding conformer).

Comparison of ^{1}H NMR spectra of peptide I-IV (full assignment)

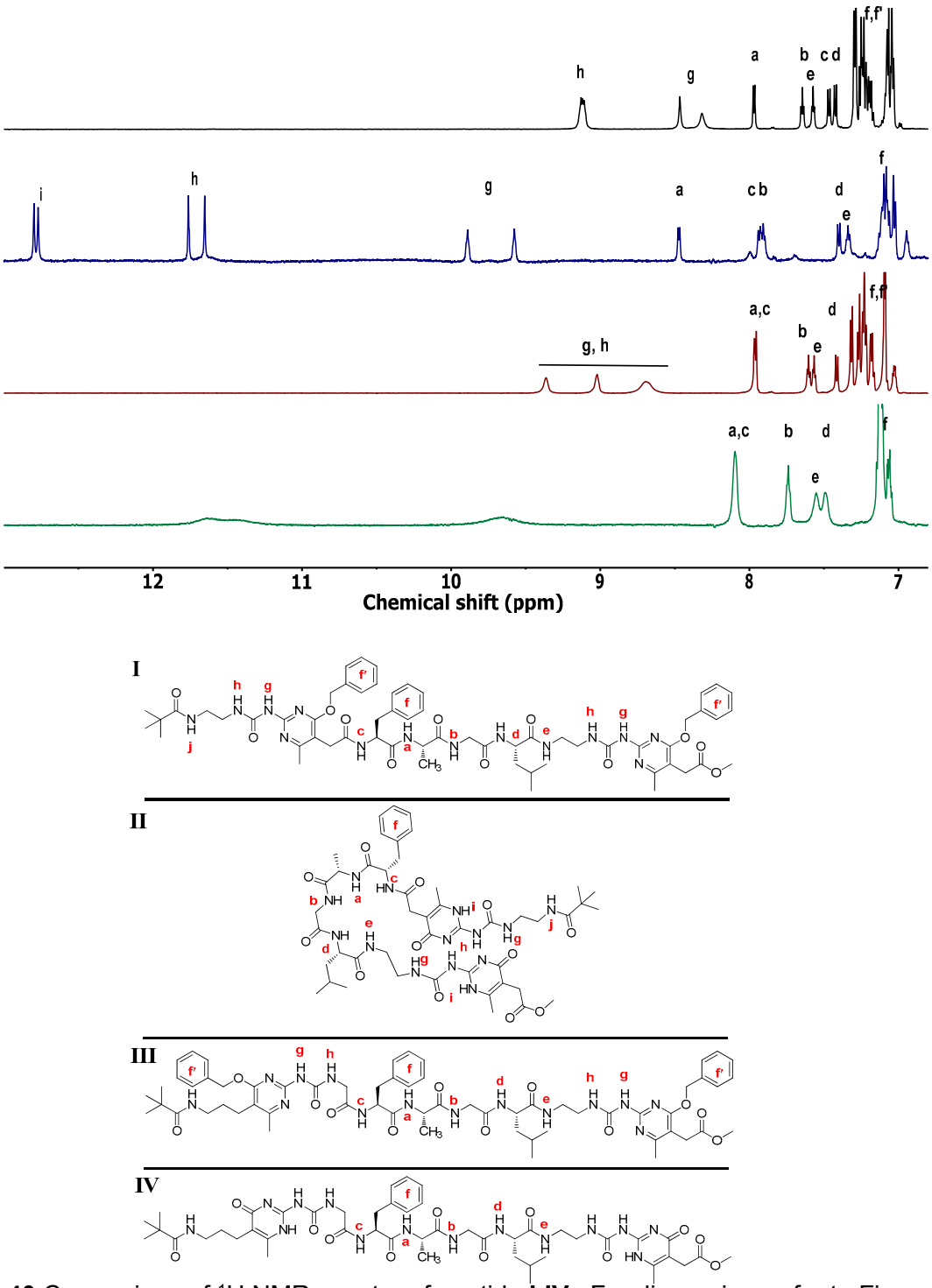

Figure 1.40 Comparison of ^{1}H NMR spectra of peptide **I-IV.** For discussion, refer to Figure 1-9 and its explanation (Section 1-10).

500 MHz ^{1}H NMR spectrum of Ac-FAGL-OH in 20% DMSO-d_6 in CD_2Cl_2

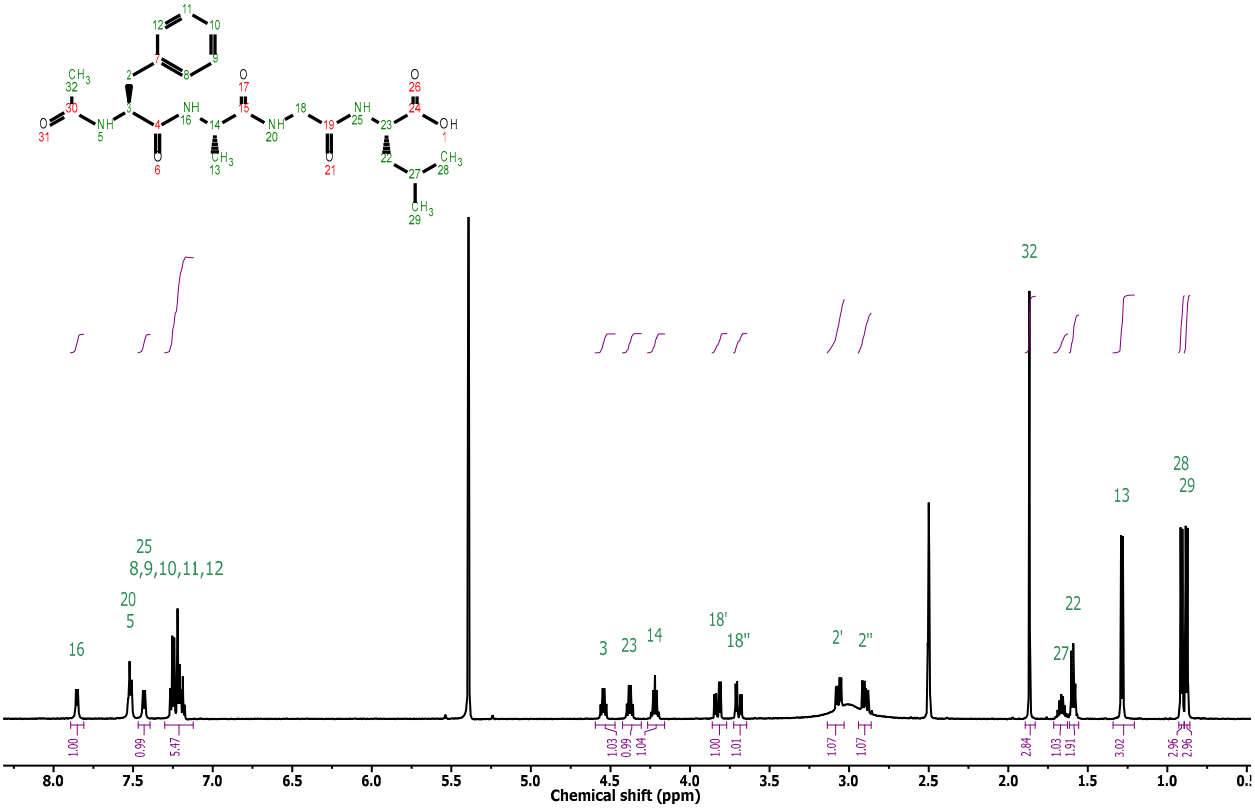

Figure 1.41 500 MHz ^{1}H NMR spectrum of Ac-FAGL-OH in 20% DMSO-d_6 in CD_2Cl_2.

500 MHz COSY spectrum of Ac-FAGL-OH in 20% DMSO-d_6 in CD_2Cl_2

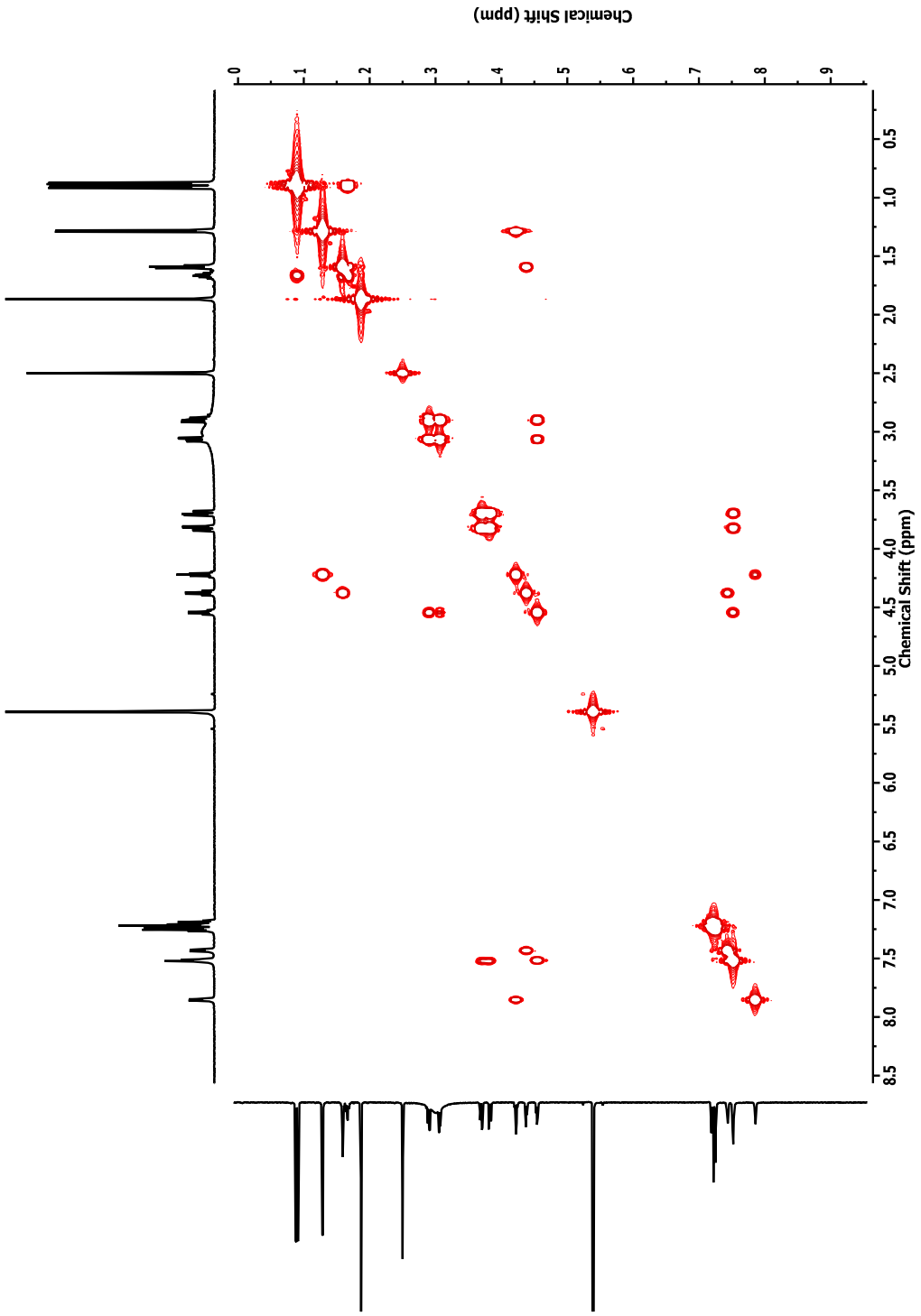

Figure 1.42 500 MHz COSY spectrum of Ac-FAGL-OH in 20% DMSO-d_6 in CD_2Cl_2.

500 MHz ^{1}H NMR spectrum of c-(KFAGL) in 20% DMSO-d_6 in CD_2Cl_2

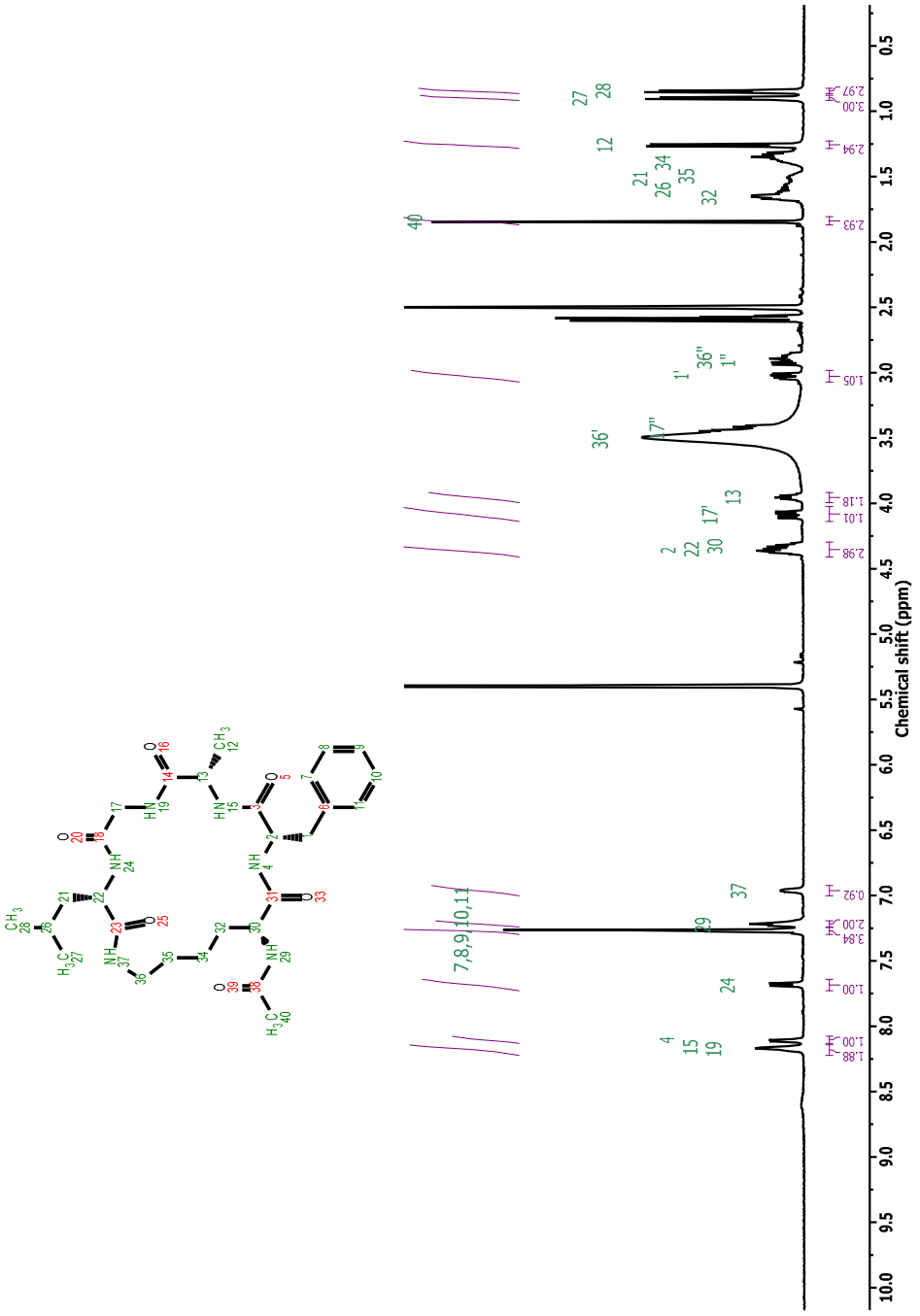

Figure 1.43 500 MHz ^{1}H NMR c-(KFAGL) in 20% DMSO-d_6 in CD_2Cl_2.

500 MHz COSY spectrum of c-(KFAGL) in 20% DMSO-d_6 in CD_2Cl_2

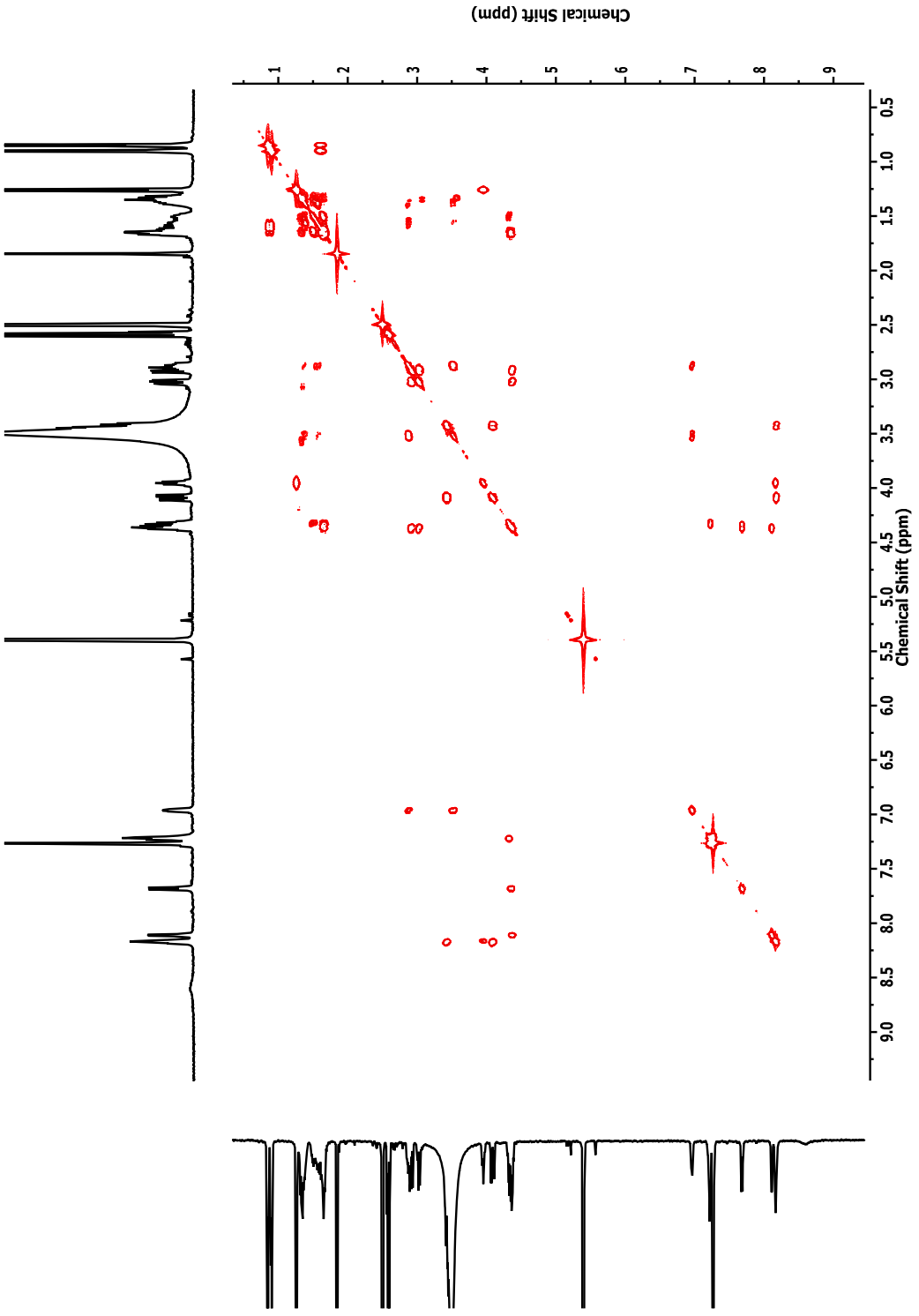

Figure 1.44 500 MHz COSY spectrum of c-(KFAGL) in 20% DMSO-d_6 in CD_2Cl_2.

Concentration dependence of ^{1}H NMR spectrum of peptide II

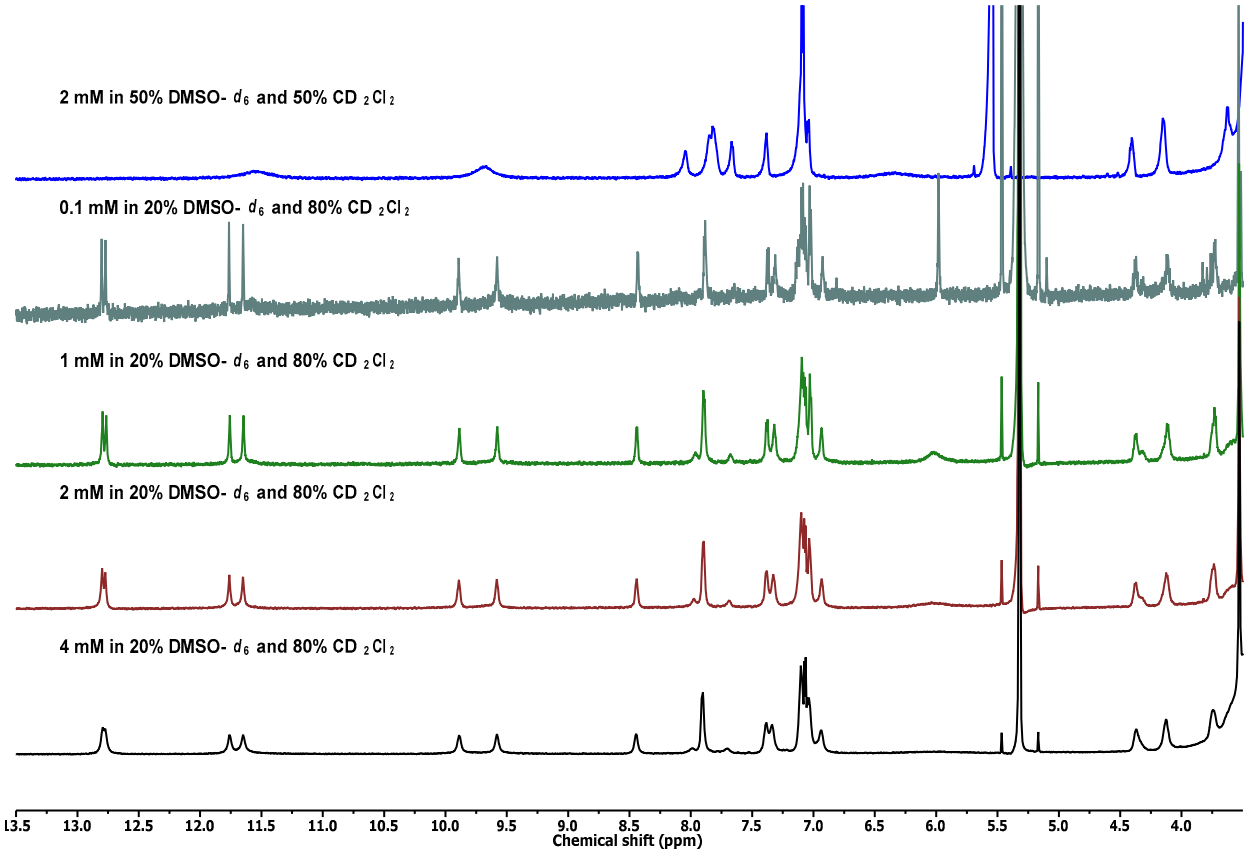

Figure 1.45 Concentration dependence of ^{1}H NMR spectrum of peptide **II** and the effect of DMSO on the peptide structure and spectrum. No change is observed over the range of 0.1-4 mM, however, addition of more DMSO perturbs the hydrogen bonding of the UPy units and denatures the peptide.

Plot of ΔδHα values for c-(KFAGL)

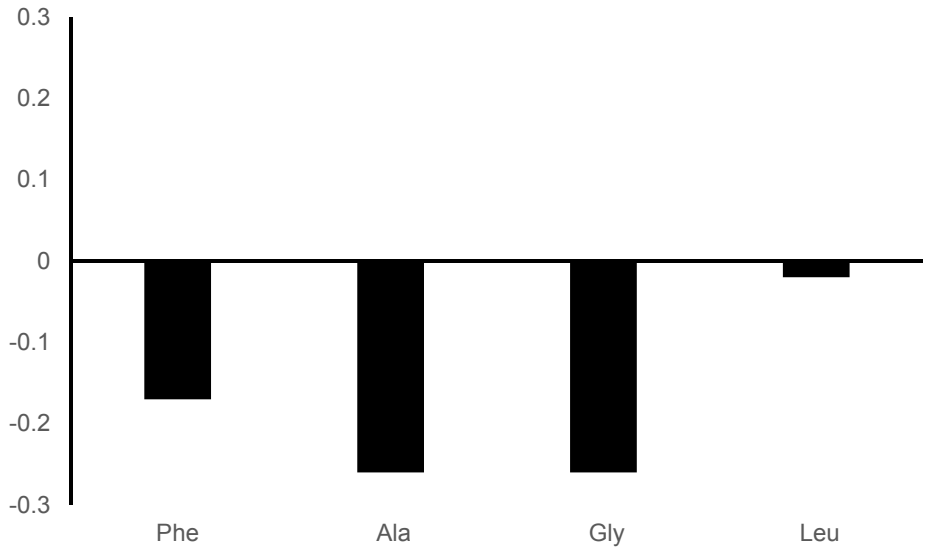

Figure 1.46 Plot of ΔδHα values for c-(KFAGL). $\Delta\delta H^{\alpha}$ [δH^{α} (cyclic) - δH^{α} (linear)]. In case of glycine, chemical shift for low field methylene proton has been plotted. c-(KFAGL) shows negative $\Delta\delta H^{\alpha}$ values consistent with a pattern of type II β-turn structure.

Energy minimized model of c-(KFAGL)

Energy minimization using AMBER* forcefield with $CHCl_3$, GB/SA implied solvent parameter, was performed using MacroModel utility after building the model in Schrödinger Maestro suite. A quick search of conformational space is performed through 2000 steps Monte Carlo conformational search.

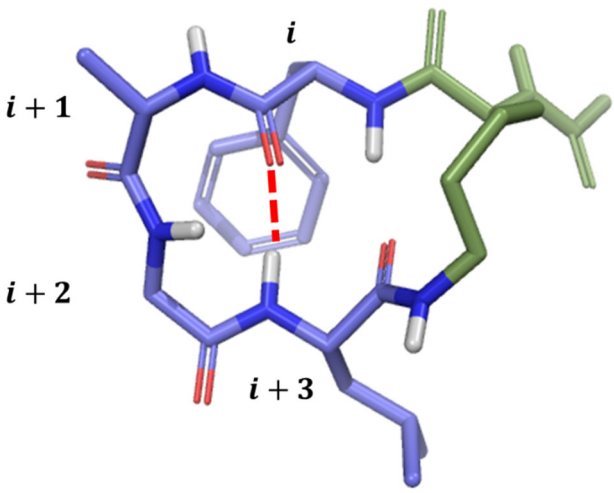

Figure 1.47 The energy minimized model of c-(KFAGL) demonstrates features of a type II β-turn. The glycine phi torsional angle, 158, is deviated from ideal type II β-turn.

Summary of ^{1}H NMR spectroscopic features of Ac-FAGL-OH and c-(KFAGL)

Table 1.5 Chemical Shift and temperature dependencies of the ^{1}H NMR chemical shifts (ppb/K) of various NH protons for Ac-FAGL-OH (4 mM in a mixture of 20% DMSO-d_6 and 80% CD_2Cl_2)[a]

	Phe	Ala	Gly	Leu
N_H (ppm)	7.51	7.85	7.53	7.43
Hα (ppm)	4.54	4.22	3.83, 3.ff	4.38
Hβ (γ, δ)	3.07, 2.90	1.87	N/A	1.59 (1.66, 0.91,0.88)
Δ $\delta N_H/\Delta T$ (ppb/K)	-8.6	-7.6	-4.0	-5.5

[a] ^{1}H NMR spectra recorded at 5 °C intervals from -5 °C to 35 °C.

Table 1.6 Chemical Shift and temperature dependencies of the ^{1}H NMR chemical shifts (ppb/K) of various NH protons for c-(KFAGL) (4 mM in a mixture of 20% DMSO-d_6 and 80% CD_2Cl_2)[a]

	Lys	Phe	Ala	Gly	Leu
N_H (ε N_H)	7.22 (6.96)	8.11	8.16	8.18	7.69
α	4.33	4.37	3.96	4.09, 3.43	4.36
β (γ, δ)	1.66	3.02, 2.91	1.26	N/A	(1.66,0.9,0.85)
Δ $\delta N_H/\Delta T$ (ppb/K)	-5.6 (-2.5)	-8.28	-7.72	-5.57	-3.8

Variable Temperature 1H NMR spectrum of peptide I in 20% DMSO-d6 in CD_2Cl_2

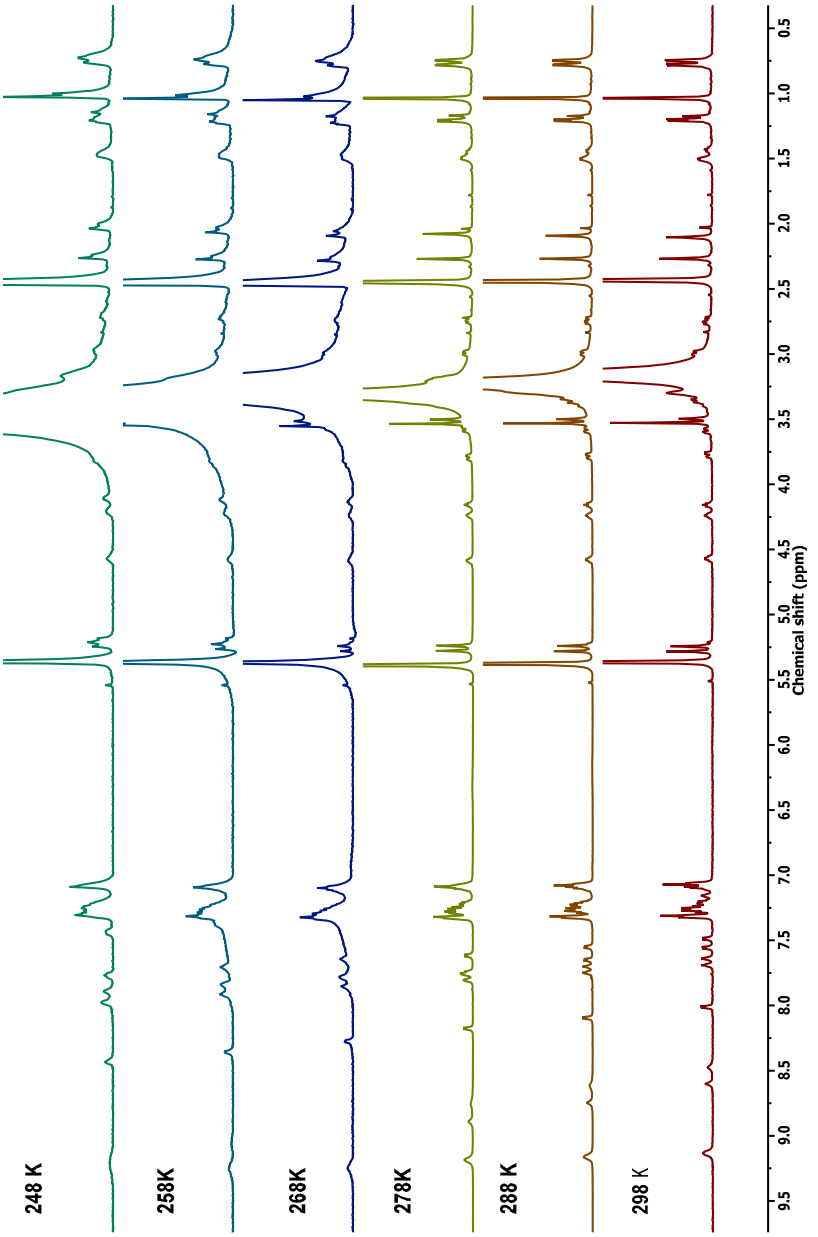

Figure 1.48 Variable Temperature ^{1}H NMR spectrum of peptide **I** in 20% DMSO-d_6 in CD_2Cl_2. The first three spectra were recorded on a GN500 machine capable of reaching lower temperature to ensure linearity of amide-temperature response.

Variable Temperature ^{1}H NMR spectrum of peptide II in 20% DMSO-d_6 in CD_2Cl_2

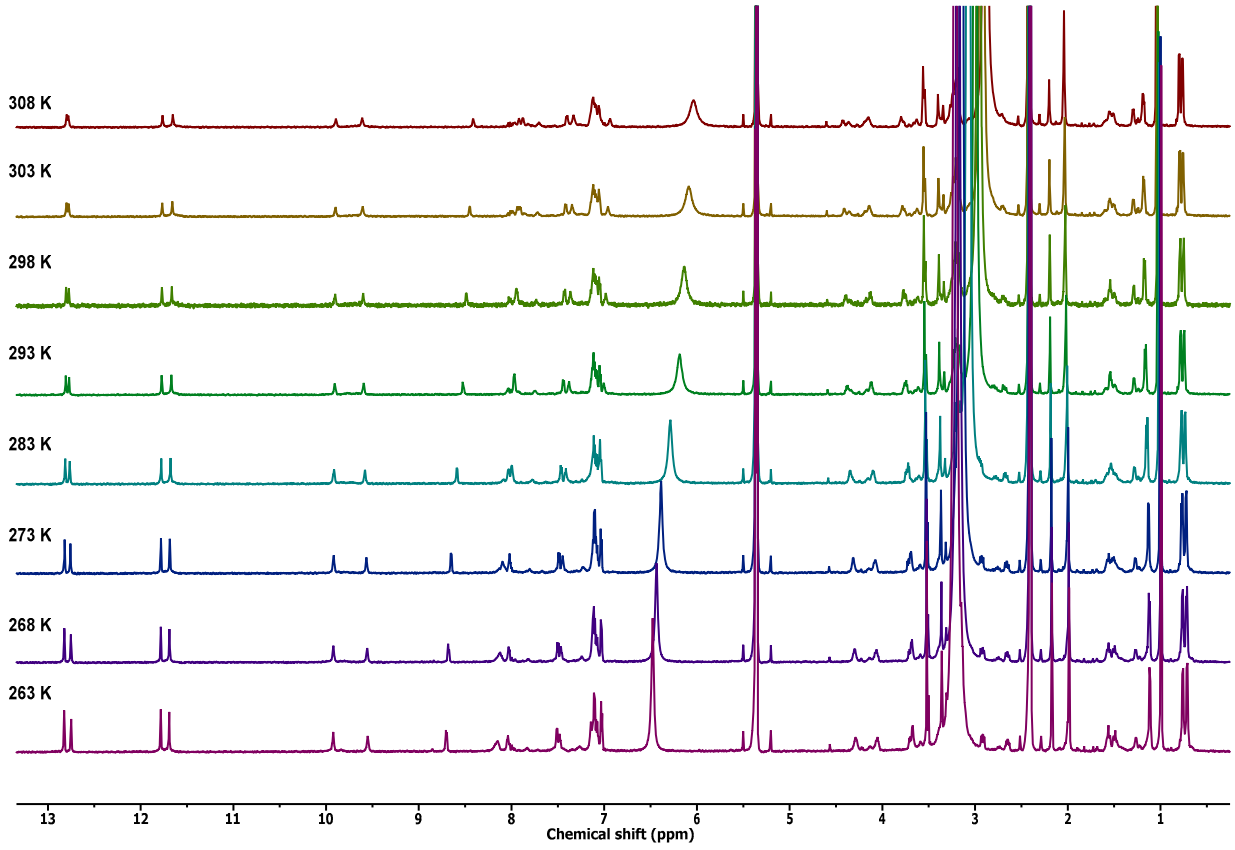

Figure 1.49 Variable Temperature ^{1}H NMR spectrum of peptide **II** in 20% DMSO-d_6 in CD_2Cl_2.

Variable Temperature ^{1}H NMR spectrum of peptide III in 20% DMSO-d_6 in CD_2Cl_2

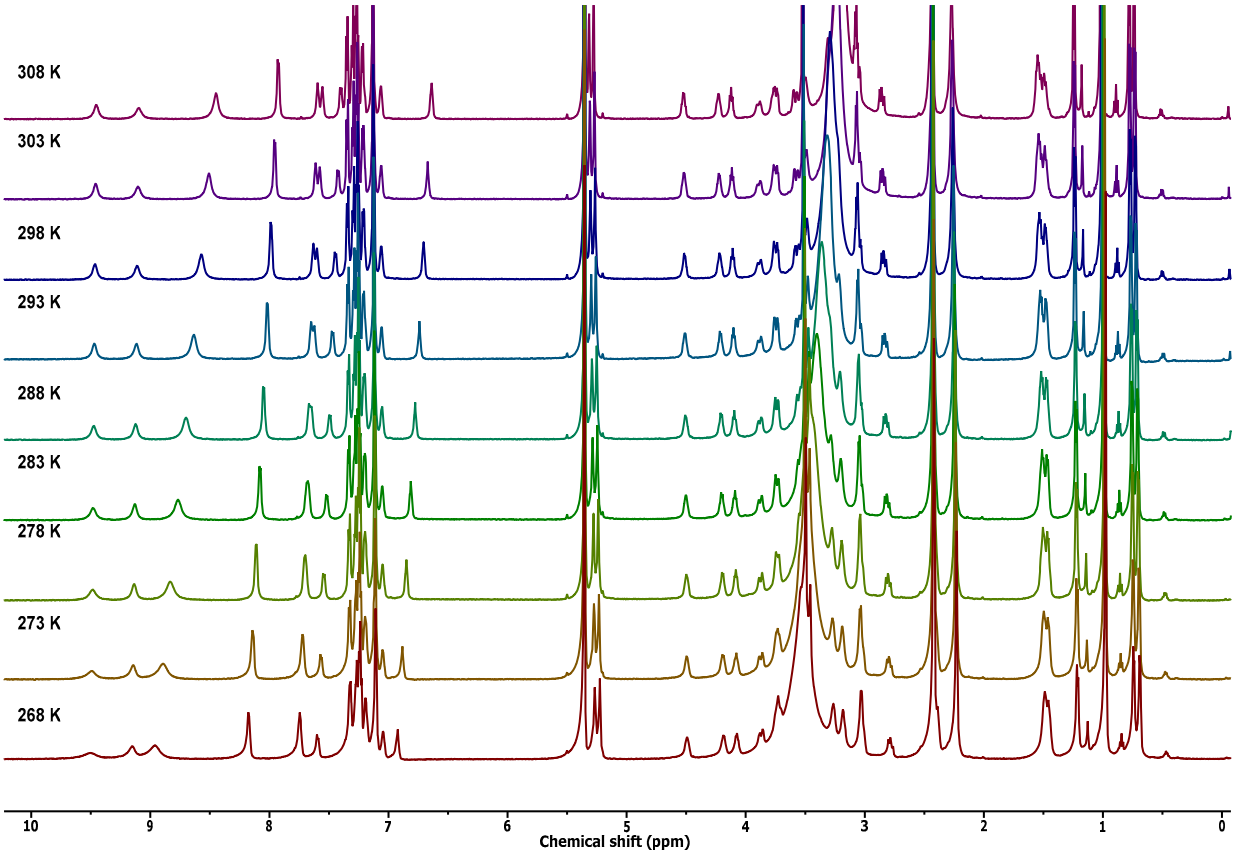

Figure 1.50 Variable Temperature ^{1}H NMR spectrum of peptide **III** in 20% DMSO-d_6 in CD_2Cl_2.

Variable Temperature ^{1}H NMR spectrum of peptide IV in 20% DMSO-d_6 in CD_2Cl_2

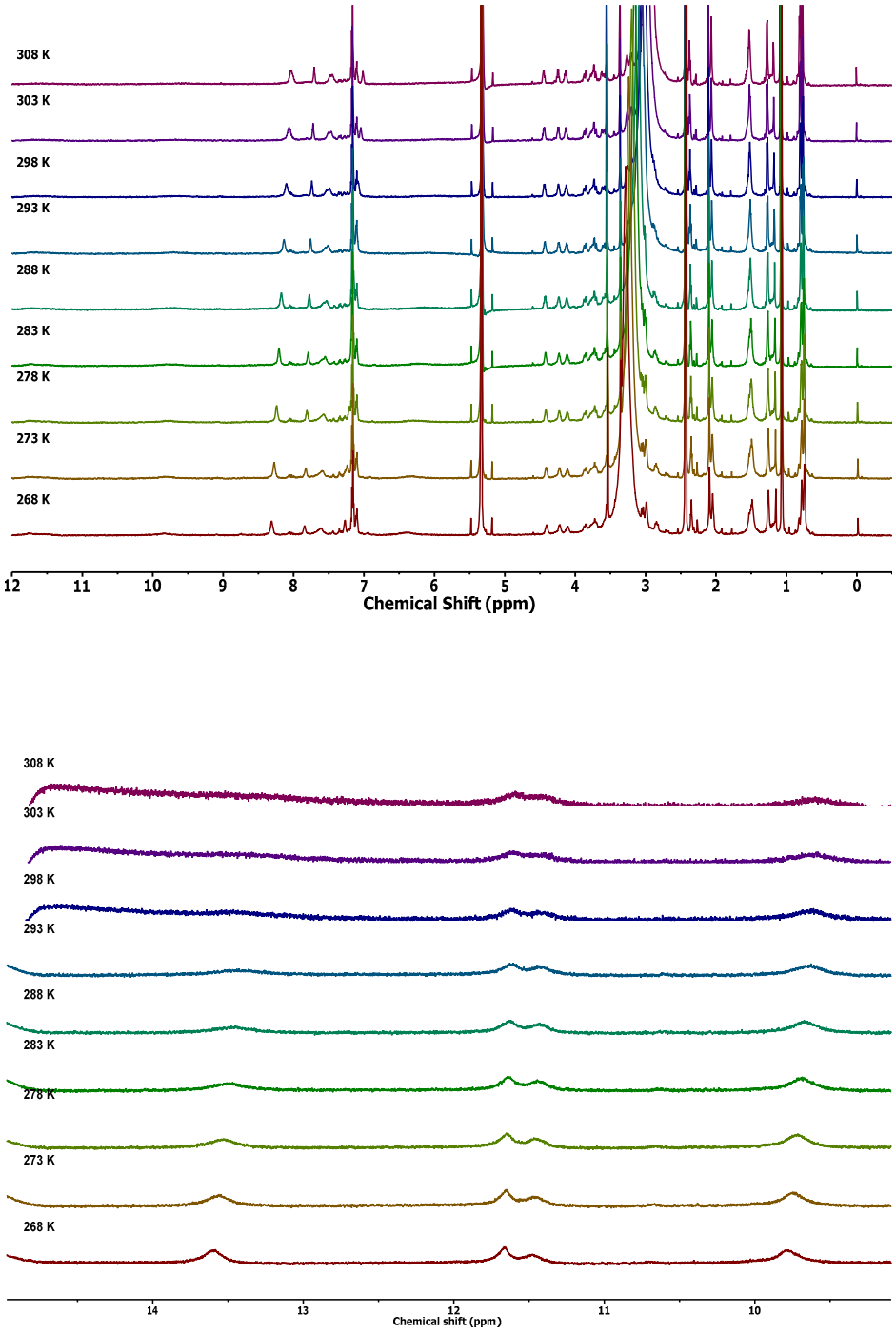

Figure 1.51 Variable Temperature ^{1}H NMR spectrum of peptide **IV** in 20% DMSO-d_6 in CD_2Cl_2.

Section of 500 MHz ROESY spectrum of peptide II in 20% DMSO-d6 in CD_2Cl_2

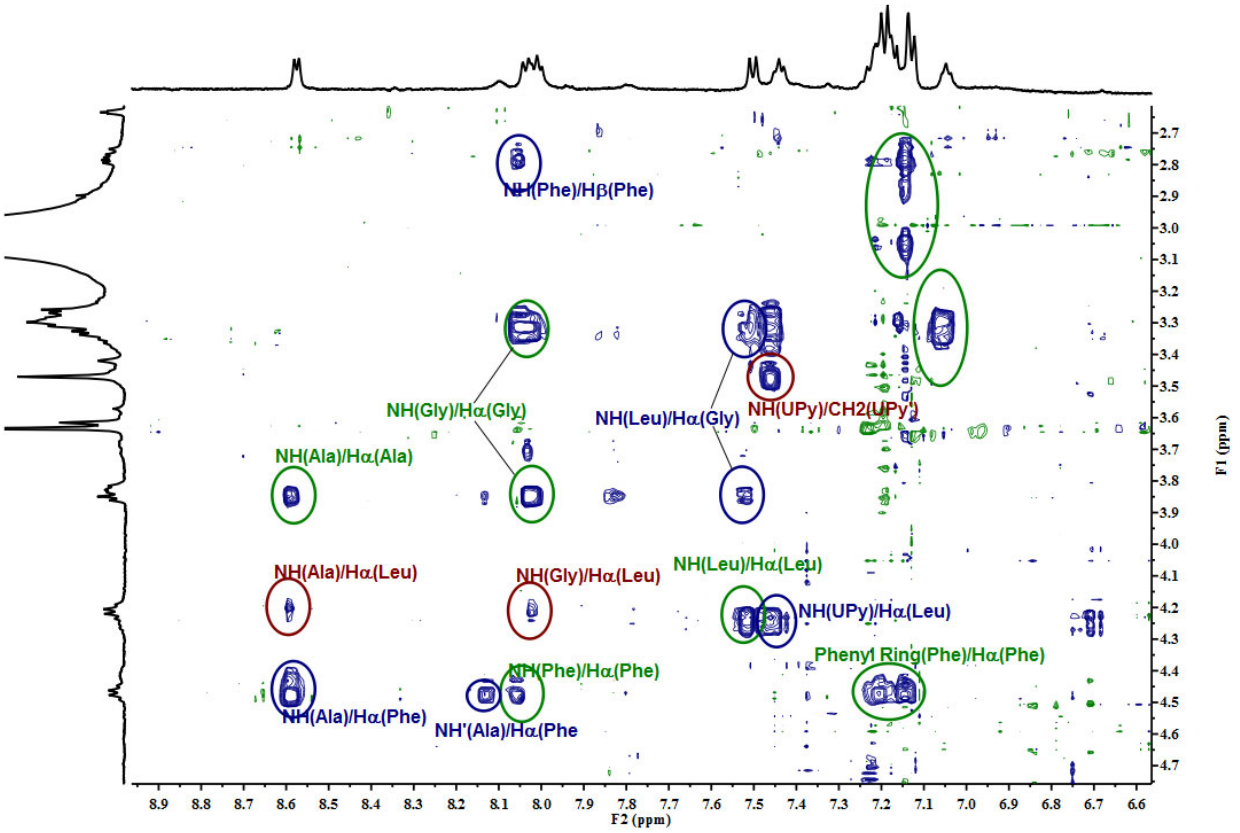

Figure 1.52 Section of 500 MHz ROESY spectrum of peptide **II** in 20% DMSO-d_6 in CD_2Cl_2 (400ms mixing time). Green: intraresidue, Blue: sequential interresidue, Red: nonsequential interresidue.

Overlay of ROESY and TOCSY spectrum of peptide II in 20% DMSO-d_6 in CD_2Cl_2

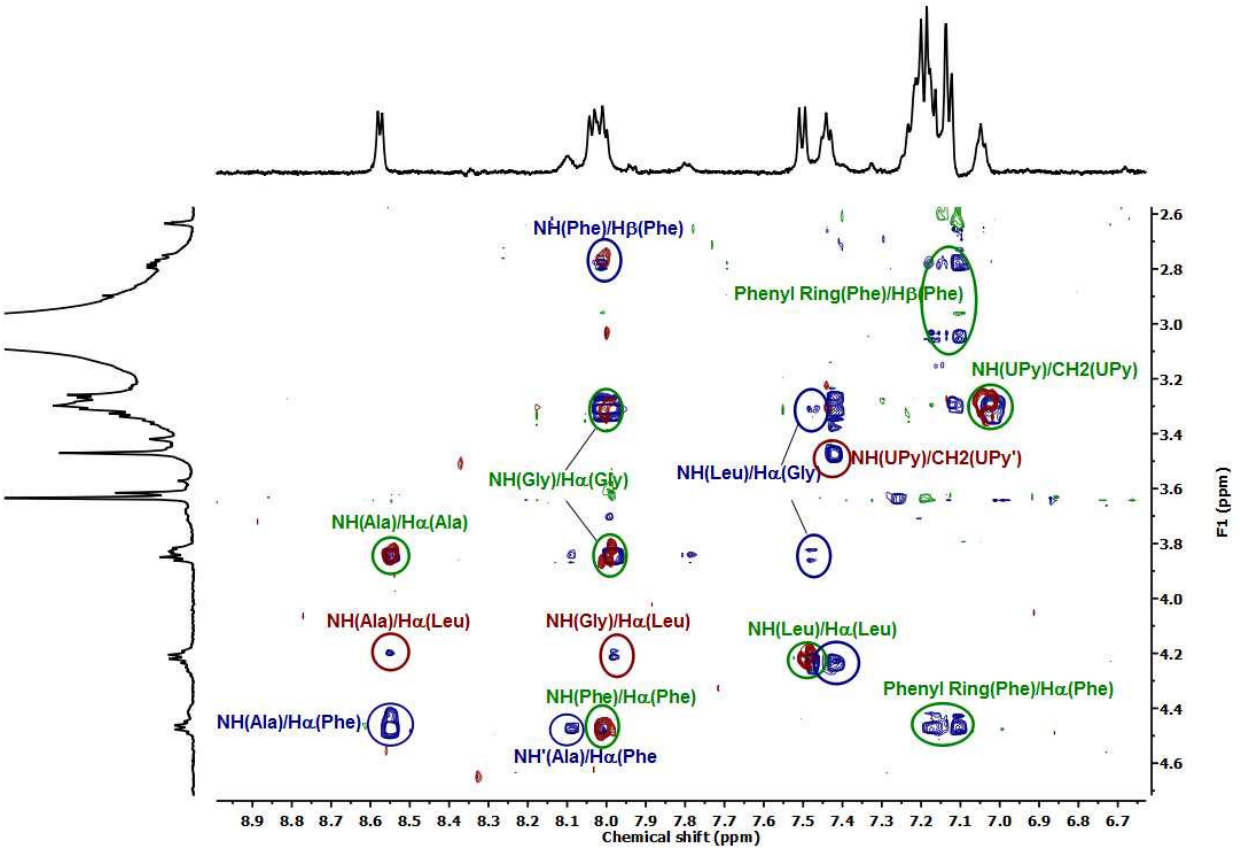

Figure 1.53 Overlay of ROESY and TOCSY spectrum of peptide **II** in 20% DMSO-d_6 in CD_2Cl_2 **.**

Green: intraresidue, Blue: sequential interresidue, Red: nonsequential interresidue.

Sections of 500 MHz ROESY spectrum of peptide II in 20% DMSO-d_6 in CD_2Cl_2 showing the EXSY cross-peaks

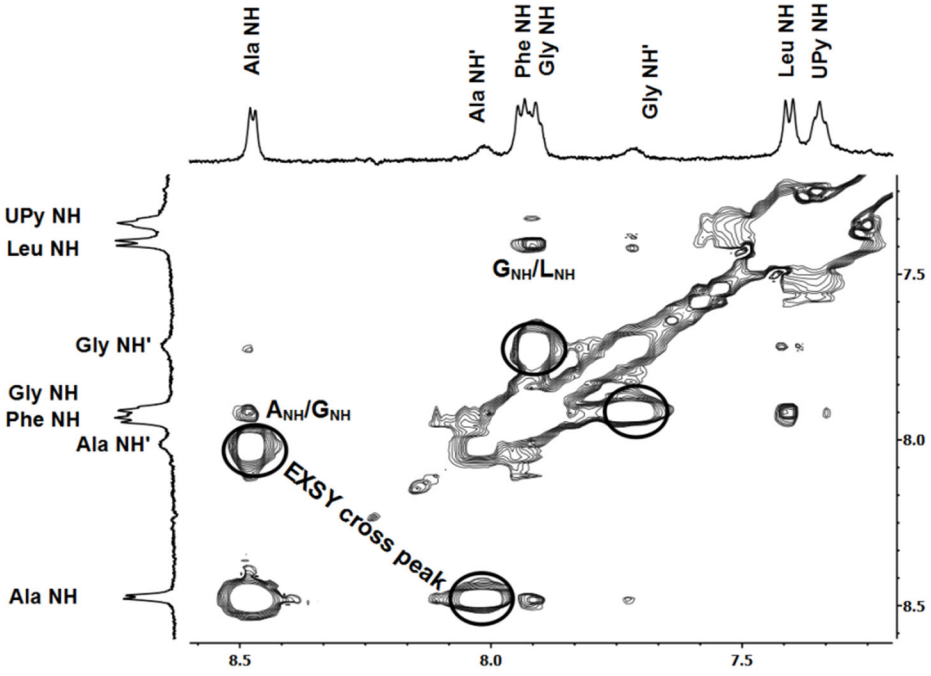

Figure 1.54 Sections of 500 MHz EXSY spectrum of peptide **II** in 20% DMSO-d_6 in CD_2Cl_2 (400ms mixing time). The EXSY cross peaks are circled, showing the connection between minor peaks and major amide resonances.

Section of 500 MHz ROESY spectrum of peptide IV in 20% DMSO-d_6 in CD_2Cl_2

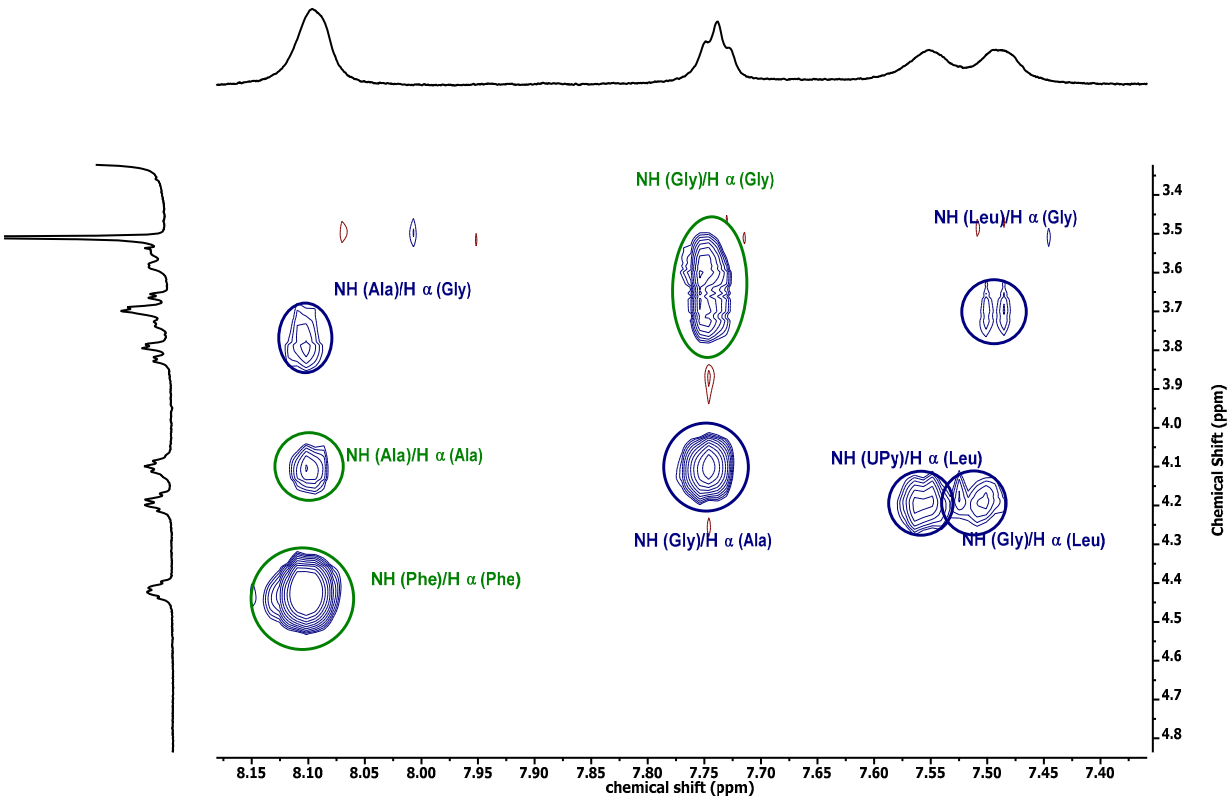

Figure 1.55 Section of 500 MHz ROESY spectrum of peptide **IV** in 20% DMSO-d_6 in CD_2Cl_2 (400ms mixing time). Green: intraresidue, Blue: sequential interresidue, Red: nonsequential interresidue.

^{1}H and ^{13}C NMR of Fmoc-CUPy(Bn)-OH and Fmoc-NUPy(Bn)-OH.

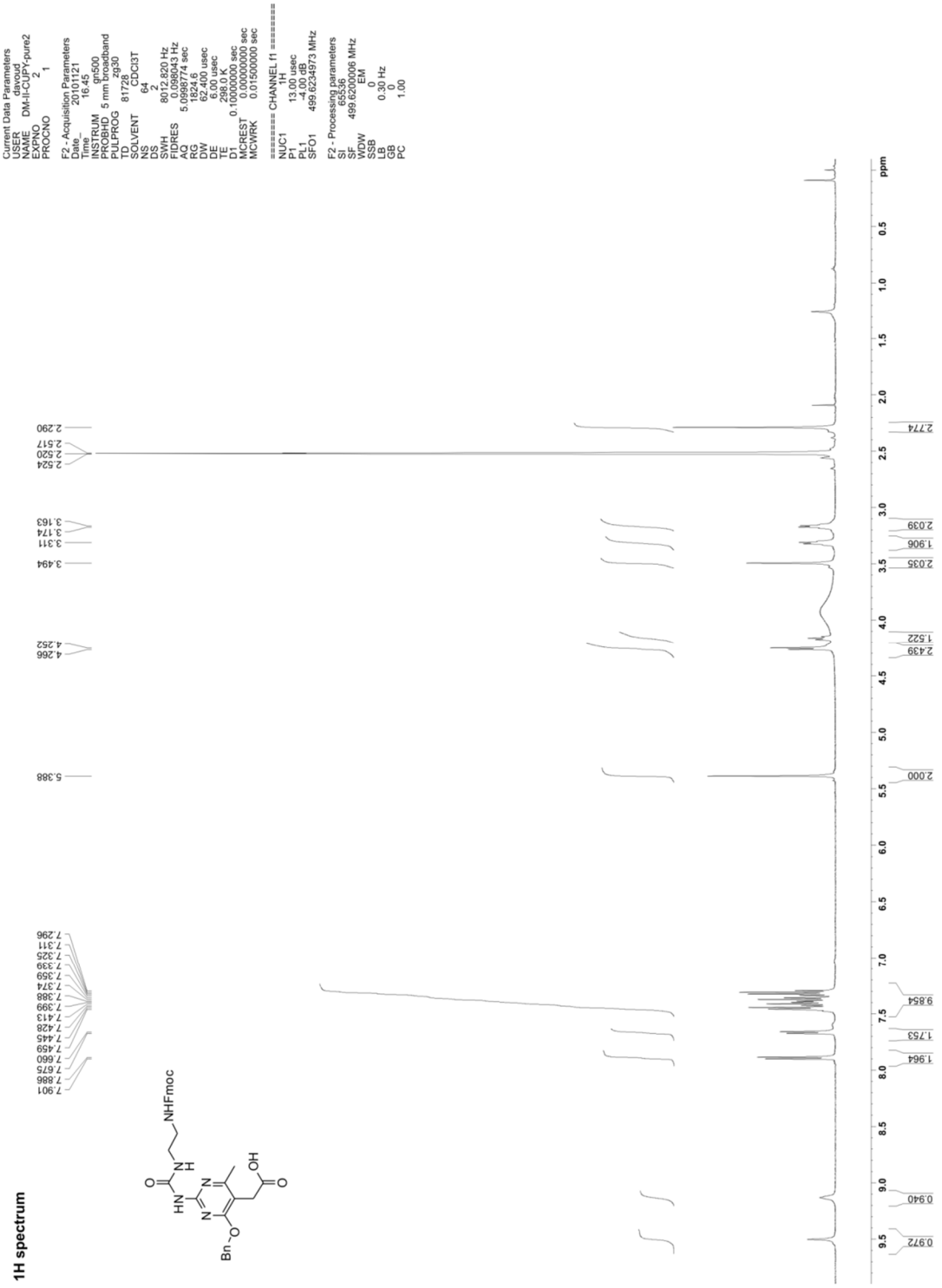

Figure 1.56 ^{1}H NMR of Fmoc-CUPy(Bn)-OH in DMSO-d_6

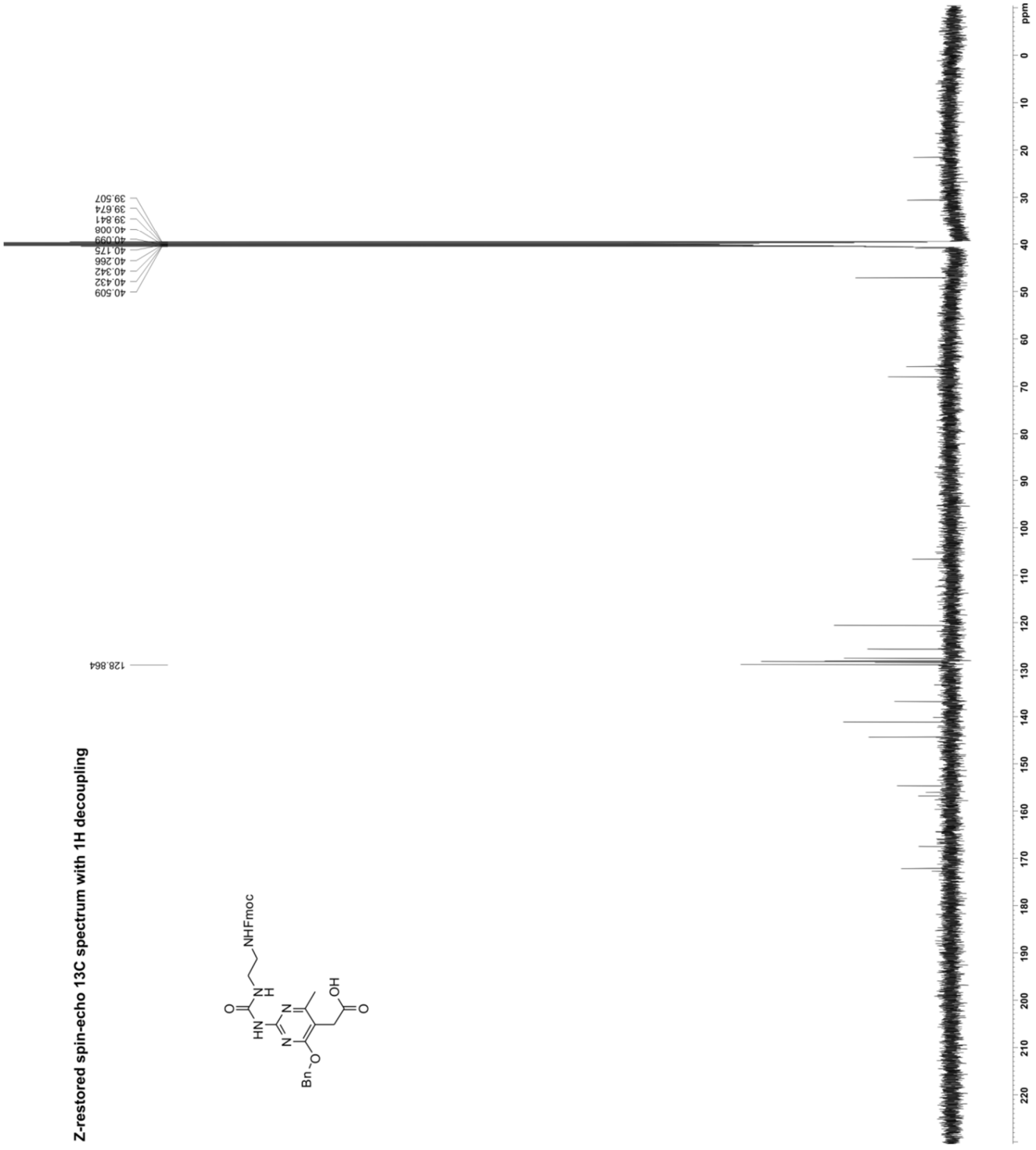

Figure 1.57 ^{13}C NMR of Fmoc-CUPy(Bn)-OH in DMSO-d_6

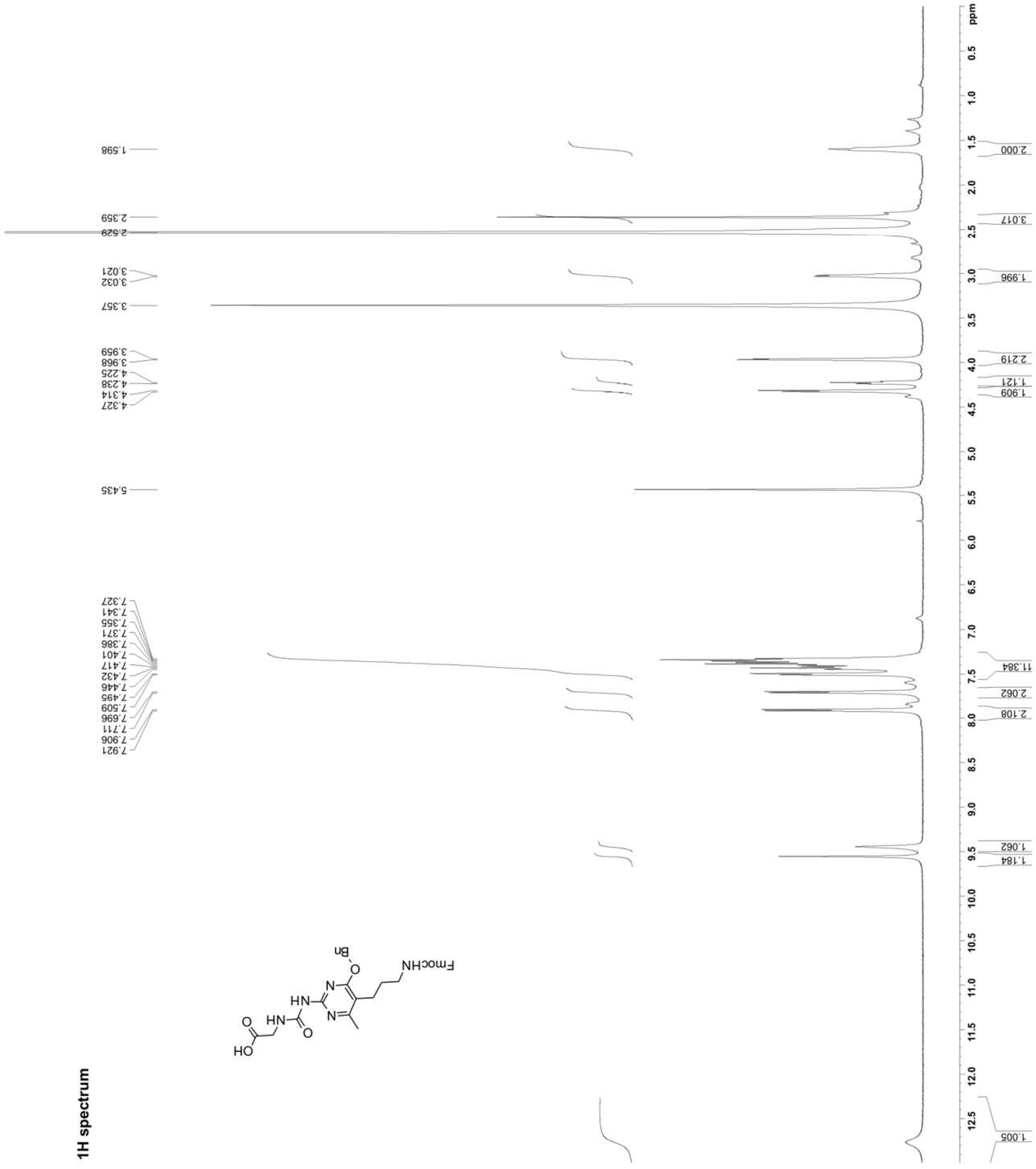

Figure 1.58 [1]H NMR of Fmoc-NUPy(Bn)-OH in DMSO-d_6.

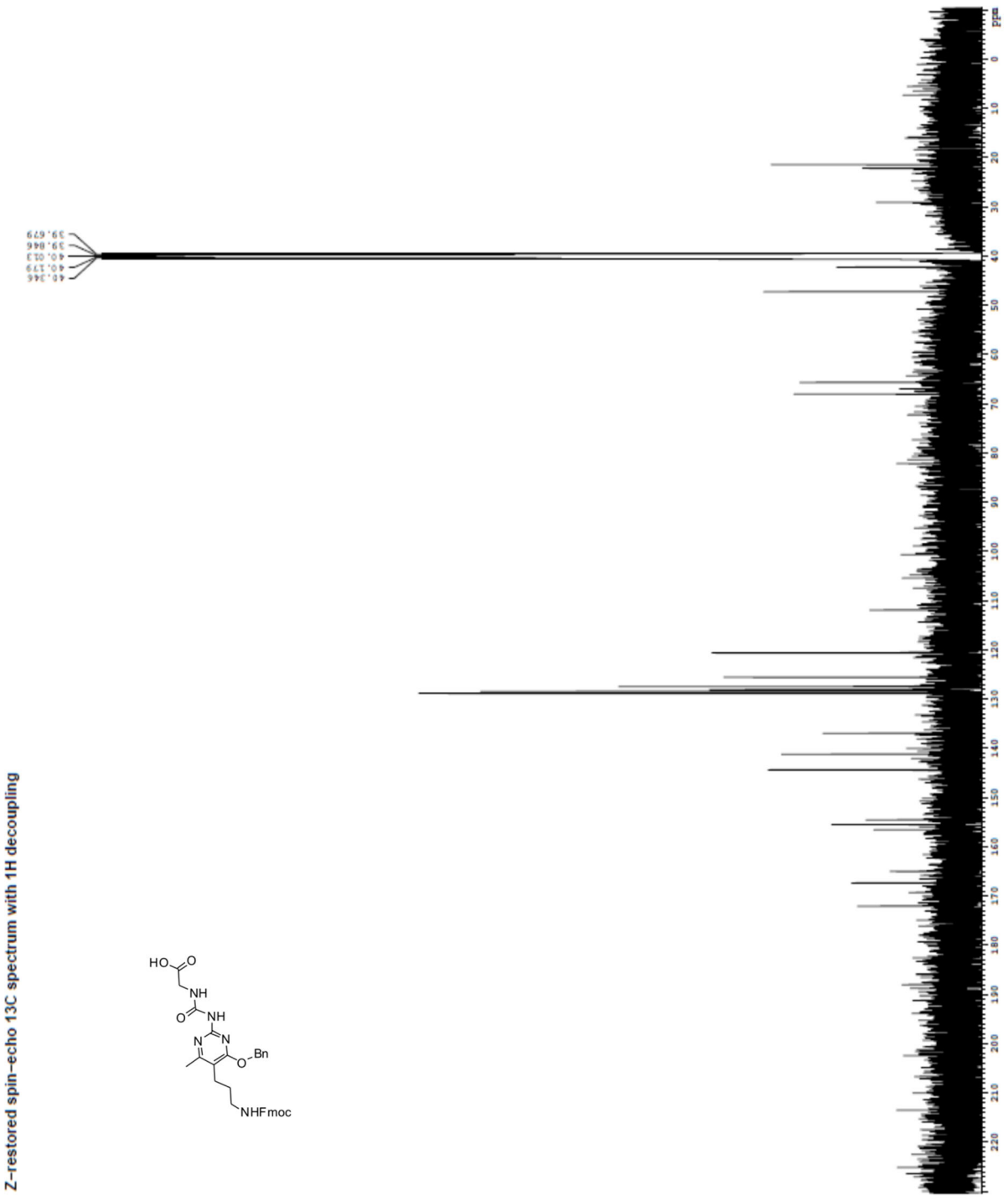

Figure 1.59 ^{13}C NMR of Fmoc-NUPy(Bn)-OH in DMSO-d_6

Synthesis of Peptide V

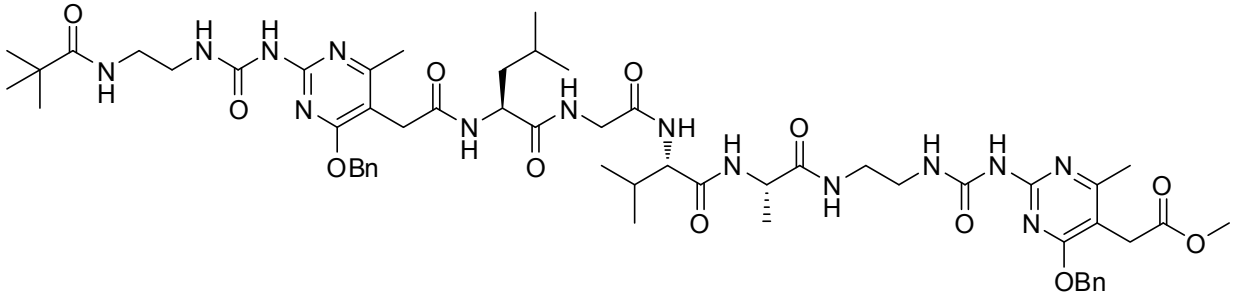

Chemical Formula: $C_{56}H_{78}N_{14}O_{12}$
Exact Mass: 1138.59

Peptide	Sequence
V	Piv-CUPy(Bn)-LGVA-CUPy(Bn)-OMe

MS (ESI), m/z calcd for $[(C_{58}H_{78}N_{14}O_{12} + 2H)/ 2]^+$ = 1139.59; found 1139.57.

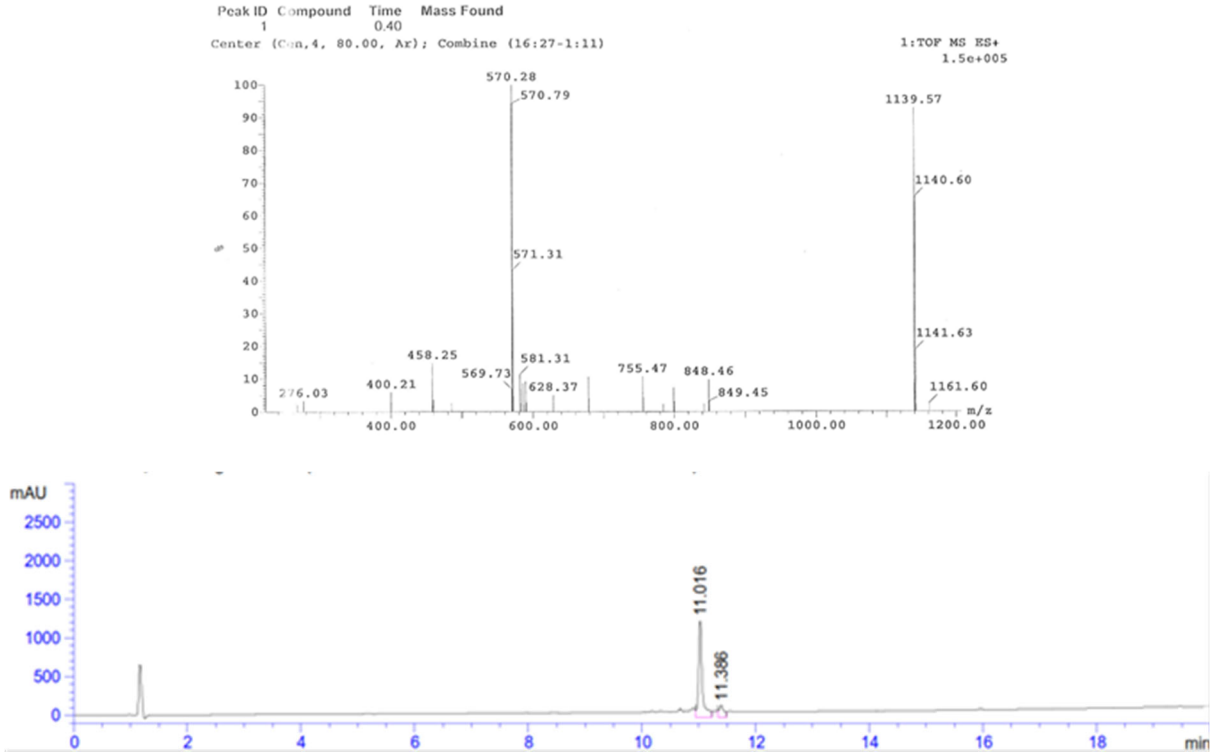

Figure 1.60 ESI-MS and analytical HPLC trace for Peptide V. (Kinetex™ LC Column 80 Å; 100 x 4.6 mm; particle size 2.6 µm; solvent A: H_2O/0.1% TFA, solvent B: CH_3CN/0.1% TFA, 0-100% CH_3CN over 20 minutes)

Synthesis of Peptide VI

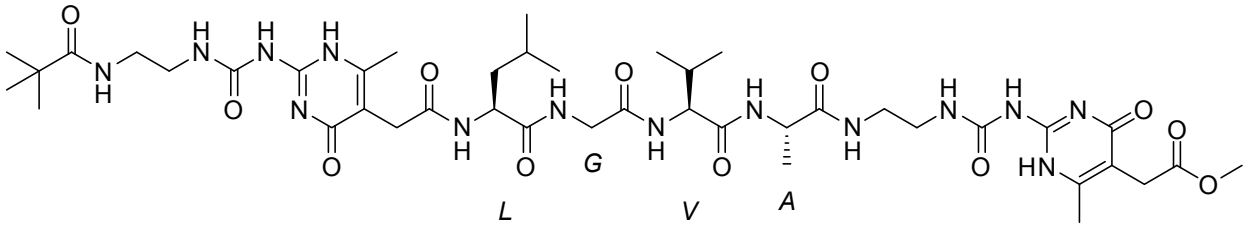

Chemical Formula: $C_{42}H_{66}N_{14}O_{12}$
Exact Mass: 958.50

Peptide	Sequence
VI	Piv-CUPy-LGVA-CUPy-OMe

MS (ESI), m/z calcd for $[(C_{42}H_{66}N_{14}O_{12} + 2H)/ 2]^+ = 959.5$; found 959.8.

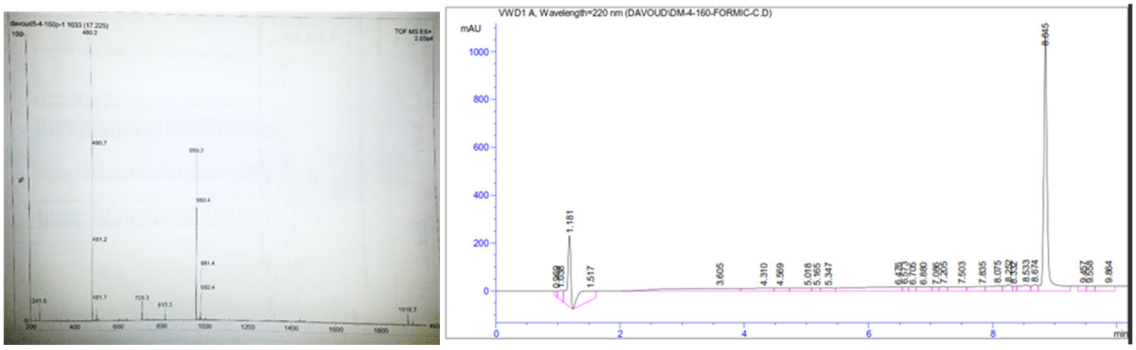

Figure 1.61 ESI-MS and analytical HPLC trace for Peptide V. (Kinetex™ LC Column 80 Å; 100 x 4.6 mm; particle size 2.6 µm; solvent A: H_2O/0.1% TFA, solvent B: CH_3CN/0.1% TFA**,** 0-100% CH_3CN over 20 minutes)

500 MHz ^{1}H NMR spectrum of peptide V in 20% DMSO-d_6 in CD_2Cl_2

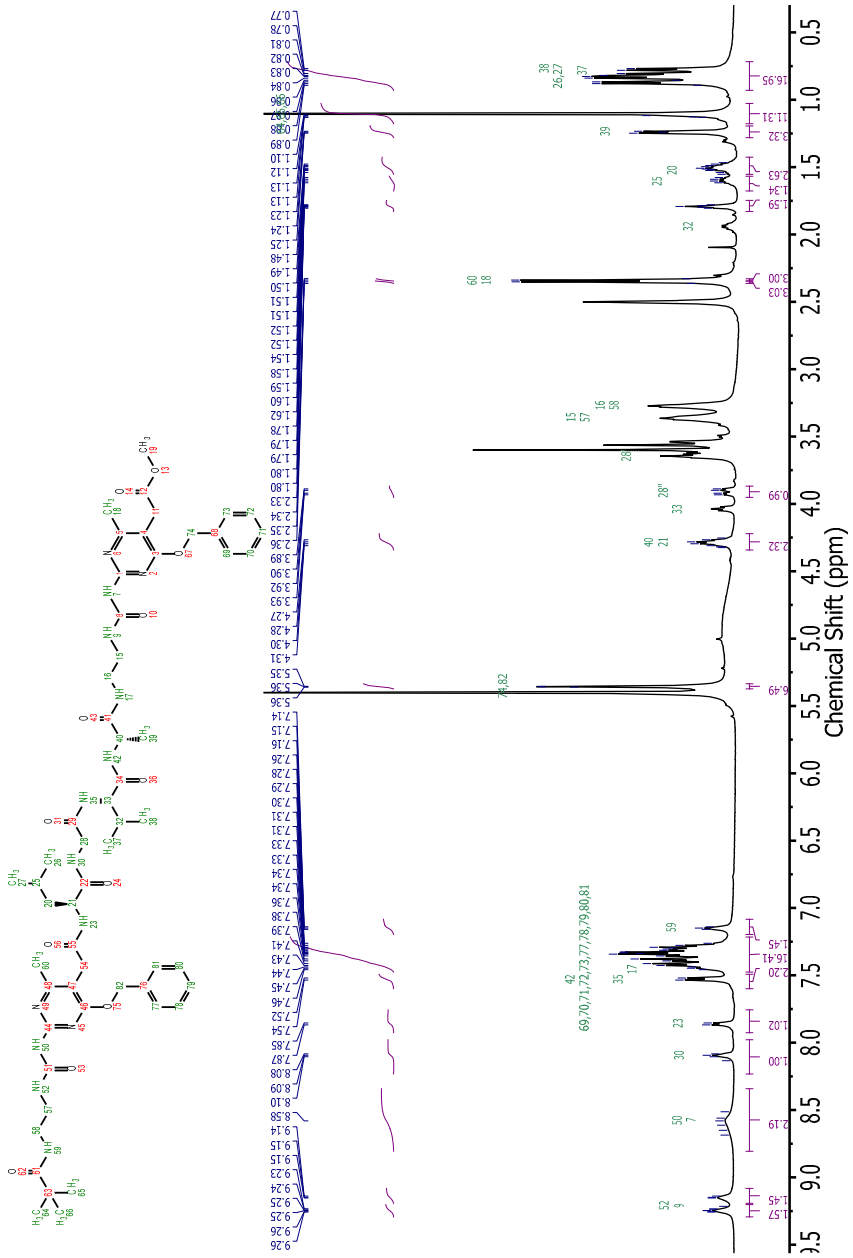

Figure 1.62 500 MHz ^{1}H NMR spectrum of peptide **V** in 20% DMSO-d_6 in CD_2Cl_2.

500 MHz COSY spectrum of peptide V in 20% DMSO-d_6 in CD_2Cl_2

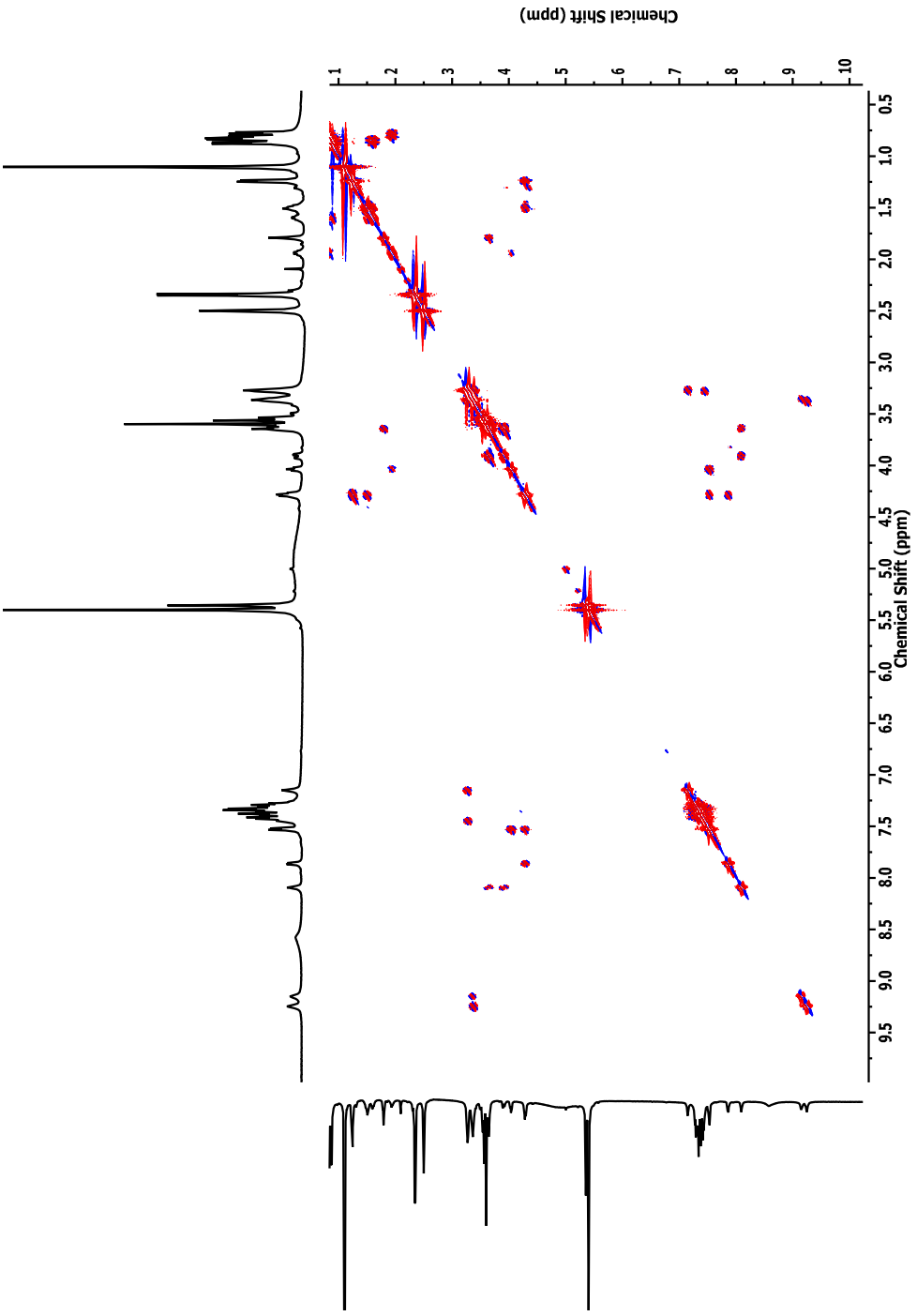

Figure 1.63 500 MHz COSY spectrum of peptide **V** in 20% DMSO-d_6 in CD_2Cl_2.

500 MHz ^{1}H NMR spectrum of peptide VI in 20% DMSO-d_6 in CD_2Cl_2

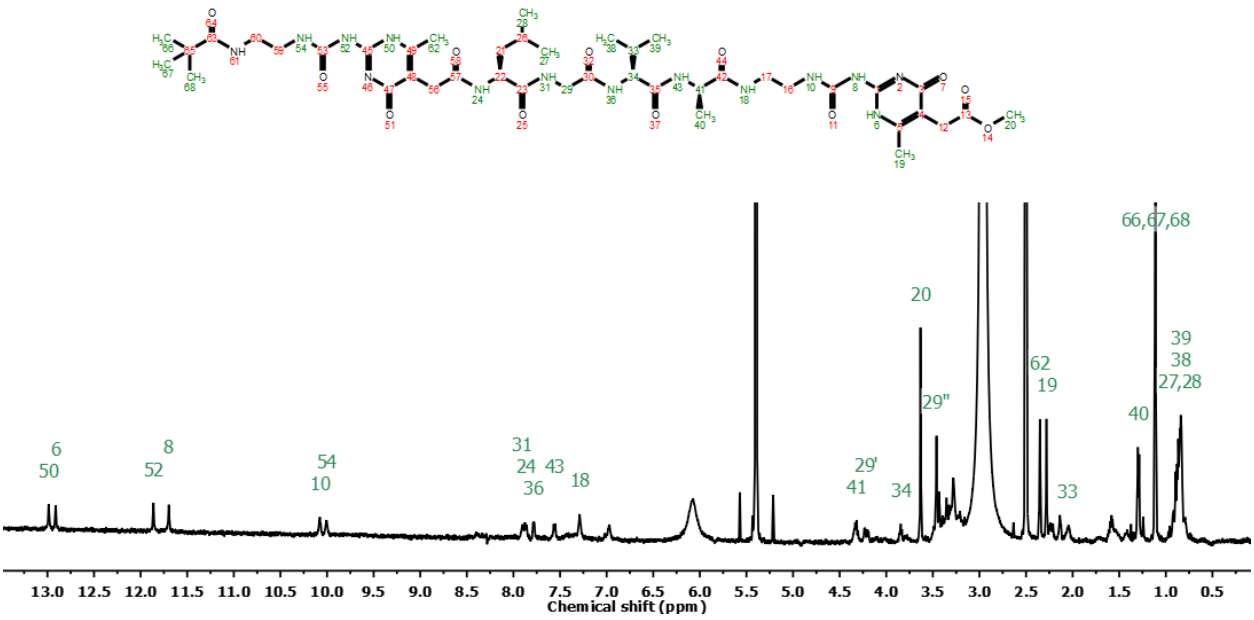

Figure 1.64 500 MHz ^{1}H NMR spectrum of peptide **VI** in 20% DMSO-d_6 in CD_2Cl_2.

500 MHz COSY spectrum of peptide VI in 20% DMSO-d_6 in CD_2Cl_2

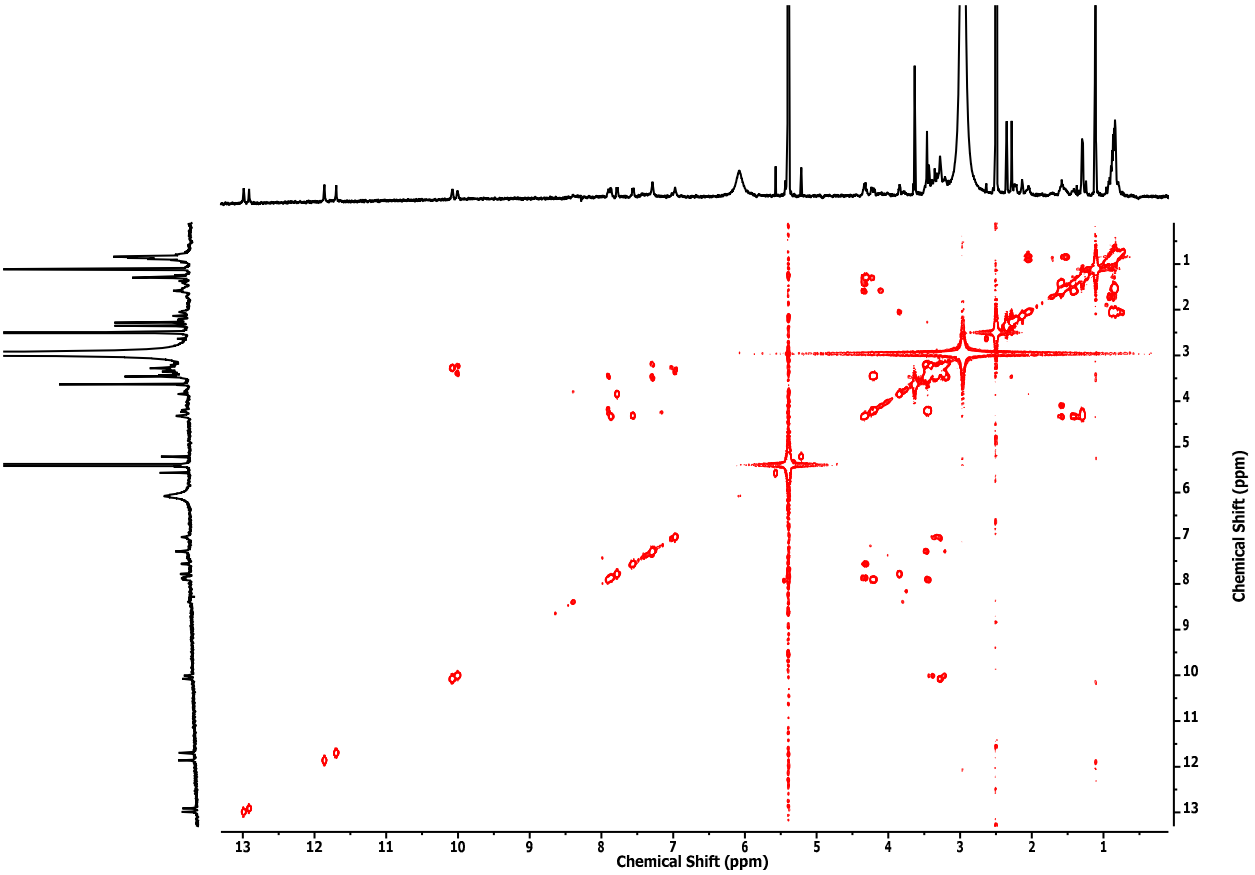

Figure 1.65 500 MHz COSY spectrum of peptide **VI** in 20% DMSO-d_6 in CD_2Cl_2.

Synthesis of Peptide VII

Peptide	Sequence
VII	NUPy(Bn)-PGADCVNITIKQHAGP-CUPy(Bn)G

MS (ESI), m/z calcd for $[(C_{106}H_{157}N_{33}O_{28}S+2H)/2]^+$ = 1187.1; found 1187; MS (ESI), m/z calcd for $[(C_{106}H_{157}N_{33}O_{28}S+3H)/3]^+$ = 791.72; found 792; MS (ESI), m/z calcd for $[(C_{106}H_{157}N_{33}O_{28}S+2H+2Na)/4]^+$ = 605.03; found 604;

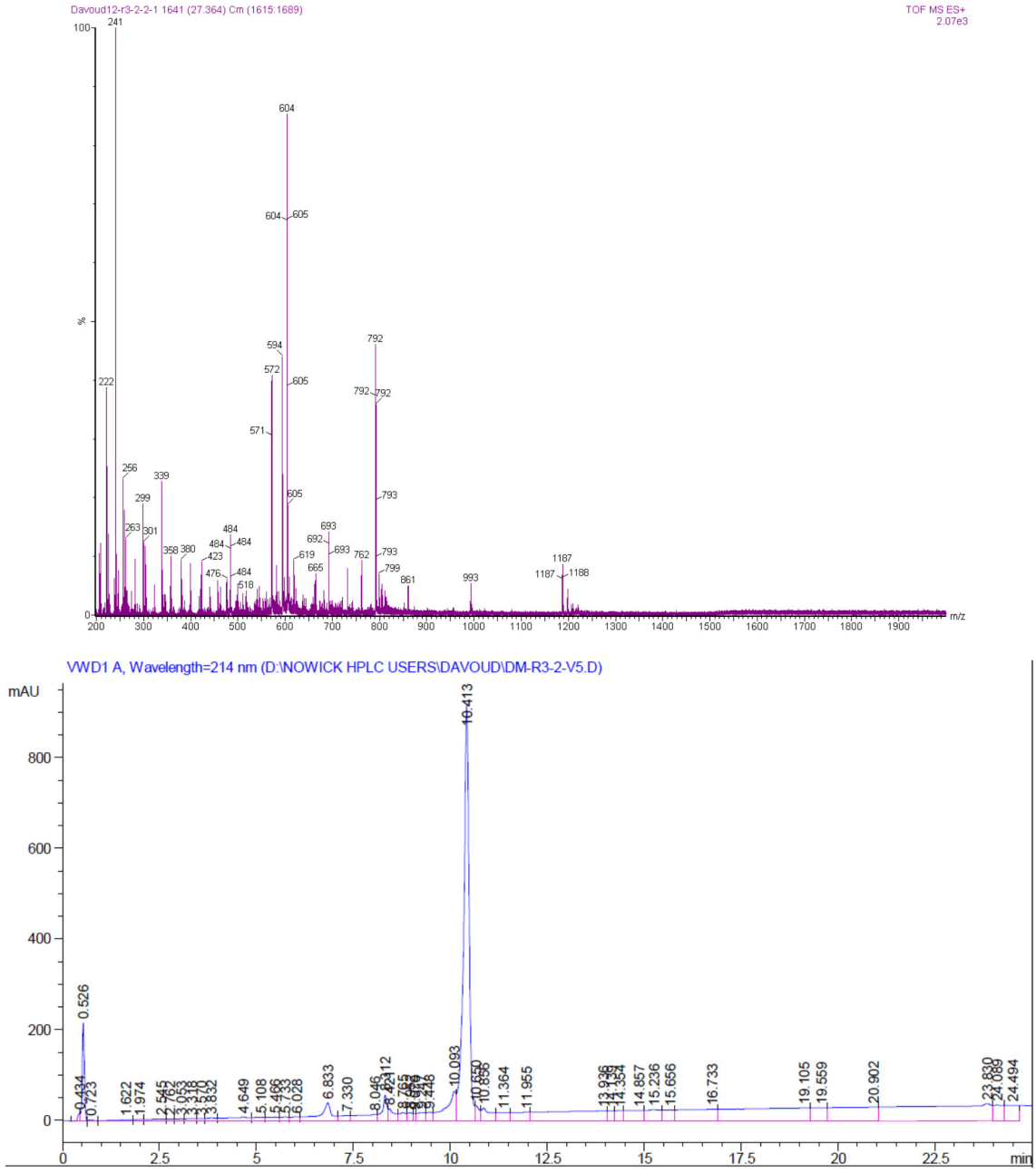

Figure 1.66 ESI-MS and analytical HPLC trace for Peptide **VII**. (Agilent Zorbax® Eclipse-XDB-C18 80 Å; 150 x 4.6 mm; particle size 5 µm; solvent A: H_2O/0.1% TFA, solvent B: CH_3CN/0.1% TFA, 0-100% CHCN over 35 minutes)

Synthesis of Peptide VIII

Peptide	Sequence
VIII	NUPy(Bn)-PAQLIAKGP-CUPy(Bn)G

MS (ESI), m/z calcd for $[(C_{78}H_{115}N_{23}O_{17} + 2H)/ 2]^+ = 823.94$; found 824; . MS (ESI), m/z calcd for $[(C_{78}H_{115}N_{23}O_{17} + 3H)/ 3]^+ = 549.63$; found 550.

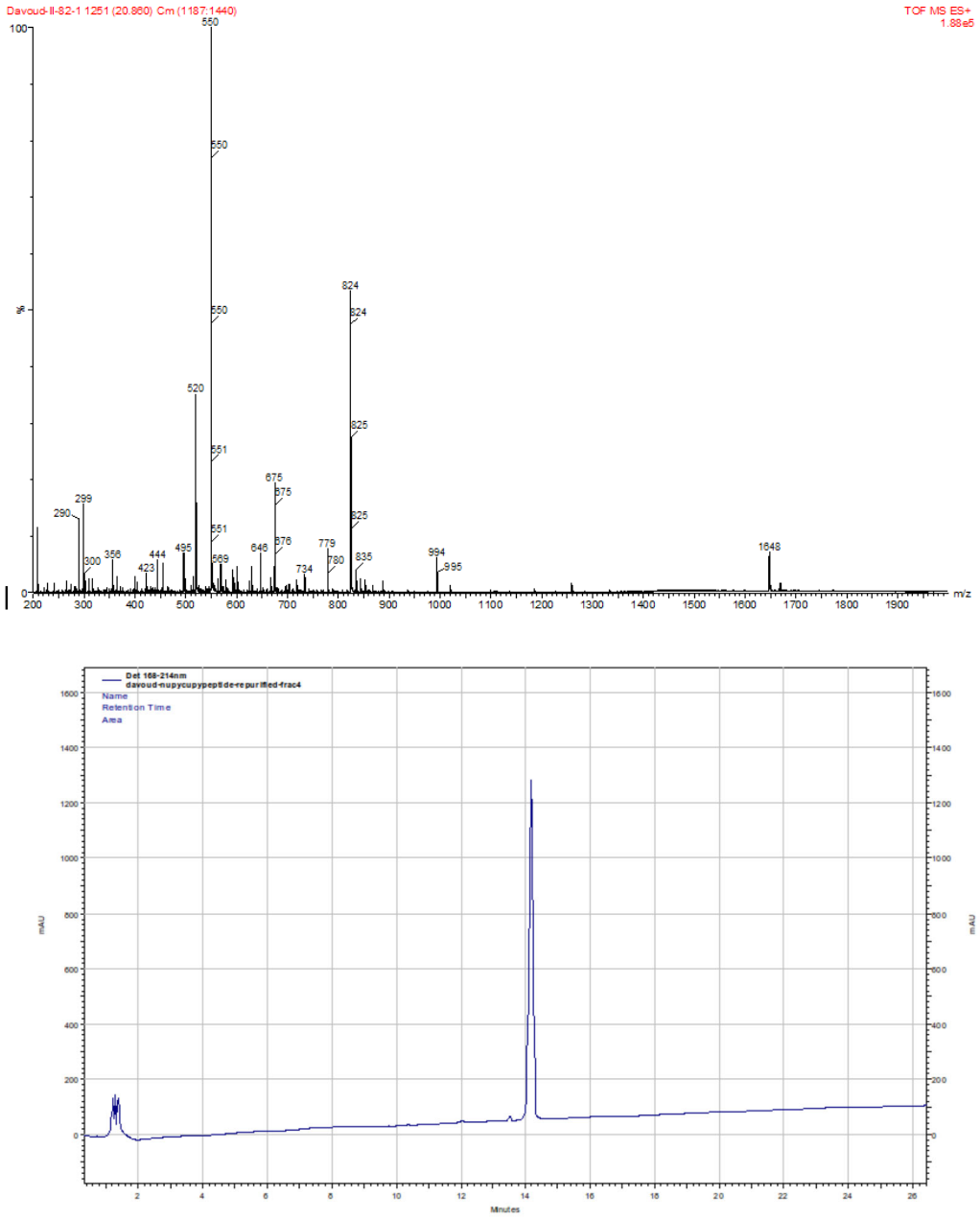

Figure 1.67 ESI-MS and analytical HPLC trace for Peptide **VIII**. (Agilent Zorbax® Eclipse-XDB-C18 80 Å; 150 x 4.6 mm; particle size 5 µm; solvent A: H_2O/0.1% TFA, solvent B: CH_3CN/0.1% TFA, 0-100% CH_3CN over 35 minutes)

Synthesis of Peptide IX

Peptide	Sequence
IX	NUPy-PAQLIAKGP-CUPyG

MS (ESI), m/z calcd for $[(C_{64}H_{103}N_{23}O_{17} + 2H)/ 2]^+ = 733.9$; found 734; . MS (ESI), m/z calcd for $[(C_{64}H_{103}N_{23}O_{17}+ 3H)/ 3]^+ = 489.6$; found 490.

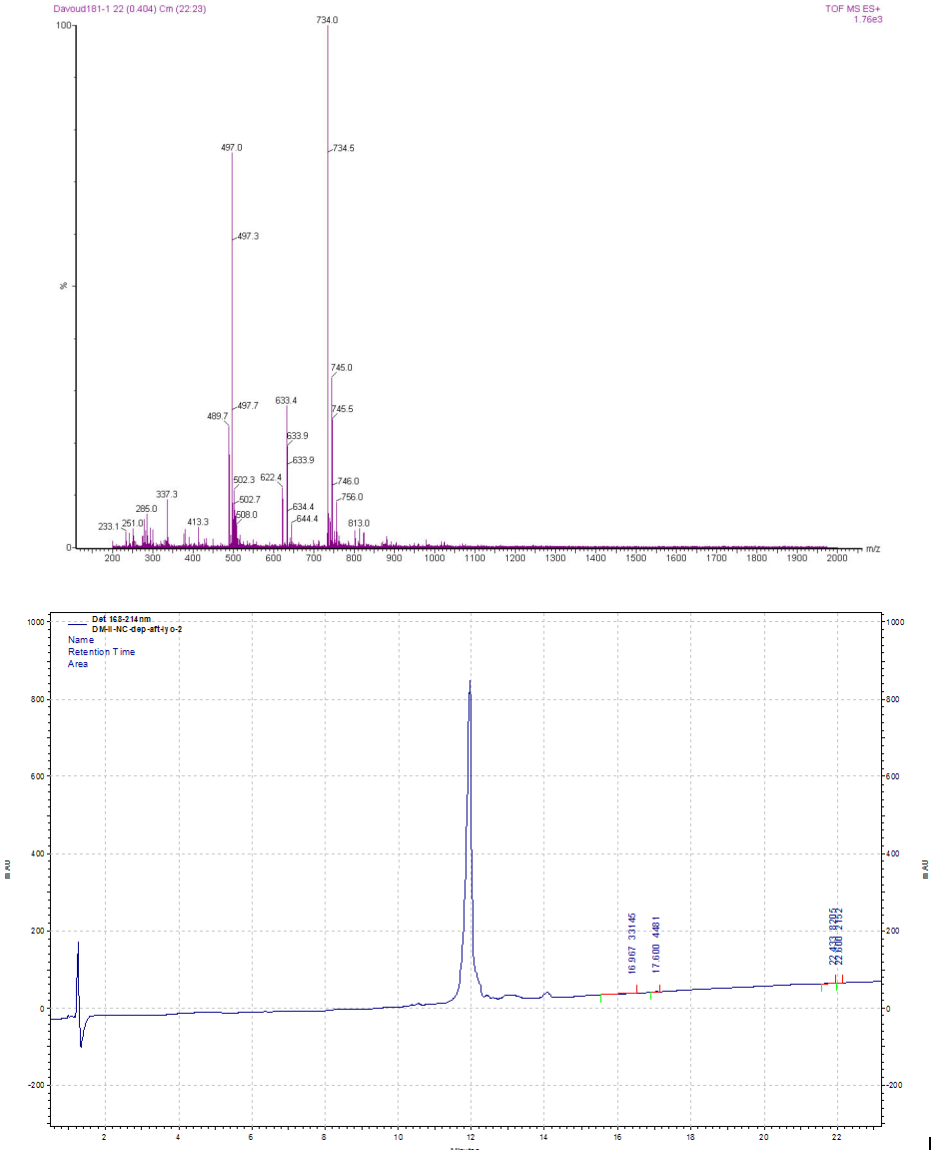

Figure 1.68 ESI-MS and analytical HPLC trace for Peptide **IX**. (Agilent Zorbax® Eclipse-XDB-C18 80 Å; 150 x 4.6 mm; particle size 5 µm; solvent A: H_2O/0.1% TFA, solvent B: CH_3CN/0.1% TFA, 0-100% CH_3CN over 35 minutes)

Synthesis of X

Peptide	Sequence
X	NUPy(Bn)-PAILIAFAGP-CUPy(Bn)G

White powder 20mg, MS (ESI), m/z calcd for $[(C_{85}H_{119}N_{21}O_{18}+ 2H)/2]^+$ = 861.93; found 862.

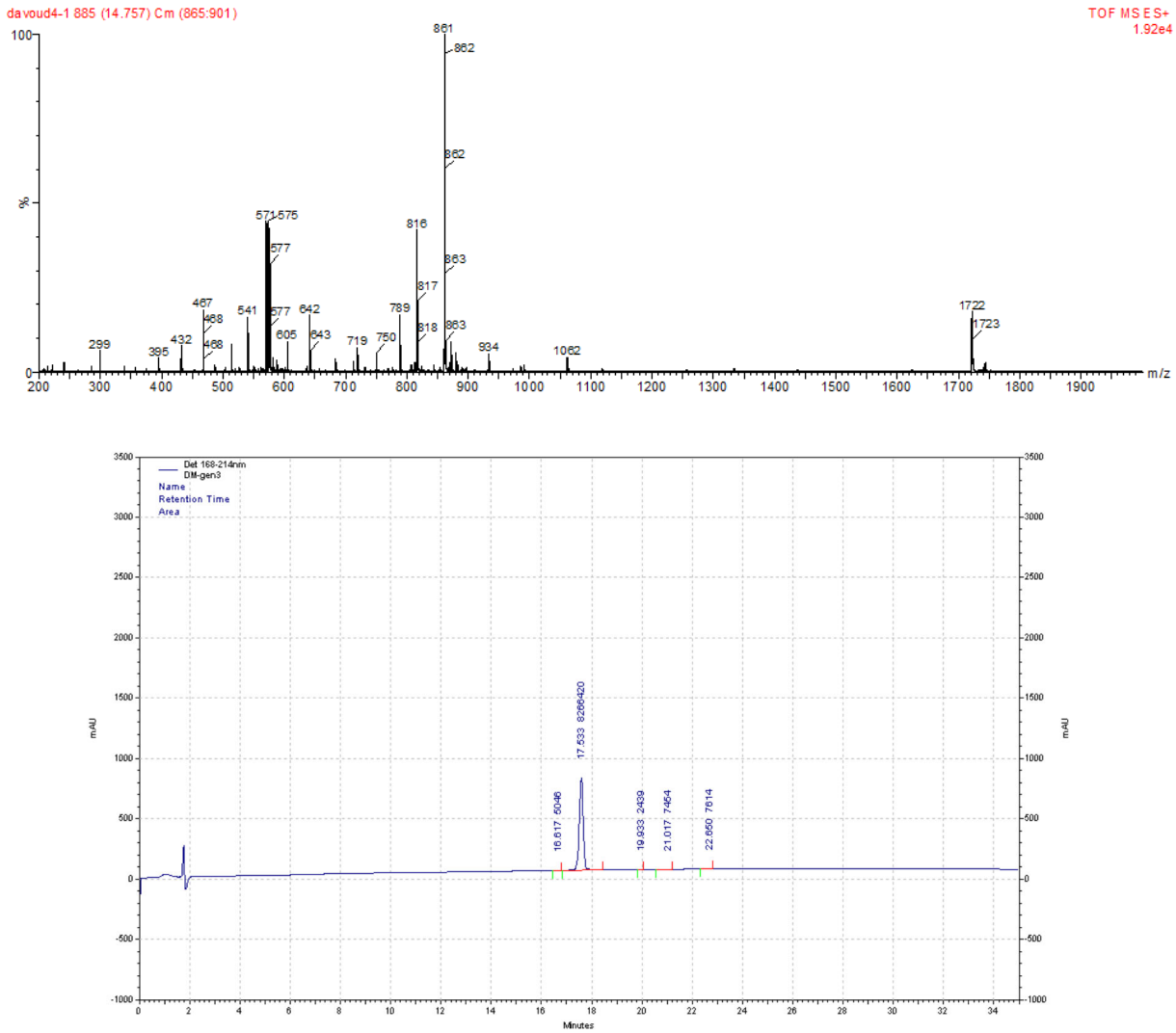

Figure 1.69 ESI-MS and analytical HPLC trace for Peptide **X**. (Agilent Zorbax® Eclipse-XDB-C18 80 Å; 150 x 4.6 mm; particle size 5 µm; solvent A: H_2O/0.1% TFA, solvent B: CH_3CN/0.1% TFA, 0-100% CH_3CN over 35 minutes)

Synthesis of XI

Peptide	Sequence
XI	NUPy-PAILIAFAGP-CUPyG

MS (ESI), m/z calcd for $[(C_{71}H_{109}N_{21}O_{18}+ 2H)/2]^+$ = 773.37; found 772.

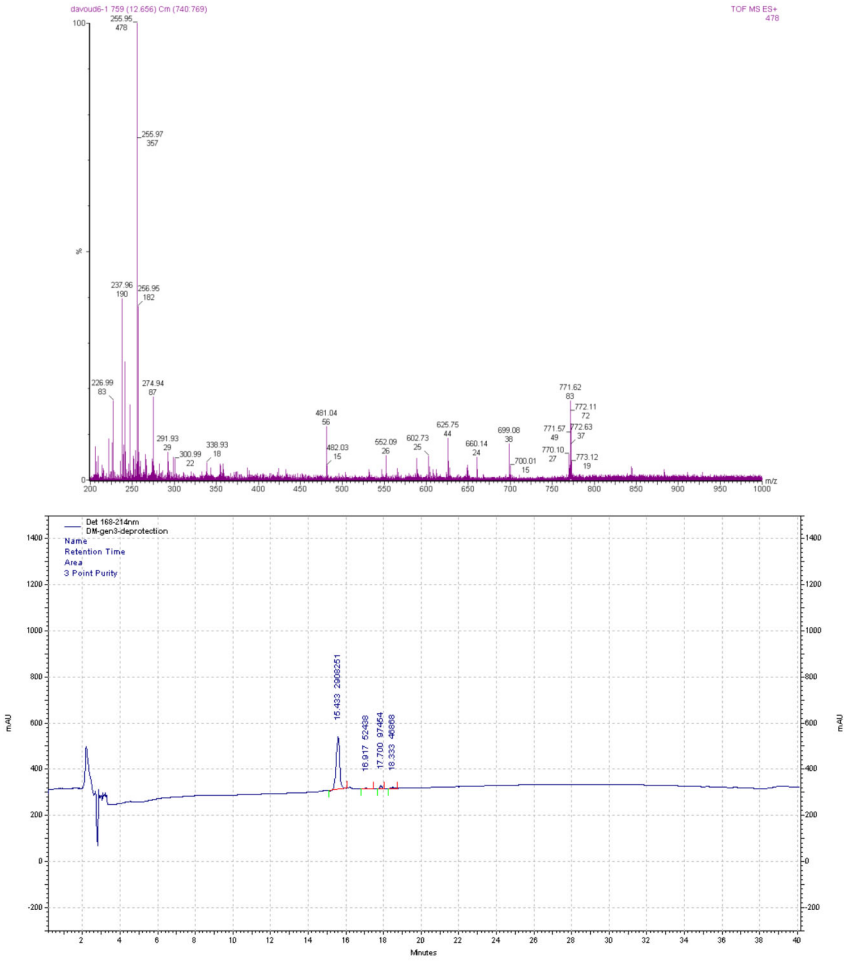

Figure 1.70 ESI-MS and analytical HPLC trace for Peptide **XI**. (Agilent Zorbax® Eclipse-XDB-C18 80 Å; 150 x 4.6 mm; particle size 5 µm; solvent A: H_2O/0.1% TFA, solvent B: CH_3CN/0.1% TFA, 0-100% CH_3CN over 35 minutes)

CD Experiments

Circular dichroism (CD) spectroscopy was performed on a Jasco J-810 spectropolarimeter at 25 °C. Data mode: CD and Abs, bandwidth 1.0 nm, response: 1 s, sensitivity: 100 mdeg, step resolution: 0.1 nm, scan speed: 100 nm min−1, three accumulations. All measurements were performed using a concentration of 150-200 µM of the respective peptide in indicated solvent. The CD-spectra were recorded using a 1 cm quartz cuvette (Hellma).

Synthesis of $(Nspe)_8$

Synthesis of $(Nspe)_8$ was conducted according to published procedure.

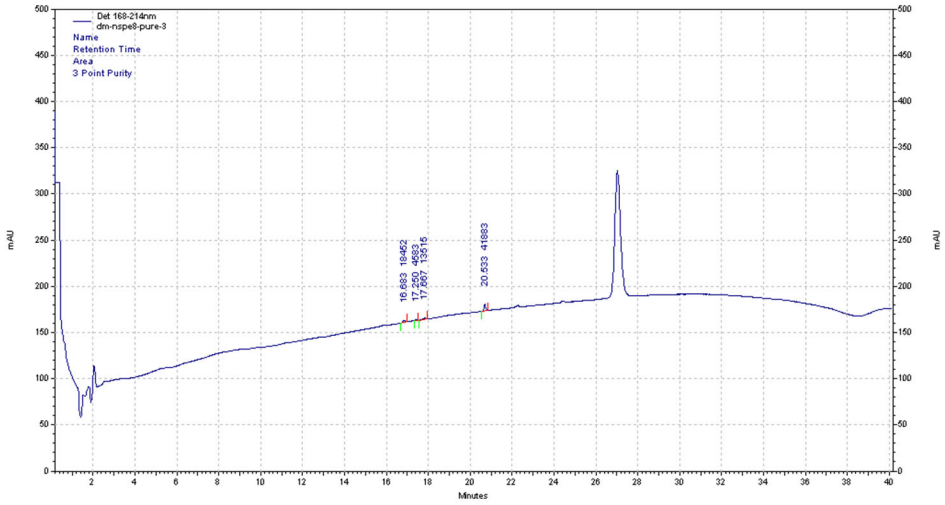

Figure 1.71 Analytical HPLC trace for peptoid $(Nspe)_8$. (Agilent Zorbax® Eclipse-XDB-C18 80 Å; 150 x 4.6 mm; particle size 5 µm; solvent A: H_2O/0.1% TFA, solvent B: CH_3CN/0.1% TFA, 0-100% CH_3CN over 35 minutes)

Synthesis of NUPy(Bn)-$(Nspe)_8$-CUPy(Bn)

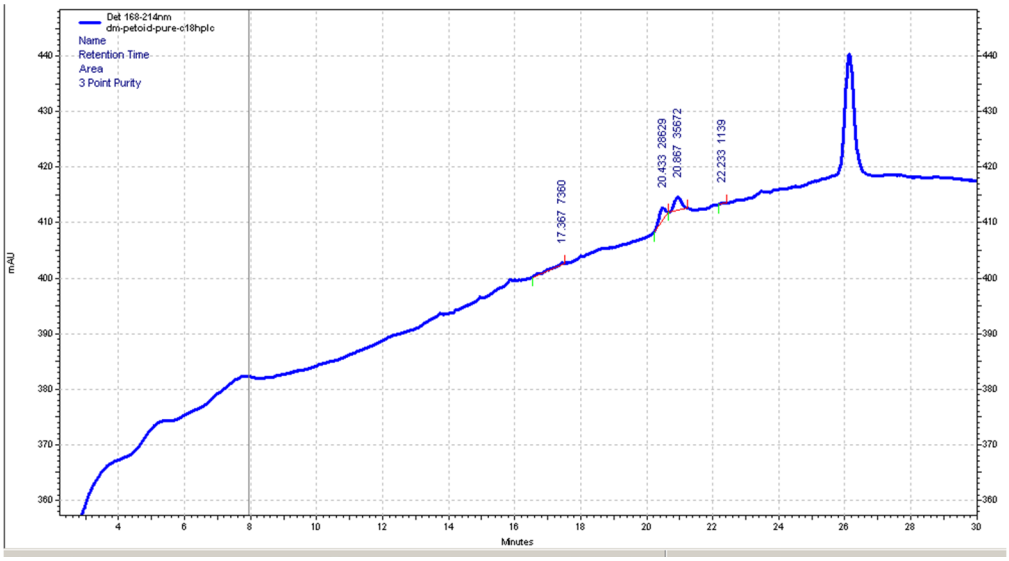

Figure 1.72 Analytical HPLC trace for peptoid NUPy(Bn)-$(Nspe)_8$-CUPy(Bn). (Agilent Zorbax® Eclipse-XDB-C18 80 Å; 150 x 4.6 mm; particle size 5 µm; solvent A: H_2O/0.1% TFA, solvent B: CH_3CN/0.1% TFA, 0-100% CH_3CN over 35 minutes)

Synthesis of $(_pG)_4$-NPGS-$(_pG)_4$-V

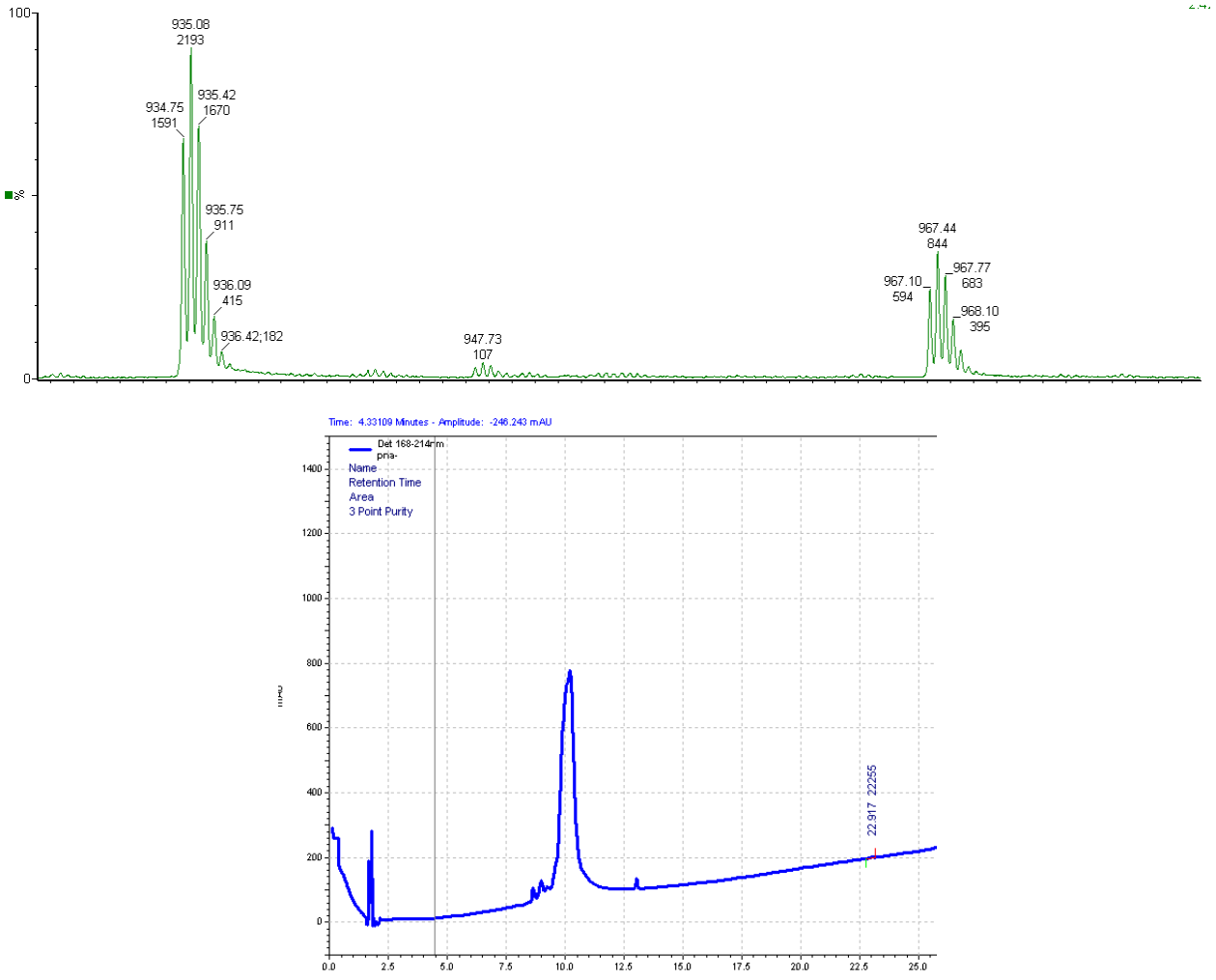

Figure 1.73 ESI-MS and analytical HPLC trace for **PNA-1** $(pG)_4$-NPGS-$(pG)_4$-V (Agilent Zorbax® Eclipse-XDB-C18 80 Å; 150 x 4.6 mm; particle size 5 µm; solvent A: H_2O/0.1% TFA, solvent B: CH_3CN/0.1% TFA, 0-100% CH_3CN over 35 minutes)

MS (ESI), m/z calcd for $[(C_{107}H_{137}N_{63}O_{31}+ 3H)/3]^+$ = 934.33; found 934.7.

Chapter 2 Self-Healing Multiphase Polymers via Dynamic Metal–Ligand Interactions

2.1 Introduction

Many biological systems have developed exquisite self-repair strategies and machineries as an important evolutionary advantage. In these systems, physical damage initiates a controlled cascade of coordinated repair processes which continue until complete healing is achieved. In contrast, synthetic man-made materials are unable to efficiently repair even small damages over their lifetime. As a result, minor damages are accumulated and eventually merge to form micro- and macro- cracks which significantly compromise the mechanical properties and increase the chances of unpredictable catastrophic failure under the physical load.

Inspired by self-repair and regeneration in nature, the idea of imparting self-healing abilities into man-made materials has received considerable interest from the scientific community. Progress toward "self-healing materials" would improve the safety, lifetime, energy efficiency, and environmental impact of manmade materials.

The remaining two chapters of this dissertation is focused on my efforts on the synthesis and study of new self-healing materials by utilizing transient interactions. In chapter 2, I will discuss the application of a labile M–L interactions as a dynamic motif and my studies on the correlation of small molecule parameters (such as M–L complex geometry, ligand exchange rate, and mechanism) to bulk mechanical properties. Chapter 3 is focused on the synthesis of strong self-healing materials from inexpensive commodity scale monomers and the study of their mechanical and self-healing properties.

For the remainder of this chapter, I will mainly focus on the self-healing and recovery of mechanical properties in synthetic polymers. However, self-healing materials are not limited to polymeric systems[1] and recovery of other physical properties such as conductivity is also highly desirable.[2]

In polymeric systems, physical damage results in chain scission and slippage thus leaving the network at a non-equilibrium state at the damage interface. It is expected that the system will eventually relax from this excited state to reestablish the equilibrium. This process is governed by thermodynamic rules, driven by enthalpic and entropic factors.

2.1.1 Chemo-mechanical approaches

Different strategies have been devised to exploit entropic and enthalpic factors toward constructive bond formation across the damaged interface, thus healing the material. Some of these strategies capitalize on the release and subsequent delivery of fluid healing agents (monomers) favored by the non-equilibrium state of newly formed crack. This bio-inspired approach is among the first strategies that have been pursued to impart self-healing properties to man-made composites and polymeric system.[3] The main idea is to store reactive healing agents inside metastable compartments within the material. Physical damage (crack initiation or propagation) then physically destroys the compartments and exposes the freely diffusing healing agents to catalysts or initiators embedded in the matrix. The crack is then filled with reacted healing agents to inhibit further propagation of cracks by healing the material (Figure 2.1).[4-6]

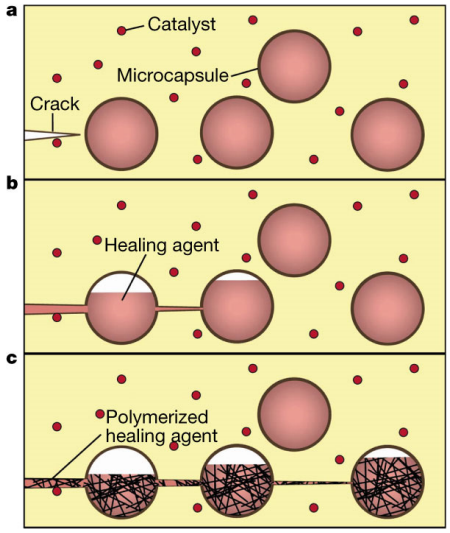

Figure 2.1 Concept of autonomous self-healing using encapsulated healing agents. (a) crack formation (b) crack propagatin and relase of healing agents (c) Self-healing after polymerization of monomer after contact with catalyst (reprinted from reference 4).

Despite the simplicity of this concept, many practical considerations have plagued the wide-spread use of this strategy. Unlike biological systems where the repair process is tightly controlled by a complex network of feedback loops, the self-healing kinetics in this system is primarily encoded at the level of physical properties of monomer and chemical reactivity of the catalyst. The interplay between the kinetics of monomer diffusion and reactivity can signifanctly affect the healing efficiency outcome thus necessitating the optimization of many parameters such as monomers[7], capsule size[8], membrane thickness[9], catalyst[10] and etc. to achieve effective self-healing.

More recently, a vasculature network was studied as the storage and the delivery platform for the healing agents.[11] This design is a step forward toward mimicking similar networks in biological systems with optimized efficiency in mass-transfer properties.[12,13] While conceptually interesting, these vascularized systems also provide a unique opportunity to control the delivery of multiple healing agents to the damaged site. This smart delivery can be modulated using a

computer controlled pressurized system and has the potential to repair damages with irregular shapes and regenerate materials at a scale never possible before (Figure 2.2).[14]

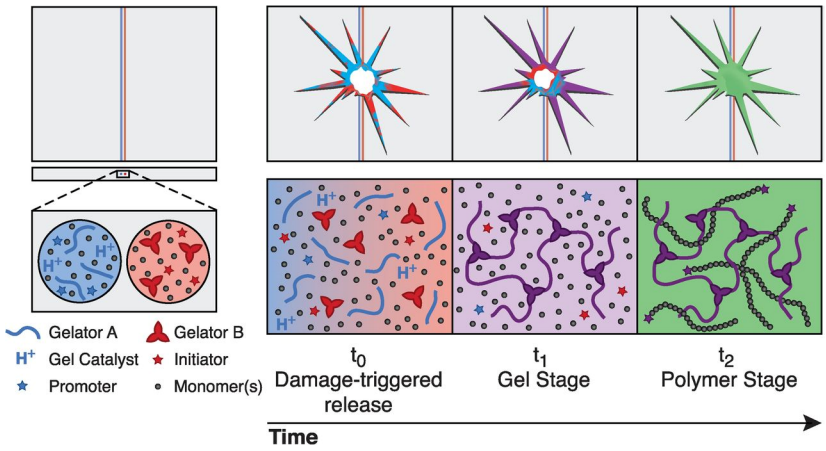

Figure 2.2 Two stage restoration of large damaged area in a polymeric system. Contolled-delivery of gellator, monomer, and catalyst can be used to cover an irregular damaged area. Fast gellation protects the monomer from dripping due to the gravity (reprinted from reference 14).

While the possibilities offered by these methods are intriguing, the fate of their wide-spread application in the near future depends on the optimization of the healing process and a generality of embedding these structures in engineering materials.

Additionally, the self-healing process in these systems depend on the delivery of healing agents *extrinsic* to the polymeric matrix. Significant effort is also devoted to design polymeric systems with *intrinsic* ability to self-repair. There are two main motivations to engineer intrinsic self-healing ability in a polymeric network. First, the ability to undergo multiple healing events (even at the same location) without the need of healing agents. Secondly, such dynamic systems may provide additional benefits during the early stages of physical damage by repairing the network at the molecular level after onset of microscopic damages. This early repair may inhibit the further accumulation of damage and extend the lifetime of material under constant stress.

As mentioned before, the damage interface presents a unique opportunity for polymer rearrangement and mobility due to its non-equilibrium state. From the thermodynamic perspective, a spontaneous repair is possible if the free energy of polymer association across the cut interface is negative.[15,16] During the damage process, chain scission and slippage are the most common microscopic events. A successful self-healing system can be designed through careful considerations of macromolecular rearrangements and chain recoupling across the damaged interface.[17] Theoretical[18,19] and early experimental work in this field has already demonstrated the important role of polymer entanglement in the process of self-healing.[20,21]

Given the low mobility of large macromolecules, the crack size has to be on the order of the effective diffusion length for efficient repair in reasonable time frame. Another recent thrust in the self-healing field has been directed at utilizing programmed shape memory transitions to bring the damaged interface closer to each other to facilitate the polymer diffusion across the cut interface for expedited healing.[22,23] The shape memory transition can be triggered by orthogonal external stimuli[24] but it is highly desirable to couple the trigger to the damage event to produce an autonomous response.[25]

2.1.2 Design of intrinsically self-healing systems

While the above aspect of self-healing (chain mobility and entanglement) has received considerable attention from theoreticians and polymer physicist, the chain scission aspects (and subsequent recombination of reactive ends) has been studied heavily by chemists. Advancements in the field of mechanochemistry, coupling of chemical and mechanical phenomenon at the molecular level, has contributed significantly to our understanding of mechanical damage process at the molecular level[26] even though many details about transductions of macroscopic forces to polymer level have remained elusive.[27] A crude approximation is that a short-lived intermediate

(likely a radical) will be formed from the scission of a strong covalent bond. This unstable intermediate is prone to undergo an unwanted side-reaction over a short time scale before finding the chance to recouple with partners across the cut interface. It is therefore desirable to either increase the half-life and the stability of the radical intermediate or find a mechanism for reshuffling of other chains across the cut interface. Many examples of self-healing systems utilize dynamic covalent and non-covalent (supramolecular) interactions to achieve the successful recombination of chemical species after mechanical damage.

We will first briefly look at some the prominent examples of dynamic covalent systems and then discuss examples of utilized non-covalent interactions in self-healing systems.

2.1.3 Self-healing systems utilizing dynamic covalent interactions

As mentioned earlier, increasing the stability of dangling chain ends after mechanical damage may provide an avenue for effective self-healing. Given the relationship between the stability of radicals and the strength of covalent bond, it has been possible to rationally incorporate cross-linkers with higher radical stability (low bond energy) into polymeric system for efficient self-healing. The core hypothesis is that the physical damage will unravel the weakest linker in the network and the resulting radical will be stable enough under the time-scale of polymer rearrangement for a successful recombination with partners across the cut interface.

The following three examples are representative of this strategy. In a pioneering example by Ghosh and Urban, chitosan (CHI) was modified with oxetane rings (1, 3-propylene oxide) and then cross-linked with a tri-functionalized isocyanate (Figure 2.3).[28] It was hypothesized that higher stability of oxetane free radical and its facile ring opening can provide a mechanism for the self-repair of this covalent network under UV irradiation. Indeed such behavior is observed

experimentally as well as some spectroscopic evidence for the presence of these hypothesized intermediates (Figure 2.3).

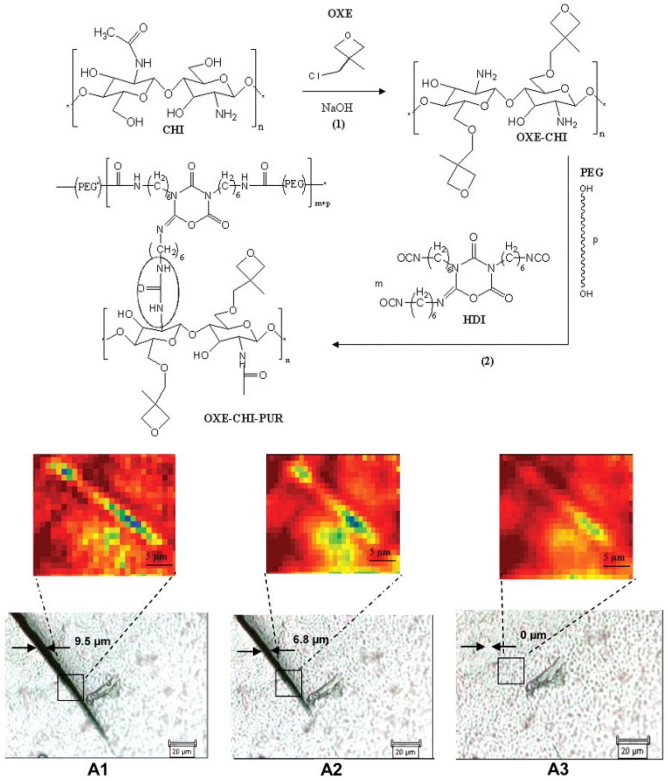

Figure 2.3 Synthesis of the cross-linked OXI-CHI-PUR network. Increased stability of oxetane radicals is utilized to repair the damaged network. IR and optical imaging of repair progress under UV (reprinted from reference 28).

In another example, a polystyrene network is cross-linked by a difunctionalized monomer containing a labile alkoxyamine subunit. This design was inspired by the dynamic nature of C-ON covalent bond that has been previously explored in nitroxide mediated living radical polymerization. After mechanical damage, polymer network healing can be achieved by heating at 130 °C for 2.5 h (Figure 2.4).[29]

Also, by increasing the steric around a covalent C-C bond, Imato *et al.* have been able to demonstrate efficient repair at ambient temperatures. Gels cross-linked with diaryl-bibenzofuranone moieties showed almost quantitative self-healing at room temperature within 24

h. The dynamic reconfiguration of this covalent network has also been reported recently (Figure 2.5).[30,31]

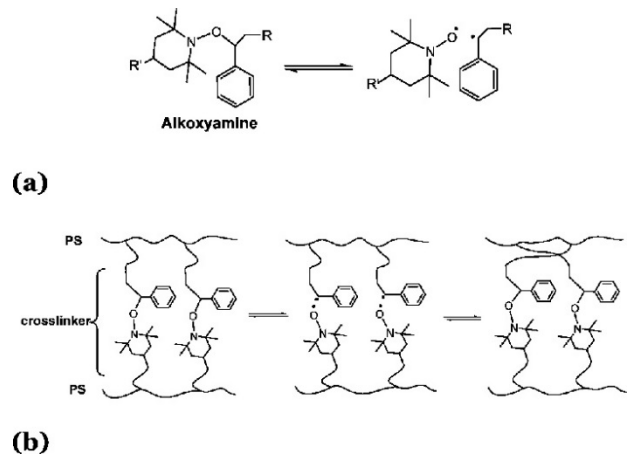

Figure 2.4 (a) The structure and dissociation product of alkoxyamines derivatives; (b) dynamic exchange reaction responsible for healing (reprinted from reference 29).

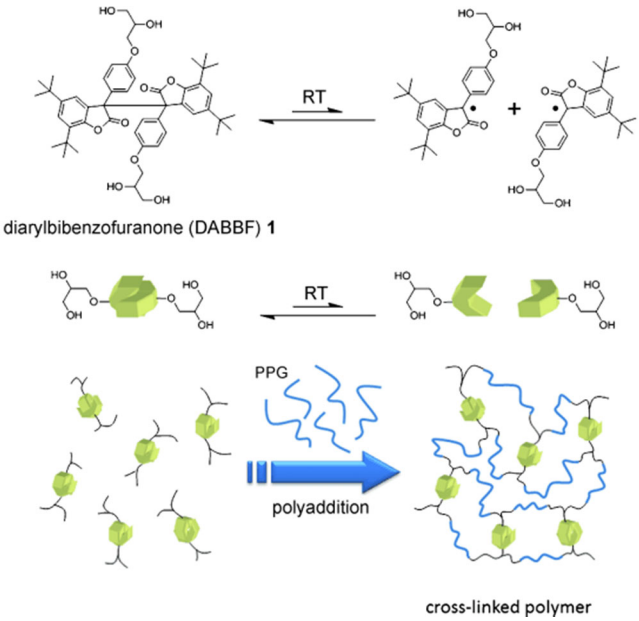

Figure 2.5 Structure of diarylbibenzofuranone and the network cross-linked by this dynamic motif (reprinted from reference 30).

Amamato *et al.* used trithiocarbonate motif (inspired by reversible addition-fragmentation chain transfer polymerization) to generate stable radicals for reshuffling of a covalently cross-linked network.[32] While the initial system required UV lights and handling under inert atmosphere, this issue was addressed in their next report by switching the dynamic motif to thiuram disulfide.[33] The new motif is dynamic and stable under visible light and an air atmosphere (Figure 2.6).

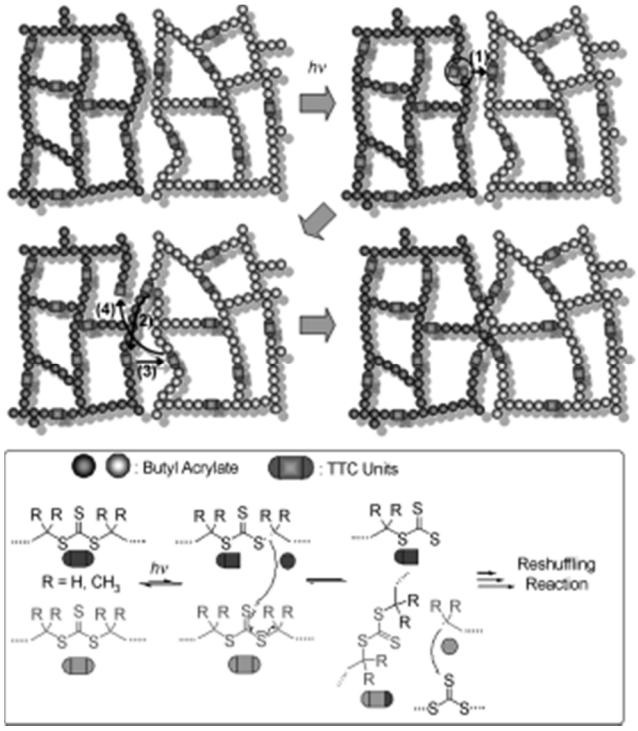

Figure 2.6 UV trigged reshuffling of trithiocarbonate cross-links for self-healing applications (reprinted from reference 32).

Similarly, examples of self-healing or dynamic systems based on thiol radicals and dynamic disulfide exchange reaction are also reported in the literature.[34,35]

Despite the successful self-healing of few radical based systems in the air, the general instability of radical intermediates to oxidative side reactions is concerning and may potentially limit the application of these systems. Therefore, it is advantageous to utilize other dynamic covalent bonds which do not produce radical intermediates after their dissociation. Cycloaddition

reactions (and their retro analogue) satisfy the above requirements and have been explored intensively for design of self-healing materials.

A cycloaddition reaction is typically exothermic and is accompanied by a decrease in the entropy of the system. The reverse reaction is thus favored thermodynamically at high temperatures due to this interplay between entropic and enthalpic factors. In a seminal report by Wudl and coworkers, a cross-linked network was prepared through Diels-Alder reaction between multi-arms maleimide and furan monomers. The reversible nature of this cross-link was then utilized to thermally re-mend a damaged sample (Figure 2.7).[36] Since this report, many other examples have emerged in the literature[37] that improve this design or expands upon this concept by utilizing other pericyclic reactions. [38-40]

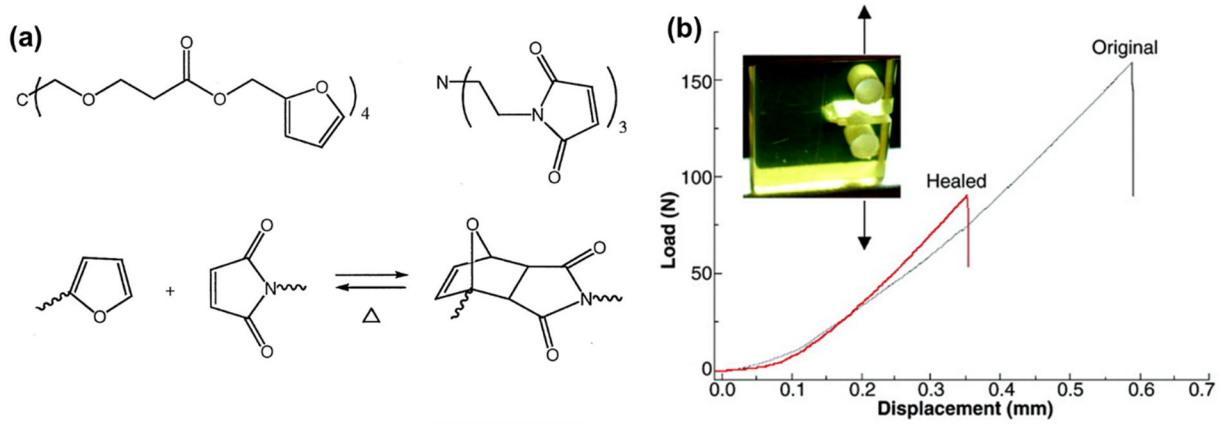

Figure 2.7 (a) Schematic of coss-linked network through DA reaction and the equilibrium between the adduct and individual components (b) Representative self-healing after heat treatment (reprinted from reference 36).

Other dynamic covalent interactions such as acylhdrazones[41-43], imine exchange[44] have also been applied to prepare self-healing or malleable systems. In these cases, an acid catalyst and residual water is required to facilitate the exchange reaction. An interesting example that does not

need water and instead utilizes the steric bulk to control the dynamic of urea dissociation is also reported recently.[45]

Anionic siloxane exchange reaction is another conceptually interesting system that has been recently utilized by Zheng *et al.* to generate a reconfigurable covalent network that exhibited malleability and self-healing properties. After polymerization shown in Scheme 2.1, some reactive tetramethylammonium dimethylsilanolate group remains at the chain end which are reportedly stable at ambient environment (no reaction with water or CO_2) and can react with the polymer chain and reshuffle the Si-O bonds for self-healing.[46]

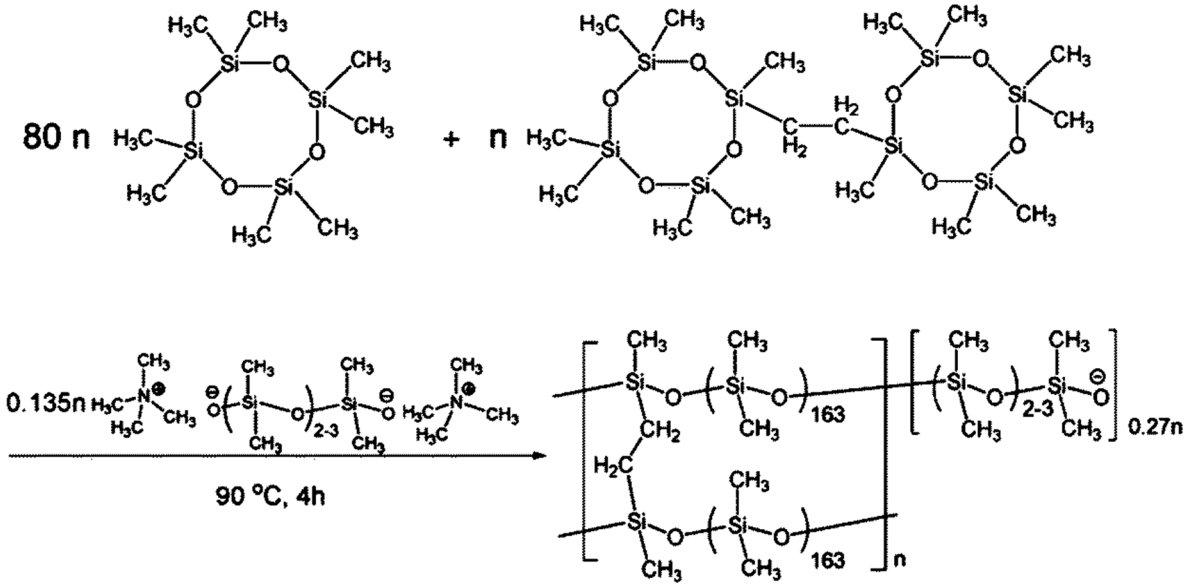

Scheme 2.1 Prepartion of "living polymer network" with anionoic chain ends capable of reshuffling Si-O bonds (reprinted from reference 46).

Stronger (and less labile) covalent bonds can be used as dynamic interaction in the presence of suitable catalysts. In a pioneering example from Leibler and coworker, an epoxy thermoset was

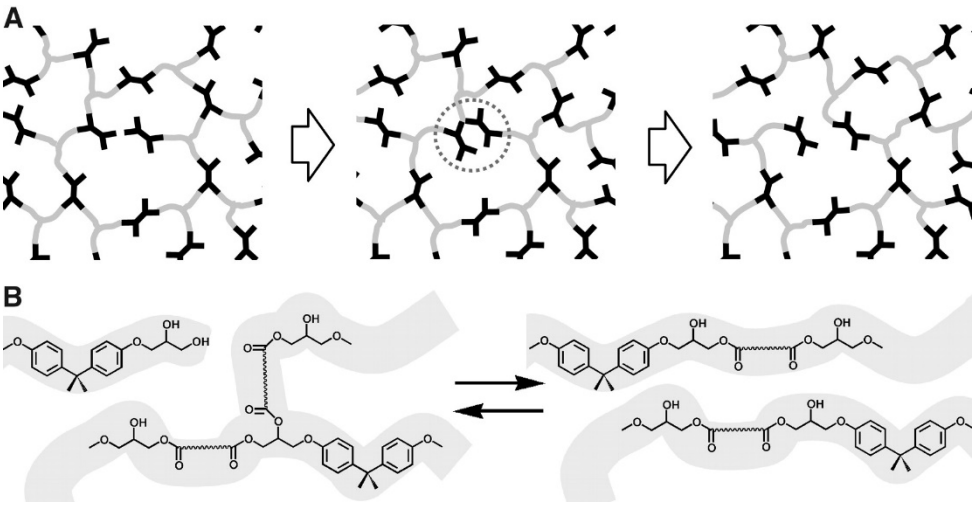

Figure 2.8 Schematic of network topological rearrangement (a) and the transesterification exchange process in hydroxy-ester networks (reprinted from reference 48).

synthesized with introduction of ester groups in the polymer backbones while maintaining a number of dangling unreacted hydroxyl groups through stoichiometric control. A Lewis acid (zinc acetate) was then used to catalyze the transesterification reaction as a route to reconfigure the covalent network. This dynamic transesterification at temperatures higher than 100 °C has been shown to impart both self-healing ability and malleability to this otherwise stationary network (Figure 2.8).[47,48]

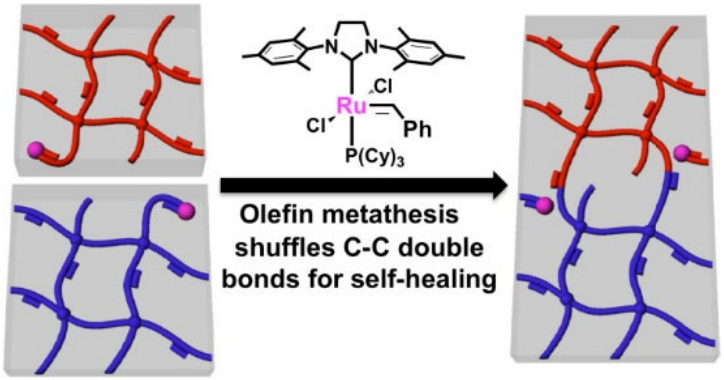

Figure 2.9 Concept of metathesis mediated shuffling of C=C for self-healing (reprinted from reference 49).

Inspired by this work and with the aim of expanding this concept to commodity olefin containing polymers and addressing the high temperature requirements, Guan and coworkers, incorporated Grubbs metathesis catalyst (G2) in a covalently cross-linked network of polybutadiene. G2 mediated reshuffling of double bonds imparts both malleability and self-healing abilities to these networks even at sub ambient temperatures (Figure 2.9).[49]

The repertoire of dynamic covalent interactions has not been exhausted and represents a great opportunity for new developments in this field.[50] To name few, boranic esters exchange[51,52], and catalyzed amide metathesis[53] may be the future stars of self-heling covalent systems.

2.1.4 Self-healing systems based on supramolecular (non-covalent) interactions

The transient nature of supramolecular interactions, reversibility of association, and the high stability of dissociated intermediates are the perfect combination for design of successful self-healing systems. In comparison with covalent interactions discussed in the previous section, supra molecular motifs have explored my actively in self-healing polymers due to the ease of incorporation and facile tuning of kinetic and thermodynamic parameters. Numerous examples of self-healing systems that utilize metal-ligand[54,55], host-guest[56,57], π–π stacking[58-60], ionic[61-63], hydrogen bonds[64-66] and etc. are now reported. It will be outside the scope of this short introduction to review every single one of them but they have been recently reviewed at length.[15,67]

Given the lower strength of these interaction compared to covalent bonds, it is not surprising that the mechanical damage unravels these transient interactions first. As shown in the Figure 2.10, mechanical damage will leave unassociated dangling chain ends on either side of the damage interface. It is however slightly surprising that these sticky ends have a considerably long half-life and can recombine with a partner across the cut interface if the two surfaces are brought back in a reasonable time frame.

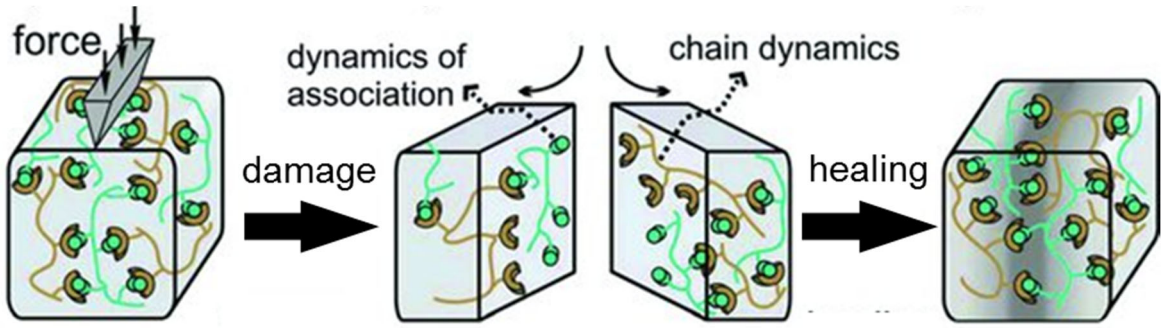

Figure 2.10 Schematic of self-healing by utilizing non-covalent interactions (reprinted from reference 67).

The extended half-life of these interactions can be attributed to slower dynamics of polymer chains in the solid state. It can be expected that association of these dangling chain ends, has to be accompanied by polymer rearrangement and configuration change to bring the dangling chains in the close proximity.

A pioneering study by Leibler and coworkers demonstrated the feasibility of using a network of hydrogen bonds to design self-healing elastomers. The load bearing and creep-resistance of this material under low loading is of particular interest and demonstrates the collective power of a pervasive network of these weak interactions.[64]

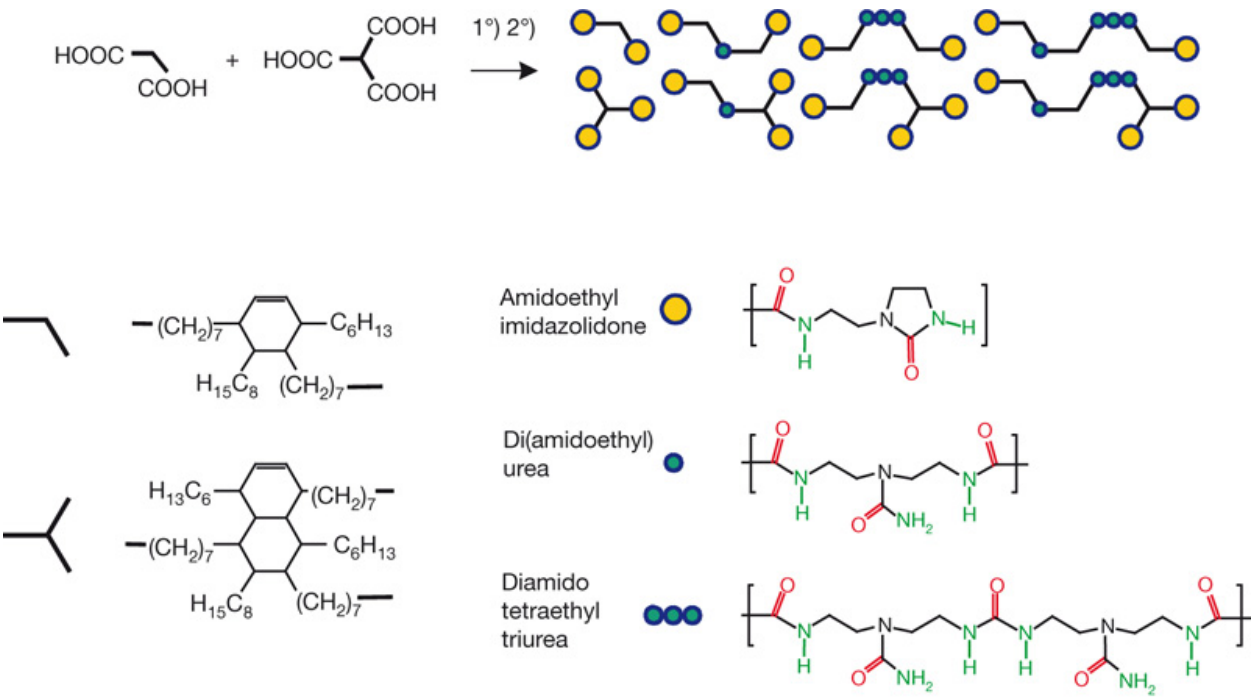

Figure 2.11 Mixture of fatty acids is functionalized with amide and urea containing motifs. The oligomeric mixture can be processed into a self-healing rubbber (reprinted from reference 64).

Despite this important demonstration, the inverse relationship between the strength and the dynamics of association has remained a perplexing dilemma for this field. Transient interactions with fast dynamics are preferred for self-healing applications but these interactions are generally weak and result in materials with compromised mechanical properties.

Guan and coworkers have demonstrated one possible solution to this problem by utilizing a multi-phase polymeric system where the glassy domain (responsible for mechanical strength) are embedded in a matrix of H-bonding monomer with higher mobility.[68] A brush copolymer was synthesized by growing polymer chain containing a hydrogen bonding unit from a polystyrene backbone (Figure 2.12). Due to the differences in the interaction parameters of backbone and brush, the polymer system phase separated in bulk state form nano-domains of polystyrene (PS) embedded in a matrix of H-bonding polymer. It was hypothesized that the mechanical damage will primarily unravel the hydrogen bonding network and self-healing will be achieved when the damaged interface are brought back together. Incorporation of polystyrene domains resulted in

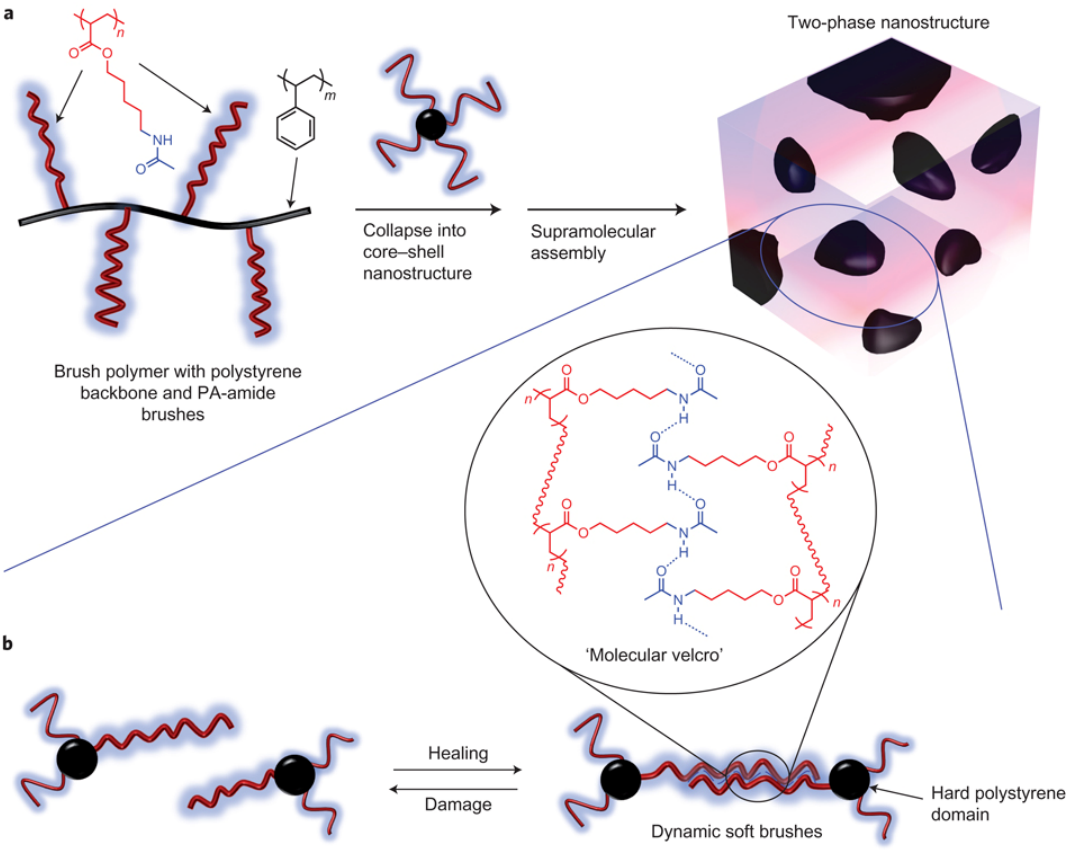

Figure 2.12 The multiphase H-bonding brush polymer. Polystyrene domain contribute to mechanical strength while the dynamic H-bond domain in the brush are responsible for self-healing (reprinted from reference 68).

emergence of thermoplastic elastomer mechanical properties and contributed significantly to the improvement of Young's modulus over the previous reports (up to 35 MPa cf. with 1 MPa in reference 63). As we will see later in this chapter, this strategy is general and compatible with other dynamic motifs such as M–L interactions.

H-bond motif has been incorporated in numerous different systems but in principle suffers from an inherent susceptibility to an unwanted competition from residual humidity in the environment. In addition, fine-tuning of their dynamic properties is non-trivial. For example, the self-healing experiment in the previous system was conducted in a desiccator with 0% relative humidity. Furthermore, despite achieving a nice control over the static mechanical properties by simply adjusting the volume fraction of polystyrene, no attempts were made to control or tune the dynamic properties of these materials.

2.1.5 M–L interaction as tunable dynamic motif

As we saw previously, covalent system generally offer stronger interactions (leading to improved mechanical properties) albeit at the sacrifice of the dynamics (which hampers the autonomous self-healing). Metal–ligand (M–L) complexes can be considered as a bridge connecting the covalent and non-covalent interaction.[69] They are promising candidates as dynamic healing motifs because the thermodynamic and kinetic parameters of M–L complexes are tunable over a broad range, which could potentially yield materials with highly tunable mechanical properties.[70,71] Furthermore, M–L interactions should be less sensitive to moisture than hydrogen bonds, which would be advantageous for practical applications.

Several self-healing gels and solid materials have been reported by using reversible metal-ligand interactions.[54,55,72-75] While there are many reports of using dynamic M–L interactions in

self-healing gels, the dynamicity of these interactions are overlooked in the solid state. For self-healing solid materials, the most commonly utilized M–L systems involve multidentate nitrogen based aromatic ligands, such as terpyridines.[54,55]

A pioneering study is conducted by Rowan, Wader and coworkers where a telechelic polymer was end capped with 2,6-bis(1′-methylbenzimidazolyl)pyridine (Mebip) ligands. Zinc or lanthanum ions were then used to cross-link this pre-polymer to form a metallosupramolecular polymer. Mechanical samples prepared from this supramolecular polymer exhibited self-healing

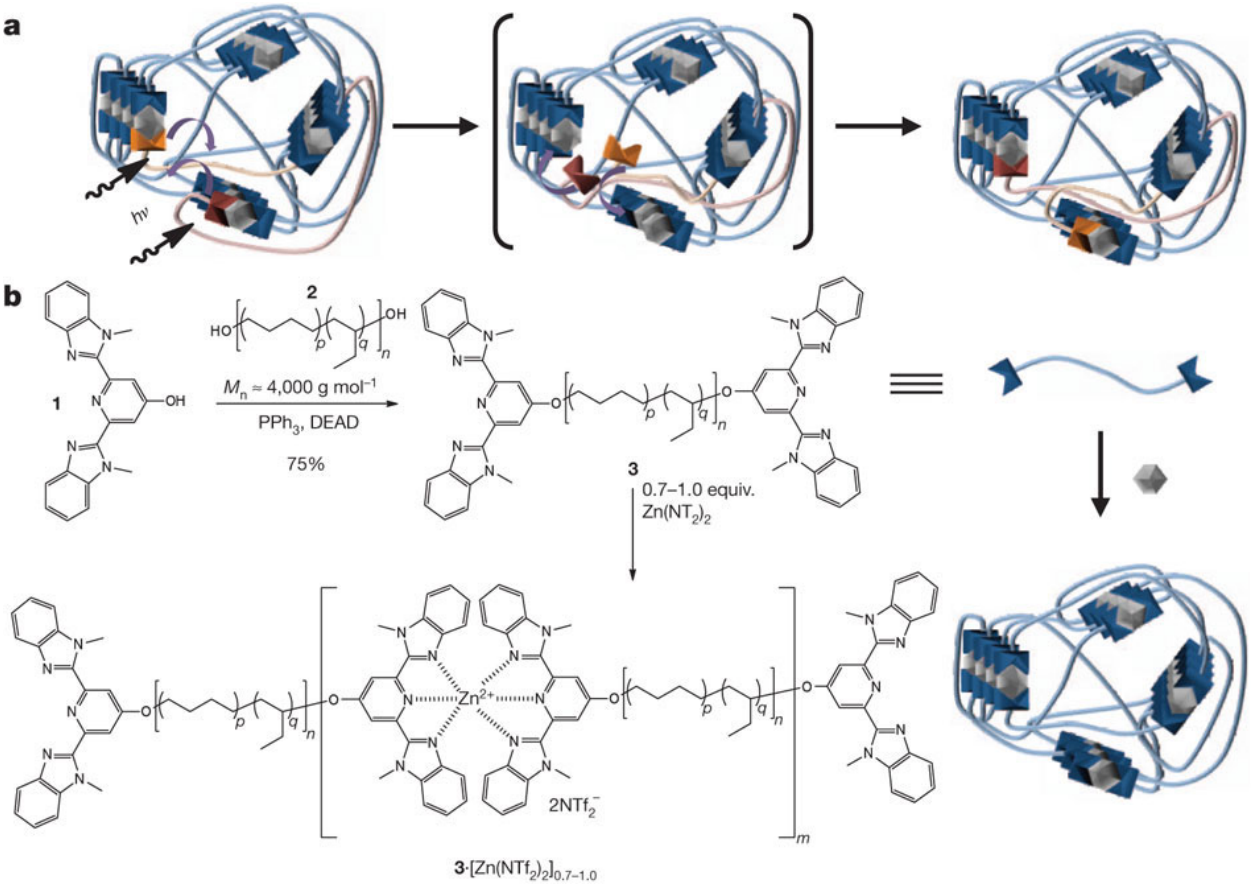

Figure 2.13 Telechelic polymers functionalized with Mebip ligand and cross-linked with zinc. Photothermal conversion results in melting of M–L clusters and self-healing (reprinted from reference 54).

under UV irradiation by a photothermal welding which melted the M–L clusters and improved the polymer mobility.[54]

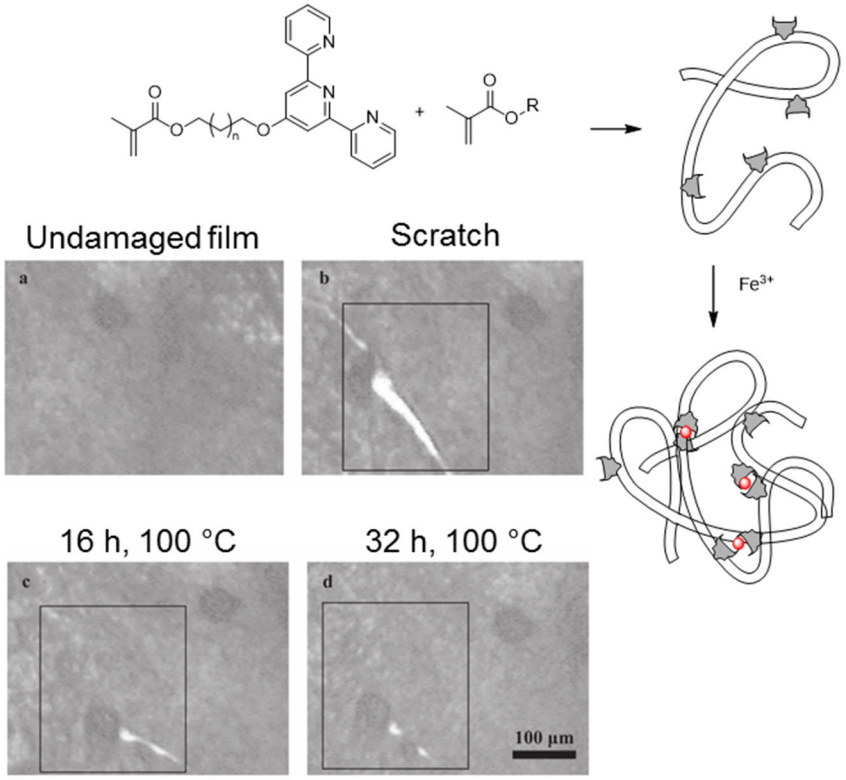

Figure 2.14 Schematic of iron cross-linked network and the observed self-healing of a small scratch (adapted and reprinted from reference 55).

In a related study by Bode *et al.,* a methacrylate polymer chain (methyl, butyl and lauryl) was functionalized with terpyridine ligands and was subsequently cross-linked with Fe^{3+} ions. It is shown that the self-healing ability is associated with the presence of M–L clusters when the polymer chain flexibility permits their formation. It is also demonstrated that these materials can self-heal small scratches with heat stimuli. In subsequent works, the healing abilities is improved by incorporation of weaker M–L interactions but no detailed comparison between mechanical properties is provided.[55,76,77]

These systems have relatively high M–L association constants and tend to phase separate with the M-L complexes residing in hard glassy or crystalline domains. Due to the high association

constants and the fact that the M–L complexes either form ionic clusters or reside in the hard, non-dynamic domains, external energy such as heat[55] or light[54] must be required to reversibly dissociate the M-L complexes to induce self-healing.

2.2 Design of self-healing M–L polymer

To realize a self-healing M–L polymer, we decided to choose a highly dynamic M–L interaction, Zn^{2+}-imidazole, as the healing motif. Compared to the previously utilized multidentate ligands, imidazole has a relatively small binding constant to metal ions and its M–L complexes have fast exchange kinetics.[78] In particular, imidazole–Zn^{2+} interactions are ubiquitous in biological systems, where the ligand exchange is known to have fast dynamics.[79] To combine good mechanical properties with self-healing capability under ambient conditions, we designed a microphase-separated soft/hard two-phase polymer system with the M–L complexes strategically embedded in the soft matrix with low glass transition temperature (T_g) (Figure 2.15).

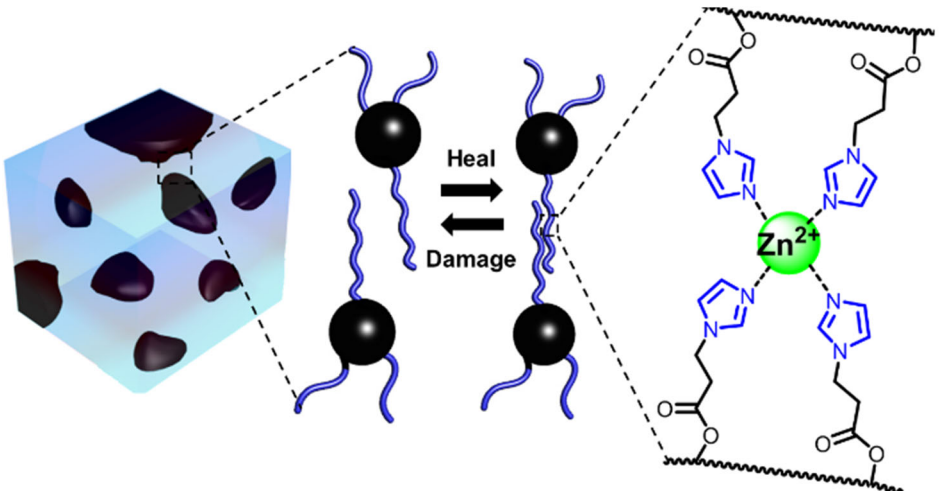

Figure 2.15 Design concept for the multiphasic self-healing materials using metal-ligand as dynamic motif.

Following our previous design of a self-healing hydrogen-bonding polymer,[68] we chose a brush polymer architecture to demonstrate our two-phase, M–L system for self-healing under ambient conditions. Specifically, a glassy polystyrene (PS) was used as the backbone, onto which multiple imidazole-containing brushes were grown. Addition of Zn^{2+} salts to the brush polymer solution induced complexation with the imidazole moieties. Upon drying, the system microphase separated into two phases with the hard PS domain contributing to the stiffness and modulus of the resulting material. Importantly, the dynamic Zn^{2+}-imidazole complexes reside in the soft matrix (Figure 2.15). With a combination of fast ligand exchange kinetics for Zn^{2+}-imidazole complex and the dynamics of the soft polymer matrix, we envision that this system can self-heal in the solid state with minimal intervention.

2.3 Synthesis of imidazole-containing brush polymers

The synthesis of the imidazole-containing brush polymers, **ICP**s, is described in Scheme 2.2. The imidazole-containing acrylate monomer, **IMZa** (**2**), was synthesized via Michael addition of imidazole to 1,4-butanediol diacrylate (Scheme 2.2a). The spacer between the imidazole ring and the acrylate moiety is necessary for lowering the glass transition temperature and enhancing the dynamics of the ligands in the soft polymer matrix (T_g of copolymer ~ -38 °C) before the addition of metal (Figure 2.35).

Reversible addition-fragmentation chain transfer polymerization (RAFT) was chosen to synthesize our brush copolymers.[80] The PS macro-chain transfer agent (**macro-CTA**) was synthesized by free radical copolymerization of styrene and varied amount of 4-vinylbenzyl chloride to obtain PS backbone with controlled amount of benzyl chloride incorporation (Scheme 2.2b). This polymer was further functionalized by treating with *in situ* generated potassium ethyl

trithiocarbonate salt to introduce RAFT chain transfer sites.[81] Two PS **macro-CTAs** were synthesized with the PS backbone of ~ 140 repeating units and the density of the RAFT chain transfer group of 5% and 10%, respectively. These **macro-CTAs** were subsequently used to initiate RAFT copolymerization of n-butyl acrylate (BA) and the custom-made monomer, **IMZa** (**2**), to grow multiple brushes from the PS backbone. The brush degree of polymerization was controlled at ~ 180 repeating units and the imidazole mole percent at 25% and 35%, respectively. To avoid the complication of hydrogen bonding in self-healing studies, we decided to use the N-substituted imidazole and BA to form our **ICP**s. For comparison, two control polymers were also synthesized: **Control-1** is a brush polymer without any imidazole (i.e., only BA homopolymer on the brushes). **Control-2** does not have the brush architecture; instead, it is a linear copolymer of

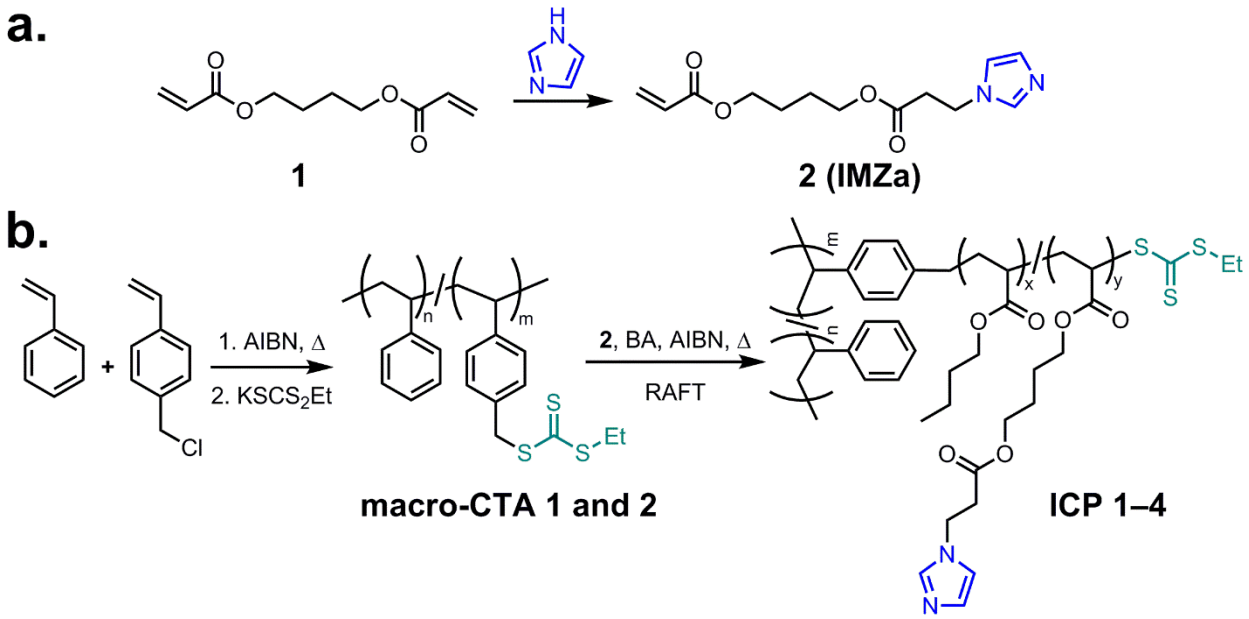

Scheme 2.2 Synthesis of the imidazole-containing monomer and brush copolymers **a.** Synthesis of imidazole acrylate monomer, **IMZa (2)**. **b.** Synthesis of **ICP**s. Styrene was first copolymerized with 4-vinylbenzyl chloride via free-radical polymerization, followed by post-functionalization of benzyl chloride to form macro-CTAs. **ICP**s were synthesized by growing copolymer brushes of BA and **IMZa** using RAFT controlled radical polymerization technique.

BA and **IMZa**. The composition of all **ICP**s and control samples are summarized in Table 2.1. The synthesis and full characterizations of both the monomer **2** and all polymers are detailed in the experimental section.

Table 2.1 Molecular compositions of **ICP 1–4** and control samples

Sample	Backbone repeat units*	CTA sites[a]	Brush repeat units[a]	mol % of IMZa[a,b]
ICP-1	140	14	180	25
ICP-2	140	14	170	33
ICP-3	139	7	167	25
ICP-4	139	7	160	34
Control-1	140	14	190	0
Control-2	-	-	170	35

* Calculated from size exclusion chromatography (SEC) using polystyrene standards in THF. [a]Estimated from ^{1}H NMR. [b] mol%, calculated from $N_{IMZa}/(N_{IMZa}+N_{BA}) \times 100$, where N is the number of repeat units for each monomer.

For M–L complexation, zinc di[bis(trifluoromethylsul-fonyl)imide], $Zn(NTf_2)_2$, was chosen as the Zn^{2+} source for its good solubility and thermal stability, as well as the high mobility of the counterion, NTf_2^-, in the solid state. With the delocalized charge, bulky size and unique shape, NTf_2^- counter ion disfavors clustering of charged species in the solid state.[82,83] Without the addition of metal ions, the **ICP**s are viscous oils with no appreciable mechanical properties. Upon addition of $Zn(NTf_2)_2$ and removal of solvent, they form robust non-tacky elastomers with tunable

mechanical properties. Thermogravimetric analysis (TGA) confirmed the complete removal of solvent (Figure 2.36).

2.4 Phase morphology characterization

The phase morphology of **ICP**s–$Zn(NTf_2)_2$ samples in solid state was investigated by small angle X-ray scattering (SAXS) and transmission electron microscopy (TEM). As shown in Figure 2.16a for **ICP-4** (L/Zn=4.0), an intense broad peak in the SAXS spectrum indicates the presence of well-defined spherical form-factor domains with inter-domain spacing ranging between 7-20 nm. In contrast, **Control-2**, which does not contain PS backbone, did not show any scattering peak, suggesting that the imidazole-$Zn(NTf_2)_2$ complex does not form large ionic clusters in solid state.[83]

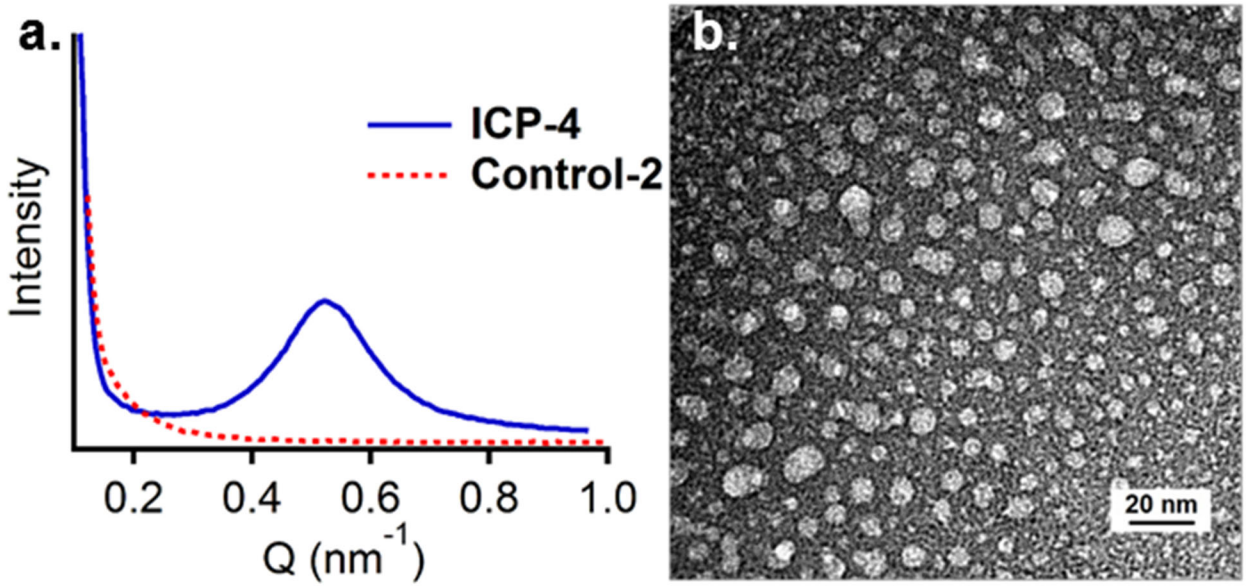

Figure 2.16 Morphological characterization of **ICP**s-$Zn(NTf_2)_2$ samples. **a.** Small angle X-ray scatterings (SAXS) supports the micro-phase separated morphology with inter-domain spacing between 7-20 nm for **ICP-4** (L/M = 4.0). The control sample (**Control-2**) does not show any scattering peaks. b. TEM imaging confirms a microphase-separated structure with a spherical PS core dispersed in a soft BA/**IMZa** matrix, which was selectively stained with uranyl acetate.

TEM provides further evidence for a two-phase morphology (Figure 2.16b). Consistent with the SAXS data, spherical PS nanodomains with size ~10 nm are dispersed in a continuous matrix of soft brushes containing dynamic zinc-imidazole complexes.

2.5 Mechanical properties of ICPs

The designed M–L multiphase polymers show characteristic thermoplastic elastomer (TPE) behavior with tunable mechanical properties by controlling several molecular parameters (Figure 2.17a). Consistent with our multiphase design strategy, the PS hard phase contributes to the high Young's modulus and TPE-like behavior. For comparison, the **Control-2** samples, which do not contain PS backbones, have lower Young's modulus and do not show the TPE behavior (Figure 2.37). The mechanical performance can be tuned by adjusting three molecular parameters: the percent incorporation of **IMZa**, the ratio of imidazole to zinc (L/Zn), and the volume fraction of hard phase or brush density. For example, increasing the **IMZa** incorporation from 25% (Figure 2.17a, green curve) to 35% (Figure 2.17a, black curve) increases the yield strength, tensile strength and extensibility. Decreasing the L/Zn from 4.5 (Figure 2.17a, black curve) to 4.0 (Figure 2.17a, blue curve) by adding more Zn^{2+} also significantly improves mechanical properties of **ICP**s by increasing the cross-linking density of polymer samples. Finally, consistent with our previous report,[68] increasing the volume fraction of the PS hard phase by reducing the brush density from 10% (Figure 2.17a, blue curve) to 5% (Figure 2.17a, red curve) resulted in an increase in Young's modulus, yield strength and tensile strength while decreasing the extensibility of material. A complete summary of the mechanical properties of **ICP**s–$Zn(NTf_2)_2$ and **Control-2** polymers with L/Zn ratio of 4.0 and 4.5 is included in the Table 2.5. Without any imidazole moiety, **Control-1**

only formed viscous oil and its mechanical properties remained almost unchanged with the addition of $Zn(NTf_2)_2$, as shown by oscillatory rheology (Figure 2.38).

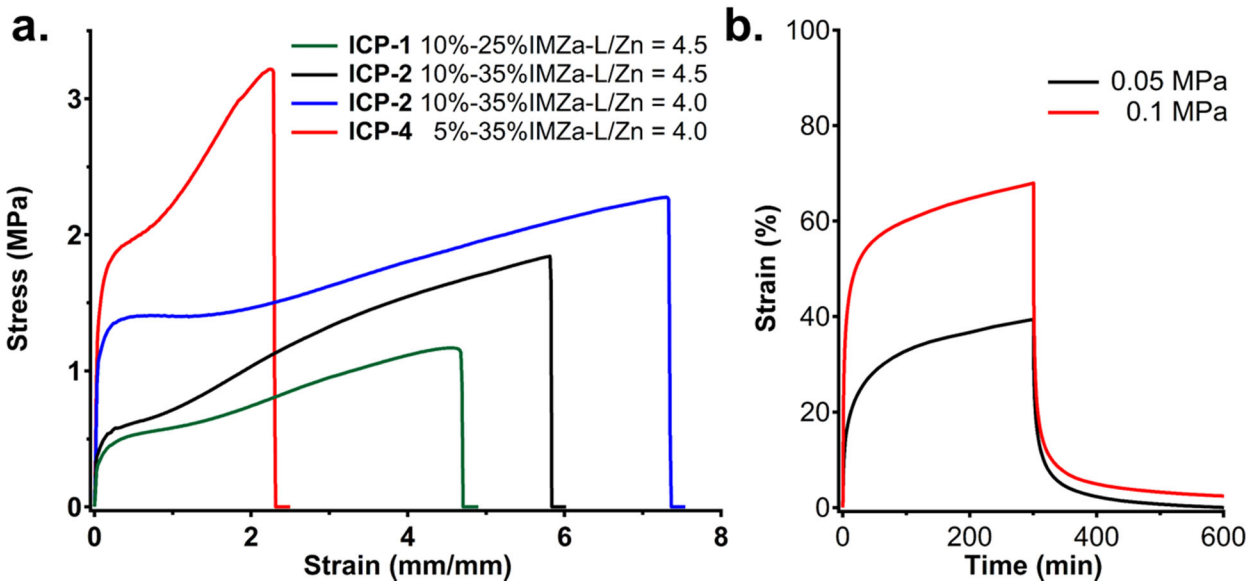

Figure 2.17 a. Static tensile tests of **ICP**s-$Zn(NTf_2)_2$ samples. It shows the TPE-like stress–strain behavior, and the mechanical properties can be tuned over a wide range by changing three molecular parameters, the **IMZa** incorporation percentage, the ratio of imidazole to zinc (L/Zn), and the brush density. **b.** Creep-recovery experiments showing **ICP-4**-$Zn(NTf_2)_2$, with L/Zn =4.0 after application of constant stress for 300 minutes followed by relaxation of stress.

The M–L multiphase polymers also exhibit reasonable creep-resistance despite the fact the soft polymer matrix is only held together by transient dynamic M-L cross-links (Figure 2.17b). At 24 °C a stress of 5×10^4 Pa applied to **ICP-4** with L/Zn ratio of 4.0 for 300 minutes, resulted in the final strain of 39%, which increased at a characteristic rate of 1.8% per hour. After releasing the applied stress, the sample completely recovered its dimension with negligible residual strain (<1%). Application of a higher stress (1.0×10^5 Pa) for the same time duration led to a strain of 70% with an incremental increase of 2.2% per hour. Release of stress left a residual strain of less

than 5%. As expected, an elastomeric network that is held together purely by transient dynamic bonds will not be able to maintain static high load indefinitely.

With the dynamic Zn^{2+}–imidazole complexes residing in the dynamic soft phase of a two-phase polymer system, our M–L system showed excellent self-healing property in the solid state. The **ICP-2** and **ICP-4** with L/Zn of 4.0 were chosen as representative samples for self-healing test because of their better mechanical properties. Samples used in self-healing studies were annealed by slowly cooling the samples from 100 °C to room temperature over 12 hours to minimize any residual stress during compression molding. Following a literature protocol,[54] we then made a well-defined cut to the depth of 70-90% of the sample thickness. The two cut interfaces were brought back together for 1 min and allowed to heal under ambient conditions (room temperature in air) without any treatment.

The damaged samples showed excellent healing with time. For all healing times, stress–strain curves show characteristic TPE behavior and follow closely the shapes of the original uncut samples (Figure 2.18). Remarkably, the damaged samples not only recovered the Young's modulus and yield stress quickly, but also recovered toughness almost quantitatively in 3 h. In contrast, previous M–L systems utilizing terpyridine-metal interactions required light-converted local heat[54], relatively long healing time under heat[55], or solvent exposure to induce healing.[74] The observed efficient healing proves our hypothesis that incorporation of pervasive dynamic M–L interactions in the soft-phase of a multiphase polymer can result in mechanically robust materials with efficient self-healing under ambient conditions. The healing efficiencies of metal–ligand system even surpasses our previous reported hydrogen bonding system.[68] Notably, our M–L polymers heal efficiently at ambient condition without showing sensitivity to moisture, which is

advantageous to hydrogen-bonding based self-healing polymers that are normally more sensitive to moisture.

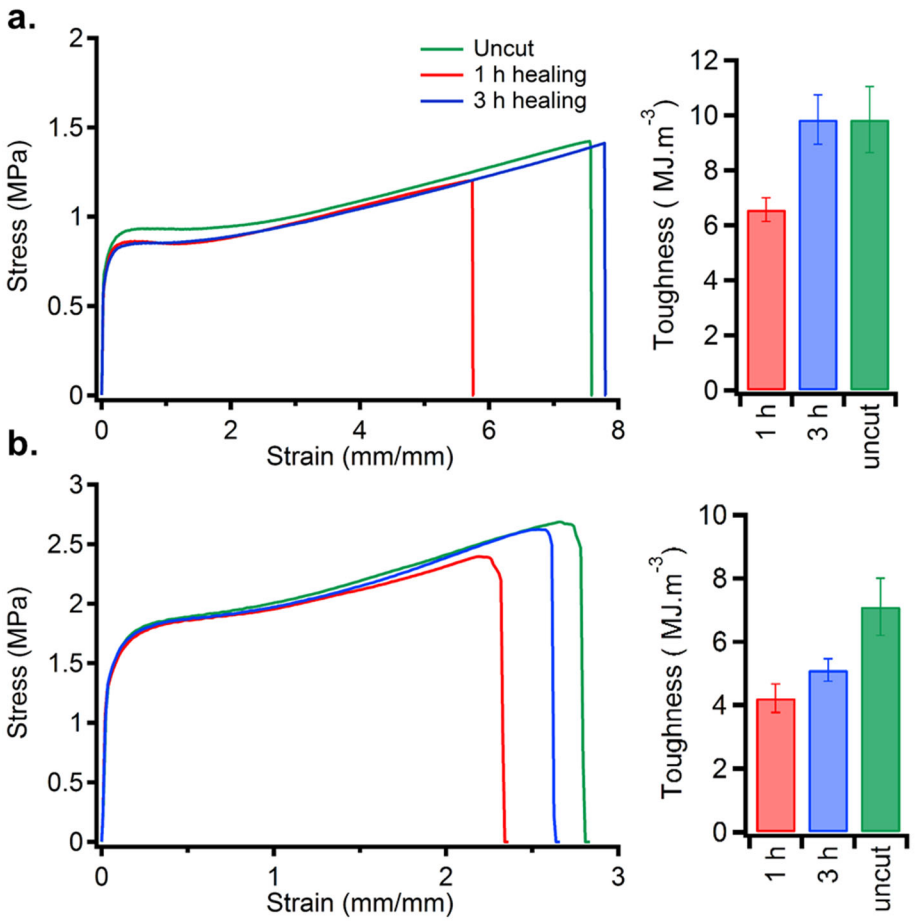

Figure 2.18 Self-healing tests for ICPs-Zn$(NTf_2)_2$ samples at room temperature with ambient humidity. **a.** Stress-strain curve for ICP-2 L/Zn=4.0. **b.** Stress-strain curve for **ICP-4** L/Zn=4.0. The bar graph summarizes the toughness recovery for each sample. Error bars are standard deviation for three measurements.

2.6 Summary of self-healing

In summary, we have demonstrated a new self-healing multiphase polymer by strategically programming a pervasive network of dynamic metal-ligand (zinc–imidazole) interactions in the

soft matrix of a hard/soft two-phase brush copolymer system. The mechanical and dynamic properties of the materials can be conveniently tuned by varying several molecular parameters (such as the backbone composition and degree of polymerization, the brush density, and the ligand density) as well as the L/M ratio. Our multiphase M–L polymers show excellent self-healing properties under ambient conditions with minimal intervention. Compared to hydrogen-bonding based self-healing systems, the M–L system may offer advantages of being less moisture sensitive and having a broad range of tunable thermodynamics and kinetics. Several other molecular parameters, such as the identity of the metal ion, counter-ions, and ligand can be varied to further improve the mechanical and self-healing properties of this new class of materials.

2.7 Toward correlation of the mechanical properties with small molecule properties

2.7.1 Introduction

Understanding the chemical origin of the mechanical properties in biological materials is a promising route toward synthesis of smart bioinspired materials with advanced properties. Pioneering work on understanding the basis of silk exceptional mechanical properties[84] or the mussel ubiquitous attachment[85] to hostile environment is just few examples of such inspirations. Correlation of the bulk mechanical properties to the small-molecule provides a unique insight into the contribution of these interactions and paves the road toward *de novo* design of materials with advanced properties.[70,86]

Metal-Ligand (M–L) interactions are a promising candidate for modular tuning of the mechanical and dynamic properties of materials across a broad range by changing the metal and

ligand components.[70,71] The reversibility of M–L interactions is utilized to increase toughness[87] and impart advanced properties such as self-healing into synthetic materials.[54]

Our design also enables us to control the imidazole to metal ratio in an exquisite manner allowing for the comparison of the variation in the mechanical property associated with varying the L/M ratio. Such analysis is missing from many other reports in the literature. We observed sharp transition of mechanical properties and stiffening of the material in the case of copper and zinc which is reminiscent of behavior observed in rag worm jaw.[88,89]

2.7.2 Synthesis of Linear Imidazole Containing Polymers (L-ICP)

A linear imidazole containing copolymer (**L-ICP**) was synthesized by copolymerization of BA and **IMZa** in the presence of small molecule chain transfer agent (Scheme 2.3). This linear copolymer, without the PS backbone was used in the solution and the polymer melt rheology experiments for two reasons. Firstly, the aggregation of PS domains in **ICP** can result in rheological complexities and secondly, the absence of PS domains in **L-ICP** improved the solubility and the accessible range of added metal salts in our studies.

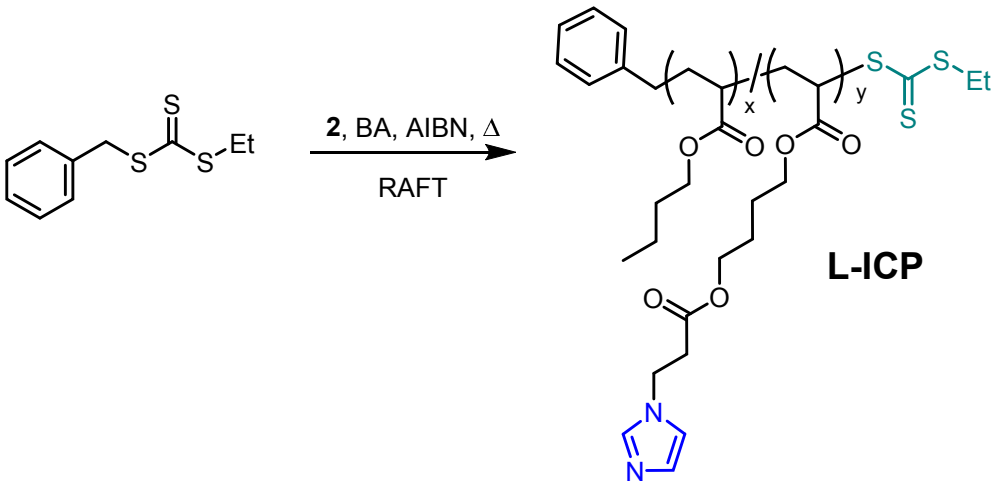

Scheme 2.3 Synthesis of **L-ICP** polymer using RAFT polymerization.

2.7.3 Metal incorporation

After determination of the imidazole content of each polymer sample using a combination of ^{1}H NMR and SEC analysis, a stock solution of polymers were prepared in CH_3CN. Bis(trifluoromethane)sulfonimide salts, $M(NTf_2)_2$ where M is cobalt, copper, nickel, and zinc, were dissolved in CH_3CN and added incrementally to the polymer solutions. A precipitate is usually formed immediately upon the addition of the metal salt which was later dissolved after brief agitation on a vortex mixer. After complete addition of metal, the clear colored solutions were poured into a Teflon dish. The solvent was removed by heating the samples in a vacuum oven overnight. The resulting coordinative cross-linked polymers were scrapped or collected from the Teflon dish and were tested using the protocols explained below.

The samples composition is described throughout this study using the following nomenclature: Polymer–Metal with L/M ratio. For example, **L-ICP–Zn** with L/Zn=4 refers to the linear imidazole containing polymer that is cross-linked with $Zn(NTf_2)_2$ at the ratio of imidazole to zinc of 4.

2.7.4 Mechanical characterization techniques and methods

2.7.4.1 Rheological characterization of polymer solutions

Rheology data were collected on an AR-G2 rheometer from TA Instruments using a cone-plate geometry (steel, 40 mm diameter with an angle of 1.988°) equipped with a Peltier temperature control system. To minimize the evaporation of solvent and subsequent change in the polymer concentration, a solvent trap, filled with small amount of acetonitrile, was used and the experiments were conducted at 20 °C. Oscillatory data were collected at 25% strain while varying the frequency between 1-50 Hz and were processed with the commercial TRIOS software.

2.7.4.2 Rheological characterization of polymer melts

Rheology data were collected on an AR-G2 rheometer from TA Instruments using a parallel plate geometry (steel, 20 mm diameter, 500 μm gap) equipped with a Peltier temperature control system. In case of polymers cross-linked with cobalt and nickel salts, it was necessary to increase the temperature to 60 °C, to soften the sample, before lowering the plate to set gap. Temperature was reduced to 20 °C and the samples were allowed to equilibrate for 30 min at this temperature. At different temperatures (20-90 °C with increments of 10 °C), the oscillatory response was monitored at 0.1% strain while varying the frequency between 0.1-100 Hz. The rheological data was processed with commercial TRIOS software and shifted according to the time-temperature superposition principle (TTS).

2.7.4.3 Static tensile measurements

Samples were prepared by hot-pressing the resin into heated Teflon molds at 100 °C and allowing them to cool down to room temperature while maintaining the pressure (cooling time approximately 30 min). Average sample size was 15 mm × 7 mm × 2 mm (length, width, thickness). The mechanical properties of the copolymers were measured using an Instron 3365

machine in standard stress/strain experiments. The specimens were extended at 100 mm/min at room temperature. Each measurement was repeated at least three times. Young's modulus (E) was determined from the initial slope of the stress-strain curves.

2.7.5 Solution viscosity studies of L-ICP–M

In the absence of metals, **L-ICP** just formed viscous oil with no appreciable mechanical properties. Upon the addition of different transition metal salts, a noticeable difference in the mechanical properties of polymer solution and melt was observed. Two observations supports that these changes can be attributed to the M–L complexation. Firstly, the viscosity of **L-ICP** solutions in CH_3CN increases as more metal salt is added and secondly, the addition of 1-methyl imidazole to the solution of **L-ICP–M** results in decreased viscosity presumably through the competition of free ligands with the polymer bound imidazole moieties for binding to the metal center (Figure 2.39).

Despite this observed increase in the viscosity, none of the **L-ICPs** cross-linked with zinc, copper, cobalt, or nickel formed stable organogels even at low L/M ratio and instead behaved as a Newtonian fluid ($G' < G''$ with constant viscosity at different shear rates, see Figure 2.19 for an example). This observed behavior is also consistent with the reported lack of hydrogel formation in imidazole functionalized tetraPEG polymers and can be explained by relatively short life of cross-linking moieties.[78]

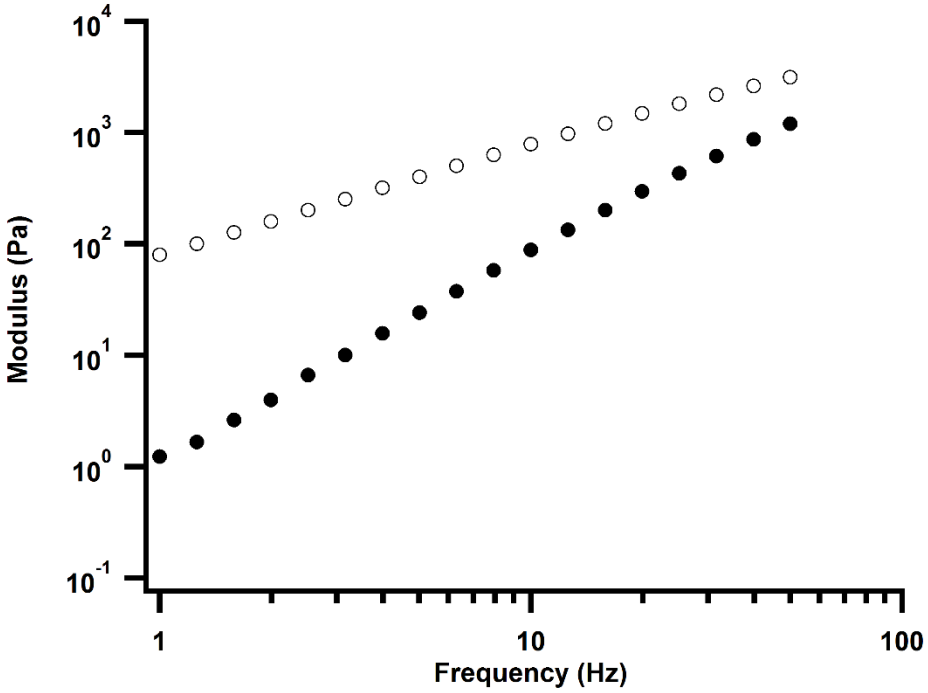

Figure 2.19 Representative rheological characterization of the solution of **L-ICP–M**. The storage (filled symbols) and loss (open symbols) modulus for **L-ICP–Zn** with L/Zn=4 is shown. None the solutions formed stable gels and behaved as Newtonian fluid across the experimental range (1-50 Hz).

Although it is possible to qualitatively correlate the observed trend in the dynamic viscosity of these solutions, η (Ni) > η (Co) > η (Zn), η (Cu), with the corresponding M–L dissociation time, τ (M) $\propto 1/k_d$ (M) , the competitive role of solvent cannot be fully excluded. We speculated that the competition of solvent (CH_3CN) and the stabilization of metal ions through coordination

of solvent molecules to empty sites can further decrease the M–L bond life and accelerate the ligand exchange reaction. It is unclear if the solvent effects are identical for all four metals here. Nonetheless, the removal of solvent can decrease the exchange rate of M–L complexes and reduce the complexities of solvent-assisted ligand exchange.

2.7.6 Rheological studies of L-ICP–M polymer melts

To gain a better understanding of the effect of M–L interactions on the dynamic properties of different **L-ICP–M**, we removed the solvent and investigated the viscoelastic response of resulting polymer melts under the shear stress. Generally there was a good agreement between the colors of each sample with the expected color of corresponding M–L complex. The only exception was copper which displayed a peculiar color change from deep blue (in solution) to green after solvent evaporation. This color remained persistent even after addition of more CH_3CN to dried samples and could be an indication for an unknown oxidation-reduction reaction. This transition is puzzling at this time because Cu^{3+} or Cu^{+} are not stable under regular air environment. Consistent with our previous work, in the absence collapsed polystyrene domains, all of the **L-ICP–M**s formed very weak materials. The physical state varied based on the identity of each metal and ranged from viscous oil-like (in the case of Zn^{2+} and Cu^{2+}) to soft solids with little creep resistance (in the case of Co^{2+} and Ni^{2+}).

L-ICP–M with L/M = 8.0 (M was cobalt, copper, nickel and zinc) were studied using rheology to probe the relaxation behavior of these materials under non equilibrium shear stress. As it is evident from the Figure 2.20 (and Figure 2.40), these materials display a broad range of dynamic responses under the shear stress due the kinetic of metal-imidazole exchange reaction. While it is not straightforward to develop constitutive relations for these materials, some qualitative assessment is useful in elucidating the molecular basis of macroscopic rheological

properties. In the low frequency regimes, all samples exhibited viscous (liquid like) behavior as illustrated by higher loss modulus (open circle) compared to storage modulus (filled circle). From low-to-intermediate frequencies, the power law dependence of loss and storage modulus seems to be conserved across **L-ICPs** cross-linked with different metals as $G'' \sim w^1$ in the low-frequency limit, $G' \sim w^2$ at low-to-intermediate frequencies, and G', G'' follow the same exponent at high frequencies (for Co^{2+}, Zn^{2+}, and Cu^{2+}). In the case of Ni, a cross-over between loss and storage modulus is observed at the reduced frequencies of ~1 Hz. After this cross-over frequency, the storage modulus levels off toward a plateau value and remains higher than loss modulus indicating an effective elastic response at high frequencies as the rate of applied shear force surpasses the inherent kinetic of Ni-imidazole exchange rates. Similar behavior is also emerged at the high limit of frequency range for cobalt.

Since no cross-over between loss and storage moduli is observed for Zn^{2+} or Cu^{2+} samples in the experimental range, we estimated the relaxation rate of each metal cross-linked sample by identifying a quasi-terminal relaxation mode where G' begins to intersect G''. Accordingly, it emerges that Cu^{2+} and Zn^{2+} have the fastest relaxation rates, which are followed by Co^{2+} and Ni^{2+} ($\omega \sim 10^{-0.5}\ s^{-1}$ for copper, $10^{-1}\ s^{-1}$ for zinc, $10^{-2}\ s^{-1}$ for cobalt, $10^{-3}\ s^{-1}$ for nickel). This trend generally agrees with previous reports of rate of ligand exchange from ditopic histidine ligands in the tetraPEG hydrogels (Ni < Co < Cu < Zn). In the hydrogel systems, zinc relaxation is reported to be faster than copper which is the opposite of our observation.

The fast rate of relaxation of these cross-linked materials in the polymer melt is surprising but it is still consistent with the inability of imidazole tetraPEG polymers and **L-ICPs** to form stable gels (due to the fast exchange dynamics) and the expedited self-healing behavior that we observed with the zinc cross-linked polymers previously.

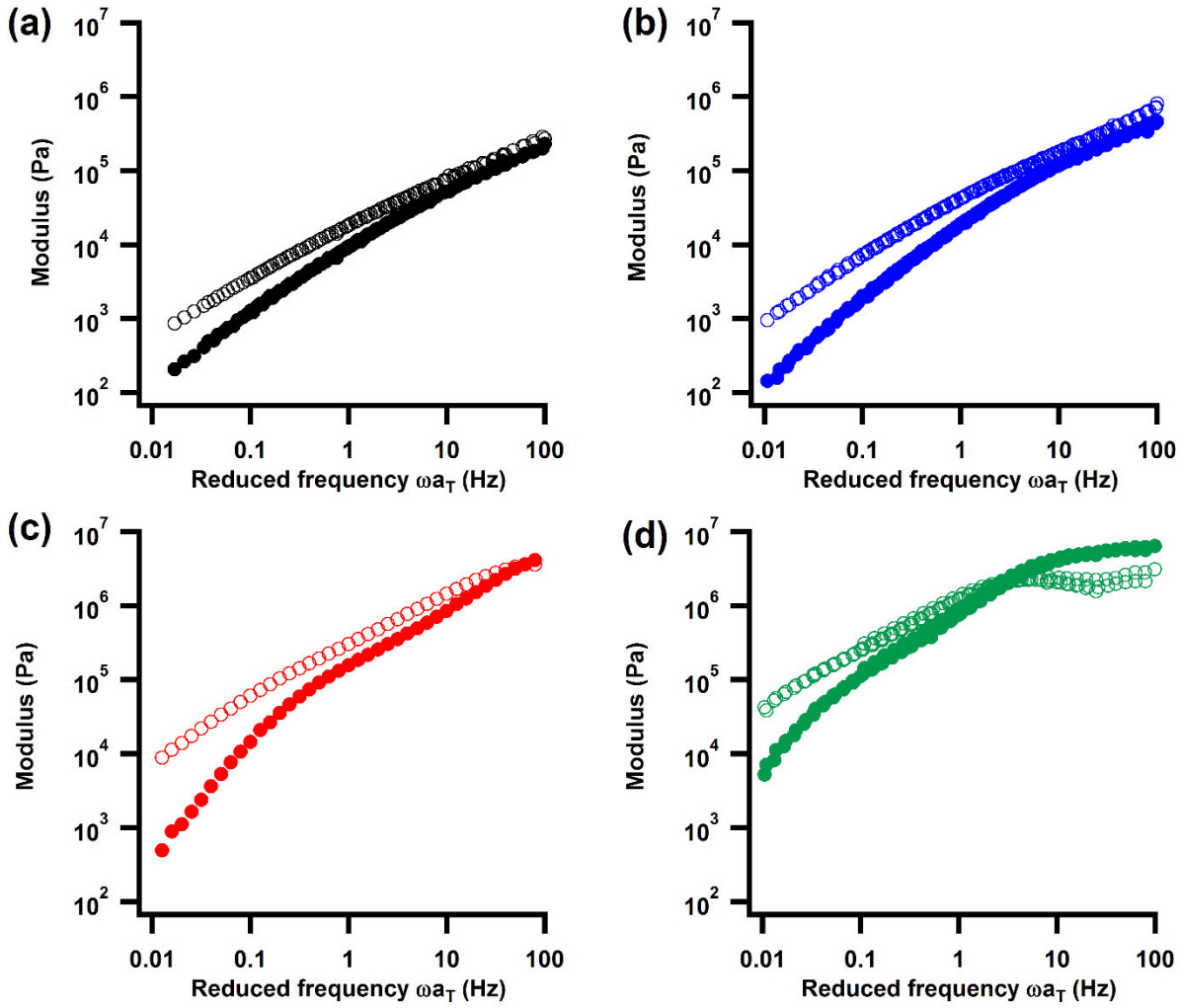

Figure 2.20 Rheological characterization of **L-ICP** cross-linked with different transition metals (L/M = 8). (a) **L-ICP–Zn** (b) **L-ICP–Cu (c) L-ICP–Co (d) L-ICP–Ni** Frequency sweep of polymer melt with storage (G') and Loss (G"), reported as filled and open symbols.

As it is evident from the rheology data, cross-linking of these low M_w polymer chains with transient imidazole-metal interaction is generally not sufficient to induce strong mechanical properties. Similarly, in biological systems these histidine rich sequences are incorporated in a

rigid collagenous network which contributes to the mechanical strength. To study the static mechanical properties, it was necessary to incorporate the PS domains by preparing samples from **ICPs**.

2.7.7 Static tensile properties of ICP–M and the dependence on L/M ratio

We anticipated that the order of relaxation rates will be preserved by switching from linear to brush architecture while the rate of polymer relaxation and dynamics might be affected by the polymer architecture and the cooperativity in metal binding.

This expectation was confirmed when nickel containing **ICP-2** samples (with slowest relaxation rate) only formed brittle and hard samples that were not processable by compression molding at medium-high temperatures. Instead, we have decided to continue the mechanical characterization of other metal containing polymers (Co, Cu, and Zn). To retain consistency, all Co and Cu samples were prepared from one polymer batch, while Zn data were collected from a different polymer batch, few representative samples were prepared from both batches and were compared to ensure that the differences in behavior is not due to differences in the polymer and can be ascribed to M/L dynamics.

We have previously demonstrated that increasing the zinc content (decreasing the L/Zn from 4.5 to 4.0) leads to higher Young's modulus and improved mechanical properties, higher ultimate strength and toughness. To further expand that study and investigate the effect of other metals, we studied samples cross-linked with Co^{2+} and Cu^{2+}, then systematically increased the metal content (decreased the L/M ratio) to investigate the mechanical properties

Some representative tensile data for each metal at different L/M ratio are shown in Figure 2.21. Before discussing the results in length, it is necessary to point out that we could only prepare

ICP-2 samples with L/M > $(L/M)_{lim}$, $(L/M)_{lim}$ was ~6 for Cobalt and ~4 for Copper. While it was sometimes possible to add very small amount of metal salt once we approached this ratio, frequently an insoluble polymer mass would be formed upon addition of more metal. This precipitation is undesirable because the resulting inhomogeneity perturbs the L/M ratio across different regions of the sample. We hypothesize that this observed $(L/M)_{lim}$ are not coincidental and are probably affected by the coordination preference of respective metal-imidazole complexes.

All samples were prepared using protocols described earlier and were tested in a static tensile test with the pulling rate of 100 mm/min. As shown in the Figure 2.21 and Table 2.2, similar to our previous report on zinc cross-linked samples, incorporation of more metals increases the Young's modulus and improves the mechanical properties of samples.

A careful comparison of different samples elucidates some interesting observations. Firstly, the Co^{2+} samples have higher Young's modulus than Cu^{2+} samples at similar L/M ratio. We attribute this to the preference of Co^{2+} to form complexes with six imidazole[90] with slower exchange kinetics (corroborated by relaxation times observed in the polymer melt rheology), which manifest itself through increased stiffness of these materials.

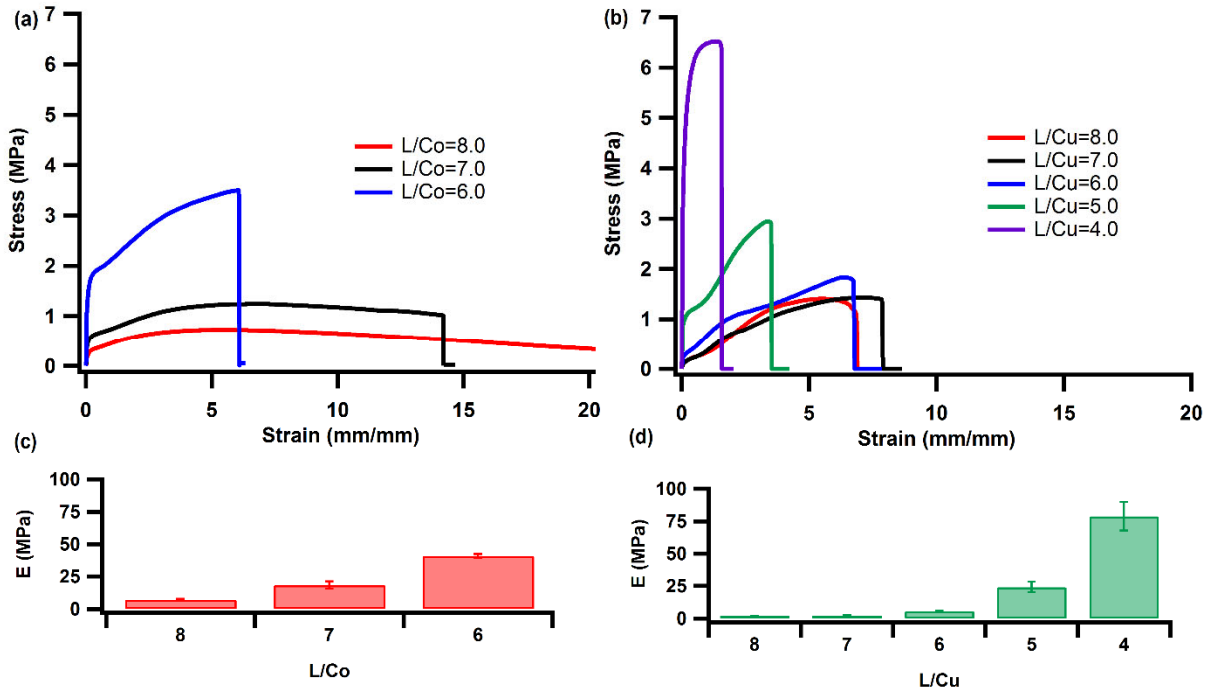

Figure 2.21 Static tensile tests of **ICP-2** cross-linked with different amount of (a) Co^{2+} and (b) Cu^{2+}. Dependence of the Young's modulus on the L/M ratio for each metal (c) Co^{2+} and (d) Cu^{2+}.

In addition to comparisons between samples with different metals at identical L/M ratio, one can also compare the transition of properties in each samples when L/M ratio is decreased gradually. The following symbol (→) is used to denote such transitions. By comparing **B-ICP-Co** samples in Figure 3a and 3c, it becomes clear that by changing the cobalt content (L/Co = 8 → 7 → 6), the mechanical properties of cobalt samples can be conveniently and gradually tuned across a broad range of extensibilities and strength. The trend is consistent with the gradual increase in the cross-linking density and a linear relationship is observed when the Young's modulus are plotted versus Co/L, as this ratio is proportional to the amount of metal and the cross-linking density.

Surprisingly, a sharper transition in the mechanical properties of copper samples was detected even though the general trend of increased stiffness (Young's modulus) and improved mechanical properties also holds true in the case of Cu^{2+} samples.

Table 2.2 Summary of mechanical properties for ICP–M cross-linked with Co^{2+} and Cu^{2+}.*

Metal	L/M	E (MPa)[a]	ε (%)[b]	σ (MPa)[c]	U_T ($MJ.m^{-3}$)[d]
Cobalt	8.0	6.9 ± 0.85	2020 ± 3§	0.66 ± 0.08	10.9 ± 1.1
	7.0	18.4 ± 2.9	1360 ± 490	1.4 ± 0.1	16.2 ± 1.6
	6.0	40.8 ± 1.5	608 ± 39	3.3 ± 0.1	16.3 ± 1.6
	5.8	37.9 ± 5.7	653 ± 62	3.2 ± 0.02	17.2 ± 2.0
Copper	8.0	1.9 ± 0.2	655 ± 27	1.3 ± 0.3	5.9 ± 1.2
	7.0	2.1 ± 0.3	838 ± 41	1.2 ± 0.2	7.1 ± 1.0
	6.0	5.5 ± 0.3	486 ± 192	1.7 ± 0.2	5.6 ± 2.8
	5.0	24.1 ± 4.0	406 ± 62	3.0 ± 0.6	8.5 ± 1.7
	4.0	78.7 ± 10.9	161 ± 46	6.1 ± 0.7	8.8 ± 3.2

*Strain rate=100 mm min^{-1}, 24 °C. [a] Young's modulus, calculated from the initial slope of stress-strain curves; [b] ultimate extensibility (mm/mm × 100); [c] ultimate tensile stress; [d] toughness, calculated by manually integrating the area under the stress-strain curve. § Samples did not break.

Firstly, in the case of Cu^{2+} the changes in the mechanical properties are more pronounced near the $(L/M)_{lim} \sim 4$. For example, when comparing L/Cu = 8 → 7 → 6, it becomes clear that the extensibility and ultimate strength are not significantly affected. Secondly, even the increase in the Young's modulus is not as predictable as the cobalt case as shown in the plot of Young's modulus versus Cu/L. Unexpectedly, the materials become significantly stiffer as L/Cu approaches 4, which

is clear by following the transition from L/Cu = 6 → 5 → 4. At L/Cu ratio of 4.0, the Young's modulus is ~80 MPa which is doubled from L/Zn = 4 from our previous report. One might suspect that stronger interaction between Cu and imidazole is the primary reason for this improved mechanical properties (although the possibility of covalent cross-linking due to some unknown oxidation reduction reaction cannot be completely excluded).

Comparison of the dependence of the mechanical properties on L/M ratio for cobalt and copper samples, prompted us to consider another explanation for the observed differences, namely the ligand exchange dynamic and mechanism. From the rheology data, it is clear that cobalt samples had longer relaxation times compared to copper cross-linked polymers. We believe that under our static tensile tests, cobalt complexes behave more akin to covalent cross-linkers due to the slower rate of ligand exchange. Addition of more cobalt (decreasing the L/Co ratio) then results in decreased extensibilities and increased ultimate strength and these changes are proportional to the cross-linking density (Co/L).

In the case of copper, we suspected that the relaxation rates are affected by a different mechanism but found it difficult to reliably study the copper samples due to the uncertainties in the oxidation-reduction evident by the color change. We were pleased to notice that zinc samples, which are free from such complexities due to Zn^{2+} inertness, undergo similar transitions as the L/Zn approaches 4, Figure 2.22.

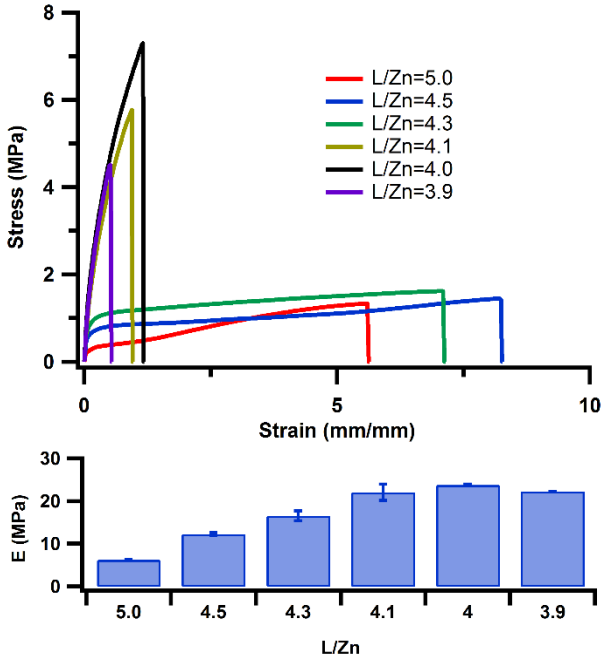

Figure 2.22 (a) Static tensile tests of **ICP-1** cross-linked with different amount of Zn^{2+}. (b) Dependence of the Young's modulus on the L/M ratio for each Sample.

Similar to copper, the transition in the mechanical properties were not noticeable at higher L/Zn ratio. Thus, we prepared samples with $3.9 \leq L/Zn \leq 5$ and studied their mechanical properties in a static tensile experiment.

An extremely noticeable transition is observed with a small change in metal content when L/Zn = 4.3 → 4.1. The mechanical properties undergo a drastic changes and the sample behavior suddenly transitions from a soft rubber into a brittle stiff plastic while the young's modulus is only increased slightly. Interestingly, such transition is absent in the case of cobalt when L/Co = 6 → 5.8 (Figure 2.41).

We reasoned that if this transition is due to the nature of metal-ligand complex, a similar behavior should be observed in the solution state where these interactions are initially formed. In fact, as mentioned previously, there was a noticeable change in the apparent viscosity of the

polymer solution after the addition of metal salts. We monitored the increase in the dynamic viscosity of **L-ICP** solutions at various L/M ratio for zinc and cobalt.

Consistent with the behavior observed in the tensile data, no significant viscosity increase was observed at L/Zn > 5. The solution viscosity was too low and close to the detection limit of our instrument. As it is shown in the Figure 2.23, by the addition of more metals, the dynamic viscosity increases dramatically (~ 400x) near the L/Zn of 4 and then reaches a plateau and does not increase further. Completely different behavior is observed in the case of cobalt, where the viscosity increases gradually by addition of more cobalt across the investigated range (3x increase with L/Co= 10 →7.2). Samples with lower L/Co ratio (6 < L/Co < 7.2) were not stable at temperature of the experiment, 20 °C, and precipitated slowly from the solution which also decreased the supernatant viscosity (Figure 2.42).

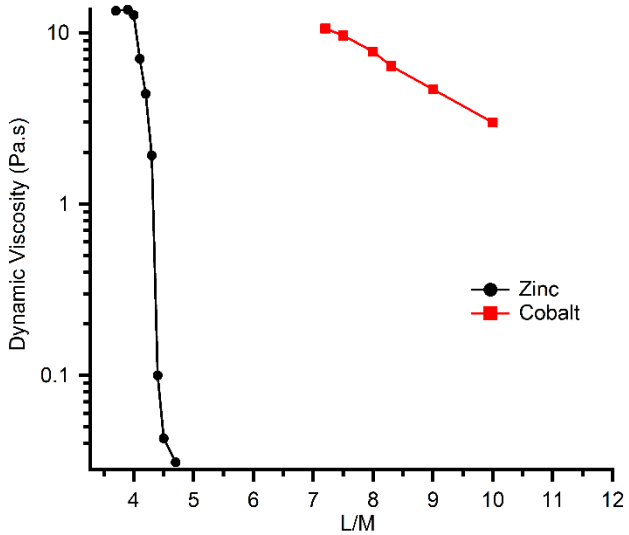

Figure 2.23 Changes in the dynamic viscosity of the solution of **L-ICP**s cross-linked with different amount of zinc (black circle) and cobalt (red square).

2.7.8 Explanation of the observed mechanical behavior through M–L exchange mechanism

We tried to explain these trends of macroscopic behavior by using a combination of polymer physics (especially transient network models[91,92]) and small-molecule reactivity[90] (complex geometry and the ligand exchange mechanism).

Even though most theories of transient networks are built to describe behaviors of gels, some aspects of these theories are relevant in our system which is cross-linked by transient coordinative bonds at the level of polymer melt and multiphase polymer. For example, network relaxation under the (shear) stress is governed by the dynamics of transient complex ligand exchange (τ_{ex}) and chain reptation (τ_{rep}).[92] Viscosity, or the resistance to flow, can be described based on the rate of cross-linkers remodeling and chain slippage. If the ligand exchange dynamic is dominant, the movement of polymer chains and the displacement of the polymer center of mass, flow, is dependent on the rate of ligand exchange reaction ($\tau_{ex} \propto 1/R_{ex}$).

We speculate that the differences in the ligand geometry and the exchange mechanism can explain the differences in the viscosity dependence on L/M. In the case of cobalt, the octahedral complex undergoes ligand exchange with dissociative mechanism where one of the polymer bound imidazole has to dissociate before the ligand exchange can occur.

$$CoL_6 \rightarrow CoL_5 + L \qquad R_{ex} = k_d\,[CoL_6]$$

This process is not dependent on the presence of another imidazole ligand and is therefore less sensitive to the concentration of free imidazole. The relaxation rate is therefore set by the k_d and the extent of cross-linking which modulates the reptation and also indirectly affects the bond real half-life (i.e. in highly cross-linked sample, the dissociation of one ligand may not be enough

for polymer movement due to the low concentration of free imidazoles and the dissociated bond between ligand and the metal center is reformed without polymer dislocation).

On the other hand, the tetrahedral geometry of $Zn(Imz)_4$ complex is more conducive to an associative-dissociative mechanism. In this case, the rate of ligand exchange depends on the concentration of both free imidazole and the complex and it is more sensitive to the presence of free imidazole.

$$ZnL_4 + L' \rightarrow ZnL_3L' + L \qquad R_{ex} = k_{ad}\,[ZnL_4][L']$$

For as associative-dissociative mechanism, the exchange rate or τ_{ex} is not only a function of added metal salt also dependends significantly on the concentration of free imidazole at any L/Zn. Near the L/Zn of 4, the concentration of free imidazole is significantly reduced by the addition more metals. In an overly simplified and idealized system of equilibriums, it is possible to calculate the theoretical rate of such associative reaction and estimate its dependence on the L/Zn ratio.

The theoretical rate of the bimolecular reaction between free imidazole and ML_4 complex can be calculated at any given L/Zn by calculating the concentration of ML_4 and L,

$$ML_4 + L' \rightarrow ML_3L' + L \quad R = k[ML_4][L]$$

The following equilibriums also exist in the system

$$M + L \rightleftharpoons ML \quad \beta_1 = \frac{[ML]}{[M][L]}$$

$$M + 2L \rightleftharpoons ML_2 \quad \beta_2 = \frac{[ML_2]}{[M][L]^2}$$

$$M + 3L \rightleftharpoons ML_3 \quad \beta_3 = \frac{[ML_3]}{[M][L]^3}$$

$$M + 4L \rightleftharpoons ML_4 \quad \beta_4 = \frac{[ML_4]}{[M][L]^4}$$

Here, the L represent the imidazole, and M represent the Zinc. The traditional concentration of each species is represented by the brackets. Totals concentration of imidazole, $[L_0]$, and Zinc, $[M]_0$, are assumed to be conserved:

$$[L_0] = [L] + [ML] + 2[ML_2] + 3[ML_3] + 4[ML_4]$$

$$[M_0] = [M] + [ML] + [ML_2] + [ML_3] + [ML_4]$$

Using equilibrium constants, the concentration of each species was determined as a function of added metal, $[M_0]$, by solving the following sets of nonlinear equations in MATHEMATICA software to obtain the concentration of each species at various L/Zn ratio (Figure 2.S for mole fraction)

$$[L_0] = [L] + \sum_{n=1}^{4} n\, \beta_n M\, [L]^n$$

$$[M_0] = [M] + \sum_{n=1}^{4} \beta_n M\, [L]^n$$

The theoretical rate of exchange reaction was calculated by using the values for $[ML_4]$ and [L] and is plotted in Figure 2.24.

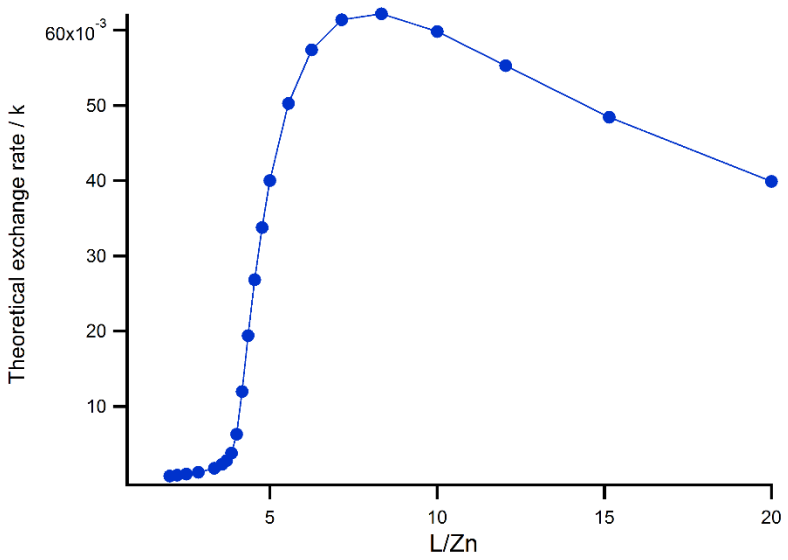

Figure 2.24 The predicted L/Zn dependence of the rate of an idealized ligand exchange reaction with associative-dissociative mechanism. A sharp transition in the rate of the reaction is observed near L/Zn ~ 4, when the concentration of free imidazole is significantly reduced by addition of more metal salt.

As the concentration of free imidazole is depleted significantly near the L/Zn ~ 4, other modes of relaxation may become dominant as the rate of associative ligand exchange is significantly reduced.

2.8 Conclusion

In summary, I explored labile zinc-imidazole interactions as a dynamic motif for self-healing in solid state. I have demonstrated that a pervasive network of these weak interactions can be effectively combined to generate tunable, strong, and tough elastomers with efficient autonomous self-healing at ambient conditions. My preliminary results demonstrated that small changes in the metal content, in the case of zinc and copper, is enough to significantly alter the mechanical properties of these materials near the $(L/M)_{lim}$. Additional experiments are needed to

pinpoint the nature of this transition but I hypothesize that an associative-dissociative mechanism may explain the nature of this transition once the free imidazole is depleted.

2.9 References

(1) Hager, M. D.; Greil, P.; Leyens, C.; van der Zwaag, S.; Schubert, U. S. *Adv. Mater.* **2010**, *22*, 5424.
(2) Odom, S. A.; Chayanupatkul, S.; Blaiszik, B. J.; Zhao, O.; Jackson, A. C.; Braun, P. V.; Sottos, N. R.; White, S. R.; Moore, J. S. *Adv. Mater.* **2012**, *24*, 2578.
(3) Dry, C. *Compos. Struct.* **1996**, *35*, 263.
(4) White, S. R.; Sottos, N. R.; Geubelle, P. H.; Moore, J. S.; Kessler, M. R.; Sriram, S. R.; Brown, E. N.; Viswanathan, S. *Nature* **2001**, *409*, 794.
(5) Keller, M. W.; White, S. R.; Sottos, N. R. *Adv. Funct. Mater.* **2007**, *17*, 2399.
(6) Cho, S. H.; Andersson, H. M.; White, S. R.; Sottos, N. R.; Braun, P. V. *Adv. Mater.* **2006**, *18*, 997.
(7) Rule, J. D.; Moore, J. S. *Macromolecules* **2002**, *35*, 7878.
(8) Rule, J. D.; Sottos, N. R.; White, S. R. *Polymer* **2007**, *48*, 3520.
(9) Brown, E. N.; Kessler, M. R.; Sottos, N. R.; White, S. R. *J. Microencapsul.* **2003**, *20*, 719.
(10) Wilson, G. O.; Caruso, M. M.; Reimer, N. T.; White, S. R.; Sottos, N. R.; Moore, J. S. *Chem. Mater.* **2008**, *20*, 3288.
(11) Toohey, K. S.; Sottos, N. R.; Lewis, J. A.; Moore, J. S.; White, S. R. *Nat. Mater.* **2007**, *6*, 581.
(12) Esser-Kahn, A. P.; Thakre, P. R.; Dong, H.; Patrick, J. F.; Vlasko-Vlasov, V. K.; Sottos, N. R.; Moore, J. S.; White, S. R. *Adv. Mater.* **2011**, *23*, 3654.
(13) Nguyen, D. T.; Kleiman, M.; Truong, R.; Esser-Kahn, A. P. *Mater. Horiz.* **2014**, *1*, 602.
(14) White, S. R.; Moore, J. S.; Sottos, N. R.; Krull, B. P.; Santa Cruz, W. A.; Gergely, R. C. R. *Science* **2014**, *344*, 620.
(15) Yang, Y.; Urban, M. W. *Chem. Soc. Rev.* **2013**, *42*, 7446.
(16) Yang, Y.; Urban, M. W. In *Healable Polymer Systems*; The Royal Society of Chemistry: 2013, p 126.
(17) Kim, Y. H.; Wool, R. P. *Macromolecules* **1983**, *16*, 1115.
(18) Wool, R. P.; O'Connor, K. M. *J. Appl. Phys.* **1981**, *52*, 5953.
(19) Prager, S.; Tirrell, M. *J. Chem. Phys.* **1981**, *75*, 5194.
(20) Lin, C. B.; Lee, S.; Liu, K. S. *Polym. Eng. Sci.* **1990**, *30*, 1399.
(21) Burattini, S.; Colquhoun, H. M.; Greenland, B. W.; Hayes, W. *Faraday Discuss.* **2009**, *143*, 251.
(22) Luo, X.; Mather, P. T. *ACS Macro Lett.* **2013**, *2*, 152.
(23) Mohr, R.; Kratz, K.; Weigel, T.; Lucka-Gabor, M.; Moneke, M.; Lendlein, A. *Proc. Natl. Acad. Sci. U. S. A.* **2006**, *103*, 3540.
(24) Kirkby, E. L.; Rule, J. D.; Michaud, V. J.; Sottos, N. R.; White, S. R.; Månson, J.-A. E. *Adv. Funct. Mater.* **2008**, *18*, 2253.
(25) Garcia, M. E.; Lin, Y.; Sodano, H. A. *J. Appl. Phys.* **2010**, *108*, 093512.

(26) Caruso, M. M.; Davis, D. A.; Shen, Q.; Odom, S. A.; Sottos, N. R.; White, S. R.; Moore, J. S. *Chem. Rev.* **2009**, *109*, 5755.
(27) Black, A. L.; Lenhardt, J. M.; Craig, S. L. *J. Mater. Chem.* **2011**, *21*, 1655.
(28) Ghosh, B.; Urban, M. W. *Science* **2009**, *323*, 1458.
(29) Yuan, C. e.; Rong, M. Z.; Zhang, M. Q.; Zhang, Z. P.; Yuan, Y. C. *Chem. Mater.* **2011**, *23*, 5076.
(30) Imato, K.; Nishihara, M.; Kanehara, T.; Amamoto, Y.; Takahara, A.; Otsuka, H. *Angew. Chem., Int. Ed.* **2012**, *51*, 1138.
(31) Imato, K.; Ohishi, T.; Nishihara, M.; Takahara, A.; Otsuka, H. *J. Am. Chem. Soc.* **2014**, *136*, 11839.
(32) Amamoto, Y.; Kamada, J.; Otsuka, H.; Takahara, A.; Matyjaszewski, K. *Angew. Chem. Int. Ed.* **2011**, *50*, 1660.
(33) Amamoto, Y.; Otsuka, H.; Takahara, A.; Matyjaszewski, K. *Adv. Mater.* **2012**, *24*, 3975.
(34) Canadell, J.; Goossens, H.; Klumperman, B. *Macromolecules* **2011**, *44*, 2536.
(35) Scott, T. F.; Schneider, A. D.; Cook, W. D.; Bowman, C. N. *Science* **2005**, *308*, 1615.
(36) Chen, X.; Dam, M. A.; Ono, K.; Mal, A.; Shen, H.; Nut, S. R.; Sheran, K.; Wudl, F. *Science* **2002**, *295*, 1698.
(37) Chen, X.; Wudl, F.; Mal, A. K.; Shen, H.; Nutt, S. R. *Macromolecules* **2003**, *36*, 1802.
(38) Murphy, E. B.; Bolanos, E.; Schaffner-Hamann, C.; Wudl, F.; Nutt, S. R.; Auad, M. L. *Macromolecules* **2008**, *41*, 5203.
(39) Klukovich, H. M.; Kean, Z. S.; Iacono, S. T.; Craig, S. L. *J. Am. Chem. Soc.* **2011**, *133*, 17882.
(40) Chung, C.-M.; Roh, Y.-S.; Cho, S.-Y.; Kim, J.-G. *Chem. Mater.* **2004**, *16*, 3982.
(41) Deng, G.; Li, F.; Yu, H.; Liu, F.; Liu, C.; Sun, W.; Jiang, H.; Chen, Y. *ACS Macro Lett.* **2012**, *1*, 275.
(42) Deng, G.; Tang, C.; Li, F.; Jiang, H.; Chen, Y. *Macromolecules* **2010**, *43*, 1191.
(43) Skene, W. G.; Lehn, J.-M. P. *Proc. Natl. Acad. Sci. U. S. A.* **2004**, *101*, 8270.
(44) Taynton, P.; Yu, K.; Shoemaker, R. K.; Jin, Y.; Qi, H. J.; Zhang, W. *Adv. Mater.* **2014**, *26*, 3938.
(45) Ying, H.; Zhang, Y.; Cheng, J. *Nat. Commun.* **2014**, *5*.
(46) Zheng, P.; McCarthy, T. J. *J. Am. Chem. Soc.* **2012**, *134*, 2024.
(47) Capelot, M.; Montarnal, D.; Tournilhac, F.; Leibler, L. *J. Am. Chem. Soc.* **2012**, *134*, 7664.
(48) Montarnal, D.; Capelot, M.; Tournilhac, F.; Leibler, L. *Science* **2011**, *334*, 965.
(49) Lu, Y.-X.; Guan, Z. *J. Am. Chem. Soc.* **2012**, *134*, 14226.
(50) Rowan, S. J.; Cantrill, S. J.; Cousins, G. R. L.; Sanders, J. K. M.; Stoddart, J. F. *Angew. Chem. Int. Ed.* **2002**, *41*, 898.
(51) He, L.; Fullenkamp, D. E.; Rivera, J. G.; Messersmith, P. B. *Chem. Commun.* **2011**, *47*, 7497.
(52) Roberts, M. C.; Hanson, M. C.; Massey, A. P.; Karren, E. A.; Kiser, P. F. *Adv. Mater.* **2007**, *19*, 2503.
(53) Bell, C. M.; Kissounko, D. A.; Gellman, S. H.; Stahl, S. S. *Angew. Chem. Int. Ed.* **2007**, *46*, 761.
(54) Burnworth, M.; Tang, L.; Kumpfer, J. R.; Duncan, A. J.; Beyer, F. L.; Fiore, G. L.; Rowan, S. J.; Weder, C. *Nature* **2011**, *472*, 334.
(55) Bode, S.; Zedler, L.; Schacher, F. H.; Dietzek, B.; Schmitt, M.; Popp, J.; Hager, M. D.; Schubert, U. S. *Adv. Mater.* **2013**, *25*, 1634.

(56) Nakahata, M.; Takashima, Y.; Yamaguchi, H.; Harada, A. *Nat. Commun.* **2011**, *2*, 511.
(57) Kakuta, T.; Takashima, Y.; Nakahata, M.; Otsubo, M.; Yamaguchi, H.; Harada, A. *Adv. Mater.* **2013**, *25*, 2849.
(58) Burattini, S.; Greenland, B. W.; Merino, D. H.; Weng, W.; Seppala, J.; Colquhoun, H. M.; Hayes, W.; Mackay, M. E.; Hamley, I. W.; Rowan, S. J. *J. Am. Chem. Soc.* **2010**, *132*, 12051.
(59) Burattini, S.; Colquhoun, H. M.; Fox, J. D.; Friedmann, D.; Greenland, B. W.; Harris, P. J. F.; Hayes, W.; Mackay, M. E.; Rowan, S. J. *Chem. Commun.* **2009**, 6717.
(60) Burattini, S.; Greenland, B. W.; Hayes, W.; Mackay, M. E.; Rowan, S. J.; Colquhoun, H. M. *Chem. Mater.* **2011**, *23*, 6.
(61) Wang, Q.; Mynar, J. L.; Yoshida, M.; Lee, E.; Lee, M.; Okuro, K.; Kinbara, K.; Aida, T. *Nature* **2010**, *463*, 339.
(62) Kalista, S. J., Jr.; Ward, T. C.; Oyetunji, Z. *Mech. Adv. Mater. Struct.* **2007**, *14*, 391.
(63) Bose, R. K.; Hohlbein, N.; Garcia, S. J.; Schmidt, A. M.; van der Zwaag, S. *PCCP* **2015**, *17*, 1697.
(64) Cordier, P.; Tournilhac, F.; Soulie-Ziakovic, C.; Leibler, L. *Nature* **2008**, *451*, 977.
(65) Hentschel, J.; Kushner, A. M.; Ziller, J.; Guan, Z. *Angew. Chem. Int. Ed.* **2012**, *51*, 10561.
(66) Phadke, A.; Zhang, C.; Arman, B.; Hsu, C.-C.; Mashelkar, R. A.; Lele, A. K.; Tauber, M. J.; Arya, G.; Varghese, S. *Proc. Natl. Acad. Sci. U. S. A.* **2012**, *109*, 4383.
(67) Herbst, F.; Doehler, D.; Michael, P.; Binder, W. H. *Macromol. Rapid Commun.* **2013**, *34*, 203.
(68) Chen, Y.; Kushner, A. M.; Williams, G. A.; Guan, Z. *Nat. Chem.* **2012**, *4*, 467.
(69) Degtyar, E.; Harrington, M. J.; Politi, Y.; Fratzl, P. *Angew. Chem. Int. Ed.* **2014**, *53*, 12026.
(70) Yount, W. C.; Loveless, D. M.; Craig, S. L. *J. Am. Chem. Soc.* **2005**, *127*, 14488.
(71) Whittell, G. R.; Hager, M. D.; Schubert, U. S.; Manners, I. *Nat. Mater.* **2011**, *10*, 176.
(72) Holten-Andersen, N.; Harrington, M. J.; Birkedal, H.; Lee, B. P.; Messersmith, P. B.; Lee, K. Y. C.; Waite, J. H. *Proc. Natl. Acad. Sci. U.S.A.* **2011**, *108*, 2651.
(73) Yang, B.; Zhang, H.; Peng, H.; Xu, Y.; Wu, B.; Weng, W.; Li, L. *Polym. Chem.* **2014**, *5*, 1945.
(74) Hong, G.; Zhang, H.; Lin, Y.; Chen, Y.; Xu, Y.; Weng, W.; Xia, H. *Macromolecules* **2013**, *46*, 8649.
(75) Wang, Z.; Urban, M. W. *Polym. Chem.* **2013**, *4*, 4897.
(76) Bode, S.; Bose, R. K.; Matthes, S.; Ehrhardt, M.; Seifert, A.; Schacher, F. H.; Paulus, R. M.; Stumpf, S.; Sandmann, B.; Vitz, J.; Winter, A.; Hoeppener, S.; Garcia, S. J.; Spange, S.; van der Zwaag, S.; Hager, M. D.; Schubert, U. S. *Polym. Chem.* **2013**, *4*, 4966.
(77) Kupfer, S.; Zedler, L.; Guthmuller, J.; Bode, S.; Hager, M. D.; Schubert, U. S.; Popp, J.; Grafe, S.; Dietzek, B. *PCCP* **2014**, *16*, 12422.
(78) Fullenkamp, D. E.; He, L.; Barrett, D. G.; Burghardt, W. R.; Messersmith, P. B. *Macromolecules* **2013**, *46*, 1167.
(79) Maret, W.; Li, Y. *Chem. Rev.* **2009**, *109*, 4682.
(80) Moad, G.; Rizzardo, E.; Thang, S. H. *Aust. J. Chem.* **2009**, *62*, 1402.
(81) Skey, J.; O'Reilly, R. K. *Chem. Commun.* **2008**, 4183.
(82) Garcia-Bernabé, A.; Compañ, V.; Burguete, M. I.; García-Verdugo, E.; Karbass, N.; Luis, S. V.; Riande, E. *J. Phys. Chem. C* **2010**, *114*, 7030.
(83) Eisenberg, A.; Hird, B.; Moore, R. B. *Macromolecules* **1990**, *23*, 4098.
(84) Vollrath, F.; Knight, D. P. *Nature* **2001**, *410*, 541.
(85) Vaccaro, E.; Waite, J. H. *Biomacromolecules* **2001**, *2*, 906.

(86) Chung, J.; Kushner, A. M.; Weisman, A. C.; Guan, Z. *Nat. Mater.* **2014**, *13*, 1055.
(87) Kean, Z. S.; Hawk, J. L.; Lin, S. T.; Zhao, X. H.; Sijbesma, R. P.; Craig, S. L. *Adv. Mater.* **2014**, *26*, 6013.
(88) Broomell, C. C.; Mattoni, M. A.; Zok, F. W.; Waite, J. H. *J. Exp. Biol.* **2006**, *209*, 3219.
(89) Broomell, C. C.; Khan, R. K.; Moses, D. N.; Miserez, A.; Pontin, M. G.; Stucky, G. D.; Zok, F. W.; Waite, J. H. *J. R. Soc. Interface* **2007**, *4*, 19.
(90) Fratiello, A.; Schuster, R. E.; Bartolini, G. *J. Am. Chem. Soc.* **1970**, *92*, 2304.
(91) Wientjes, R. H. W.; Jongschaap, R. J. J.; Duits, M. H. G.; Mellema, J. *J. Rheol.* **1999**, *43*, 375.
(92) Vermonden, T.; van Steenbergen, M. J.; Besseling, N. A. M.; Marcelis, A. T. M.; Hennink, W. E.; Sudhölter, E. J. R.; Cohen Stuart, M. A. *J. Am. Chem. Soc.* **2004**, *126*, 15802.
(93) Liu, B. K.; Wu, Q.; Qian, X. Q.; Lv, D. S.; Lin, X. F. *Synthesis* **2007**, *2007*, 2653.

2.10 Experimental details and supporting information

General materials and methods

^{1}H spectra were recorded on 500 MHz and 600 MHz Bruker instruments. ^{13}C NMR was recorded at 125 MHz on Bruker instruments. Chemical shifts were reported in standard format as values in ppm relative to deuterated solvents. Gel permeation chromatography (GPC) was performed in THF (1 mL/min) using an Agilent LC 1100 Series equipped with Polymer Laboratory's PLgel 5 μm mixed-C column to determine molecular weights and molecular weight distributions, M_w/M_n, of the macro-CTAs with respect to polystyrene (PS) standards (Varian, Palo Alto, CA). Brush copolymers were analyzed using GPC in DMF with 0.1% LiBr (w/v) (1 mL/min) using an Agilent LC 1100 Series equipped with OHpak SB-803 HQ column from Shodex to determine molecular weights and molecular weight distributions, M_w/M_n, with respect to poly(ethylene glycol) (PEG) standards (Sigma Aldrich). GC-MS was obtained on ThermoFinnegen Trace MS+ instrument with DB-5 column (30m × 0.25 mm × 0.25μm film) with helium gas as carrier on positive EI mode. The oven was held at 50 °C for 1 minute then heated at a rate of 10 °C min^{-1} to 290 °C and held for an additional minute. The mass spectrometry used electron ionization (70 eV) scanning (1/sec) from m/z 50-650.

$Zn(NTf_2)_2$ and 1,4-dutanediol diacrylate were purchased from Strem Chemical and Alfa Aesar respectively. All other chemicals were purchased from Sigma Aldrich and were used as received. Inhibitors were removed by passing the monomers through basic alumina column for butyl acrylate and styrene. 4-vinylbenzyl chloride, technical grade, was used as received and was not passed through basic column before polymerization.

Thin layer chromatography, TLC, plates were stained by $KMnO_4$ for presence of double bonds and ninhydrin for the presence of the amine groups. The monomer was purified using CombiFlash® Rf+ automatic column using RediSep Rf Gold® Normal-Phase Silica as described in the monomer synthesis section.

Synthesis and characterization

IMZa

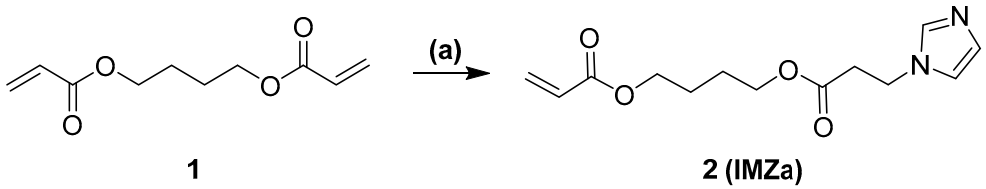

Scheme 2.4 Synthesis of **IMZa (2)**. (a) Imidazole, 1-methyl imidazole, CH_3CN, 18 h.

1,4-butanediol diacrylate (39.8 mL, 88.2 mmol, 2 equiv), 1-methylimidazole (1.68 mL, 21.1 mmol, 0.2 equiv), triethylamine (14.7 mL, 105 mmol, 1 equiv) were dissolved in 90 mL CH_3CN:DMF mixture (5:4 v/v). Imidazole (7.18 g, 105 mmol) was dissolved in 18 mL of DMF and was added dropwise using a syringe pump over the course of 12 h to the stirred solution. The reaction was stirred for another 6 h after which the solvent was evaporated *in vacuo*. To avoid unwanted polymerization of the monomer, a radical inhibitor (4-methoxyphenol, 200 ppm) was added to the reaction mixture before removing the solvent. The residual light pink oil was dissolved in 100 mL ethyl acetate and washed twice with 50 mL water and once with 50 mL brine. The organic layer was dried over $MgSO_4$ and concentrated *in vacuo* after filtration of drying agent. Crude mixture was purified by silica flash column chromatography by eluting unreacted **1** from column using a gradient of hexane and ethyl acetate (0 → 100% EtOAc) and then switching the eluent to 5% MeOH in EtOAc. The fractions containing the product were combined and

concentrated to afford **2** as colorless oil (9.39 g, 40%). The purity of monomer was confirmed using GC-MS and ^{1}H, ^{13}C NMR. TLC plates were stained using $KMnO_4$ and ninhydrin to detect vinyl group and the doubly substituted product respectively.[93]

^{1}H NMR (600 MHz, $CDCl_3$) δ 7.55 (s, 1H), 7.04 (s, 1H), 6.93 (s, 1H), 6.39 (dd, J = 17.3, 1.4 Hz, 1H), 6.11 (dd, J = 17.3, 10.5 Hz, 1H), 5.82 (dd, J = 10.5, 1.4 Hz, 1H), 4.27 (t, J = 6.6 Hz, 2H), 4.24 – 4.05 (m, 4H), 2.78 (t, J = 6.6 Hz, 2H), 1.75 – 1.66 (m, 4H). ^{13}C NMR (125 MHz, $CDCl_3$) δ 170.66, 166.31, 137.39, 131.00, 129.82, 128.48, 118.96, 64.79, 63.97, 42.40, 36.07, 25.33, 25.29. HRMS (GC-CI) m/z: $[M + H]^+$ Calcd for $C_{13}H_{18}N_2O_4H$ 267.1345; Found 267.1339.

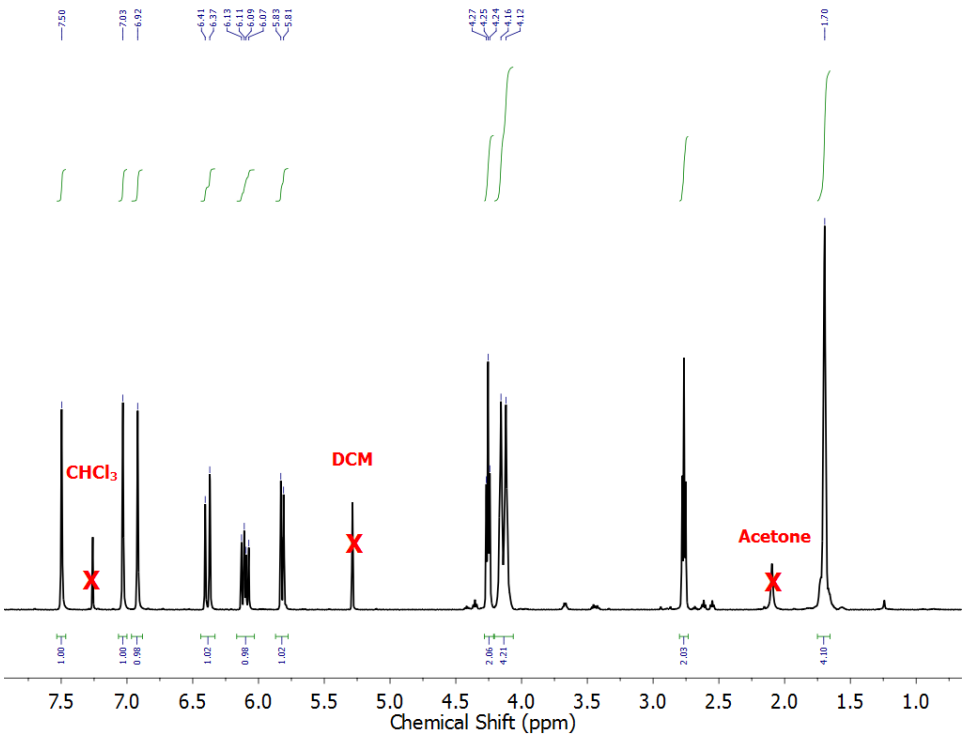

Figure 2.25 ^{1}H NMR spectrum of **IMZa** monomer (**2**) (600 MHz, $CDCl_3$, 298 K).

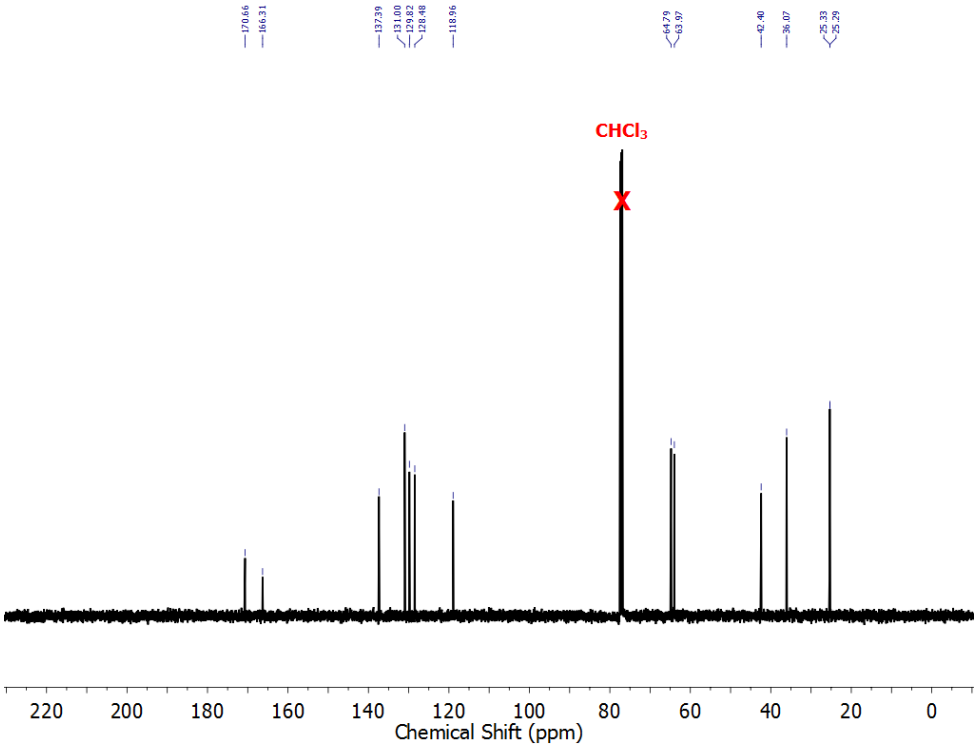

Figure 2.26 ^{13}C NMR spectrum of **IMZa** monomer (**2**) (125 MHz, $CDCl_3$, 298 K).

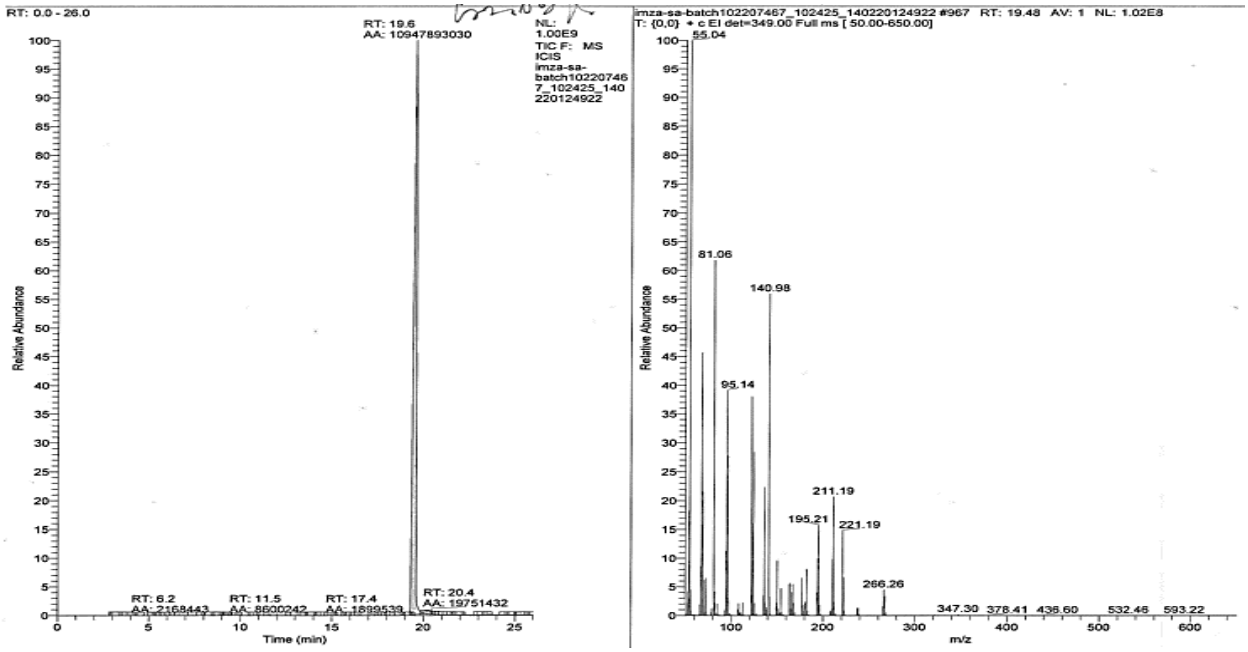

Figure 2.27 GC-MS trace of **IMZa** monomer (**2**) after purification. The trace demonstrates the complete removal of 1,4-butanediol diacrylate after purification on silica column (left). The EI-mass spectrum (right) shows the parent compound mass at m/z=266.26 in addition to the fragmentation pattern.

Typical macro-CTA synthesis

Step 1: Styrene (28.5 mL, 249 mmol) and 4-vinylbenzyl chloride, VBC, (3.96 mL, 25.3 mmol, technical grade, 90%, used as received without removing the inhibitor) and 150 mL of toluene. AIBN (150 mg, 0.91 mmol) was added to the reaction mixture. Reaction flask was sealed with a rubber septum and heated to 75 °C for 18 h. The reaction was stopped by cooling the mixture to room temperature. Approximately half of the solvent was removed *in vacuo* and copolymer was precipitated by slowly adding the reaction mixture to 800 mL of hexane under stirring. After filtration, the polymer was dissolved in DCM and precipitated twice into stirring MeOH. The white solid was collected by vacuum filtration.

macro-CTA 1: M_n = 15.9 kDa, M_w/M_n = 1.7 (GPC, THF eluent, polystyrene as standard), and 5% VBC incorporation by ^{1}H NMR.

macro-CTA 2: M_n = 15.7 kDa, M_w/M_n = 1.9 (GPC, THF eluent, polystyrene as standard), and 10% VBC incorporation by ^{1}H NMR.

^{1}H NMR (500 MHz, CD_2Cl_2) δ 7.06-6.95 (br, aromatic), 6.60-6.3(br, aromatic), 4.53(C$\underline{H}_2$Cl), 2.09-1.3(br, m, aliphatic region).

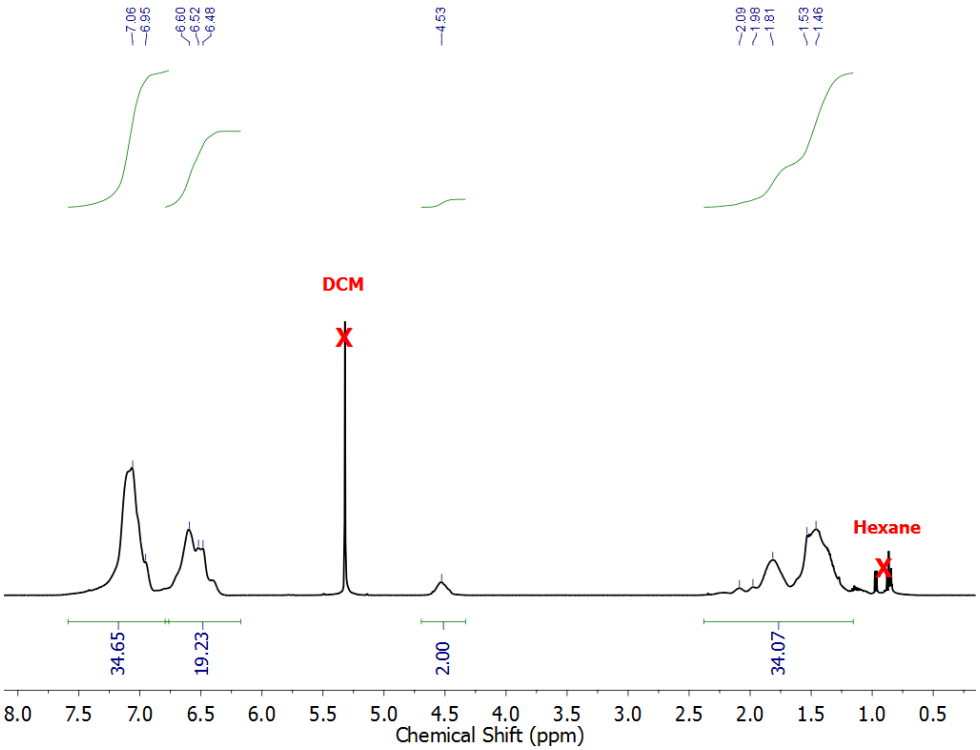

Figure 2.28 ^{1}H NMR spectrum of poly(styrene-*co*-vinylbenzyl chloride) (600 MHz, CD_2Cl_2, 298 K).

Step 2: K_3PO_4 (3.34 g, 15.8 mmol) was suspended in acetone (10 mL). Ethanethiol (1.10 mL, 14.00 mmol) was added via a disposable syringe resulting in a color change to pale yellow. After stirring for 5 min, carbon disulfide (1.90 mL, 31.5 mmol) was added to the reaction mixture and the reaction color almost immediately changed to dark yellow. The mixture was stirred for 45 min before 2 g of the polymer (1.75 mmol of VBC/g of polymer) was added to the reaction mixture. Additional 20 mL of solvent, acetone and DMF 1:1 (v/v), was added to ensure complete solubility of the polymer. The reaction was stirred for 10 h. Water (150 mL) was added to the reaction mixture and the polymer was extracted into 100 mL of DCM. The organic layer was washed twice with 50 mL of water and three times with 50 mL of brine. The DCM layer was separated and was added slowly to 1 L of MeOH under stirring. The pale yellow polymer was collected by vacuum filtration and dried over Büchner funnel.[81]

^{1}H NMR (600 MHz, CD_2Cl_2) δ 7.3-6.9 (br, aromatic), 6.7-6.3(br, aromatic), 4.54 ($C\underline{H}_2SCS_2$), 3.38 ($SC\underline{H}_2CH_3$), 1.9-1.3 (br, aliphatic region).

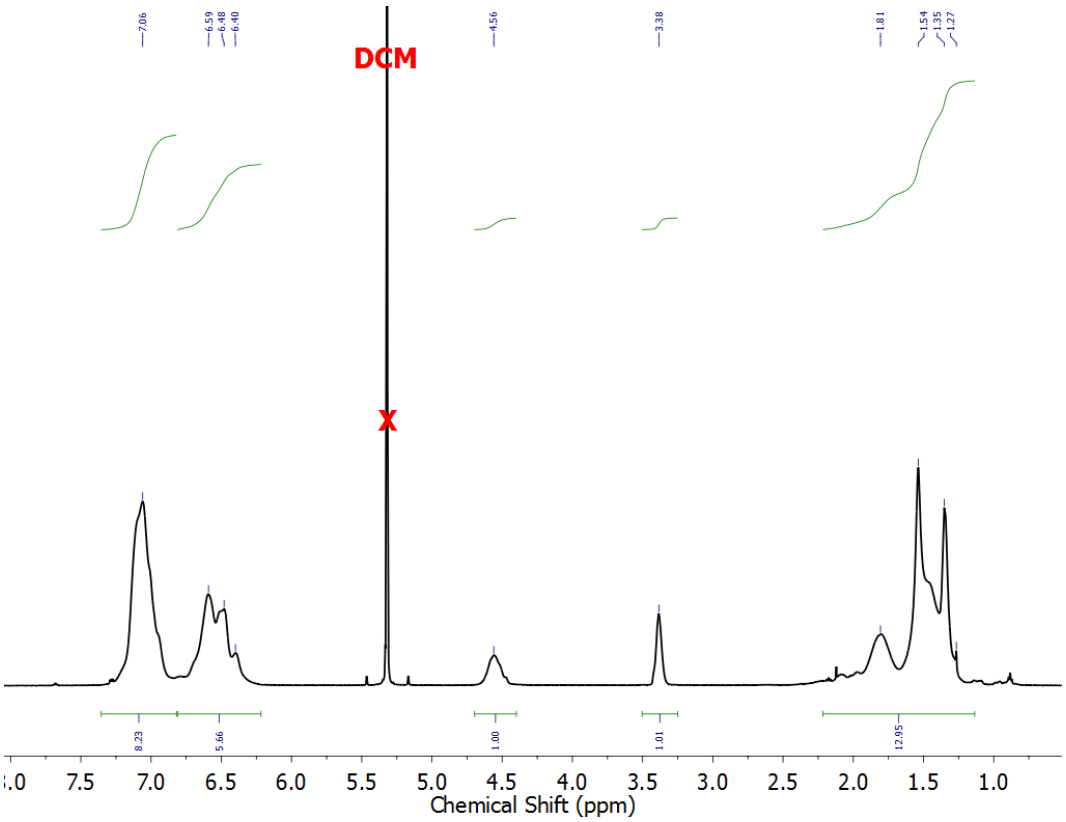

Figure 2.29 ^{1}H NMR spectrum of macro-CTA1 (600 MHz, CD_2Cl_2, 298 K).

Synthesis of imidazole-containing polymers (ICPs)

A typical procedure for synthesis of imidazole-containing brush polymers using RAFT polymerization is given below. The control polymer samples were prepared by similar RAFT polymerization method. **Control-1** was synthesized with the same brush architecture but the brush is a homopolymer of *n*-butyl acrylate (BA) without any imidazole comonomer. **Control-2** was synthesized by using a small molecular RAFT chain transfer agent instead of macro-CTA, resulting in a linear copolymer of BA and **IMZa** comonomer (**2**).

Macro-CTA2 (200 mg, 0.176 mmol) was added to a Schlenk flask. **IMZa** (**2**) (4.10 g, 15.40 mmol), BA (4.10 mL, 28.6 mmol), 1 mL anisole as NMR internal standard were dissolved in DMF (29.3 mL, 1.5 M with respect to vinyl moiety). Stock solution of AIBN (20.5 mg/mL in DMF) was prepared and 282 μL (5.78 mg, 0.035 mmol) was transferred to reaction flask ([Monomer]:[CTA]:[AIBN] = 250:1:0.2). 50 μL sample was taken for calculating the conversion using ^{1}H NMR and reaction flask was sealed by a rubber septum. The reaction mixture was then purged with a stream of N_2 for 45 min followed by 15 min of head space purging. Schlenk flask was immersed in an oil bath thermostatted at 65 °C. After 150 min, the reaction was removed from the oil bath and was cooled on ice. The conversion was determined with ^{1}H NMR by comparing the integration of vinyl protons with respect to anisole protons (OCH_3). 10 mg of 4-methoxyphenol was added as radical inhibitor and the reaction and the reaction mixture was evaporated *in vacuo*. The residue was transferred to Nalgene centrifuge tubes and the polymer was precipitated in Et_2O/Hexane mixture, (1:3 v/v) followed by centrifugation at 8500 rpm, for 10 min at 4 °C. The supernatant was decanted and the polymer was dissolved in CH_3CN and precipitated three more time in Et_2O/Hexane (4:1 v/v). The polymer was then dissolved in CH_3CN and the stock solution was kept at 4 °C. To quantify the concentration of polymer (mg/mL), known volume of polymer solution was transferred to three oven dried pre-tared 1 dram vials. The solution was then completely dried by placing the vials in pre-heated oven at 80 °C for 18 h under reduced pressure (< 1 mTorr). The average mass of these three samples was used to calculate the concentration of stock solution.

M_n = 74.9 kg/mol, M_w/M_n=1.2 (GPC, DMF as eluent, PEG as standard).

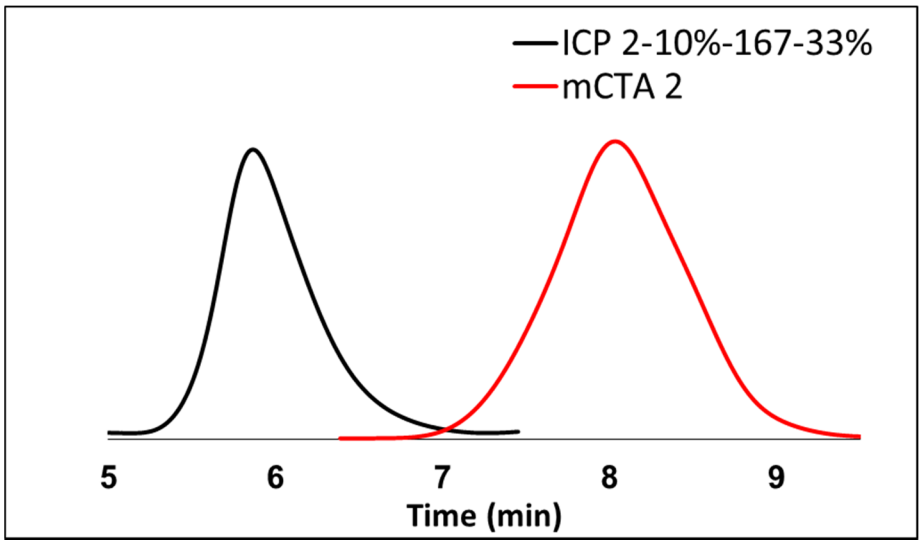

Figure 2.30 Representative GPC traces of **ICP-2** and macro-CTA2 in DMF showing increase in M_n (decrease in elution time) after RAFT polymerization. The molecular weight distribution (M_w/M_n) is becoming narrower because the RAFT polymerization produced multiple brushes with well-defined brush degree of polymerization.

Table 2.3 Molecular weight and molecular weight distributions of polymers measured by GPC using DMF as eluent, and PEG as standard.

Polymer	M_n (kg/mol)	M_w/M_n
ICP-1	90.5	1.2
ICP-2	74.9	1.2
ICP-3	51.4	1.2
ICP-4	57.0	1.3
Control-1	59.6	1.2
Control-2	6.27	1.7

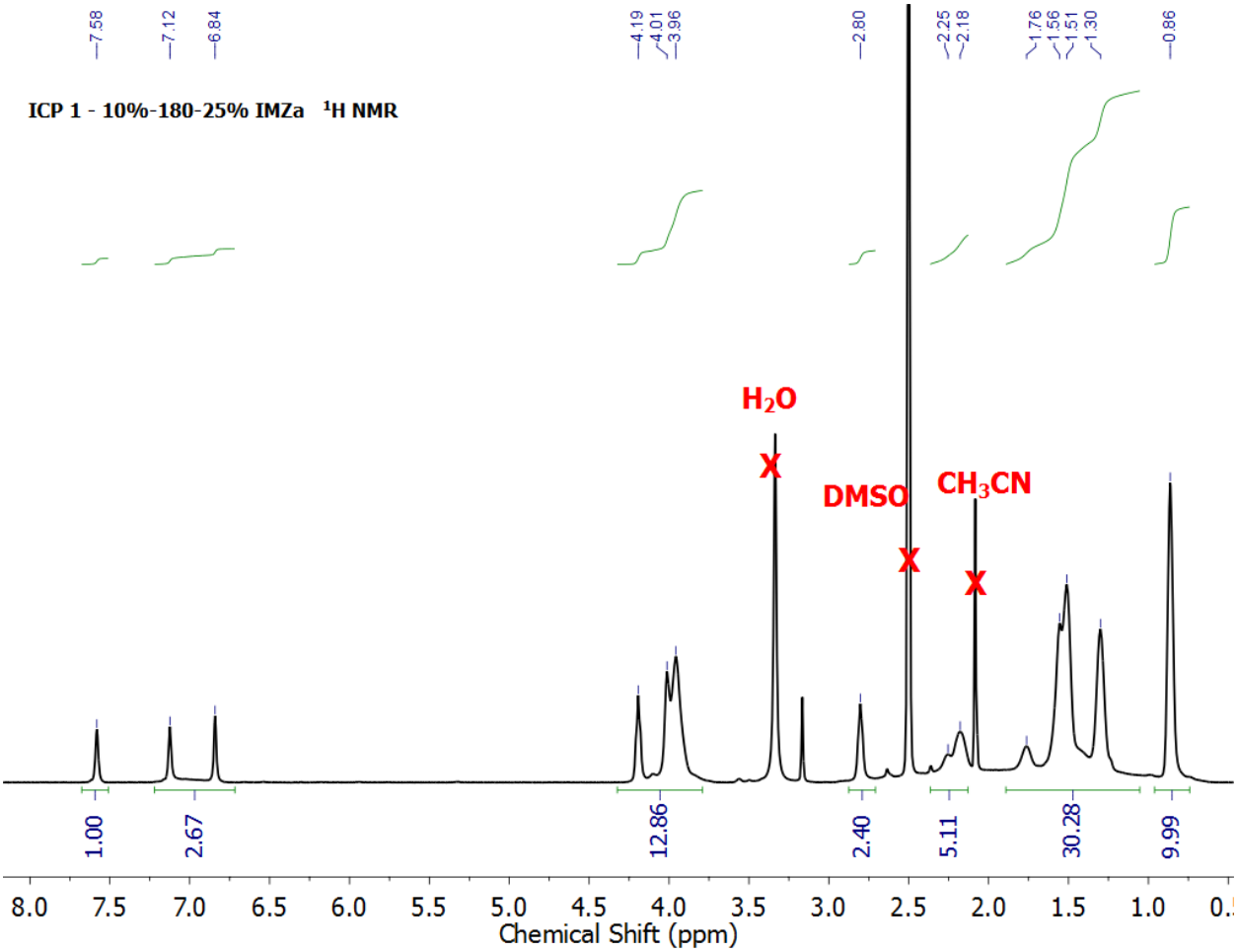

Figure 2.31 ^{1}H NMR spectrum of **ICP-1** (600 MHz, DMSO-d_6, 298 K). The molecular composition, as determined by NMR, is reported in the following format: graft density%- brush degree of polymerization- mol percent of **IMZa** (**2**) in each brush, defined as $N_{IMZa}/(N_{IMZa}+N_{BA}) \times 100$, N is the number of repeat units for each monomer.

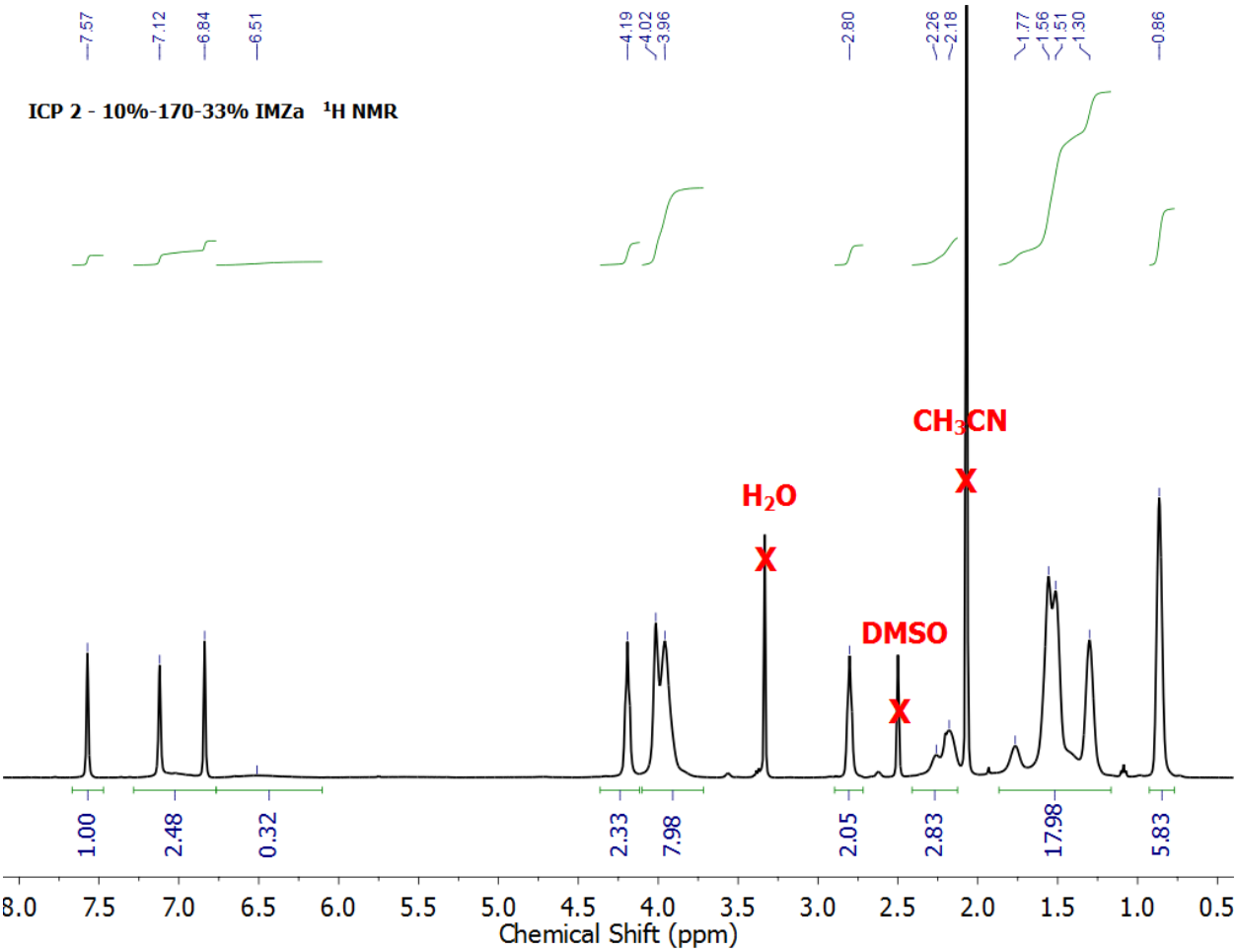

Figure 2.32 ^{1}H NMR spectrum of **ICP-2** (600 MHz, DMSO-d_6, 298 K). The molecular composition, as determined by NMR, is reported in the following format: graft density%- brush degree of polymerization- mol percent of **IMZa** (**2**) in each brush, defined as $N_{IMZa}/(N_{IMZa}+N_{BA}) \times 100$, N is the number of repeat units for each monomer.

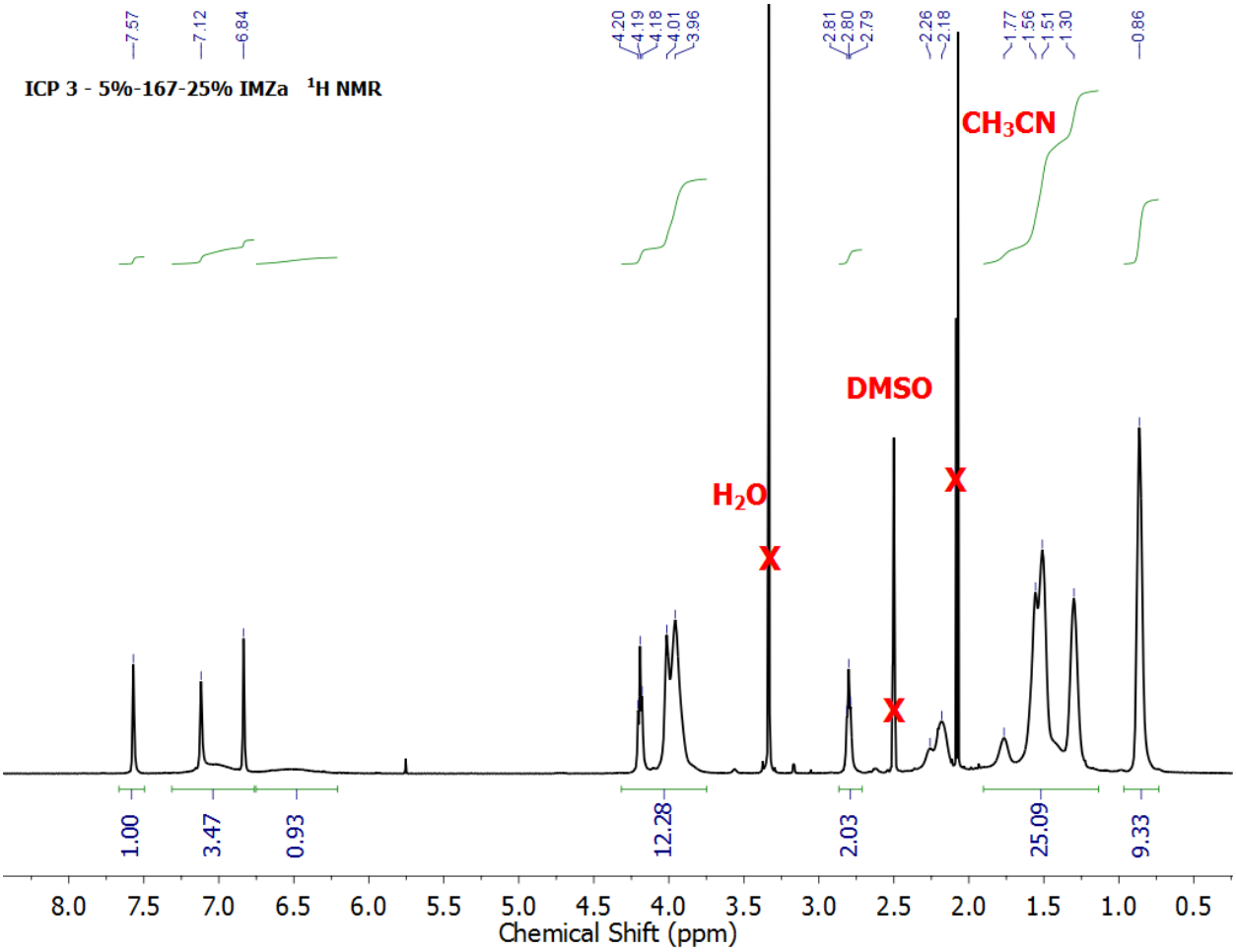

Figure 2.33 ^{1}H NMR spectrum of **ICP-3** (600 MHz, DMSO-d_6, 298 K). The molecular composition, as determined by NMR, is reported in the following format: graft density%- brush degree of polymerization- mol percent of **IMZa** (**2**) in each brush, defined as $N_{IMZa}/(N_{IMZa}+N_{BA}) \times 100$, N is the number of repeat units for each monomer.

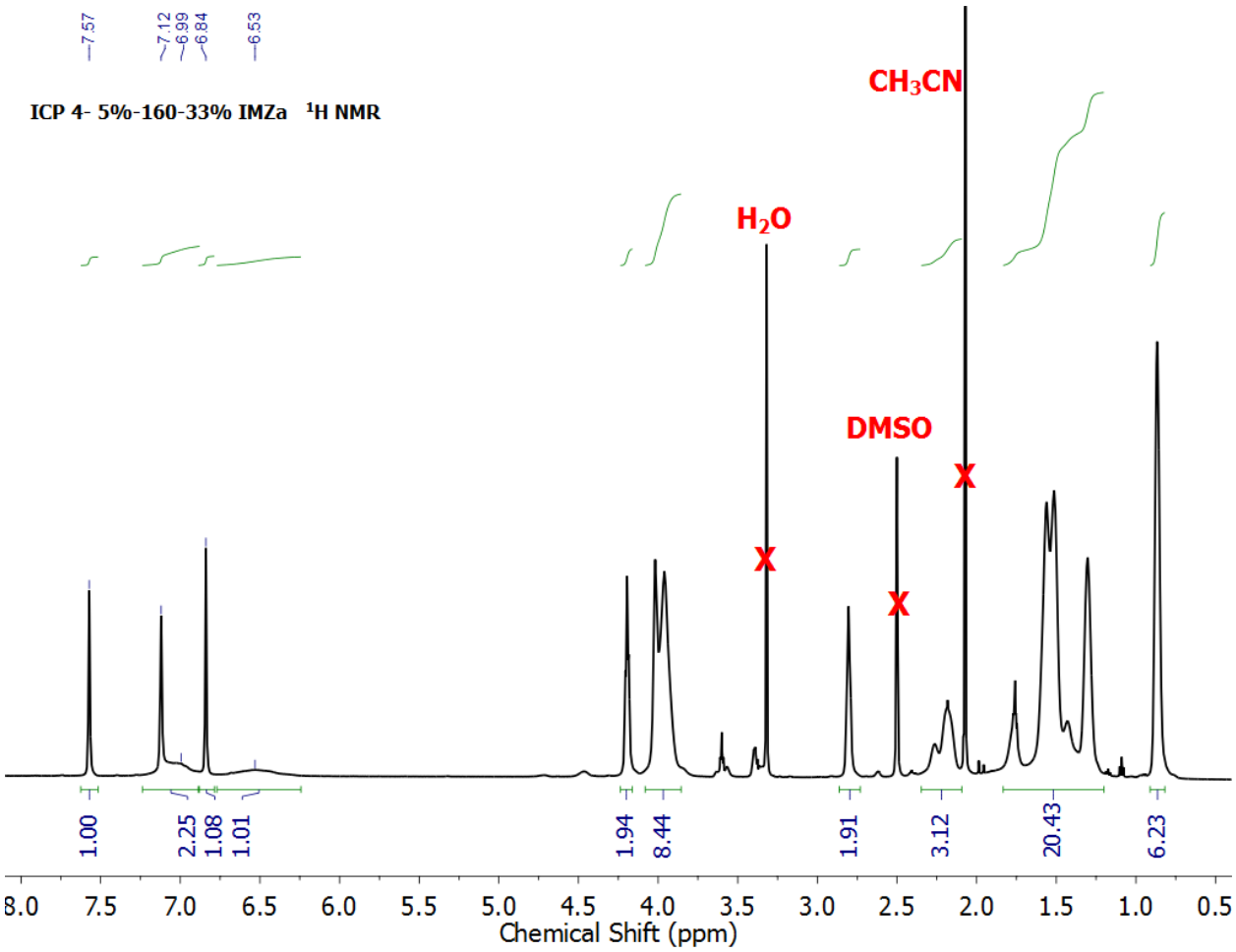

Figure 2.34 ^{1}H NMR spectrum of **ICP-4** (600 MHz, DMSO-d_6, 298 K). The molecular composition, as determined by NMR, is reported in the following format: graft density%- brush degree of polymerization- mol percent of **IMZa** (**2**) in each brush, defined as $N_{IMZa}/(N_{IMZa}+N_{BA}) \times 100$, N is the number of repeat units for each monomer.

Calculation of theoretical imidazole content

The theoretical imidazole content of each polymer was calculated after characterization of copolymers using ^{1}H NMR by considering the average brush degree of polymerization and incorporation of **IMZa**. A sample calculation is provided below. Imidazole content for other polymers are reported in Table 2.5.

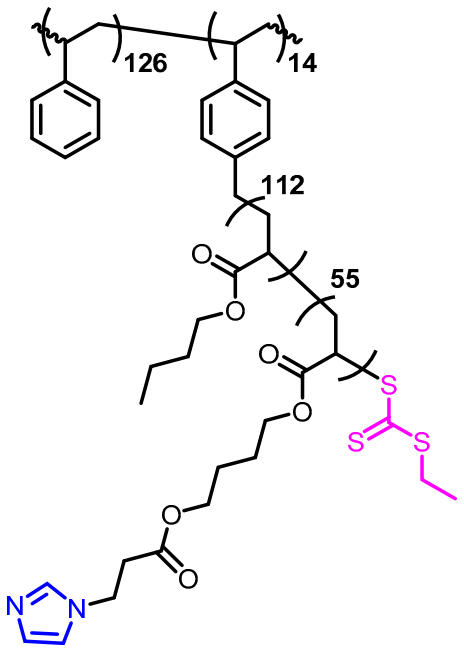

$$\text{mmol of } \mathbf{IMZa} \text{ in 1 g of polymer } = \frac{1\ \mathrm{g}_{polymer}}{M_n\left(\frac{\mathrm{g}}{mol}\right)} \times \frac{\text{mmol of } \mathbf{IMZa}}{1\ mol_{polymer}} = \frac{mmol\ \mathbf{IMZa}}{M_n}$$

$$= \frac{(\text{Avearge number of brushes per backbone}) \times (\text{Average number of IMZa per brush}) \times 1000\left(\frac{\text{mmol}}{\text{mol}}\right)}{(\text{Number average molar mass of PS backbone}) + (\text{Number of brushes}) \times (\text{Number average molar mass of brush})}$$

$$= \frac{14 \times 55 \times 1000}{(126 \times 104.15 + 14 \times 254.42) + 14 \times (55 \times 266.30 + 112 \times 128.17)} = 1.82$$

Table 2.4 Theoretical **IMZa** content (mmol/g) for various **ICP**s and control polymers.

Polymer	IMZa content (mmol/g)
ICP 1	1.44
ICP 2	1.82
ICP 3	1.40
ICP 4	1.80
Control-1	0
Control-2	1.88

This theoretical value is used to calculate L/Zn ratio where the Zn is mmol of $Zn(NTf_2)_2$ added.

Metal incorporation

Zinc di[bis(trifluoromethylsulfonyl)imide] was dissolved in 1.5 mL of CH_3CN and added incrementally (100 μL) to solution of polymer in CH_3CN (stock solution concentration 100-150 mg/mL). The sample was then agitated with a vortex mixer and/or by brief sonication until transparent, yellow solution was obtained before another aliquot of metal salt was added. The resulting homogenous solution was then transferred to a Teflon mold and the solvent was allowed to evaporate overnight under ambient conditions. Polymer sample was further dried for 12 h at 80 °C in a vacuum oven (100 Torr). To ensure the complete removal of solvents, samples were heated for another 4 h at 80 °C (1 mTorr). The bubbles were removed by compression molding the polymer film between two disks of Teflon after heating to 100 °C.

Morphological characterization of ICPs

TEM and SAXS method

TEM was performed on a FEI/Philips CM-20 conventional TEM operated at an accelerating voltage of 200 kV. The polymer was drop casted from acetonitrile and the polyacrylate phase was stained by floating the TEM grid on a 0.5 wt % aqueous solution of uranyl acetate for 1 minute, followed by removing excess solvent by placing the sample on filter paper. The samples were annealed at 80 °C overnight under vacuum.

Small angle X-ray scattering (SAXS) studies on polymer films were carried out at the Materials Research Laboratory of the University of California, Santa Barbara. Data were collected on a house built SAXS instrument equipped with a microfocus X-ray source (XENOCS Genix 50W X-ray microsource, focus size 50 micron), operating at $\lambda = 0.154$ nm. The instrument is equipped with a mar345 detector (marResearch, image plate detector, plate diameter 345mm). Source-to-sample distance was 1700 mm and the sample-to-detector distance was 1385 mm. Samples were mounted on a metal rack and fixed using tape. The scattering patterns were corrected for the beam stop and the background (Scotch tape) prior to evaluations and scaling to absolute intensity. The measurement time for the samples was 1 h in all cases.

Additional details of the homebuilt SAXS setup can be found at:

http://www.mrl.ucsb.edu/x-ray-facility/instruments/small-angle-x-ray-scattering-saxs-diffractometer.

Thermal characterization

Differential Scanning Calorimetry (DSC)

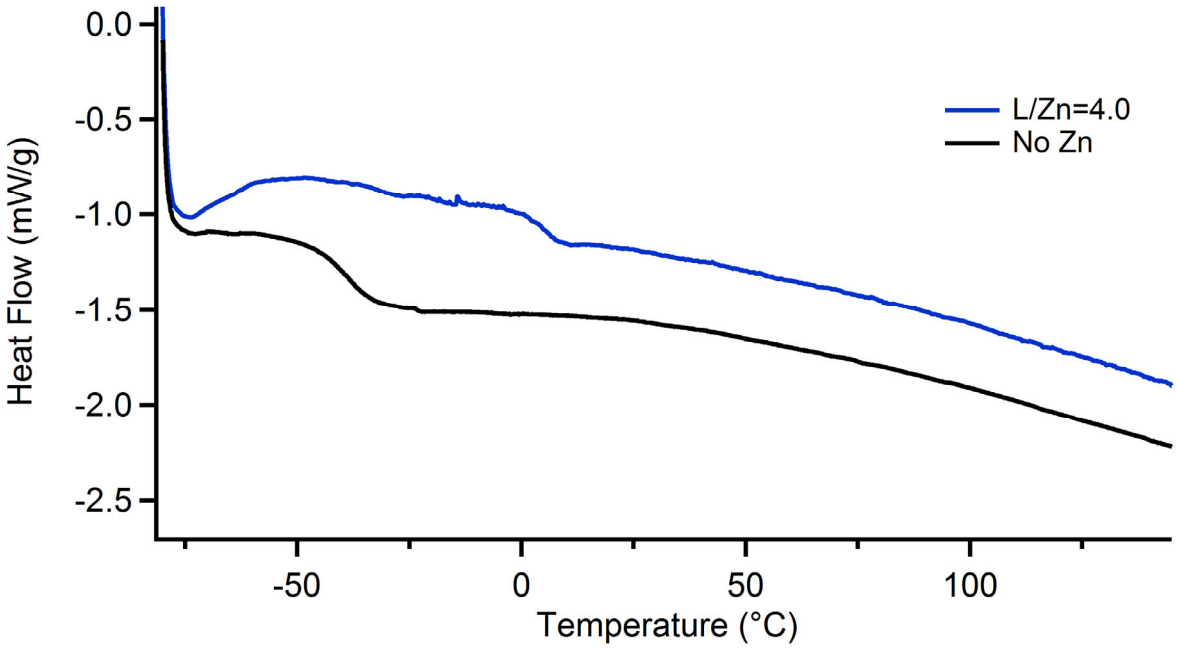

Figure 2.35 Differential scanning calorimetry (DSC) of **ICP-2** samples with no zinc, black curve, and L/Zn=4.0, blue curve. Glass transition temperature, T_g, of samples increased from -37.8 °C to 4.5 °C following the introduction of zinc which is consistent with zinc-imidazole cross-link formation.

Thermal Gravimetric Analysis (TGA)

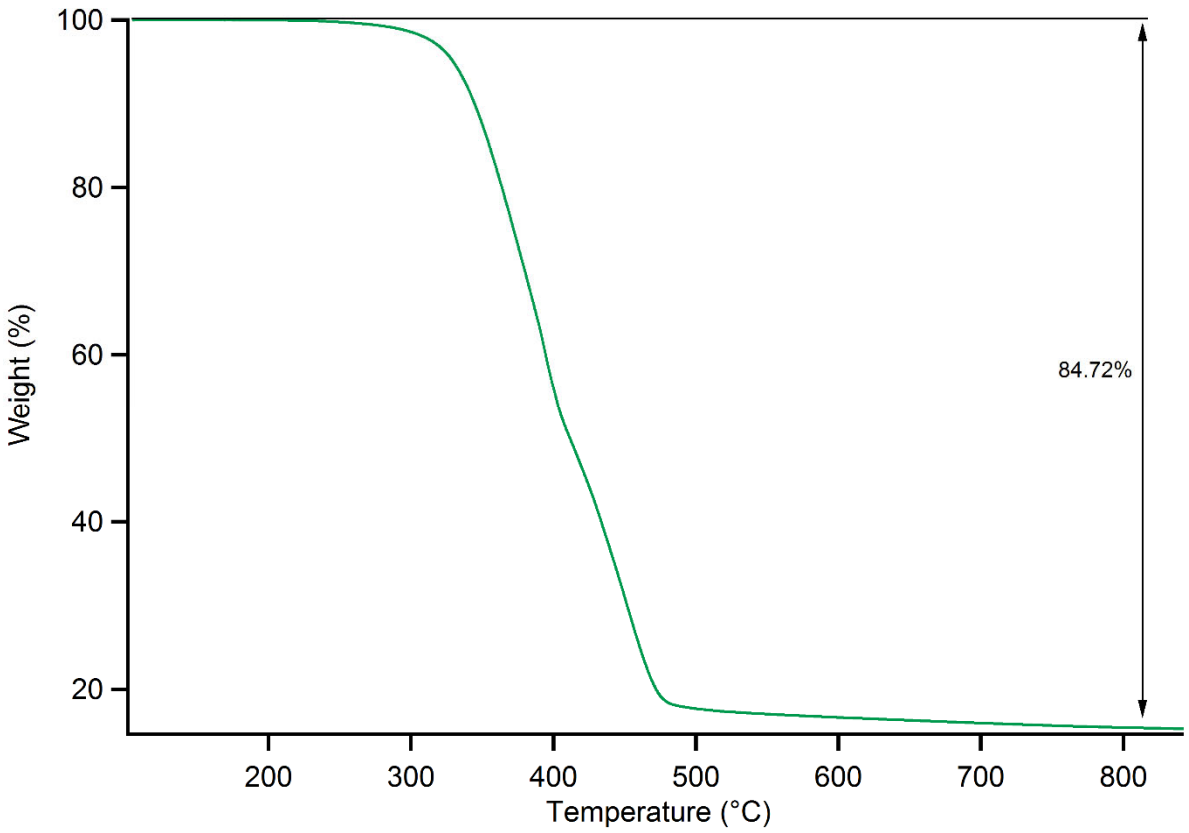

Figure 2.36 Thermogravimetric analysis (TGA) for **ICP-2** with L/Zn=4.0. No weight loss was observed below 200 °C, confirming no water or unbound residual acetonitrile in the polymer samples. The remaining mass after 800 °C corresponds to the zinc component.

Mechanical characterization

Sample preparation

Samples were prepared by hot-pressing the resin into heated Teflon molds at 100 °C and allowing them to cool down to room temperature while maintaining the pressure (cooling time approximately 30 min). Basic mechanical properties (Figure 2.17a and Table 2.5) were measured as described in the next section, mechanical testing procedure. Average sample size was 15 mm × 7 mm × 2 mm (length, width, thickness).

Samples used for self-healing studies (pristine controls and cut samples) were prepared by compression molding at 100 °C followed by cooling them gradually to room temperature over the course of 12 hours (while maintaining the pressure) to minimize any residual stress from compression molding and cooling procedure. Average sample size was 15 mm × 7 mm × 2 mm (length, width, thickness). Samples self-healing was then tested according to the procedure described in "Sample damaging and healing tests section".

All the standard deviations are calculated from independent measurements on samples with similar processing conditions.

Mechanical testing procedure

The mechanical properties of the copolymers were measured using an Instron 3365 machine in standard stress/strain experiments. The specimens were extended at 100 mm/min at room temperature. Each measurement was repeated at least three times. Young's modulus (E) was determined from the initial slope of the stress-strain curves. Creep recovery and stress-relaxation experiments were performed using a TA Instruments DMA Q800. The films were pulled at a certain stress for 300 min, and then the stress was released and the films were recovered for another 300 min at 24 °C.

Table 2.5 Summary of mechanical properties for various **ICP–Zn**.*

Polymer	L/Zn	E (MPa)[a]	σ_y (MPa)[b]	ε (%)[c]	σ (MPa)[d]	U_T(MJ.m^{-3})[e]
ICP-1	4.5	8.6 ± 1.3	0.33 ± 0.04	418 ± 35	1.1 ± 0.1	3.2 ± 0.5
	4.0	19.4 ± 0.7	1.40 ± 0.04	77 ± 11	4.9 ± 0.5	2.3 ± 0.4
ICP-2	4.5	14.3 ± 2.5	0.42 ± 0.06	593 ± 10	1.7 ± 0.1	6.8 ± 0.4
	4.0	30.7 ± 0.8	1.16 ± 0.17	623 ± 66	2.4 ± 0.1	10.4 ± 1.8
ICP-3	4.5	12.3 ± 0.4	0.59 ± 0.03	695 ± 83	1.4 ± 0.1	7.3 ± 1.1
	4.0	23.8± 0.16	1.63 ± 0.03	136 ± 20	7.0 ± 0.3	6.5 ± 0.9
ICP-4	4.5	26.8 ± 2.3	0.96 ± 0.09	370 ± 28	2.3 ± 0.2	6.5 ± 0.7
	4.0	41.0 ± 5.4	1.52 ± 0.14	221 ± 12	3.4 ± 0.5	5.5 ± 0.6
Control-2	4.5	10.8 ± 0.3	0.38 ± 0.02	2001 ± 0.0§	0.5 ± 0.0	4.6 ± 0.1
	4.0	24.3 ± 0.2	1.61 ± 0.02	84 ± 13	6.5 ± 0.6	3.4 ± 0.8

*Strain rate=100 mm min^{-1}, 24 °C. [a] Young's modulus, calculated from the initial slope of stress-strain curves; [b] yield stress, taken as strength at 10% strain; [c] ultimate extensibility (mm/mm × 100); [d] ultimate tensile stress; [e] toughness, calculated by manually integrating the area under the stress-strain curve. § Samples did not break. See Figure 2.37 for stress-strain curves. **Control-1**

samples are mechanically weak and could not be cast into films for tensile testing. See Figure 2.38 for storage and loss moduli, G′ and G″.

Effect of L/Zn on the mechanical properties

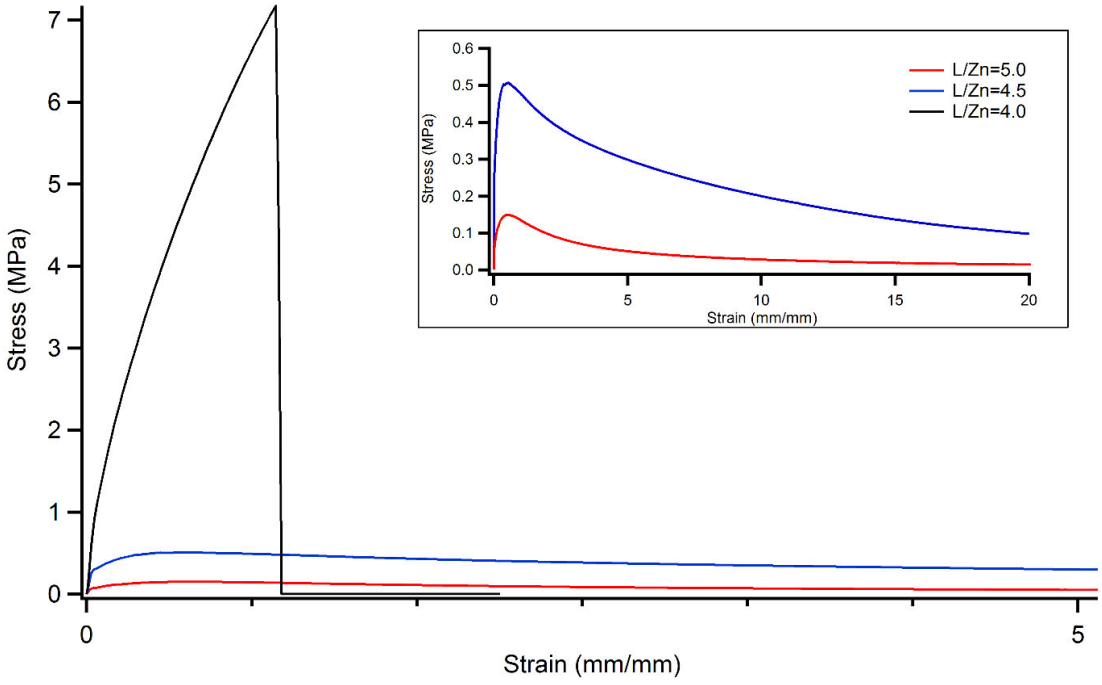

Figure 2.37 Stress–strain curves of **control-2** samples with varying amount of $Zn(NTf_2)_2$, shown as different L/Zn ratio. The inset plot depicts the range of extensibility (more than 20 times the original length) for samples with L/Zn=5 and 4.5. Critical role of collapsed polystyrene phase in initial stiffness, strength, overall extensibility and toughness is evident by comparison with Figure 3a.

Supplementary discussion

Control-2 is still cross-linked by a large number of M-L complexes despite the absence of polystyrene hard phase. Young's modulus of a cross-linked elastomer increases with the cross-

linking density. Nevertheless, addition of polystyrene hard phase significantly enhances the mechanical properties. For example, **ICP-2** contains only < 4 wt% polystyrene but shows 25% higher Young's modulus and up to 300% higher toughness. **ICP-4**, which contains the similar brush composition but with higher PS content (~8%), has a Young's modulus that is 68% higher than the **Control-2**. **Control-2** is not a typical TPE. At L/Zn ratio higher than 4, the control sample is very weak and shows strain thinning. At ligand/Zn ratio of 4.0, the sample becomes stiff but not elastomeric. In addition, **Control-2** does not show any strain hardening, which is commonly seen in stress-strain profile of normal TPEs. Furthermore, typical TPEs are microphase-separated systems; but **Control-2** does not show any microphase separation (SAXS data, Figure 2.16a).

Rheological studies

Rheology data were collected on an AR-G2 Rheometer from TA Instruments (20mm parallel steel plate, 500 μm gap). **Control-1**, brush polymer with poly(butyl acrylate) homopolymer as the brush (0% IMZa), samples were studied in a time sweep experiments to obtain the moduli of the material at 1 Hz and 1% strain at 25 °C.

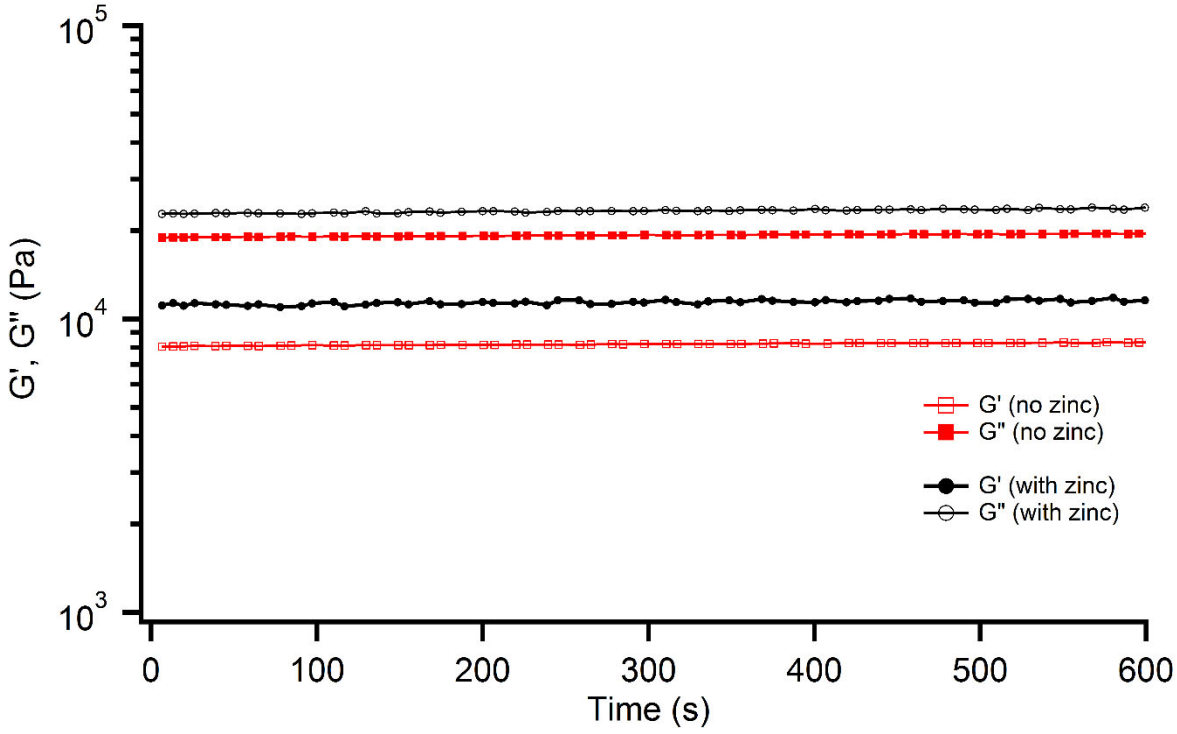

Figure 2.38 Time-sweep measurements of rheological moduli of dried poly(butyl acrylate) brush control polymer samples with (circle) and without zinc (square). Experiments were conducted at 1 Hz and 1% strain at 25 °C. Amount of zinc was calculated based on **ICP-2** polymers (35% IMZa, L/Zn=4 and 7). Only L/Zn=7 samples were homogenous after removal of acetonitrile.

Sample damaging and healing tests

For self-healing tests, a well-defined cut was applied to the depth of 70-90% of sample thickness using a razor blade. The cut faces were pressed together for 1 minute and then the sample

was let to heal at room temperature and ambient humidity for various times. The self-healed samples were then subjected to stress-strain tests at room temperature at 100 mm/min pulling rate.

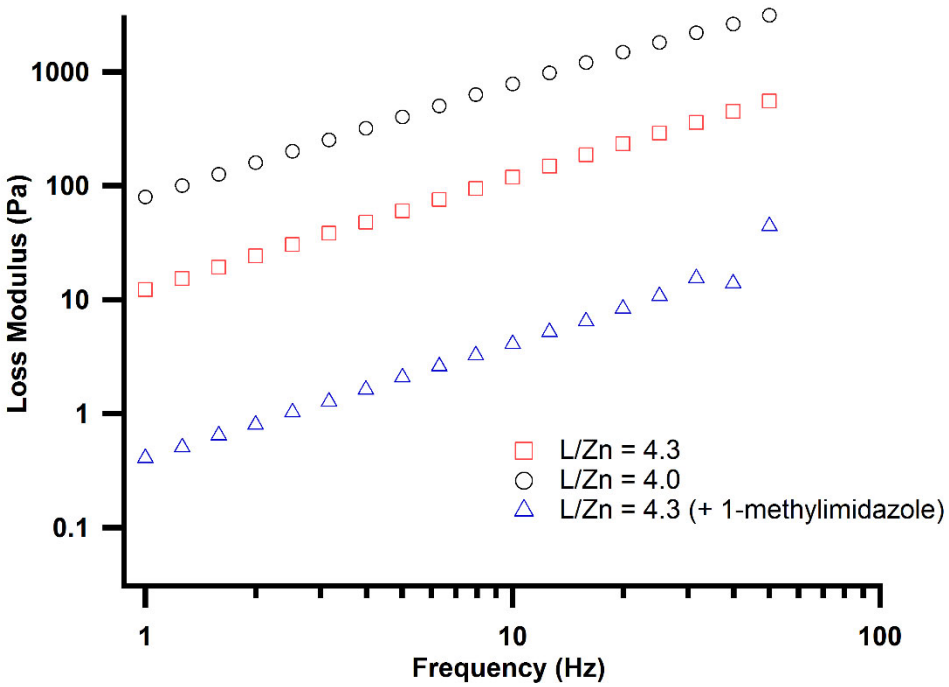

Figure 2.39 Loss modulus and dynamic viscosity of **L-ICP**–Zn solution correlates with the amount of added metal (L/Zn) and competing ligands (1-methyl imidazole). These experiments demonstrate that the emergence of mechanical properties of ICP can be attributed to M–L interactions.

Figure 2.39 Supplementary discussion

Increase in the viscosity of solution can be correlated to metal ligand complexation. Viscosity of **L-ICP** solutions ($\boldsymbol{\eta = G''/\omega}$) increases by decreasing the L/Zn from 4.3 (red squares) to 4.0 (black circles). Addition of enough 1-methylimidazole (which competes with polymer

bound imidazole moieties for binding to Zinc) to this solution, changes L/Zn to 4.3 (blue triangle). The final mixture exhibits lower viscosity than original solution with L/Zn=4.3.

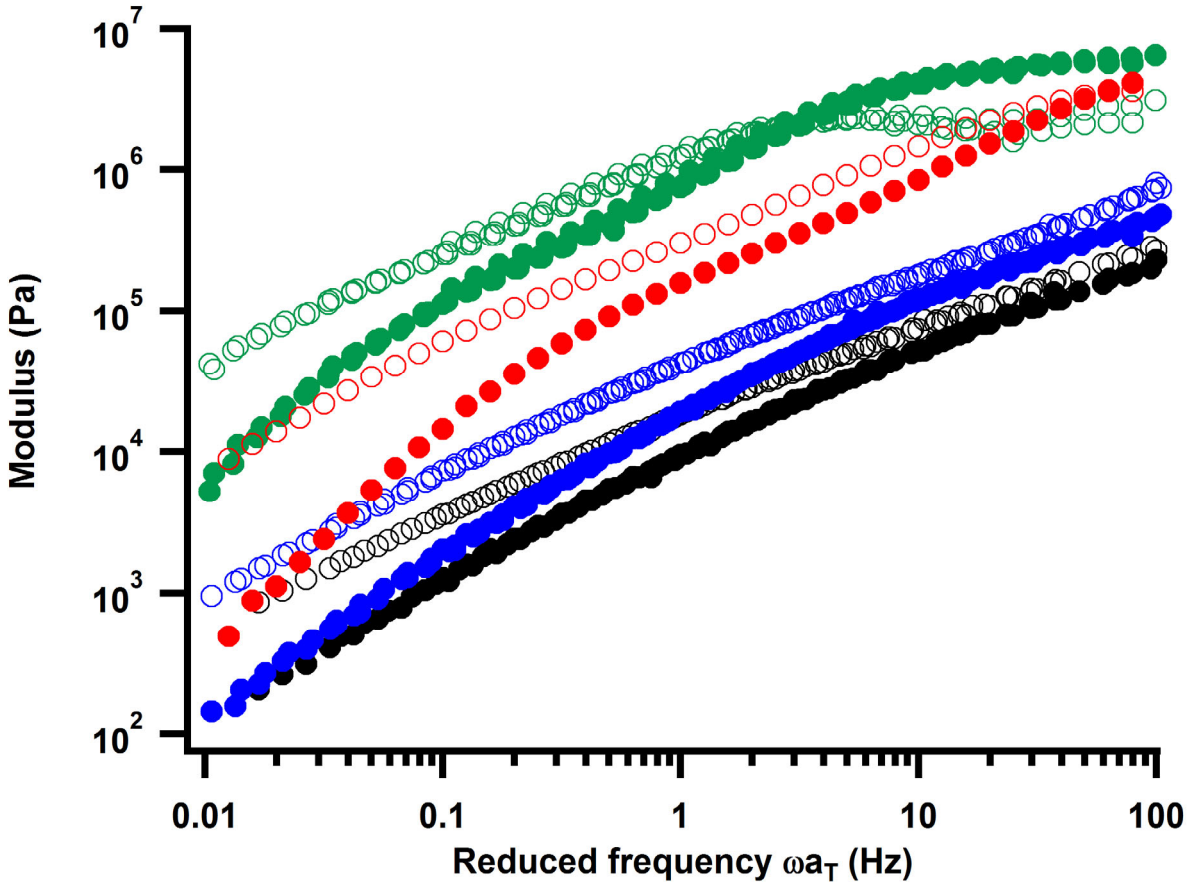

Figure 2.40 Rheological characterization of **L-ICP** cross-linked with different transition metals (L/M = 8).Frequency sweep of polymer melt with storage (G') and Loss (G"), reported as filled and open symbols. **L-ICP–Zn** (black), **L-ICP–Cu** (blue)**, L-ICP–Co** (red)**, L-ICP–Ni** (green).

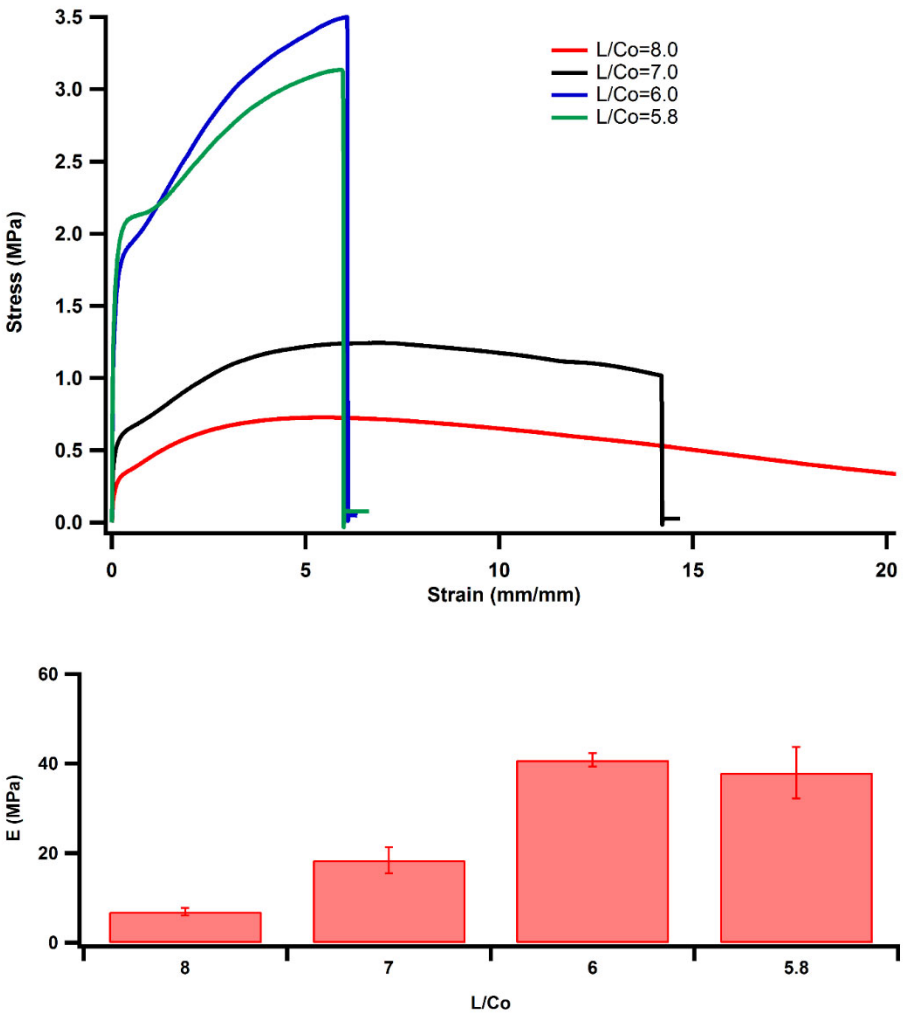

Figure 2.41 Absence of rapid transition in the mechanical properties of **ICP2–Co** near the $(L/Co)_{lim}$.

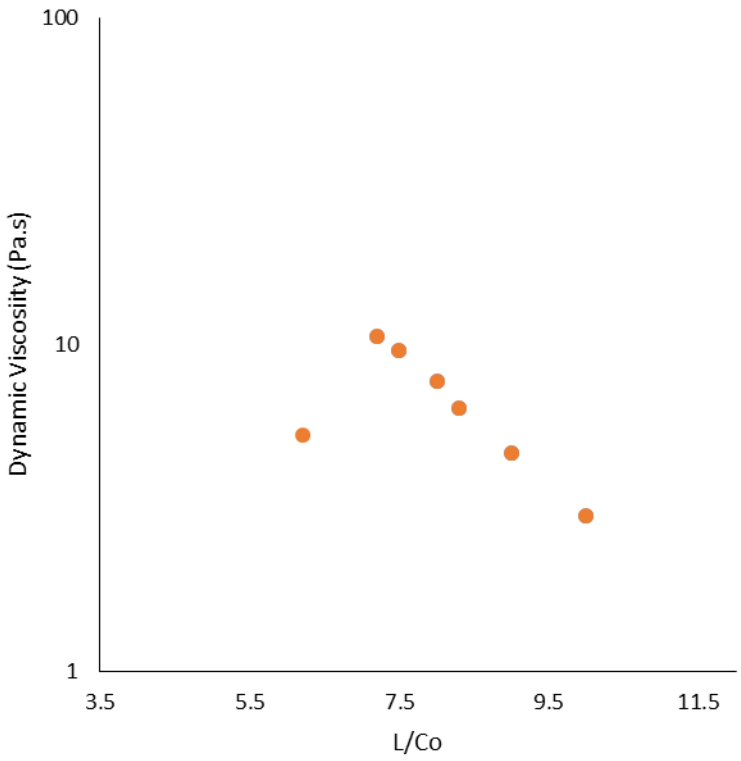

Figure 2.42 Dynamic viscosity of **L-ICP-Co** with L/Co =6.2 decreases after the precipitation of polymer samples at 20 °C.

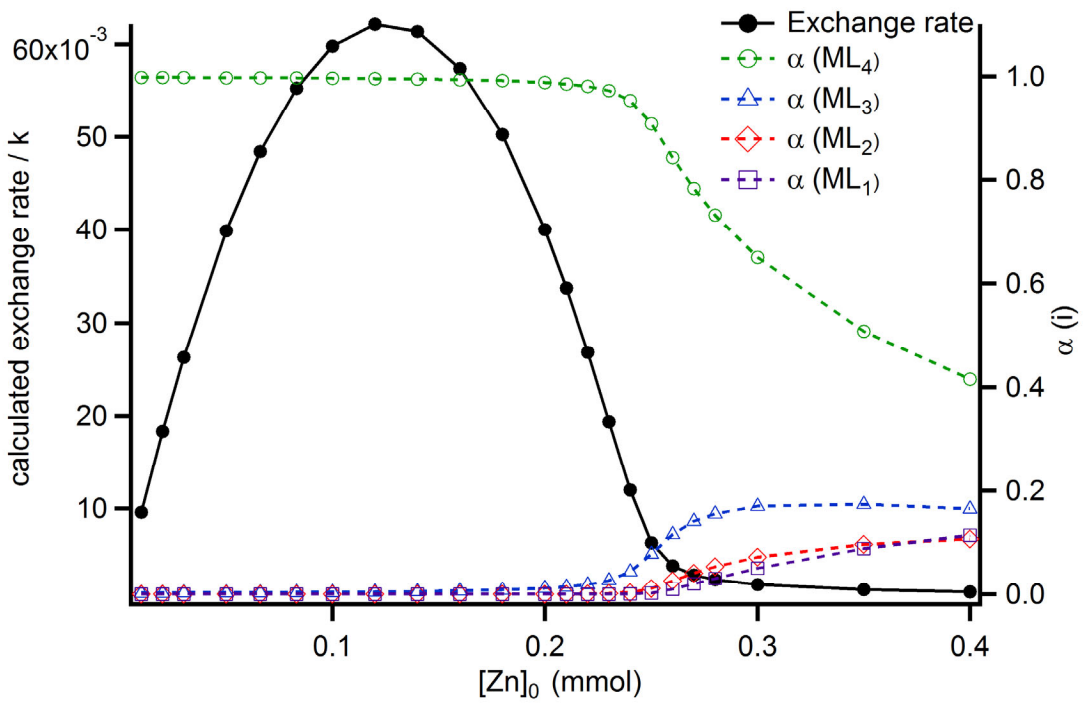

Figure 2.43 Theoretical exchange rate of ML_4 complex with L' and alpha fractions of ML_n complexes is plotted versus added zinc, $[Zn]_0$. The initial concentration of imidazole groups is assumed to be 1 mM consistent with experimental condition, this $[Zn]_0$=0.25 corresponds to L/Zn=4.

Chapter 3 Practical Synthesis of Multiphase Self-Healing Polymers from Commodity Monomers

3.1 Introduction

Progress toward inexpensive, strong, and tunable self-healing materials will significantly accelerate their adoption into commercial applications. As discussed in the chapter 2, this area of research has been under intense investigation and many strategies have emerged for the design of self-healing materials have emerged recently.[1,2] One self-healing approach is to store the reactive healing agents in the material[3-5] or delivering them via vasculature network to the damage site.[6,7] Programmed shape memory transitions are investigated to physically close the damaged gap and facilitate polymer diffusion across the cut interfaces and subsequent healing.[8] Additionally, significant efforts have been directed at the discovery of new intrinsically self-healing polymers to design materials that can efficiently repair themselves after multiple cycles of damage. During the last decade, many new covalent bonds (i.e. metathesis of double bonds[9], disulfide bond exchange[10], thiuram disulfide[11], siloxane exchange[12], exchange of catechol-based boronic ester[13], Diels-Alder reaction[14], and etc.) and non-covalent interactions[15] have been explored as dynamic motif. Supramolecular interactions, such as metal-ligand[16,17], host-guest[18], π–π stacking[19], ionic[20], hydrogen bonds[21] and etc., have been also a subject of intensive investigation since the broad tunability of their kinetic and thermodynamic parameters can be productively utilized to control mechanical and self-healing properties.[22]

Over the past few years, our laboratory contributed to the development of self-healing systems utilizing dynamic interactions.[9,23-25] We demonstrated that a multiphasic copolymer that phase separates into glassy domains with high glass transition temperature (T_g) embedded in a

matrix of dynamic non-covalent interactions, H-bond or metal-ligand interactions, with high mobility is a promising route to combine efficient self-healing and strong mechanical properties. This multiphase approach overcame one major obstacle to realizing the wide spread use of self-healing polymers utilizing non covalent, dynamic interactions. By introducing a discontinuous glassy hard phase (to improve stiffness and yield strength) covalently connected to a continuous soft phase bearing a robust network of dynamic motifs, we circumvented the inherent trade-off between stiff low-strain mechanical response and stimulus-free dynamic self-healing to effect nearly quantitative self-healing after catastrophic macroscopic damage.

Many previously reported self-healing materials, including some of our previous systems, require custom designed monomers and polymers, making them economically unfeasible for large-scale manufacturing and practical applications. To move the field forward, it is critical to devise a practical and scalable synthesis to access self-healing polymers with robust properties. Herein, we developed an easy and scalable synthesis of strong self-healing materials with tunable mechanical properties by using simple commercially available building blocks. Specifically, we have adopted a brush copolymer architecture we used previously[25], in which a glassy polystyrene backbone (PS) backbone was grafted with multiple brushes containing multivalent hydrogen bonding sites. We employed a simple commodity monomer, acrylamide monomer (**AM**), as the hydrogen bonding building block, because of its robust hydrogen bonding capability and low cost. In order to maintain dynamics in the continuous soft phase for spontaneous healing under mild conditions, we

copolymerized **AM** with another inexpensive commodity monomer, n-butyl acrylate (**BA**) for the brush synthesis (Figure 3.1)

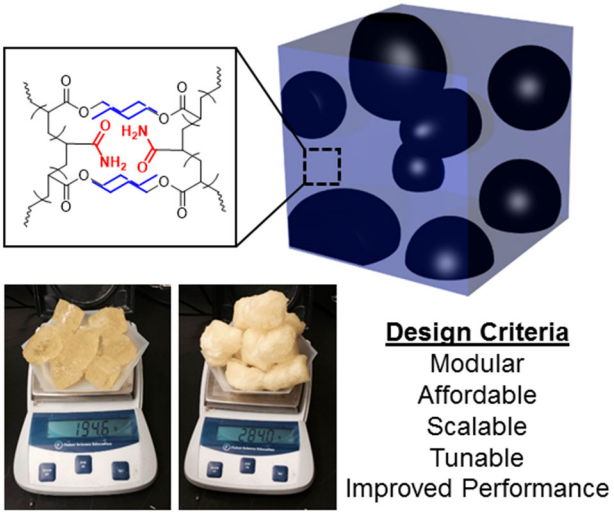

Figure 3.1 Schematic of modular multiphasic self-healing materials from inexpensive commercially available monomers. **AM** is used as the dynamic H-bond motif and T_g is controlled by the incorporation of **BA**. The modular synthesis is scalable and provides an affordable way to synthesize tunable and strong self-healing polymers (scale up photos by Dr. Aaron Kushner).

3.2 Synthesis and characterization

We adapted our previous synthesis to obtain a scalable protocol for the synthesis of brush copolymers containing **BA** and **AM**, hence referred to as **BAAM**, covalently connected to a polystyrene domain at one end (Scheme 3.1). The polystyrene backbone, which phase-separates into stiff glassy nano-domains in the final bulk structure, was synthesized via free radical polymerization of styrene and 4-vinylbenzyl chloride, followed by substitution by trithiocarbonate to yield macro-chain transfer agents, **mCTA**s. For this study, we prepared 3 different backbones with an approximate length of 140 repeat units and different density of chain transfer agents (5, 10 and 15 mol%, corresponding to 7, 14, and 21 brushes per backbone), to test whether changes in

graft density, which likely affect the dynamics of phase separation and self-assembly of the glassy styrene domains, can be used as an effective structure/property design handle.

From this series of **mCTA**s we grew **BAAM** brush copolymers of independently varying brush length and composition to probe the effects of changing hard-phase volume fraction and soft-phase glass transition temperature on the mechanical properties of the resulting brush copolymers. We chose reversible addition fragmentation chain transfer polymerization (RAFT) as a living/controlled radical polymerization method for the brush synthesis.[26] All intermediates and products could be effectively isolated and purified using simple precipitation technique, which reduces the cost of synthesis and makes it easy to scale up. The details of synthetic protocols, characterization, and full brush copolymer study series are reported in the Supporting Information.

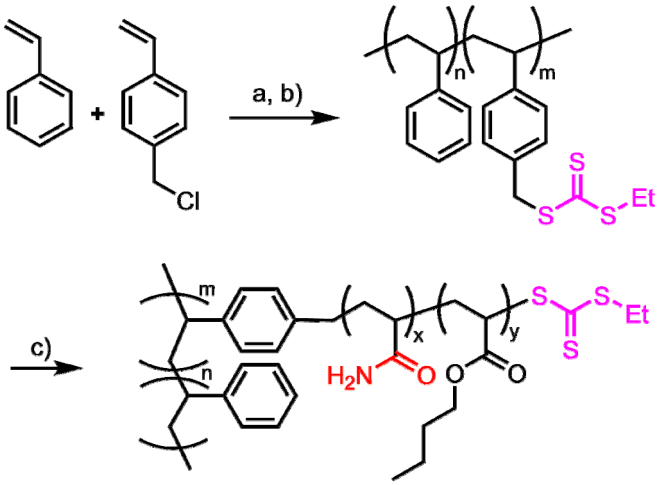

Scheme 3.1 Synthesis of **BAAM** copolymers. Conditions a) AIBN, toluene, 75 °C; b) Potassium ethyl trithiocarbonate ($KSCS_2Et$), acetone; c) **BA**, **AM**, AIBN, DMF, 55 °C. AIBN = azobisisobutyronitrile, **BA** = n-butyl acrylate, **AM** = acrylamide, DMF = dimethylformamide.

Following this simple, robust protocol, we synthesized a series of **BAAM** brush copolymers to investigate the tunability of the new system. Table 3.1 summarizes the molecular

compositions of the **BAAM** brush copolymers and a control polymer (which lacks the polystyrene backbone) prepared for this study.

Table 3.1 Molecular parameters of BAAM copolymer system.

Polymer	Graft Density[a]	# of repeat units on each brush [b]	AM mol%[b]
BAAM 1	5	270	16%
BAAM 2	5	250	22%
BAAM 3	5	290	30%
BAAM 4	5	94	24%
BAAM 5	5	224	22%
BAAM 6	10	190	23%
BAAM 7	10	240	22%
BAAM 8	15	170	23%
Control-1 *	N/A	180	22%

[a] Estimated from ^{1}H NMR of polystyrene backbones. Backbone length (degree of polymerization) was kept constant at ~140. [b] Estimated from ^{1}H NMR of final brush copolymer after deuterium exchange. The **AM mol%** is defined as the mol percent of **AM** in the brushes. More details are provided in the supporting information. * **Control-1** lacks the polystyrene backbone.

3.3 Mechanical characterization

After purification and molecular characterization, the mechanical properties of each polymer were tested both in static tensile experiments and dynamic mechanical thermal analysis (DMTA). Mechanical properties of **BAAM** copolymers can be easily tuned over an order-of-magnitude range by varying a few easily controlled molecular parameters (Figure 3.2).

3.3.1 Tuning of mechanical properties by changing AM incorporation

BAAM 1-3 polymers were first synthesized to study the effect of the concentration of **AM** monomer in the brushes on mechanical properties. For this series, the graft density and brush

length (degree of polymerization, DP) were kept constant (~ 5% graft density, DP = 270) with the **AM** content being varied by changing **BA**/**AM** feed-ratio during RAFT polymerization (**BAAM-1** 16 mol% **AM**, **BAAM-2** 22 mol% **AM**, and **BAAM-3** 30 mol% **AM**). Static tensile tests show that **BAAM-1** polymer, with the lowest **AM** ratio (16 mol%; black line Figure 3.2a), was highly extensible (*ca.* 1400%) with relatively low Young's modulus (*ca.* 5 MPa). Increasing the AM incorporation to 22 mol% in **BAAM-2** (red line Figure 3.2a) resulted in an increase in the Young's modulus (ca. 18 MPa) and the ultimate strength (3.2 MPa) while reducing the extensibility to 870%. The expected trend continued when more **AM** was incorporated in the brush copolymer: in **BAAM-3** with 30 mol% **AM** (blue line Figure 3.2a) the Young's modulus and ultimate tensile strength were increased to 162 MPa and 11 MPa respectively, while samples remained intact on extension beyond 600% strain. As can be seen in Figure 3.2a, the mechanical properties at room temperature can be continuously varied from soft rubber, to stiff rubber/tough leather, to strong and tough thermoplastic elastomer, with a relatively minor change in molecular composition (change in **AM** mol% < 15%). A summary of mechanical properties of **BAAM 1-8** is reported in Table 3.2. We also studied the dynamic response of **BAAM 1-3** across a range of temperatures (-30 °C to +65 °C) to complement the static uniaxial tension experiments (See Figure 3.17-3.19 for complete curves). Figure 3.2a inset shows the dependence of loss-ratio (tan δ) peak position on the **BA/AM** ratio. DMTA characterizations reveals that as expected the simple copolymerization for brush growth offers a convenient handle to control the T_g (defined here as the location of tan δ peak) of the soft phase by simply adjusting the **BA/AM** ratio (See Figure 3.15 for an approximation of T_g using Flory-Fox equation and an explanation of observed discrepancies as well as observed linear dependence).

3.3.2 Tuning of mechanical properties by changing graft density and brush length

The mechanical properties of the brush copolymers can also be tuned by changing the graft density and the brush length of the copolymers while keeping the **AM** mol% ~ 22. For this purpose, a new series, **BAAM 4-8**, were synthesized for mechanical investigation. Figure 3.2b shows the additional tunability of our system by varying the graft density and brush length (degree of polymerization) for **BAAM 4**, **6** and **8** polymers. A summary of static mechanical properties of all

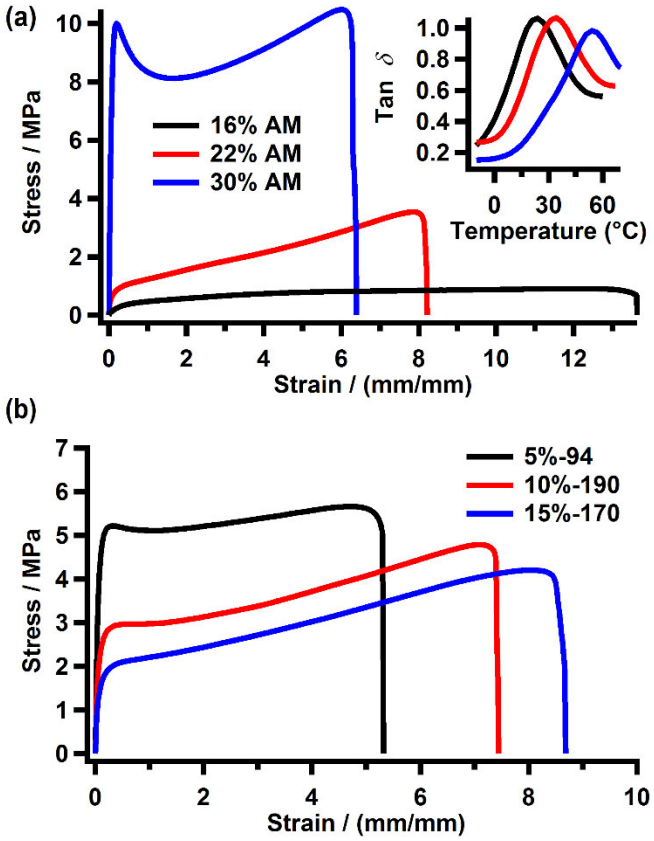

Figure 3.2 Tunability of **BAAM** copolymer mechanical properties by varying molecular parameters. **(a)** Static tensile stress-strain curves of polymers with varying incorporation of **AM** monomer (graft density of 5% and brush length of ~ 270 repeat unit.). Inset illustrates the modulation of tan δ peak by varying the AM% in the polymer sample. **(b)** Tunability of **BAAM** copolymer mechanical properties by varying molecular parameters (summarized as graft density-brush lenght). Mechanical properties such as Young's modulus, Yield strength, extensibility can be further fine-tuned by changing graft density and graft-length.

polymers is reported in the Table 3.2. In general, the mechanical properties of the polymers correlate with the volume fractions of the hard and soft phases. The Young's modulus, tensile strength, and extensibility can be easily modulated by adjusting the volume fraction of PS hard phase in the final copolymers. **BAAM-4** (Figure 3.2b, black line), with the lowest graft density (5%) and shortest brush length (94 repeat units), has the highest Young's modulus (ca. 95 MPa) and ultimate strength (ca. 6 MPa). By increasing the brush length (190 monomer repeat units) and the density of brushes (to 10%) in **BAAM-6** (Figure 3.2b, red line), the Young's modulus can be tuned to 54.5 MPa and higher extensibility (712%) is achieved. Further increasing the graft density from 10% to 15% (**BAAM-8**) results in additional decrease in the Young's modulus and yield strength while increasing the sample extensibility (Figure 3.2b, blue line). The control sample that lacks the PS hard phase has a much lower ultimate strength (0.4 MPa) and does not display any strain hardening behavior.

For polymers with small PS content, with high brush length (**BAAM- 5** and **7**) or high different graft density (**BAAM-8**), the changes in volume fraction of the hard phase is negligible and some of their static mechanical properties, such as Young's Modulus and ultimate strength converges. Yield strength and extensibility are still tunable and are probably affected by the spacing between the brushes which regulates their assembly and interactions. These changes in molecular compositions also affects the rate of self-healing, *vide infra*. To our satisfaction, static tensile data quickly revealed that our affordable, modular system with increased scalability and design exhibits improved mechanical characteristics bringing the performance into closer alignment with commercial thermoplastic elastomer systems (Figure 3.23), which possess no intrinsic, spontaneous self-healing function.

Table 3.2 Summary of static mechanical properties of **BAAM 1-8** and **Control-1**.

Polymer	Composition[a]	E (MPa)[b]	ε (%)[c]	σ_{ult} (MPa) [d]	U_T (MJ/m^3)[e]
BAAM-1	5%-270-16%	5.0 ± 1.2	1230 ± 130	1.2 ± 0.3	11.6 ± 2.7
BAAM-2	5%-250-22%	18.3± 1.1	867 ± 61	3.1 ± 0.3	17.2 ± 0.7
BAAM-3	5-290-30%	163 ± 26	647 ± 68	10.9 ± 1.3	60.1 ± 10.5
BAAM-4	5%-94-24%	95.3 ± 3.4	591 ± 46	5.8 ± 0.3	31.7 ± 3.3
BAAM-5	5%-224-22%	30.3 ± 4.4	1006 ± 53	4.2 ± 0.4	29.9 ± 0.8
BAAM-6	10%-190-23%	54.5 ± 2.0	712 ± 40	4.8 ± 0.2	26.1± 2.0
BAAM-7	10%-24022%	32.8 ± 3.7	778 ± 134	4.1 ± 0.4	20.5 ± 2.3
BAAM-8	15%-170-23%	32.0 ± 2.9	802 ± 92	4.0 ± 0.4	25.4 ± 3.6
Control-1	N/A-180-22%	7.6 ± 1.24	2270 ± 137	0.36 ± 0.02	2.0 ± 0.2

[a] Reported as graft density (%)-degree of polymerization-**AM** mol%. See Table 3.1 and experimental section for detailed characterization information. [b] Calculated from the initial slope of stress-strain curves. [c] Ultimate extensibility [d] Ultimate Strength-at-break [e] Toughness, calculated from integrating the area under the stress-strain curve. All static tensile experiments are conducted with the strain rate of 100 mm.min^{-1}, at 24 °C.

3.4 Phase morphology characterization

The phase morphology of **BAAM** polymer samples in the solid state was investigated by transmission electron microscopy (TEM). As shown in Figure 3.3, spherical PS nanodomains with size (diameter) ~25 nm are dispersed in a continuous matrix of soft brushes containing dynamic hydrogen bonds which are stained by uranyl acetate to appear darker. This is consistent with our previous reports and demonstrates that the two-phase morphology is retained despite the change in monomer compositions.

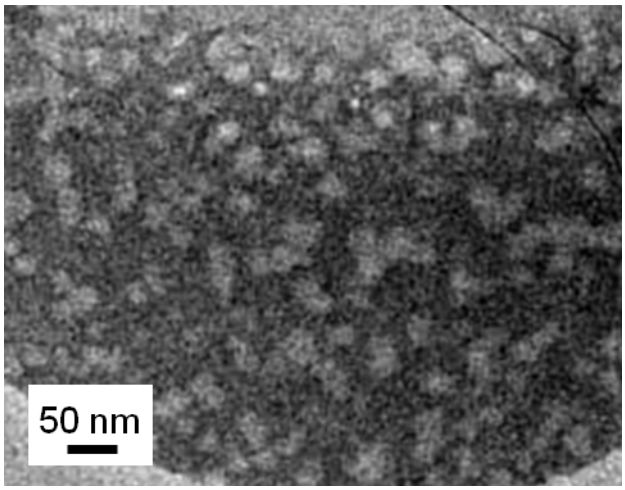

Figure 3.3 Morphological characterization of **BAAM** system. TEM image shows spherical PS aggregated in a matrix of **BA/AM** brushes (TEM images by Olivia Cromwell).

3.5 Investigation of self-healing properties

Finally, we investigated the self-healing properties of **BAAM** polymers. All **BAAM** polymer samples with **AM** incorporation of 16 mol% and 22 mol% healed spontaneously under mild conditions. The T_g for 30 mol% **AM** polymer, **BAAM-3**, was higher than 50 °C, which understandably prohibits self-healing at room temperature (intermediate-to-long range chain mobility is a requirement for effective healing performance). We focused our self-healing studies on **BAAM 4-8** with 22 mol% **AM** polymers. Each tensile specimen was damaged by making a

well-defined cut to the depth of 70-90% of sample thickness using a razor blade. The two cut interfaces were then pressed back together for 1 min.

The damaged samples showed very good self-healing ability. For all healing times, stress–strain curves closely followed the shapes of the original uncut samples. While all samples quickly recovered their strength up to the yield point, samples with lower brush length (**BAAM-6** and **BAAM-8,** average brush length 180 units) recovered more than 85% of their original strength and extensibility in 15 h (Figure 3.4a and 3.22). Polymer samples with longer brush length (**BAAM-5, BAAM-7** with an average brush length of 230) had an improved the rate of self-healing:

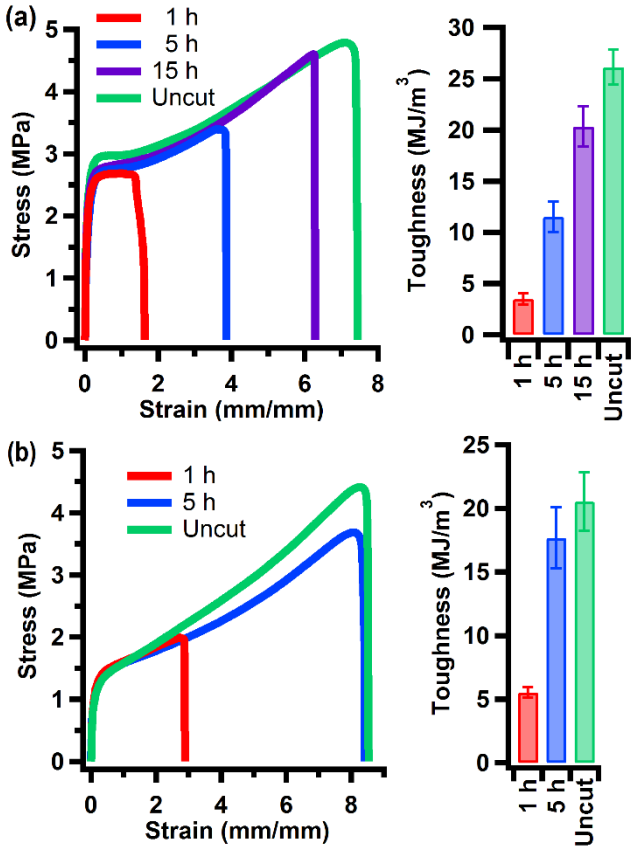

Figure 3.4 Representative self-healing tests for (a) **BAAM-6** (10%-190) and (b) **BAAM-7** (10%-240) at 30 °C and ambient humidity. The bar graph summarizes the toughness recovery for any time point. Error bars are standard deviation of three-five measurements.

recovery of extensibility and ultimate strength was achieved in 5 h (Figure 3.4b and 3.21). **BAAM-4**, with the shortest brush length and lowest graft density, recovered up to 60% of the ultimate strength of the pristine sample and 70% of original extensibility (Figure 3.20).

3.6 summary and conclusion

In summary, we have demonstrated that strong, tunable, and self-healing polymer materials can be synthesized from simple commercially available building blocks in a facile and scalable manner. The mechanical properties of the materials can be conveniently tuned by varying several molecular parameters including the acrylamide ratio, the brush length and density. The new multiphase polymers show excellent self-healing performance under mild conditions. We expect that this new class of materials to have a broad impact given the simplicity of synthesis, commercial availability of all building blocks, and high level of tunability of mechanical properties.

3.7 References

(1) Murphy, E. B.; Wudl, F. *Prog. Polym. Sci.* **2010**, *35*, 223.
(2) Yang, Y.; Urban, M. W. *Chem. Soc. Rev.* **2013**, *42*, 7446.
(3) Dry, C. *Compos. Struct.* **1996**, *35*, 263.
(4) Cho, S. H.; Andersson, H. M.; White, S. R.; Sottos, N. R.; Braun, P. V. *Adv. Mater.* **2006**, *18*, 997.
(5) White, S. R.; Sottos, N. R.; Geubelle, P. H.; Moore, J. S.; Kessler, M. R.; Sriram, S. R.; Brown, E. N.; Viswanathan, S. *Nature* **2001**, *409*, 794.
(6) Toohey, K. S.; Sottos, N. R.; Lewis, J. A.; Moore, J. S.; White, S. R. *Nat. Mater.* **2007**, *6*, 581.
(7) White, S. R.; Moore, J. S.; Sottos, N. R.; Krull, B. P.; Santa Cruz, W. A.; Gergely, R. C. R. *Science* **2014**, *344*, 620.
(8) Kirkby, E. L.; Rule, J. D.; Michaud, V. J.; Sottos, N. R.; White, S. R.; Manson, J.-A. E. *Adv. Funct. Mater.* **2008**, *18*, 2253.
(9) Lu, Y.-X.; Guan, Z. *J. Am. Chem. Soc.* **2012**, *134*, 14226.
(10) Canadell, J.; Goossens, H.; Klumperman, B. *Macromolecules* **2011**, *44*, 2536.
(11) Amamoto, Y.; Otsuka, H.; Takahara, A.; Matyjaszewski, K. *Adv. Mater.* **2012**, *24*, 3975.
(12) Zheng, P.; McCarthy, T. J. *J. Am. Chem. Soc.* **2012**, *134*, 2024.

(13) He, L.; Fullenkamp, D. E.; Rivera, J. G.; Messersmith, P. B. *Chem. Commun.* **2011**, *47*, 7497.
(14) Chen, X.; Dam, M. A.; Ono, K.; Mal, A.; Shen, H.; Nut, S. R.; Sheran, K.; Wudl, F. *Science* **2002**, *295*, 1698.
(15) Herbst, F.; Doehler, D.; Michael, P.; Binder, W. H. *Macromol. Rapid Commun.* **2013**, *34*, 203.
(16) Burnworth, M.; Tang, L.; Kumpfer, J. R.; Duncan, A. J.; Beyer, F. L.; Fiore, G. L.; Rowan, S. J.; Weder, C. *Nature* **2011**, *472*, 334.
(17) Bode, S.; Zedler, L.; Schacher, F. H.; Dietzek, B.; Schmitt, M.; Popp, J.; Hager, M. D.; Schubert, U. S. *Adv. Mater.* **2013**, *25*, 1634.
(18) Nakahata, M.; Takashima, Y.; Yamaguchi, H.; Harada, A. *Nat. Commun.* **2011**, *2*, 1521/1.
(19) Burattini, S.; Greenland, B. W.; Merino, D. H.; Weng, W.; Seppala, J.; Colquhoun, H. M.; Hayes, W.; Mackay, M. E.; Hamley, I. W.; Rowan, S. J. *J. Am. Chem. Soc.* **2010**, *132*, 12051.
(20) Kalista, S. J., Jr.; Ward, T. C.; Oyetunji, Z. *Mech. Adv. Mater. Struct.* **2007**, *14*, 391.
(21) Cordier, P.; Tournilhac, F.; Soulie-Ziakovic, C.; Leibler, L. *Nature* **2008**, *451*, 977.
(22) Aida, T.; Meijer, E. W.; Stupp, S. I. *Science* **2012**, *335*, 813.
(23) Hentschel, J.; Kushner, A. M.; Ziller, J.; Guan, Z. *Angew. Chem., Int. Ed.* **2012**, *51*, 10561.
(24) Mozhdehi, D.; Ayala, S.; Cromwell, O. R.; Guan, Z. *J. Am. Chem. Soc.* **2014**, *136*, 16128.
(25) Chen, Y.; Kushner, A. M.; Williams, G. A.; Guan, Z. *Nat. Chem.* **2012**, *4*, 467.
(26) Moad, G.; Rizzardo, E.; Thang, S. H. *Aust. J. Chem.* **2009**, *62*, 1402.

3.8 Experimental details and supporting information

General materials and methods

^{1}H spectra were recorded on 500 MHz and 600 MHz Bruker instruments. Chemical shifts were reported in standard format as values in ppm relative to deuterated solvents. Gel permeation chromatography (GPC) was performed in THF (1 mL/min) using an Agilent LC 1100 Series equipped with Polymer Laboratory's PLgel 5 μm mixed-C column to determine molecular weights and molecular weight distributions, M_w/M_n, of the macro-CTAs with respect to polystyrene (PS) standards (Varian, Palo Alto, CA). Brush copolymers were analyzed using GPC in DMF with 0.1% LiBr (w/v) (1 mL/min) using an Agilent LC 1100 Series equipped with OHpak SB-803 HQ column from Shodex to determine molecular weights and molecular weight distributions, M_w/M_n, with respect to poly(ethylene glycol) (PEG) standards (Sigma Aldrich).

All other chemicals were purchased from Sigma Aldrich and were used as received. Inhibitors were removed by passing the monomers through basic alumina column for butyl acrylate and styrene. 4-vinylbenzyl chloride, technical grade, was used as received and was not passed through basic column before polymerization.

Synthesis and characterization

Typical macro-CTA synthesis

Macro-CTA synthesis was carried out as previously described.[24]

Synthesis of brush copolymers, BAAM

A typical procedure for the synthesis of **BAAM** brush copolymers using RAFT polymerization is given below. **Control-1** was synthesized by RAFT polymerization using a small molecule chain transfer agent instead of macro-CTA, resulting in a linear copolymer of **BA** and **AM** comonomer.

m-CTA 2 (1.0 g, 0.45 mmol CTA) was added to a Schlenk flask. BA (8.9 mL, 62 mmol) and 2 mL anisole as NMR internal standard were dissolved in DMF (60 mL) and added to the flask under stirring. After complete dissolution of m-CTA2 polymer, acrylamide (Stock solution of AIBN (20.5 mg/mL in DMF) was prepared and 282 μL (5.78 mg, 0.035 mmol) was transferred to reaction flask ([Monomer]:[CTA]:[AIBN] = 250:1:0.2). 50 μL sample was taken for calculating the conversion using ^{1}H NMR and reaction flask was sealed by a rubber septum. The reaction mixture was then purged with a stream of N_2 for 45 min followed by 15 min of head space purging. Schlenk flask was immersed in an oil bath thermostatted at 55 °C. After 11.5 h, the reaction was removed from the oil bath and was cooled on ice. The conversion was determined with ^{1}H NMR by comparing the integration of vinyl protons with respect to anisole protons (OCH_3). 10 mg of 4-methoxyphenol was added as radical inhibitor and the solvent was evaporated *in vacuo*. The polymer was precipitated by slow addition of viscous residue to 1 L of methanol-water mixture, (1:1 v/v). Magnetic stir bars were not effective in stirring the solution during the precipitation of the polymer. It was necessary to use a mechanical overhead stirrer in a large beaker to successfully precipitate the polymer under continued stirring. The supernatant was carefully decanted polymer

was washed sequentially with hexane (2x) and methanol-water solution (2x, 1:1 v/v) to remove the unreacted monomer. Finally, the polymer was resuspended in methanol-chloroform solution and was transferred to a Teflon dish. Solvent was allowed to evaporate at room temperature overnight and the residual solvent was removed by heating the samples in a vacuum oven overnight at 80 °C.

M_n and M_w/M_n for each polymer was characterized by size exclusion chromatography using DMF as solvent and PEG as standard. The results are summarized in Table 3.3 Molecular composition was characterized by ^{1}H NMR, according to the protocol that is described in the next section.

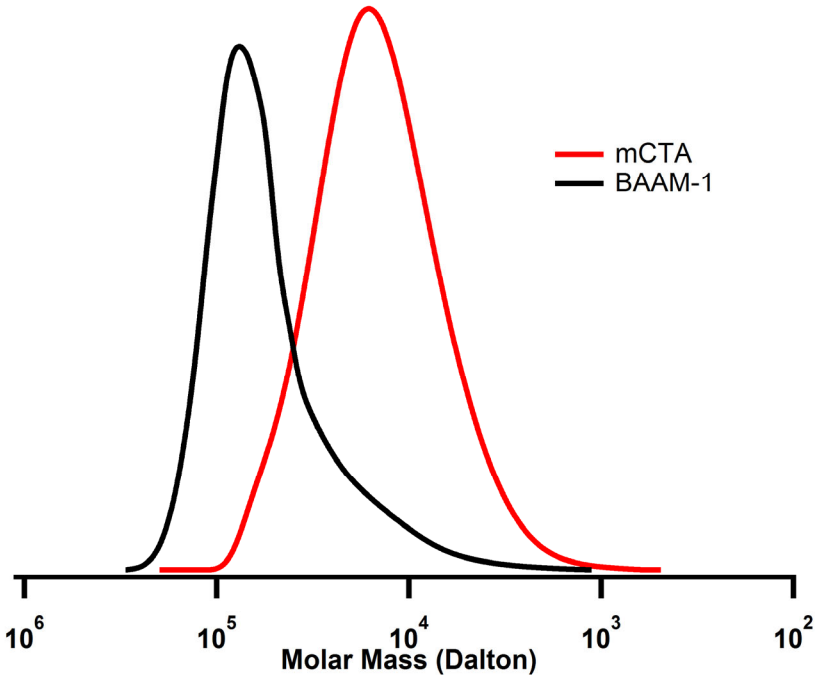

Figure 3.5 Representative GPC traces of **m-CTA** and **BAAM-1** in DMF showing increase in M_n (decrease in elution time) after RAFT polymerization.

Table 3.3 Molecular weight and molecular weight distributions of polymers measured by GPC using DMF as eluent, and PEG as standard.

Polymer	M_n (kg/mol)	M_w/M_n
BAAM-1	38.7	1.8
BAAM-2	43.7	1.7
BAAM-3	44.2	1.7
BAAM-4	28.2	1.8
BAAM-5	27.2	1.9
BAAM-6	22.2	2.9*
BAAM-7	28.9	2.2*
BAAM-8	15.9	4.0*
Control-1	6.27	1.12

* Minor shoulder (~10%) is observed after the main polymer peak. This is presumably due to the presence of free polymer brush that did not couple to the polystyrene backbone.

Characterization of copolymers using ^{1}H NMR

Due to the overlap of signals corresponding to the **AM** monomer, with signals from PS backbone and other backbone protons, the following protocol was followed to characterize the polymer compositions using ^{1}H NMR. Each polymer was initially dissolved in DMSO-d_6 and a proton spectrum was recorded to ensure the removal of unreacted monomers (Figure 3.6, blue spectrum). The amide protons were then exchanged with deuterium by the addition of 200 μL of CD_3OD and 20 μL of deuterated trifluoroacetic acid (TFA-d, acid catalyst to facilitate the exchange). Another proton spectrum was recorded after 5 min, to ensure the completion of H–D exchange reaction (Figure 3.6, black spectrum). The average brush degree of polymerization and **AM** content of each

polymer was calculated for each **BAAM** samples from the second spectrum. A sample calculation is provided below.

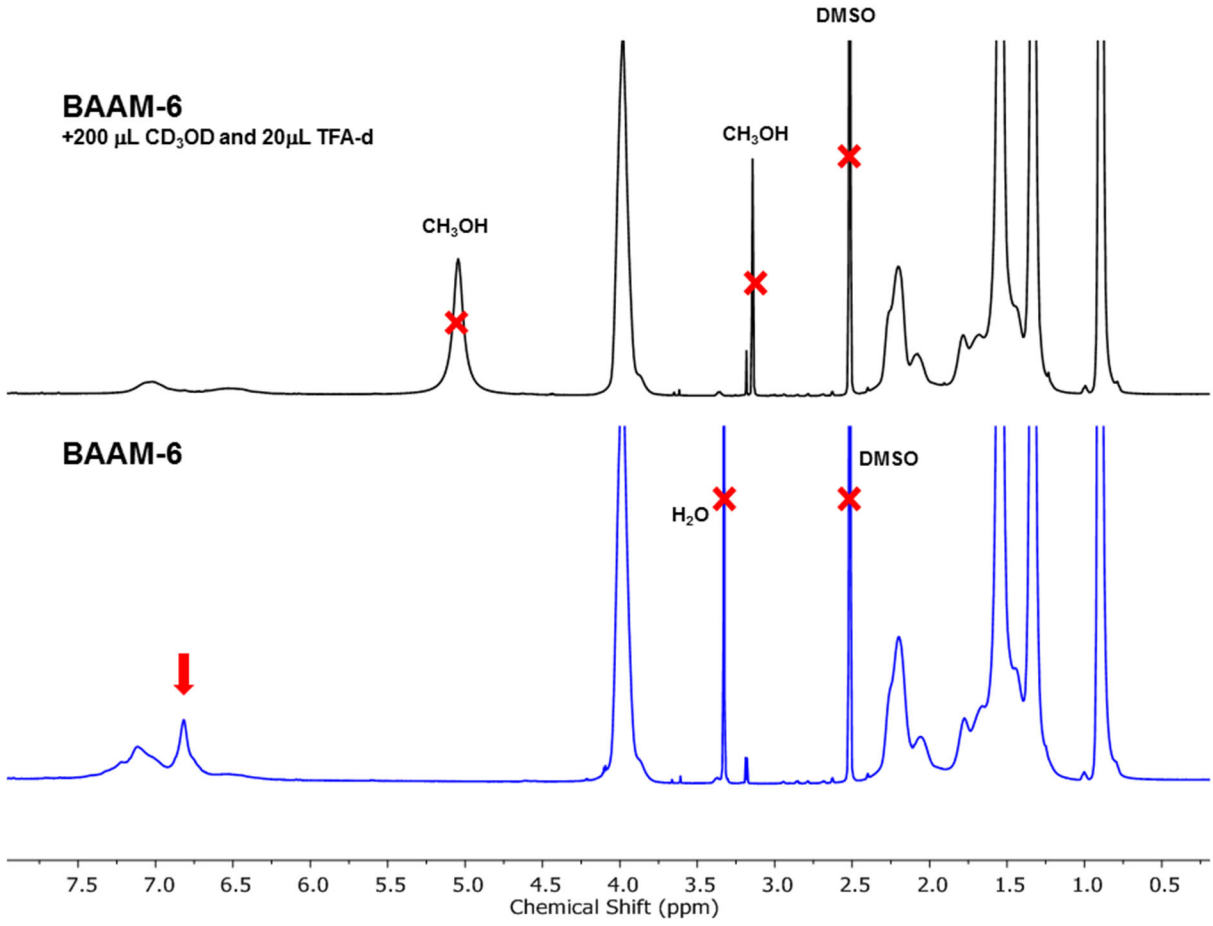

Figure 3.6 ^{1}H NMR spectrum of **BAAM-6** in DMSO-d_6 before (bottom, blue spectrum) and after H–D exchange (top, black spectrum). To circumvent the signal overlap, between the amide protons of AM (marked with a red arrow) and PS backbone, H–D exchange was conducted by the addition of CD_3OD and TFA-d.

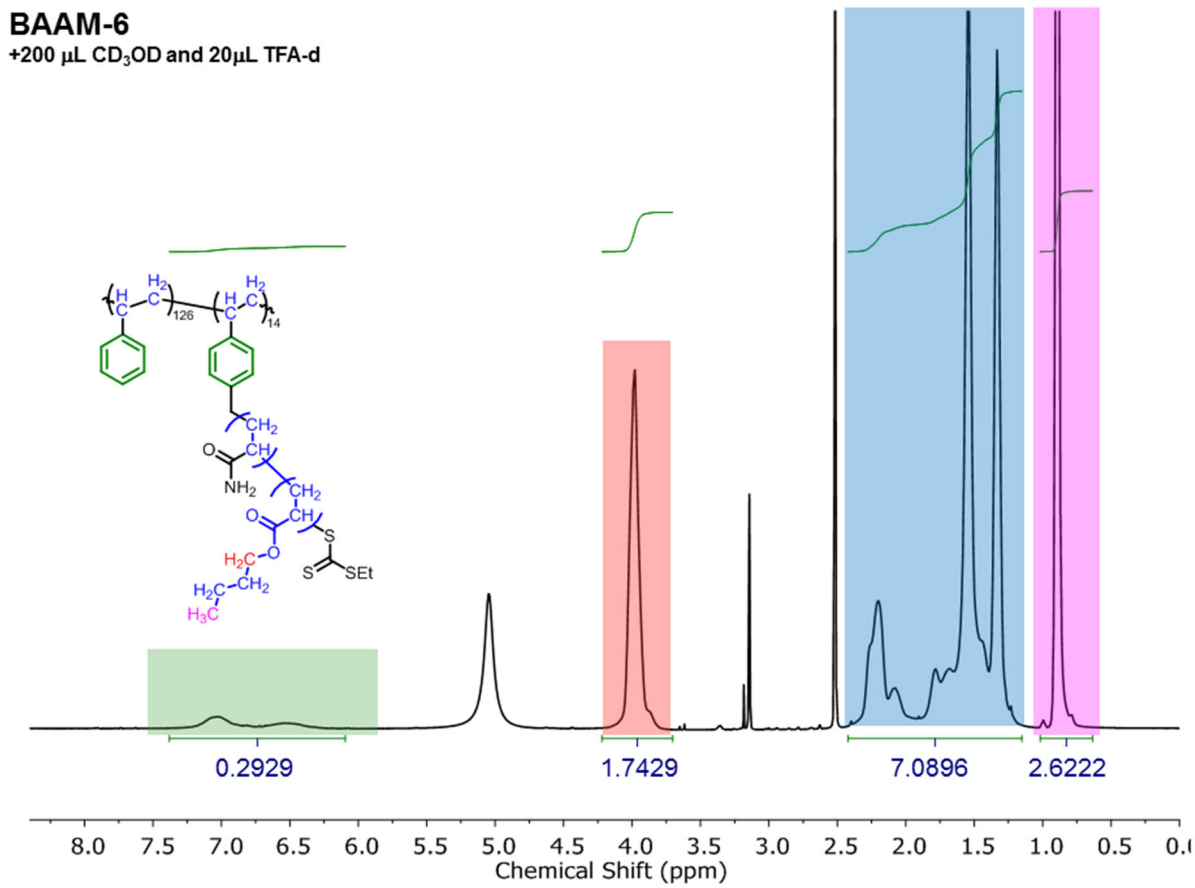

Figure 3.7 ^{1}H NMR spectrum of **BAAM-6** in DMSO-d_6 after H–D exchange. Different signals and protons are color coded for the ease of visualization. A sample calculation is provided for calculation of the degree of polymerization and **AM** mol%.

Sample Calculation:

x and y are the number of **BA** and **AM** repeat units in each brush respectively.

$$\frac{14 \times 2x}{14 \times 4 + 126 \times 5} = \frac{1.7429}{0.2929} \rightarrow x = 145.8$$

$$\frac{(3 \times 126 + 3 \times 14) + (3 \times 14y) + (3 \times 14x) + (4 \times 14y)}{28x} = \frac{7.0896}{1.7429} \rightarrow y = 45.1$$

DP=145.7 + 45.1 = 190, AM mol%= 23%

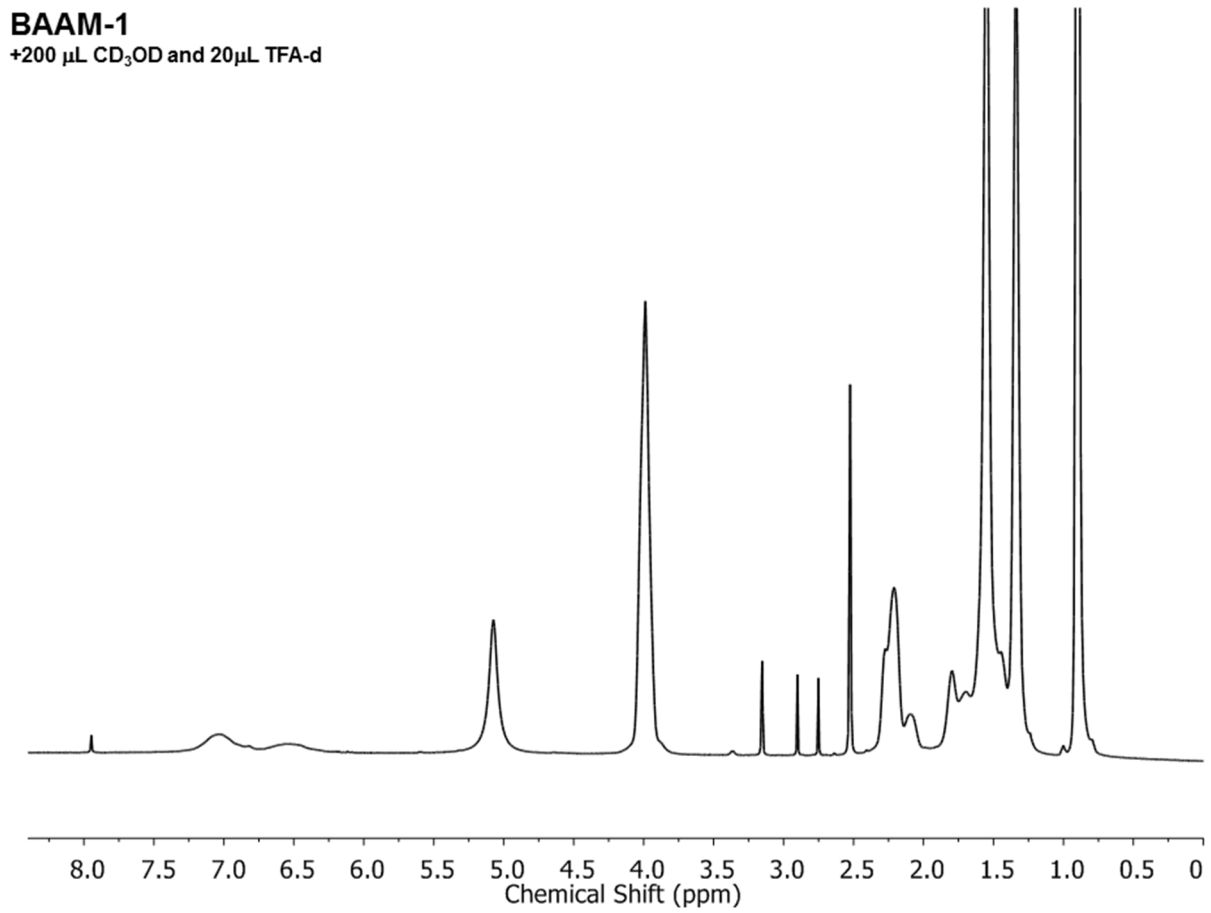

Figure 3.8 ^{1}H NMR spectrum of **BAAM-1** (5%-270-16%) after H–D exchange (600 MHz, DMSO-d_6, 298 K). The molecular composition, as determined by NMR, is reported in the following format: graft density%–brush degree of polymerization–**AM** mol% in each brush ($N_{AM}/(N_{AM}+N_{BA}) \times 100$, N is the number of each monomer).

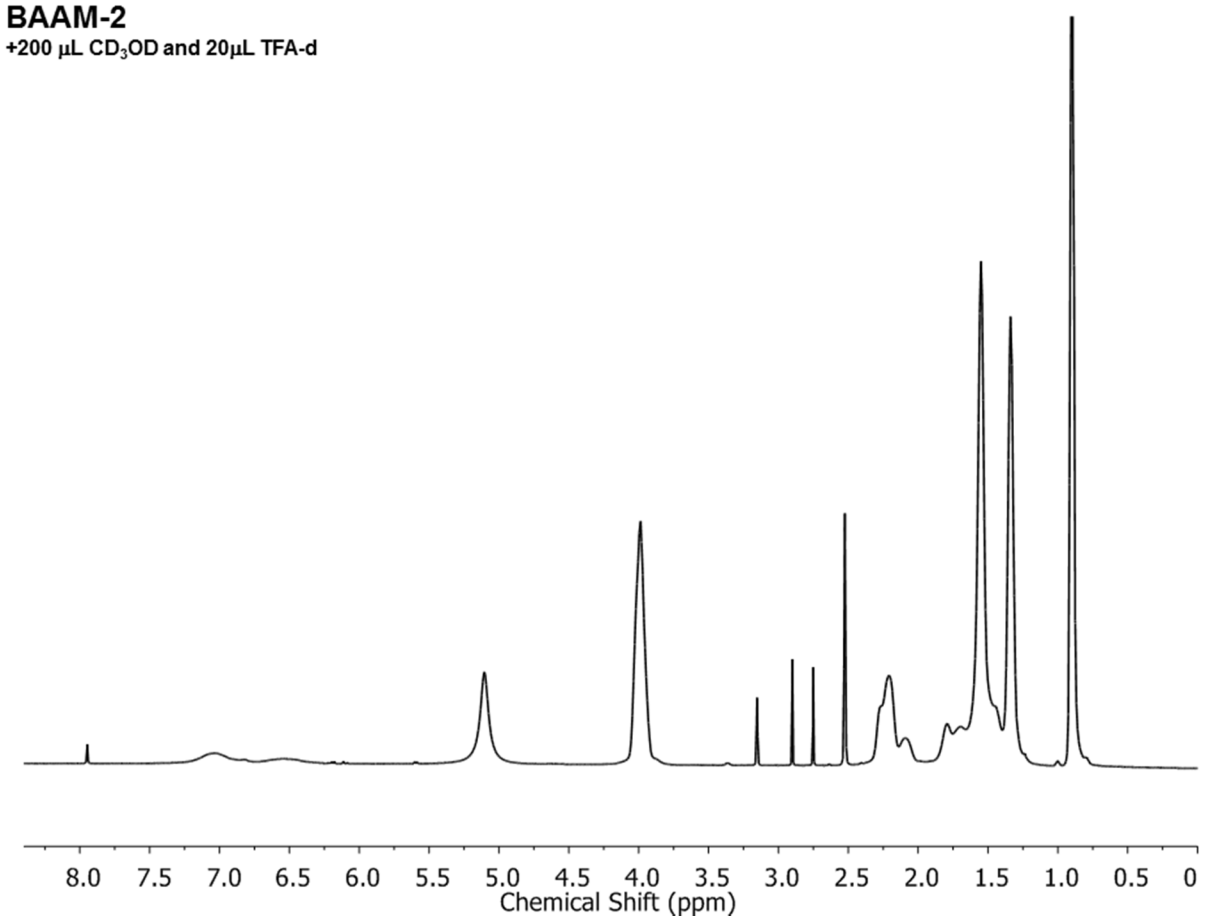

Figure 3.9 ^{1}H NMR spectrum of **BAAM-2** (5%-250-22%) after H–D exchange (600 MHz, DMSO-d_6, 298 K). The molecular composition, as determined by NMR, is reported in the following format: graft density%–brush degree of polymerization–**AM** mol% in each brush ($N_{AM}/(N_{AM}+N_{BA}) \times 100$, N is the number of each monomer).

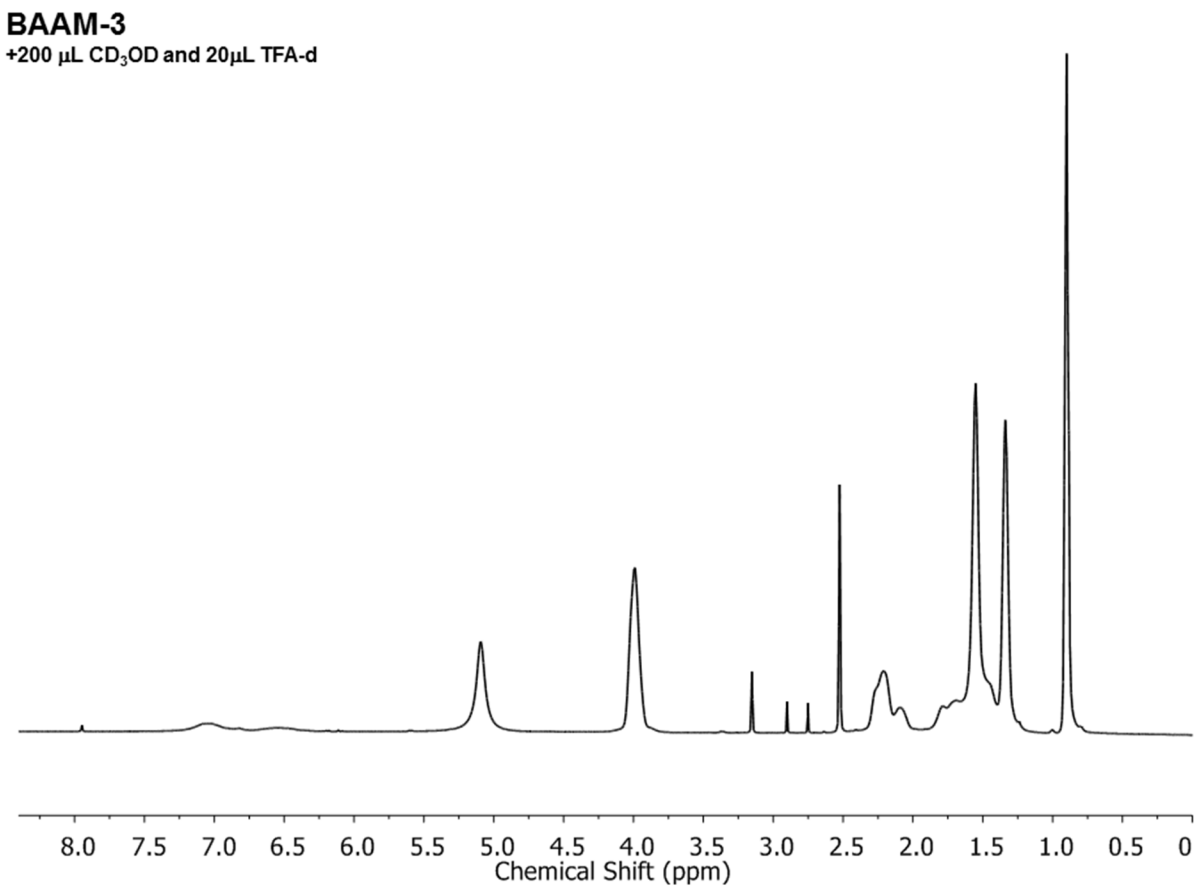

Figure 3.10 ^{1}H NMR spectrum of **BAAM-3** (5%-290-30%) after H–D exchange (600 MHz, DMSO-d_6, 298 K). The molecular composition, as determined by NMR, is reported in the following format: graft density%–brush degree of polymerization–**AM** mol% in each brush ($N_{AM}/(N_{AM}+N_{BA}) \times 100$, N is the number of each monomer).

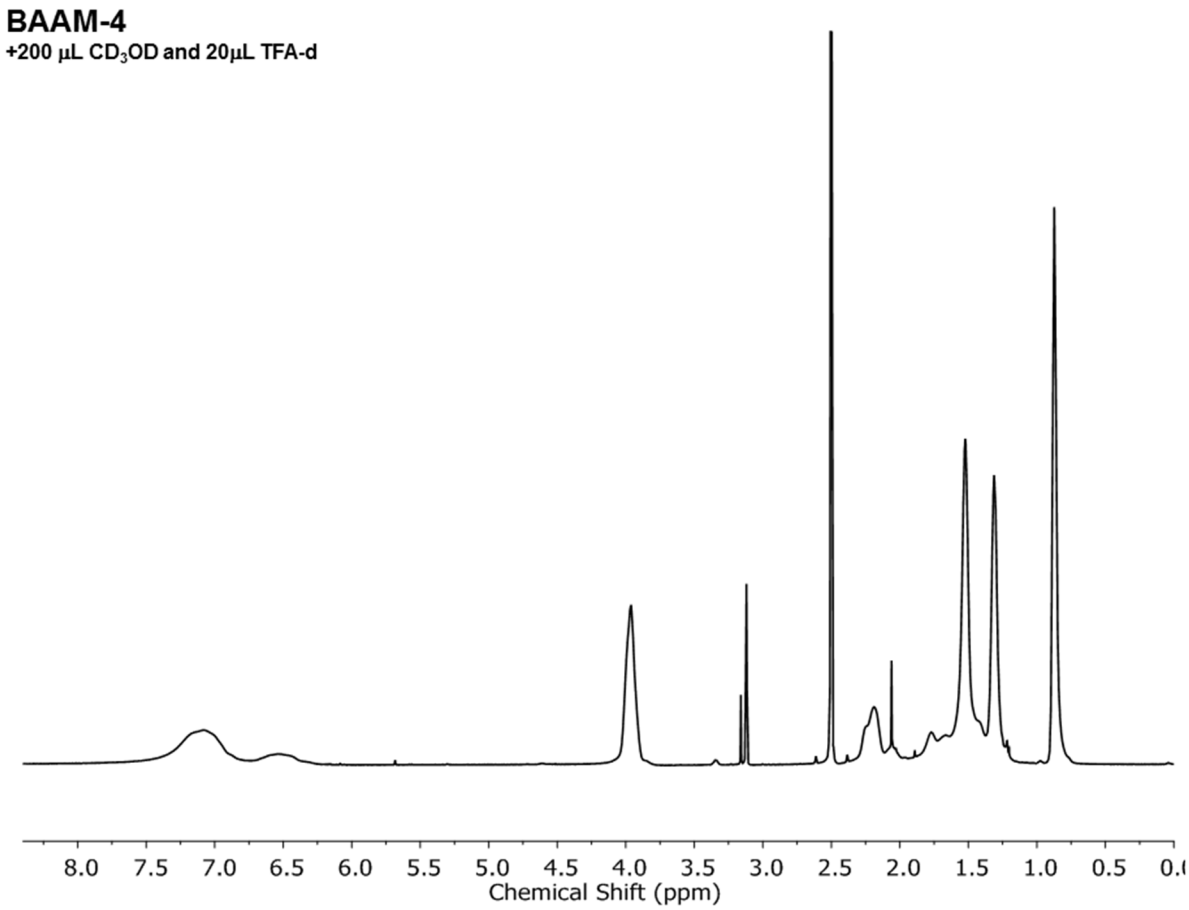

Figure 3.11 ^{1}H NMR spectrum of **BAAM-4** (5%-94-24%) after H–D exchange (600 MHz, DMSO-d_6, 298 K). The molecular composition, as determined by NMR, is reported in the following format: graft density%–brush degree of polymerization–**AM** mol% in each brush ($N_{AM}/(N_{AM}+N_{BA}) \times 100$, N is the number of each monomer).

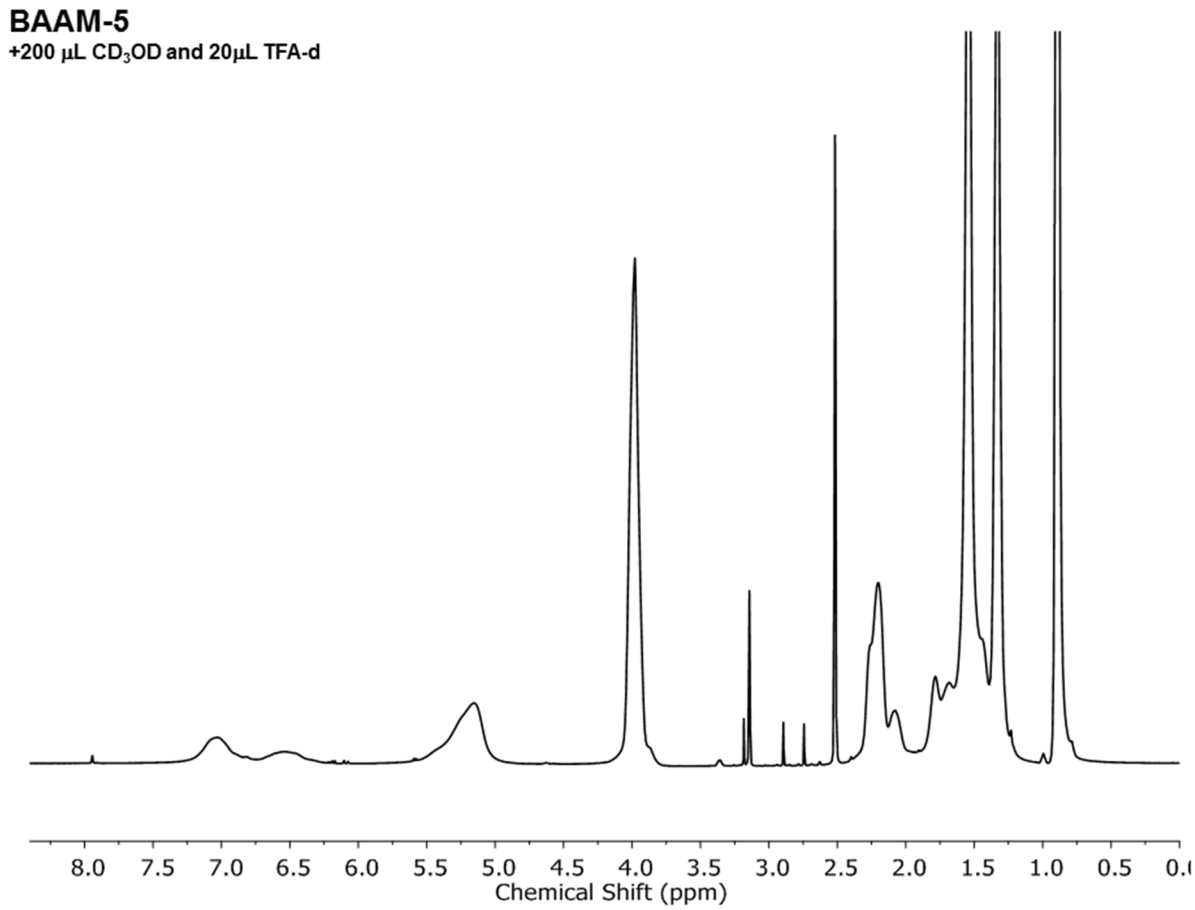

Figure 3.12 ^{1}H NMR spectrum of **BAAM-5** (5%-224-22%) after H–D exchange (600 MHz, DMSO-d_6, 298 K). The molecular composition, as determined by NMR, is reported in the following format: graft density%–brush degree of polymerization–**AM** mol% in each brush ($N_{AM}/(N_{AM}+N_{BA}) \times 100$, N is the number of each monomer).

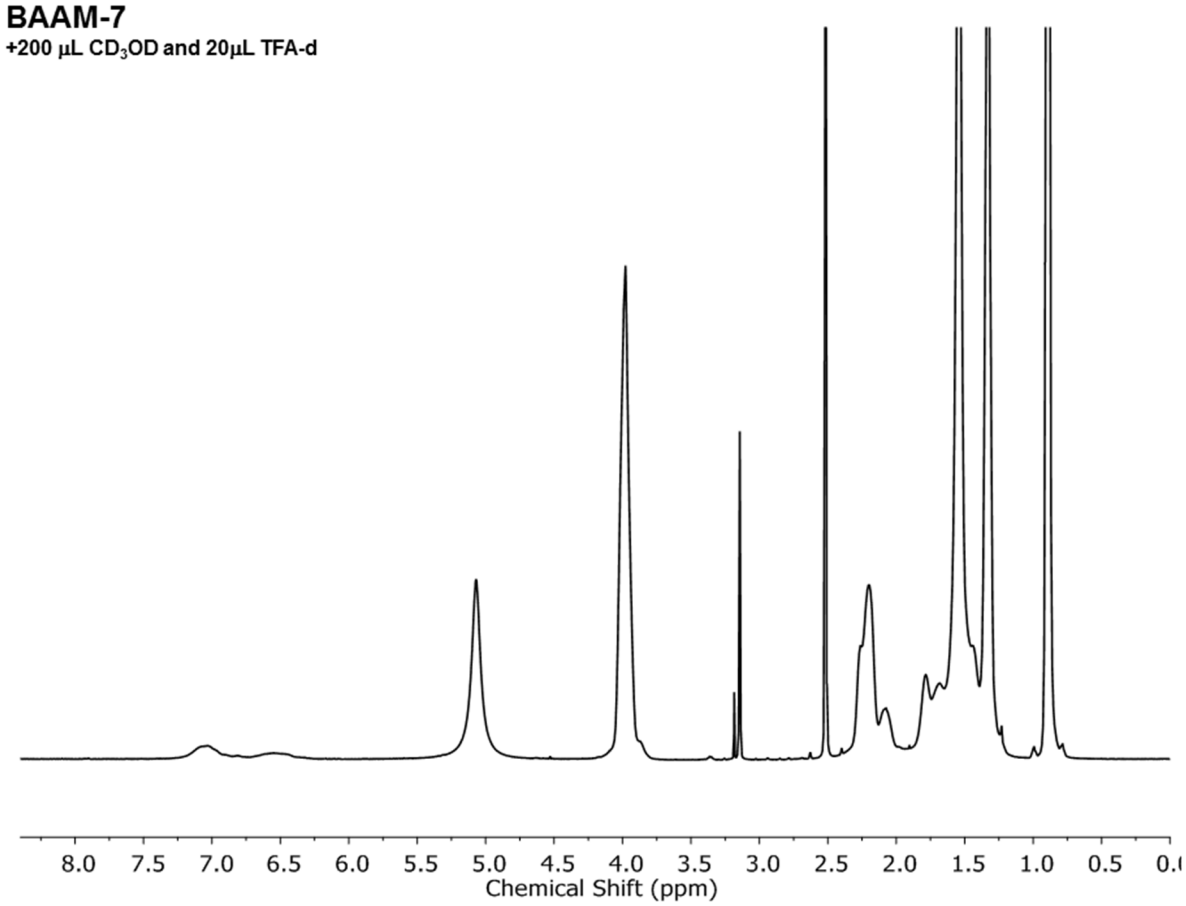

Figure 3.13 ^{1}H NMR spectrum of **BAAM-7** (10%-240-22%) after H–D exchange (600 MHz, DMSO-d_6, 298 K). The molecular composition, as determined by NMR, is reported in the following format: graft density%–brush degree of polymerization–**AM** mol% in each brush ($N_{AM}/(N_{AM}+N_{BA})$ × 100, N is the number of each monomer).

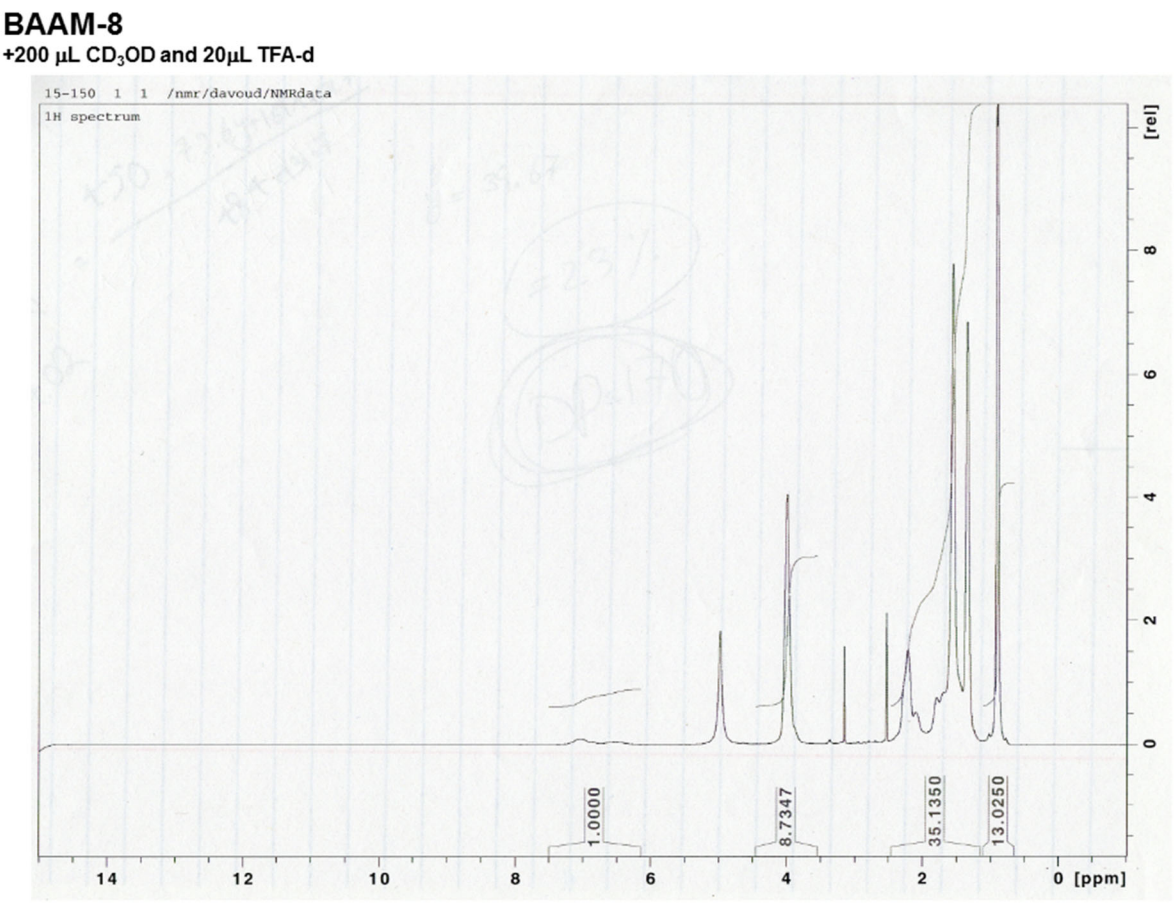

Figure 3.14 ^{1}H NMR spectrum of **BAAM-8** (15%-170-23%) after H–D exchange (600 MHz, DMSO-d_6, 298 K). The molecular composition, as determined by NMR, is reported in the following format: graft density%–brush degree of polymerization–**AM** mol% in each brush ($N_{AM}/(N_{AM}+N_{BA})$ × 100, N is the number of each monomer).

Morphological characterization of BAAM copolymers

TEM method

TEM was performed on a FEI/Philips CM-20 conventional TEM operated at an accelerating voltage of 200 kV. The polymer was drop casted from MeOH and DCM mixture (1:1 v/v, polymer concentration 10 mg/mL) and the soft phase was stained by floating the TEM grid (purchased from Ted Pella) on a 0.5 wt % aqueous solution of uranyl acetate for 30 s followed by removing excess solvent by placing the sample on filter paper. The samples were annealed at 80 °C overnight under vacuum.

Thermal characterization

Differential Scanning Calorimetry (DSC)

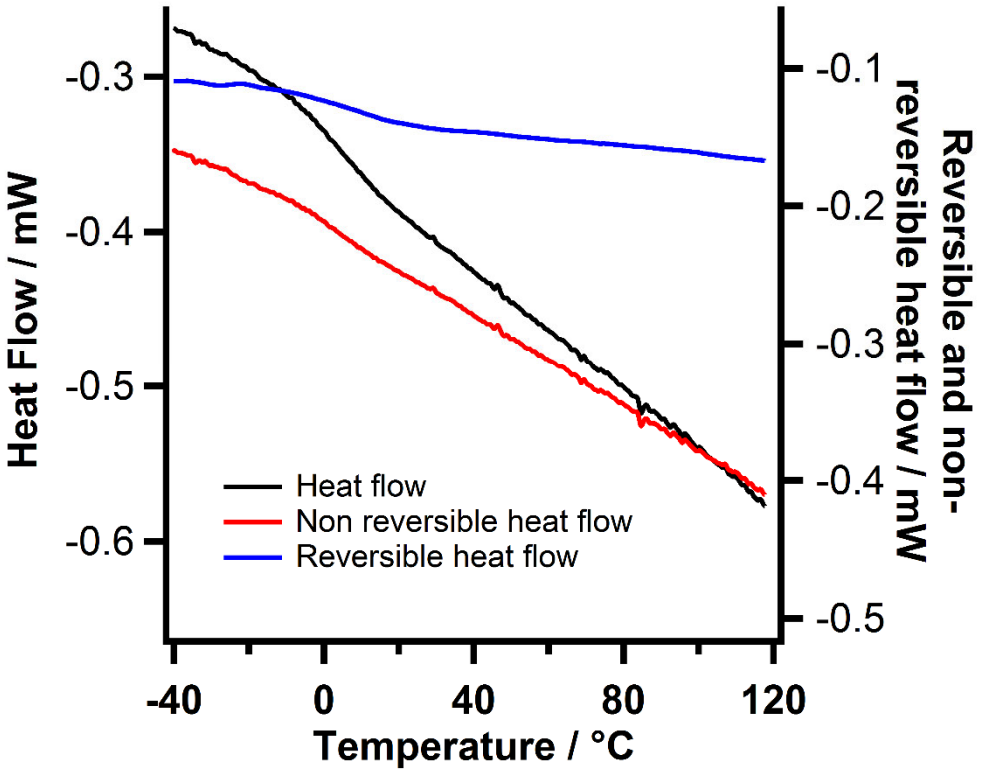

Figure 3.15 Modulated differential scanning calorimetry of **BAAM-7**. Experiments were conducted at a heating rate of 3 °C/min under nitrogen atmosphere (black, heat flow; blue, reversible heat flow; red, non-reversible heat flow).

Calculation of T_g using Flory-Fox equation and comparison with DSC and DMA data

Flory-Fox equation (below) can be used to estimate the T_g of a random copolymer from the weight percent of each monomer and the T_g of homopolymers of each component.

$$\frac{1}{T_g} = \frac{w_1}{T_{g1}} + \frac{w_2}{T_{g2}}$$

In the above equation, w_1 and w_2 represent the weight fraction of each component and T_{g1} and T_{g2} are the glass transition temperatures for the homopolymers of each monomer. In this case, component 1 is **AM** (T_g ~ 165 °C) and component 2 is **BA** (T_g ~ -54 °C). The PS weight fraction is negligible and is therefore excluded from the calculation. The following table summarizes the expected T_g for the different **AM** weight% according to FF equation.

Table 3.4 Summary of **AM** mol%, weight%, and calculated T_g from FF equation for **BAAM 1-3.**

Sample (AM mol%)	**AM** weight%	Calculated T_g from FF equation (°C)
BAAM-1 (16%)	9.5%	-42.
BAAM-2 (22%)	13.5%	-38
BAAM-3 (30%)	19.2%	-31

The difference between the calculated values and the observed T_g according to the DSC experiment (Figure 3.15 for **BAAM-7** with **AM** mol% ~ 22) is presumably due to the difference in the architecture of polymers. FF equation is applicable to linear polymers while in our case, the proximity of brushes can change the mobility and resulting T_g.

Differences between DMA and DSC results are expected as the former is a functional measure of T_g and it is known that the T_g shifts to a higher value as the frequency of DMA experiment is increased (See Figure 3.17).

Plotting the calculated T_g versus the **AM** mol% is expected to result in a non-linear graph. Nonetheless, this curve can be approximated with a line if the changes in the **AM** content is sufficiently small (as it is case here).

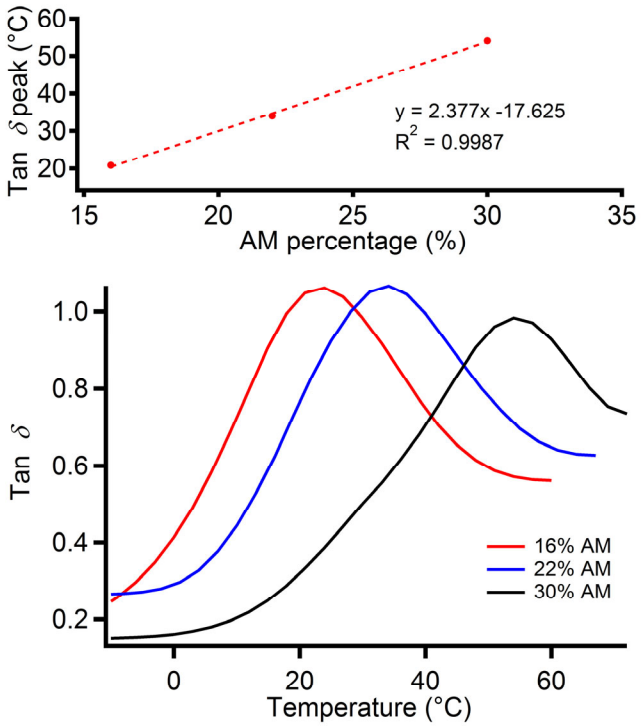

Figure 3.16 Changing the **AM** mol% in the copolymers is an easy handle to modulate the T_g as evident by the changes in the Tan delta peak location for different **AM** mol%.

Mechanical characterization

Sample preparation

Samples were prepared by hot-pressing the resin into heated Teflon molds at 100 ℃ and allowing them to cool down to room temperature while maintaining the pressure (cooling time approximately 30 min). Basic mechanical properties (Figure 3a and Table S3) were measured as described in the next section, mechanical testing procedure. Average sample size was 15 mm × 7 mm × 2 mm (length, width, thickness).

Preparation of samples from commercially available polymers

Kraton pellets (12 g) were added slowly to a stirred solution of toluene maintained at 80 °C until all of the polymer was dissolved. The resulting clear solution was then poured into Teflon mold and the solvent were removed by heating in a vacuum oven. The resulting clear film was removed from the mold and the tensile samples were prepared by compression molding at 170 °C. Average sample size was 15 mm × 7 mm × 2 mm (length, width, thickness).

Mechanical testing procedure

The mechanical properties of the copolymers were measured using an Instron 3365 machine in standard stress/strain experiments. The specimen were extended at 100 mm/min at room temperature. Each measurement was repeated at least three times. Young's modulus (E) was determined from the initial slope of the stress-strain curves. Dynamic thermal mechanic analysis experiments were performed using a TA Instruments DMA Q800. The dynamic response of polymers was measured across multiple temperature and frequencies. Storage, loss modulus and tan delta (ratio of loss/storage moduli) were plotted versus the temperature. Generally, the response of different BAAM copolymers were similar and only the location of tan delta peak shifted

significantly across different samples. A representative graph for **BAAM-3** (30% AM) is shown in Figure S11 for multiple frequencies. For the other percentages of AM (16% and 22%), the data is only shown for the frequency of 1 Hz.

In all cases, the location of peak of tan delta versus temperature at 1 Hz is considered as a functional measure of T_g.

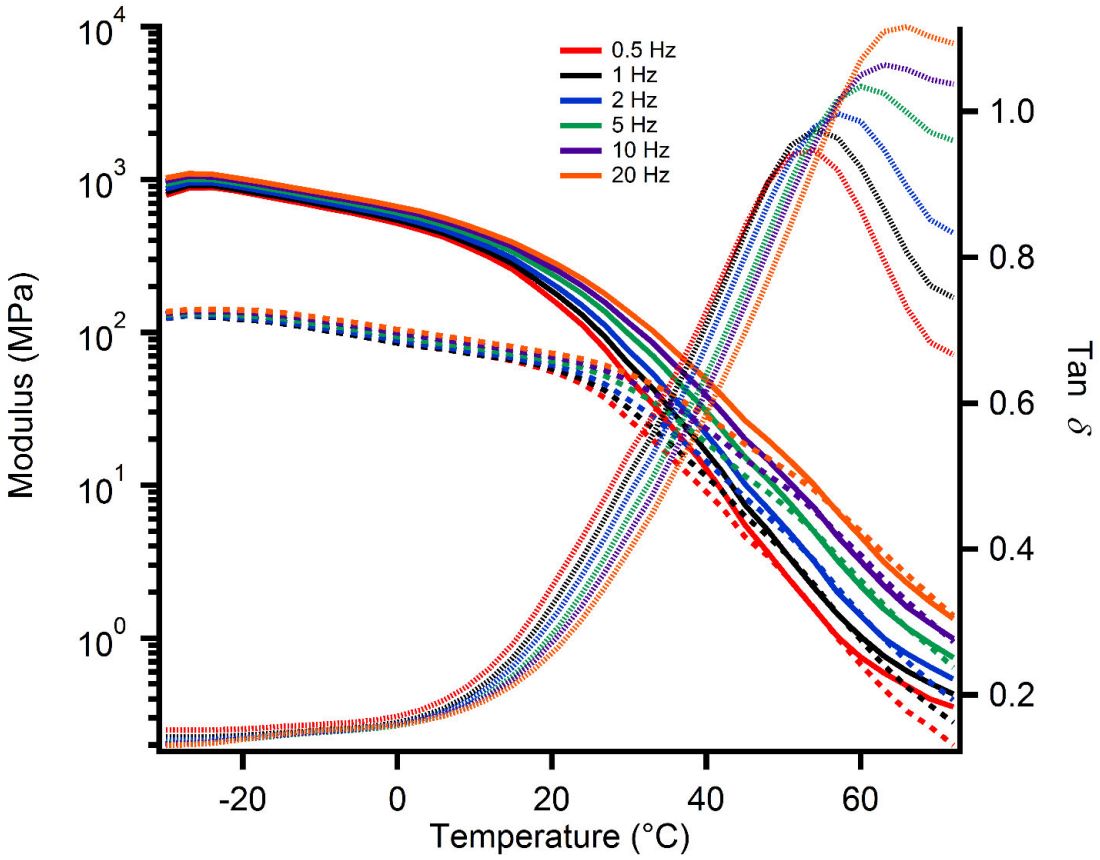

Figure 3.17 Dynamic Mechanical Thermal Analysis (DMTA) traces of BAAM-3 from -30 °C to 70 °C; storage modulus (solid), loss modulus (dash), and tan δ (dot). Multi-frequency (0.5, 1, 2, 5,

10, and 20 Hz) temperature sweep of polymer sample using DMA. The α transition occurs at approximately 50–65 °C.

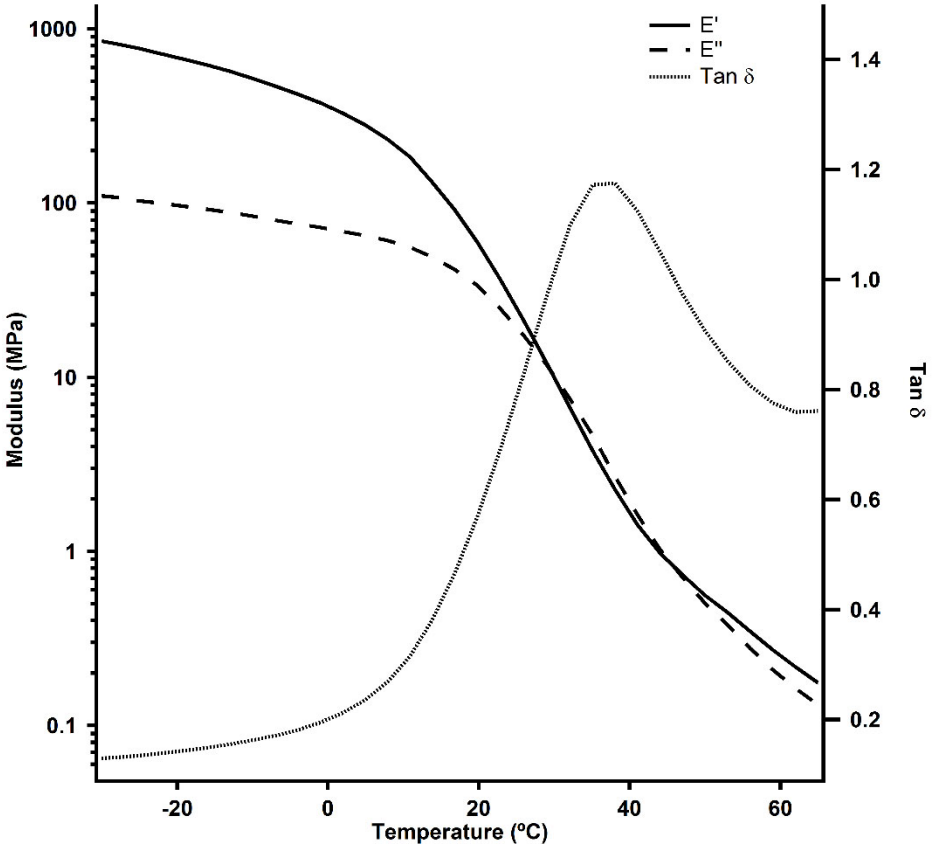

Figure 3.18 Dynamic Mechanical Thermal Analysis (DMTA) traces of BAAM-2 from -30 °C to 70 °C; storage modulus (solid), loss modulus (dash), and tan δ (dot). Temperature sweep at the frequency of 1 Hz is shown.

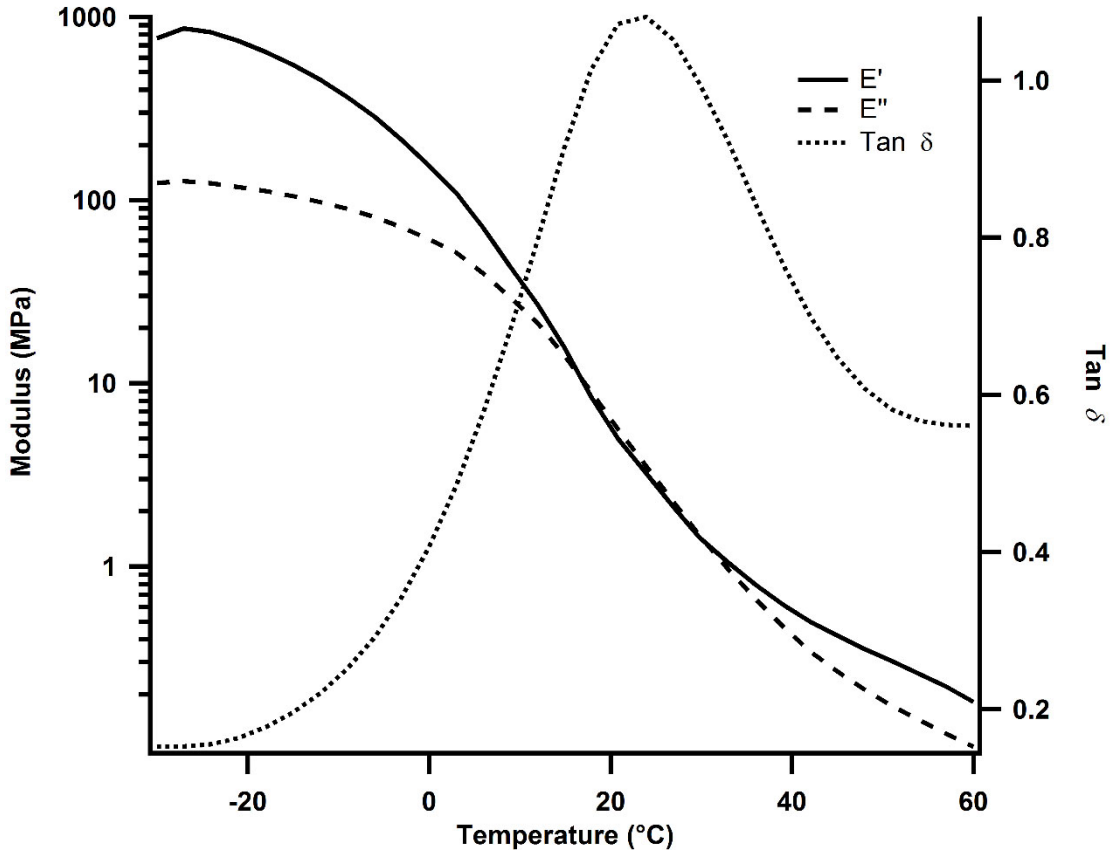

Figure 3.19 Dynamic Mechanical Thermal Analysis (DMTA) traces of BAAM-1 (16% AM) from -30 °C to 60 °C; storage modulus (solid), loss modulus (dash), and tan δ (dot). Temperature sweep at the frequency of 1 Hz is shown.

Sample damaging and healing tests

For self-healing tests, a well-defined cut was applied to the depth of 70-90% of sample thickness using a razor blade. The cut faces were pressed together for 1 minute and then the sample was let to heal at 30 °C for various times. The self-healed samples were then allowed to cool down to room temperature (5-10 min) and were subjected to stress-strain tests at room temperature at 100 mm/min pulling rate.

Table 3.5 Summary of self-healing results

Polymer	Self-healing		
	ε_{rec} (%)[a]	σ_{rec} (%)[b]	$U_{T,\,rec}$ (%)[c]
BAAM-4	424 (70%)	3.4 (60%)	11.5 (36%)
BAAM-5	966.5 (96%)	3.86 (91%)	26.3 (87%)
BAAM-6	4.61 (96%)	553 (78%)	20.6 (80%)
BAAM-7	3.54 (86%)	776 (100%)	17.7 (86%)
BAAM-8	3.45 (86%)	673 (84%)	16.2 (64%)

[a] Ultimate extensibility followed by percent recovery of extensibility compared to pristine samples). [b] Ultimate strength (MPa) followed by percent recovery of ultimate strength compared to pristine samples). [c] Toughness (MJ/m^3), calculated from integrating the area under the stress-strain curves, followed by percent recovery of toughness compared to pristine samples).

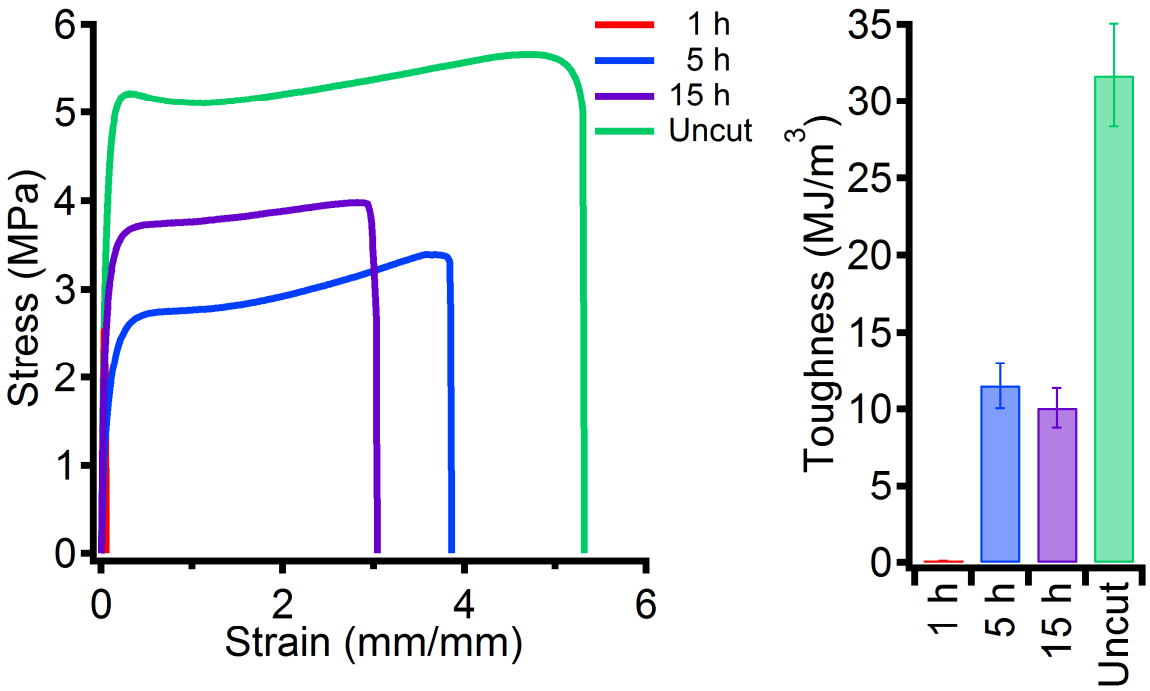

Figure 3.20 Self-healing tests for **BAAM-4** samples at 30 °C with ambient humidity. The bar graph summarizes the toughness recovery for any time point. Error bars are standard deviation for minimum of three measurements.

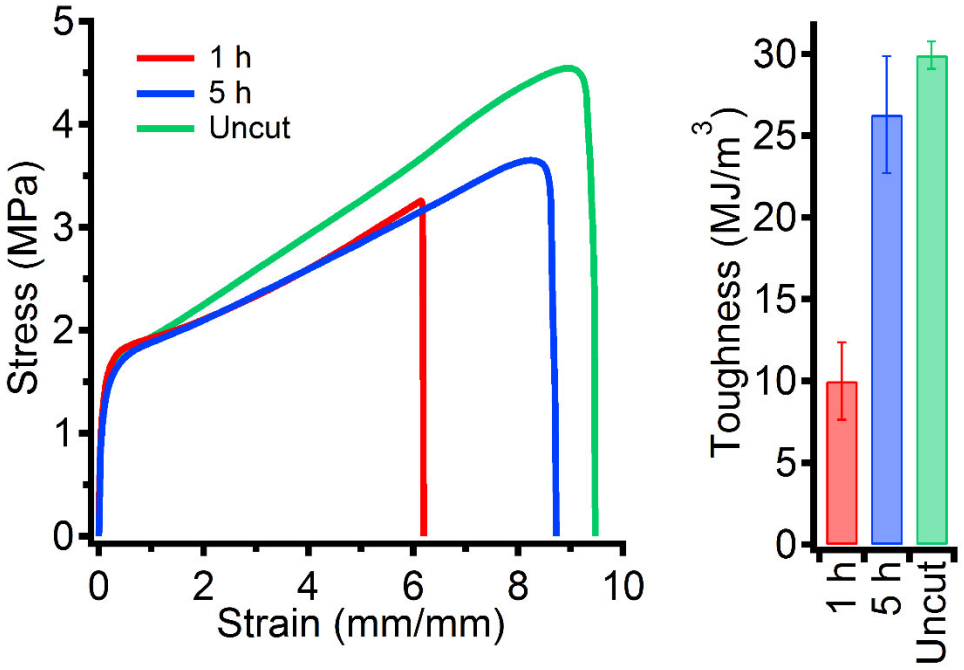

Figure 3.21 Self-healing tests for **BAAM-5** samples at 30 °C with ambient humidity. The bar graph summarizes the toughness recovery for any time point. Error bars are standard deviation for minimum of three measurements.

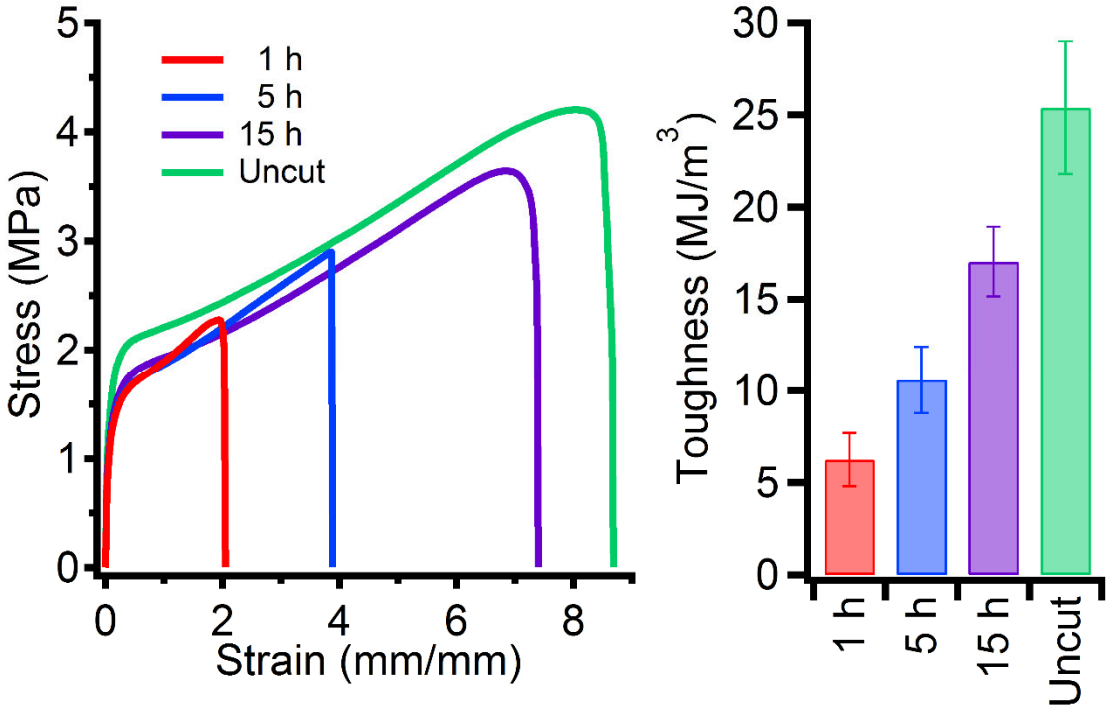

Figure 3.22 Self-healing tests for **BAAM-8** samples at 30 °C with ambient humidity. The bar graph summarizes the toughness recovery for any time point. Error bars are standard deviation for minimum of three measurements.

Miscellaneous Figures

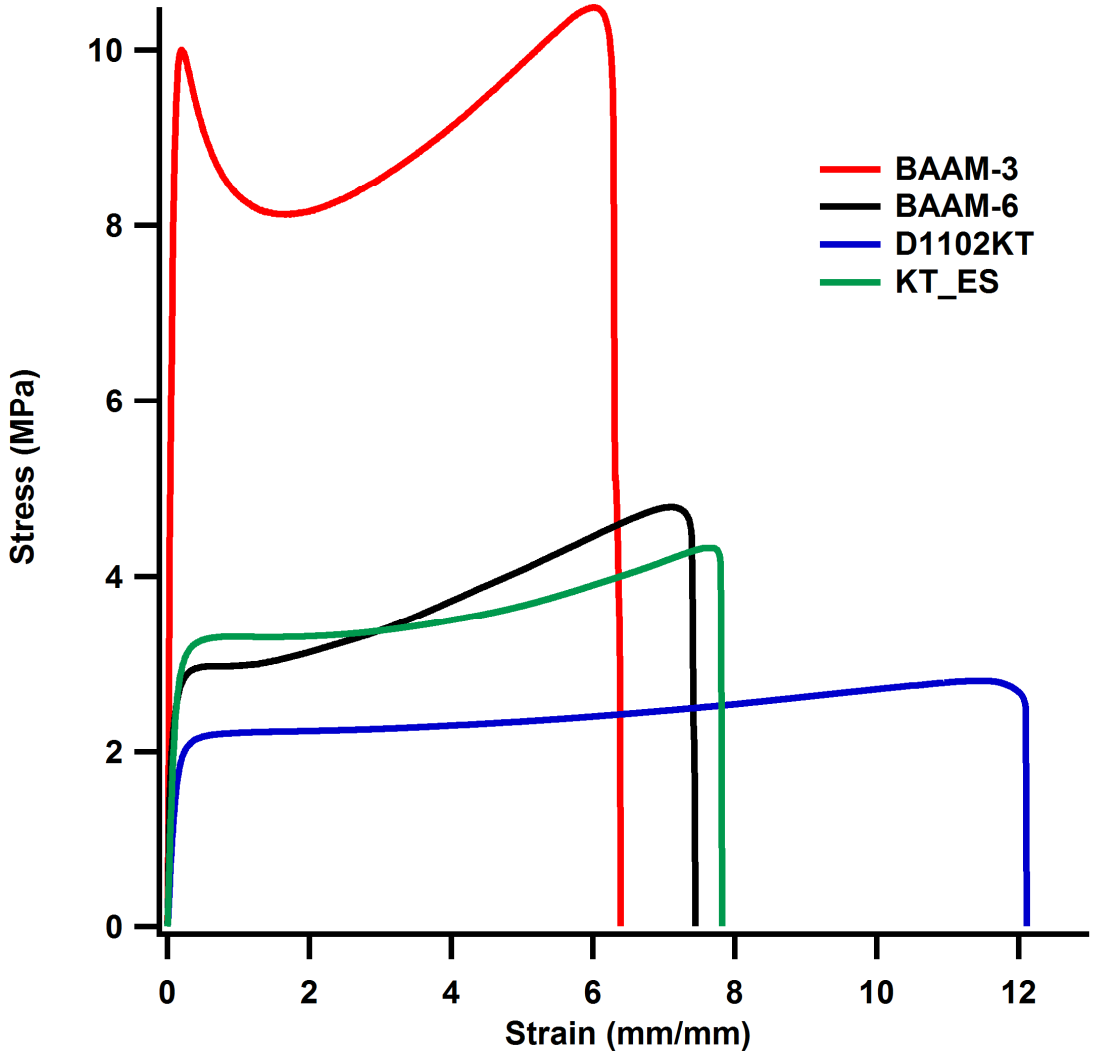

Figure 3.23 Comparison of tensile data between **BAAM-3** (red curve, strongest sample), **BAAM-6** (black curve, with optimal mechanical properties and efficient self-healing under ambient conditions), and commercially available polymers (Kraton D1102 and Kraton D1116 ES).

FIGURE CREDIT

Figure 1.2	Adapted with permission from Hill, D. J.; Mio, M. J.; Prince, R. B.; Hughes, T. S.; Moore, J. S. *Chem. Rev.* **2001**, *101*, 3893. Copyright 2001 American Chemical Society.
Figure 1.3	Reprinted by permission from Macmillan Publishers Ltd: Nature Structural Biology Dill, K. A.; Chan, H. S. *Nat. Struct. Mol. Biol.* **1997**, *4*, 10, copyright 1997.
Figure 1.4a	From Mutter, M.; Dumy, P.; Garrouste, P.; Lehmann, C.; Mathieu, M.; Peggion, C.; Peluso, S.; Razaname, A.; Tuchscherer, G. *Angew. Chem. Int. Ed. Engl.* **1996**, *35*, 1482. Copyright © 1996 by John Wiley & Sons, Inc. Reprinted by permission of John Wiley & Sons, Inc.
Figure 1.4b	Reprinted with permission from Ghadiri, M. R.; Choi, C. *J. Am. Chem. Soc.* **1990**, *112*, 1630. Copyright 1990 American Chemical Society.
Figure 1.4c	Reprinted with permission from Kemp, D. S.; Allen, T. J.; Oslick, S. L. *J. Am. Chem. Soc.* **1995**, *117*, 6641. Copyright 1995 American Chemical Society.
Figure 1.4d	Reprinted with permission from Liu, J.; Wang, D.; Zheng, Q.; Lu, M.; Arora, P. S. *J. Am. Chem. Soc.* **2008**, *130*, 4334. Copyright 2008 American Chemical Society.
Figure 1.4e	From Harrison, R. S.; Shepherd, N. E.; Hoang, H. N.; Ruiz-Gómez, G.; Hill, T. A.; Driver, R. W.; Desai, V. S.; Young, P. R.; Abbenante, G.; Fairlie, D. P. *Proc. Natl. Acad. Sci. U. S. A.* **2010**, *107*, 11686. Copyright 2010 National Academy of Sciences, USA.
Figure 1.5	Reprinted with permission from DeGrado, W. F.; Summa, C. M.; Pavone, V.; Nastri, F.; Lombardi, A. *Annu. Rev. Biochem.* **1999**, *68*, 779. Copyright 1999 Annual Reviews.
Figure 1.6a	From Kamtekar, S.; Schiffer, J. M.; Xiong, H. Y.; Babik, J. M.; Hecht, M. H. *Science* **1993**, *262*, 1680. Reprinted with permission from American Association for the Advancement of Science.
Figure 1.6b	From Struthers, M. D.; Cheng, R. P.; Imperiali, B. *Science* **1996**, *271*, 342. Reprinted with permission from American Association for the Advancement of Science.
Figure 1.6c	From Fletcher, J. M.; Harniman, R. L.; Barnes, F. R. H.; Boyle, A. L.; Collins, A.; Mantell, J.; Sharp, T. H.; Antognozzi, M.; Booth, P. J.; Linden, N.; Miles, M. J.; Sessions, R. B.; Verkade, P.; Woolfson, D. N. *Science* **2013**, *340*, 595. Reprinted with permission from American Association for the Advancement of Science.
Figure 1.8 to Figure 1.11	Mozhdehi, D.; Guan, Z. *Chem. Commun.*, **2013**, *49*, 9950-9952. Reproduced by permission of The Royal Society of Chemistry.
Figure 1.19	Reprinted with permission from Ghosh, P. S.; Hamilton, A. D. *J. Am. Chem. Soc.* **2012**, *134*, 13208. Copyright 2012 American Chemical Society.
Figure 1.20 to Figure 1.59	Mozhdehi, D.; Guan, Z. *Chem. Commun.*, **2013**, *49*, 9950-9952. Reproduced by permission of The Royal Society of Chemistry.

Figure 2.1	Reprinted by permission from Macmillan Publishers Ltd: Nature White, S. R.; Sottos, N. R.; Geubelle, P. H.; Moore, J. S.; Kessler, M. R.; Sriram, S. R.; Brown, E. N.; Viswanathan, S. *Nature* **2001**, *409*, 794, copyright 2001.
Figure 2.2	From White, S. R.; Moore, J. S.; Sottos, N. R.; Krull, B. P.; Santa Cruz, W. A.; Gergely, R. C. R. *Science* **2014**, *344*, 620. Reprinted with permission from American Association for the Advancement of Science.
Figure 2.3	From Ghosh, B.; Urban, M. W. *Science* **2009**, *323*, 1458. Reprinted with permission from American Association for the Advancement of Science.
Figure 2.4	Reprinted with permission from Yuan, C. e.; Rong, M. Z.; Zhang, M. Q.; Zhang, Z. P.; Yuan, Y. C. *Chem. Mater.* **2011**, *23*, 5076. Copyright 2011 American Chemical Society.
Figure 2.5	From Imato, K.; Nishihara, M.; Kanehara, T.; Amamoto, Y.; Takahara, A.; Otsuka, H. *Angew. Chem., Int. Ed.* **2012**, *51*, 1138. Copyright © 2012 by John Wiley & Sons, Inc. Reprinted by permission of John Wiley & Sons, Inc.
Figure 2.6	From Amamoto, Y.; Kamada, J.; Otsuka, H.; Takahara, A.; Matyjaszewski, K. *Angew. Chem. Int. Ed.* **2011**, *50*, 1660. Copyright © 2011 by John Wiley & Sons, Inc. Reprinted by permission of John Wiley & Sons, Inc.
Figure 2.7	From Chen, X.; Dam, M. A.; Ono, K.; Mal, A.; Shen, H.; Nut, S. R.; Sheran, K.; Wudl, F. *Science* **2002**, *295*, 1698. Reprinted with permission from American Association for the Advancement of Science.
Scheme 2.1	Reprinted with permission from Zheng, P.; McCarthy, T. J. *J. Am. Chem. Soc.* **2012**, *134*, 2024. Copyright 2012 American Chemical Society.
Figure 2.8	From Montarnal, D.; Capelot, M.; Tournilhac, F.; Leibler, L. *Science* **2011**, *334*, 965. Reprinted with permission from American Association for the Advancement of Science.
Figure 2.9	Reprinted with permission from Lu, Y.-X.; Guan, Z. *J. Am. Chem. Soc.* **2012**, *134*, 14226. Copyright 2012 American Chemical Society.
Figure 2.10	From Herbst, F.; Doehler, D.; Michael, P.; Binder, W. H. *Macromol. Rapid Commun.* **2013**, *34*, 203. Copyright © 2013 by John Wiley & Sons, Inc. Reprinted by permission of John Wiley & Sons, Inc.
Figure 2.11	Reprinted by permission from Macmillan Publishers Ltd: Nature Cordier, P.; Tournilhac, F.; Soulie-Ziakovic, C.; Leibler, L. *Nature* **2008**, *451*, 977, copyright 2008.
Figure 2.12	Reprinted by permission from Macmillan Publishers Ltd: Nature Chemistry Chen, Y.; Kushner, A. M.; Williams, G. A.; Guan, Z. *Nat. Chem.* **2012**, *4*, 467, copyright 2012.
Figure 2.13	Reprinted by permission from Macmillan Publishers Ltd: Nature Burnworth, M.; Tang, L.; Kumpfer, J. R.; Duncan, A. J.; Beyer, F. L.; Fiore, G. L.; Rowan, S. J.; Weder, C. *Nature* **2011**, *472*, 334, copyright 2011.
Figure 2.14	From Bode, S.; Zedler, L.; Schacher, F. H.; Dietzek, B.; Schmitt, M.; Popp, J.; Hager, M. D.; Schubert, U. S. *Adv. Mater.* **2013**, *25*, 1634. Copyright © 2013 by John Wiley & Sons, Inc. Adapted by permission of John Wiley & Sons, Inc.
Figure 2.15 to Figure 2.18	Reprinted with permission from Mozhdehi, D.; Ayala, S.; Cromwell, O. R.; Guan, Z. *J. Am. Chem. Soc.* **2014**, *136*, 16128. Copyright 2014 American Chemical Society.

Scheme 2.2	Reprinted with permission from Mozhdehi, D.; Ayala, S.; Cromwell, O. R.; Guan, Z. *J. Am. Chem. Soc.* **2014**, *136*, 16128. Copyright 2014 American Chemical Society.
Scheme 2.4	Reprinted with permission from Mozhdehi, D.; Ayala, S.; Cromwell, O. R.; Guan, Z. *J. Am. Chem. Soc.* **2014**, *136*, 16128. Copyright 2014 American Chemical Society.
Figure 2.25 to Figure 2.38	Reprinted with permission from Mozhdehi, D.; Ayala, S.; Cromwell, O. R.; Guan, Z. *J. Am. Chem. Soc.* **2014**, *136*, 16128. Copyright 2014 American Chemical Society.